PLANAR DYNAMICS AND CONTROL OF TETHERED SATELLITE SYSTEMS

by

SATYABRATA PRADHAN

B.Sc.(Engg., Honours), Sambalpur University, India, 1987
M.E.(Distinction), Indian Institute of Science, Bangalore, India, 1989

A THESIS SUBMITTED IN PARTIAL FULFILMENT OF
THE REQUIREMENTS FOR THE DEGREE OF

DOCTOR OF PHILOSOPHY

in

The Faculty of Graduate Studies
Department of Mechanical Engineering

We accept this thesis as conforming
to the required standard

THE UNIVERSITY OF BRITISH COLUMBIA

December 1994

In presenting this thesis in partial fulfilment of the requirements for an advanced degree at the University of British Columbia, I agree that the Library shall make it freely available for reference and study. I further agree that permission for extensive copying of this thesis for scholarly purposes may be granted by the head of my department or by his or her representatives. It is understood that copying or publication of this thesis for financial gain shall not be allowed without my written permission.

(Signature)

Department of Mechanical Engineering

The University of British Columbia
Vancouver, Canada

Date 4 January 1995

DE-6 (2/88)

ABSTRACT

A mathematical model is developed for studying the inplane dynamics and control of tethered two-body systems in a Keplerian orbit. The formulation accounts for:

- elastic deformation of the tether in both the longitudinal and inplane transverse directions;
- inplane libration of the flexible tether as well as the rigid platform;
- time dependent variation of the tether attachment point at the platform end;
- deployment and retrieval of the point mass subsatellite;
- generalized force contributions due to various control actuators (e.g. momentum gyros, thrusters and passive dampers);
- structural damping of the tether;
- shift in the center of mass of the system due to the tether deployment and retrieval.

The governing nonlinear, nonautonomous and coupled equations of motion are obtained using the Lagrange procedure. They are integrated numerically to assess the system response as affected by the design parameters and operational disturbances.

Attitude dynamics of the system is regulated by two different types of actuators, thruster and tether attachment point offset, which have advantages at longer and shorter tether lengths, respectively. The attitude controller is designed using the Feedback Linearization Technique (FLT). It has advantages over other control methods, such as gain scheduling and adaptive control, for the class of time varying systems under consideration. It is shown that an FLT controller based on the rigid system model, can successfully regulate attitude dynamics of the original flexible

system. A hybrid scheme, using the thruster control at longer tether lengths and the offset control for a shorter tether, is quite attractive, particularly during retrieval, as its practical implementation for attitude control is significantly improved. Introduction of passive dampers makes the hybrid scheme effective even for vibration control during the retrieval.

For the stationkeeping phase, the offset control strategy is also used to regulate both the longitudinal as well as inplane transverse vibrations of the tether. The LQG/LTR based vibration controller using the offset strategy is implemented in conjunction with the FLT type attitude regulator utilizing thrusters as before. This hybrid controller for simultaneous regulation of attitude and vibration dynamics is found to be quite promising. The performance of the vibration controller is further improved by introduction of passive dampers. The LQG based vibration controller is found to be robust against the unmodelled dynamics of the flexible system.

Finally, effectiveness of the FLT and LQG based offset controllers is assessed through a simple ground based experiment. The controllers successfully regulated attitude dynamics of the tethered system during stationkeeping, deployment and retrieval phases.

TABLE OF CONTENTS

LIST OF SYMBOLS

$\bar{d}_p$	offset of the tether attachment point; distance between the origins of coordinate systems F_p and F_t
d_{py}	$y-$component of $\bar{d}_p$, $D_{py} + D_y$
d_{pz}	$z-$component of $\bar{d}_p$, $D_{pz} + D_z$
$\bar{d}_s$	distance between the tether attachment point and the subsatellite centre of mass at the subsatellite end
$\bar{f}_t(y_t)$	flexible deformation vector of the tether at a distance of y_t along the axis Y_t
$\bar{i}_n$	unit vector along X_n, $n = p, t, s$
$\bar{j}_n$	unit vector along Y_n, $n = p, t, s$
$\bar{j}_o$	unit vector along the local vertical
$\bar{k}_n$	unit vector along Z_n, $n = p, t, s$
$\{l_i\}$	direction cosines of the local vertical (Y_o-axis) with respect to the i^{th} body fixed frame
m_1	$m_s L + \rho_t L^2/2$
m_2	$m_s + \rho_t L$
m_a	$\rho_t L + m_o + m_s$
m_c	$1 - m_a/M$
m_o	mass of the offset mechanism
m_p	mass of the platform
m_s	mass of the subsatellite
m_t	mass of the deployed tether, $\rho_t L(t)$
m_{α_t}	$m_s L^2 + \rho_t L^3/3$

q	vector of the generalized coordinates or parameter for the LQG/LTR design
$\bar{r}_i$	position of an elemental mass on the i^{th} body with respect to the i^{th} body fixed frame
t	time
$u_t(y_t, L, t)$	deformation of the tether along the X_t–direction
$v_t(y_t, L, t)$	deformation of the tether along the Y_t–direction
$w_t(y_t, L, t)$	deformation of the tether along the Z_t–direction
y_t	distance measured along the Y_t–axis
A	cross–sectional area of the tether or the system matrix in the linear state equation
A_i	i^{th} mode generalized coordinate for the out-of-plane transverse tether vibration
$\{B\}$	$\left\{B_i\right\}_{i=1}^{N_l}$
$\{B_e\}$	equillibrium value of $\{B\}$
B_i	i^{th} mode generalized coordinate for the longitudinal tether vibration
$\{C\}$	$\left\{C_i\right\}_{i=1}^{N_t}$
C_{dl}	damping coefficient of the passive damper along the tether
C_{dt}	damping coefficient of the passive damper perpendicular to the tether
C_i	i^{th} mode generalized coordinate for inplane transverse tether vibration
$\{D\}$	offset vector required by the controller
$\{D_p\}$	specified offset vector
D_{py}	specified offset along the local vertical, $y-$component of $\{D_p\}$

D_{pz}	specified offset along the local horizontal, $z-$component of $\{D_p\}$
D_y	offset required by the controller along the local vertical, $y-$component of $\{D\}$
D_z	offset required by the controller along the local horizontal, $z-$component of $\{D\}$
E^*	equivalent Young's modulus of the tether material in the presence of structural damping, $E + iE_I$
E	real component of E^*; Young's modulus of the tether material in the absence of structural damping
E_I	imaginary part of E^*
$F(q, \dot{q}, t)$	vector of nonlinear terms in the equations of motion due to centrifugal, gravitational, and coriolis force contributions
F_{dl}	damping force along the undeformed tether due to passive damper
F_{dt}	damping force perpendicular to the undeformed tether due to passive damper
$F_i,\ i = p, t, s$	i^{th} body fixed frame
F_o	orbital frame
F_I	inertial frame
F_p	platform body–fixed frame
F_t	tether body–fixed frame
F_s	subsatellite body–fixed frame
$\{F_\phi\}$	$\left\{\Phi_i(y_t, L)\right\}_{i=1}^{N_t}$
$\{F_\psi\}$	$\left\{\Psi_i(y_t, L)\right\}_{i=1}^{N_l}$

G	universal gravitational constant
$[I_i]$, $i = p, t, s$	inertia dyadic of the i^{th} body with respect to the frame F_i
I_{px}, I_{py}, I_{pz}	moments of inertia of the platform about the X_p, Y_p and Z_p axes, respectively
I_{pyz}	product of inertia of the platform about Y_p, Z_p axes
L	unstretched length of the tether
$\dot{L}$	deployment/retrieval velocity
M	total mass of the system, $m_p + m_o + \rho_t L + m_s$
M_e	mass of Earth
$M(q,t)$	mass matrix
M_x	torque applied by the control moment gyros about the X_p axis
N_l	number of admissible functions used to represent longitudinal vibration of the tether
N_t	number of admissible functions used to represent inplane transverse vibration of the tether
N_{tl}	$N_t + N_l$
Q_q	vector of generalized forces corresponding to generalized coordinates q
$\bar{R}_c$	orbit radius
$\bar{R}_{dm_i}$, $i = p, t, s$	position vector of an elemental mass in the i^{th} body with respect to the inertial frame
$\bar{R}_i$, $i = p, t, s$	distance between the origin of the i^{th} body fixed frame (F_i) and the orbital frame
$\bar{R}_{SM}$, $\{R_{SM}\}$	shift in the centre of mass of the system; also distance between the origins of F_p and F_o

R_{SM_y}	shift in the centre of mass along the local vertical
R_{SM_z}	shift in the centre of mass along the local horizontal
T_i	kinetic energy of the i^{th} body
T	kinetic energy of the entire system
$[T_{ij}]$	transformation matrix from the frame F_j to the frame F_i
T_L	control thrust along the undeformed tether applied at the subsatellite end
T_{α_t}	control thrust perpendicular to the undeformed tether applied at the subsatellite end
U_{G_i}	gravitational potential energy of the i^{th} body
U_G	gravitational potential energy of the entire system
U_S	strain energy of the system
U	potential energy of the system, $U_S + U_G$
V_t	volume of the unstretched tether, $AL(t)$
$\alpha_i, \beta_i, \gamma_i, i = p, t, s$	Euler angles between the frames F_i and F_o
θ	true anamoly
$\dot{\theta}$	orbital angular velocity
$\ddot{\theta}$	orbital angular acceleartion
$\{\omega_i\}, i = p, t, s$	angular velocity of the i^{th} body fixed frame with respect to the inertial frame
ρ_t	mass per unit length of the tether
ϵ	strain in an elemental tether mass
μ	$GM_e/2R_c^3$
σ	stress in an elemental tether mass without energy dissipation
σ_d	stress in the tether causing energy dissipation

η	E_I/E
$\Phi_i(y_t, L)$	i^{th} shape function for the tether transverse vibration
$\Psi_i(y_t, L)$	i^{th} shape function for the tether longitudinal vibration

Dot above a character refers to differentiation with respect to time

Subscripts 'p', 't', and 's' refer to platform, tether and subsatellite, respectively

LIST OF FIGURES

LIST OF TABLES

ACKNOWLEDGEMENT

I am thankful to Prof. V. J. Modi and Prof. A. K. Misra (McGill University, Canada) for their guidance throughout the research project.

A word of appreciation must be extended to my colleagues, Dr. C. A. Ng, Dr. A. K. Grewal, Dr. S. Hokamoto and Dr. F. Karray, for useful discussions and suggestions as well as to Dr. I. Marom, Mr. S. R. Munshi, Mrs. M. Seto and Mr. Y. Chen for their advice in planning of the experimental test-program. Assistance of Mr. John Richards in construction of the electronics hardware used during the experimental study is gratefully acknowledged.

The research project was supported by the Natural Sciences and Engineering Research Council's grant (A-2181) held by Prof. V. J. Modi.

1. INTRODUCTION

1.1 Preliminary Remarks

Over the past decades, a number of proposals have been made for the space exploration using Tethered Satellite Systems (TSS). The concept involves two or more satellites connected by a tether upto $100km$ in length (Fig.1-1). In a typical mission, the Space Shuttle carries the tether connected subsatellite payload. After a desired orbit is achieved, the subsatellite is deployed from the orbiter to the required altitude. Intended scientific measurements are carried out at a fixed tether length. Subsequently the subsatellite is retrieved back to the Shuttle (Fig.1-1).

The innovative idea of the TSS is attributed to the Russian scientist Tsiolkovsky, who explored the effect of gravity force on an individual climbing up a tower extending upto geosynchronous altitude and beyond [1]. This analysis uncovered the principle that a string orbiting in a central force field always remains in tension due to the gravity gradient, and led to the development of the TSS. So far as the actual application is concerned, interest in the system was initially associated with the retrieval of a stranded astronaut by throwing a buoy on a tether from a rescue vehicle and reeling in the tether. Starly and Adlhock [2] have shown that the rotational motions of the tether grow continuously as it was reeled in. A proposal was made to use tether for stationkeeping between two orbiting space vehicles [3], however, the idea was abandoned due to the difficulties involved in determining and controlling the required tether tension. On the other hand, Gemini XI and XII flights have successfully demonstrated useful applications of a tethered system [4]. The former used a rotating configuration aimed at artificial gravity generation while

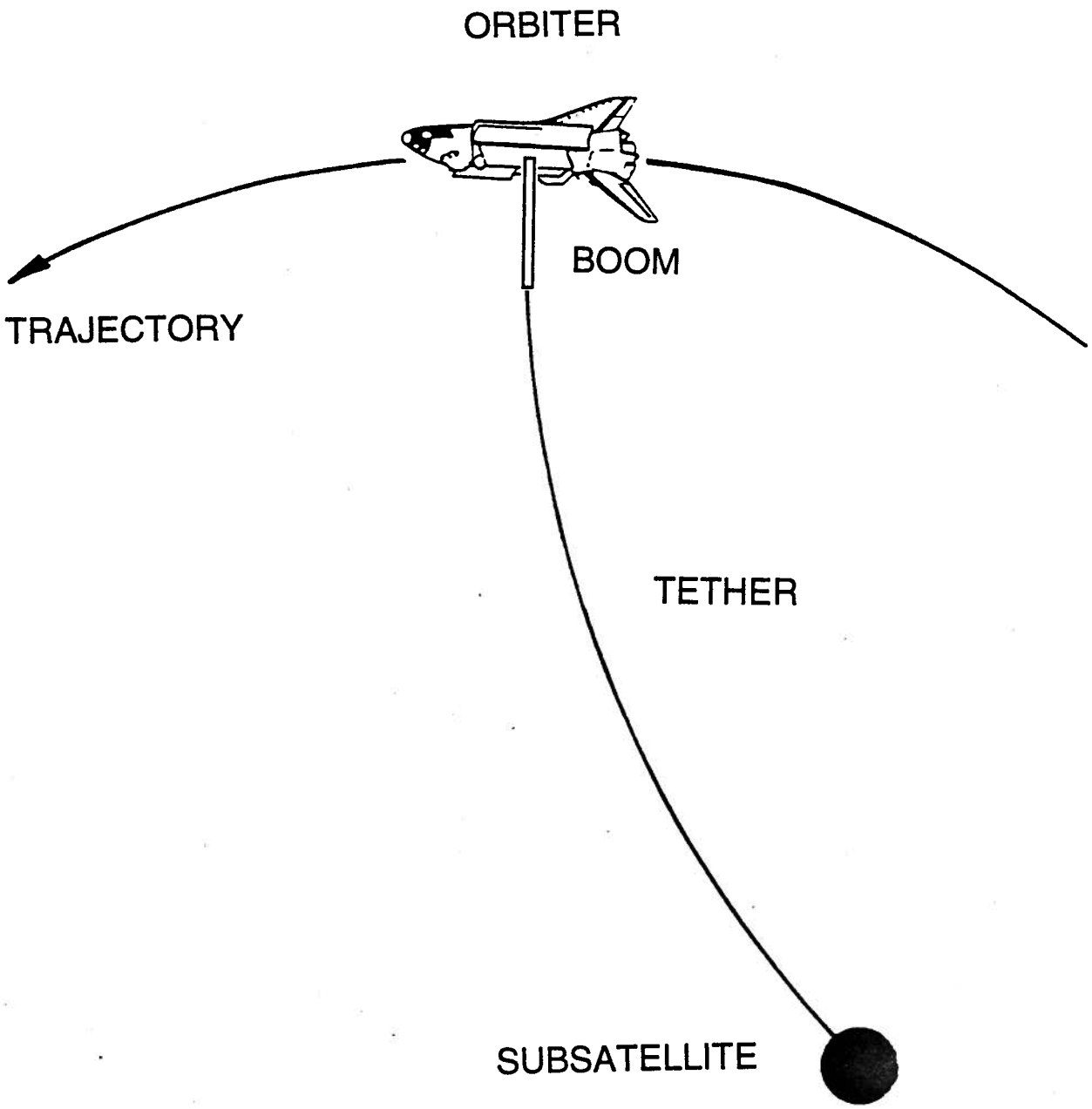

Figure 1-1 Schematic diagram of the Space Shuttle based Tethered Satellite System (TSS).

the latter had a gravity-gradient stabilized configuration.

After one and half decade, a joint U.S.A.–Japan space project called the TPE (Tethered Payload Experiment) used a sounding rocket based tether to conduct a series of tests aimed at near earth environmental studies [5]. The technical and scientific data obtained in the TPE supported the electrodynamic tether mission TSS-1 (Tethered Satellite System-1) launched in August 1992 [6]. The TSS mission is a collaborative project between NASA and the Italian space agency (ASI). Because of the mechanical failure, the mission objectives of the TSS-1 were not met, but the information gathered during the short deployment upto 259 m, as compared to the desired length of 20 km, demonstrated the fundamental concepts of orbital tether flights in many ways. Another series of sounding rocket experiments called the OEDIPUS (Observation of Electrified Distributions in the Ionosheric Plasma – a Unique Strategy) are being carried out by the Canadian Space Agency (CSA) [7]. The objective is to make passive observation of the auroral ionoshere and gain better insight into pane and sheath–wave propagation in plasmas using a radio transmitter. The first mission, called OEDIPUS-A, was successfully launched in January 1989 which deployed a tether upto 958 m. The next mission, OEDIPUS-C, planned for January 1995, will include a payload for tether dynamics measurements.

The deployment of 20 km long tether was successfully completed in SEDS (Small Expendable Deployment System) missions [8]. SEDS-I and SEDS-II missions flew in March 1993 and March 1994, respectively. Each deployed a 26 kg instrumented probe to a distance of 20 km from the second stage of a DELTA II rocket while in orbit around the Earth. These tether missions have successfully demonstrated the feasibility of tether deployment. On the other hand, retrieval of a tether still remains to be realized in a real flight. With the advent of the Space Shuttle and

the proposed Space Station, several applications of the tethered subsatellite system has been suggested which can be summarised as:

- sophisticated scientific experiments aimed at gravity gradient, magnetic, ionospheric, aero-thermodynamics and radio astronomy experiments (e.g. OEDIPUS-A and C);
- use of tethered system as a flying wind tunnel [9];
- deployment of payloads to new orbits [10] and retrieval of satellites for servicing;
- provision of a desired controlled microgravity environment for scientific experiments and space manufacturing [11];
- generation of electricity (electrodynamic tether, TSS-1);
- power and cargo transfer between two orbiting bodies;
- collection of atmospheric dust by a small probe tethered to a larger orbiting spacecraft thus avoiding landing [12];
- expansion of the geostationary orbit resource by having tethered chain satellites [13, 14];
- large antena reflector (≈ 1 km aperture) using tethers for gravity gradient stabilization and shape control [15];
- orbiting optical astronomical interferometer consisting of three telescopes at the corners and one at the center of a tethered triangle [16];
- use of multiple tethers for attitude stabilization of satellites in elliptic orbit [17];

and many others [10, 18]. Some of these applications are illustrated in Fig.(1-2).

The fundamental principle governing the tether dynamics can be illustrated

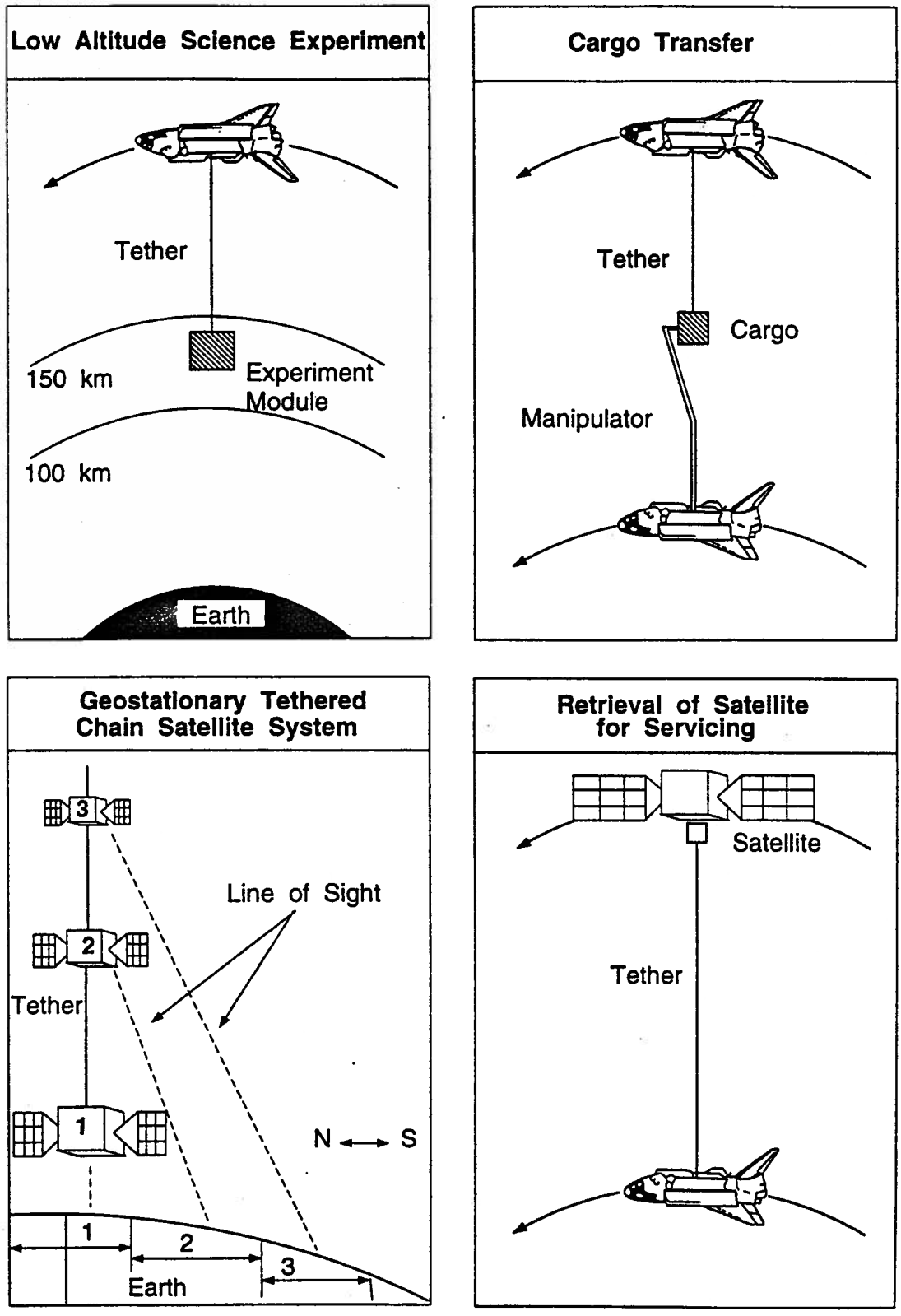

Figure 1-2 Some applications of the tethered satellite systems.

by a simple two-body tethered system as shown in Fig.1-3. Consider a 'dumbbell' satellite in a circular orbit around the Earth. The top mass experiences a larger centrifugal force than the gravitational force, being in an orbit higher than that of the centre of mass. The reverse occurs at the lower mass. The resultant moment causes the system to oscillate like a pendulum with the tether maintained taut under tension. Now, as the length of the tether decreases during retrieval, the conservation of angular momentum dictates the swinging oscillation of the tether to amplify. For a space platform supported tethered satellite system, the swing motion could increase to the point that the tether wraps itself around the platform. Furthermore, reduced gravity induced tension at smaller lengths together with large amplitude oscillations may render the tether slack. The presence of any offset between the tether attachment point and the centre of mass of the end-bodies (platform and subsatellite) imposes an additional moment on the bodies involved. Flexibility of the tether, along with the above mentioned factors makes the system dynamics rather challenging. Obviously, a fundamental understanding of complex interactions between librational dynamics, flexibility, deployment and retrieval maneuvers, as well as development of appropriate control strategies is essential for successful completion of the proposed tether missions.

1.2 Review of the Relevant Literature

The possible applications of the TSS being numerous and diverse, considerable amount of literature has developed, particularly during the past 30 years, which was reviewed quite effectively by Misra and Modi [19, 20]. The growing importance of this new technology is reflected in a special issue published in *The Journal of the Astronautical Sciences* [21]. Objective here is to briefly touch upon more important

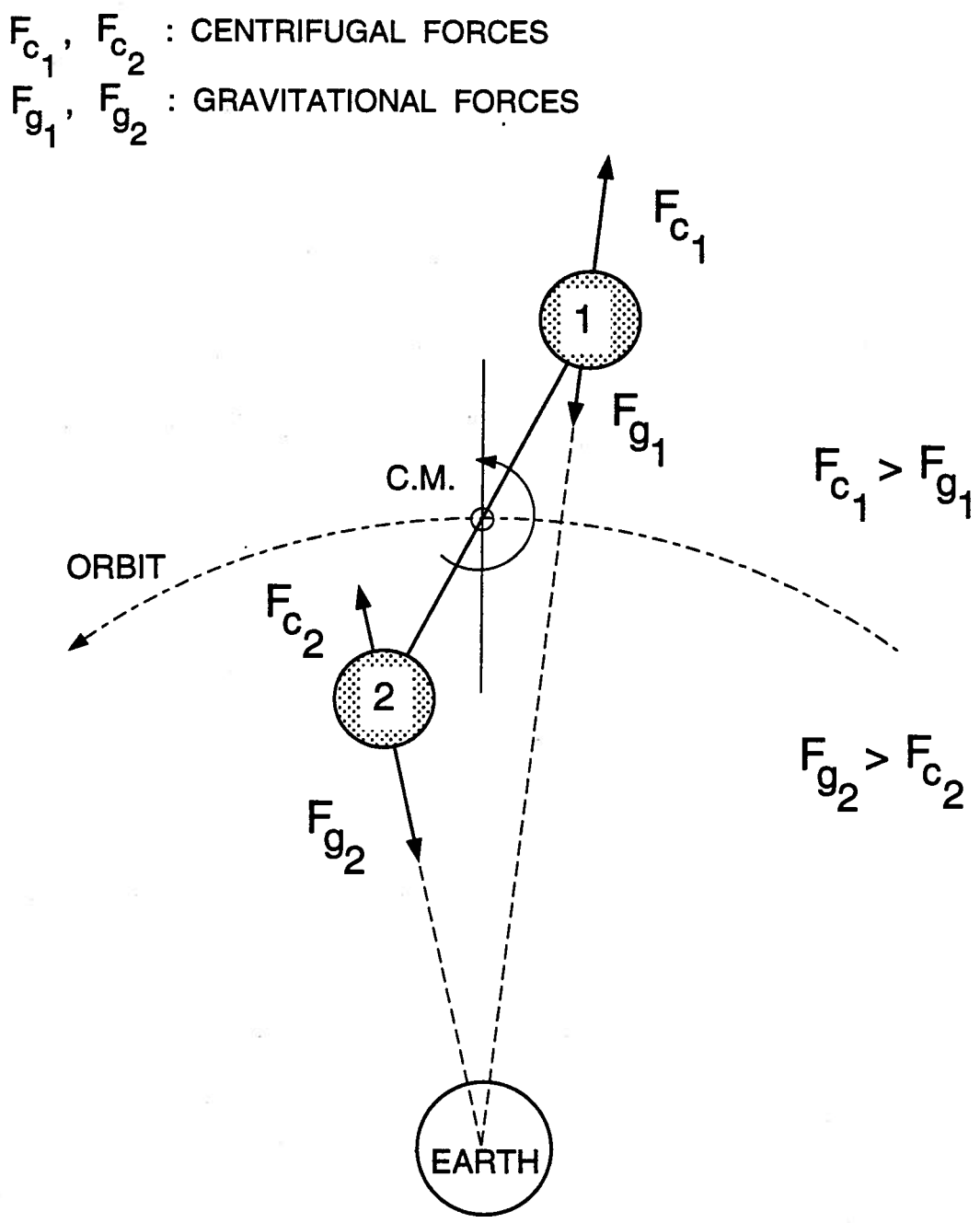

Figure 1-3 Dumbbell satellite and the associated forces.

contributions directly relevant to the present study.

1.2.1 Dynamical modelling

The dynamics of a TSS consists of three major phases of operation depending on whether the unstretched length of the tether is constant (stationkeeping phase) or varies with time (if increasing, deployment; when decreasing, retrieval). The dynamics during stationkeeping is simpler than the other two phases and is quite similar to that of other cable connected bodies, e.g. the space station-cable-counterweight system [22]. It has been investigated extensively by various researchers who concluded that the gravity gradient can excite longitudinal as well as transverse vibrations of the tether [22, 23]. However, a small amount of damping (1% of the critical damping) is quite effective in stabilizing the system [24].

Perhaps the first systematic effort at understanding dynamics of the TSS was made by Rupp [25]. In his pioneering study, the librational motion in the orbital plane was analyzed and the growth of pitch oscillations during retrieval phase noted. The system was further investigated by Baker *et al.* [26] taking into account the three dimensional character of the dynamics as well as the aerodynamic drag in the rotating atmosphere. During either deployment or retrieval, the out-of-plane rotational motion cannot be neglected if the orbit is in a nonequatorial plane. It is excited by the rotating atmosphere induced aerodynamic drag. Even when the orbit is in the equatorial plane, the initial out-of-plane disturbances may couple the inplane and out-of-plane dynamics. Fortunately, in general, such disturbances are found to be small. Furthermore, their effects can be minimized through the design of an appropriate active control system. Thus the coupling between the inplane and out-of-plane motions can be neglected, for systems in the equatorial orbit, at least

in the preliminary design stage.

The other important parameters, which make the system dynamics complicated, are mass and flexibility of the tether. The mass of the tether is expected to be of the same order of magnitude as that of the subsatellite, particularly when the tether is long, and hence it can not be neglected. Because the tether diameter is expected to be small (around few millimeters) and the length quite long (upto 100km), the system shows considerable flexibility (the longitudinal stretch for a 100km long tether can be around hundred meters). The axial vibration has been represented in an approximate fashion by a single longitudinal displacement similar to that of a spring mass system by several authors [26, 27, 28]. However, as the mass is distributed along the tether, a more accurate representation in terms of combination of axial modes, similar to that of an elastic bar, would be more appropriate [29, 30].

Furthermore, the tether can have transverse displacements causing it acquire curvature. This happens mainly due to two reasons. The aerodynamic drag not only causes the subsatellite to lag behind the platform but also forces the tether to assume a curved equilibrium position. Secondly during deployment or retrieval, the Coriolis force acts in the transverse direction. Since the tether has distributed mass and elasticity, transverse vibrations are also excited. They can influence system dynamics substantially, particularly during retrieval [31]. The transverse oscillations of the tether have been studied using two distinct approaches. Quadrelli and Lorenzini [32] discretized the system using the lumped-mass approach. On the other hand, Kohler et al. [33], Modi and Misra [27], and Xu, Misra and Modi [30] adopted the continuum model with admissible functions. To reduce the computational effort involved in simulation, a combination of lumped-mass and continuum model has been proposed called the *semi-bead model* [34].

When the masses of the two end bodies are comparable, the system centre of mass does not remain fixed with respect to any of the body fixed frames. The shift in the centre of mass may become an important parameter in such situation and has to be accounted for. The major conclusions based on the available literature may be summarized as follows:

- stationkeeping phase is normally stable;
- deployment can be an unstable operation if velocity exceeds the critical rate;
- retrieval is inherently unstable ;
- particularly during the deployment and retrieval phases, the transverse vibrations can build up due to the Coriolis force induced excitation even though there may not be any initial disturbance.

The other aspects of practical importance are the damping in the tether [35], aerodynamics drag [36, 37], and orbital lifetime analysis [38]. The dynamics of tethered systems in different configurations, which has less relevance to the present study, have been addressed by Misra and Diamond [39], and DeCou [40, 16]. In real systems, there is always a chance of accident. The dynamics of the tether connected to the orbiter after a catastrophic failure has been studied by Bergamaschi [41].

1.2.2 Control of the TSS

Control of the TSS, particularly during deployment and retrieval, is a challenging problem. Successful control of the unstable retrieval dynamics is of great concern since it is directly related to the success of the mission. Over the years, several control strategies have been proposed, which can be categorized into three types:

(a) tension control and the law based on rotational rate of the tether reel (length

rate control or torque control);

(b) thruster augmented active control;

(c) offset control.

(a) Tension and length rate control

Among the control laws mentioned, the tension control law was developed first. Rupp [25] formulated this strategy to control the inplane rotation during deployment and stationkeeping. The retrieval problem was also touched upon briefly. Here the tension level is modulated as a function of the instantaneous length, length rate, and desired lengths of the tether. Several investigators have subsequently modified Rupp's tension control procedure, however the inherent approach remains the same [26, 42–44]. For example, Bainum and Kumar [44] developed an optimal control law, based on an application of the linear regulator theory, which modulates the tether tension to achieve acceptable level of the tether swing.

As opposed to the tension control law, in the length rate scheme the 'nominal' unstretched length or its time derivative are modulated to achieve the desired system response. The law corresponds to modulating the rotation of the reel of the deployment mechanism. This can also be implemented by monitoring the torque applied to the reel mechanism. In principle, tension control, length rate control and torque control affect the system dynamics by changing the tension in the tether. The differences are in the mathematical modelling of the system used for the controller design and its implementation. This type of control law was originally proposed by Kohler et al. [33], and used by Misra and Modi [45] and others to regulate the planar longitudinal and transverse vibrations.

(b) Thruster augmented active control

During retrieval, as length of the tether reduces to a small value, the equilibrium tension in the tether due to gravity gradient approaches zero; and during a dynamical situation, the tether may become slack. Thus a tension control law or its modification, such as a length rate law, becomes ineffective. To alleviate this difficulty, Banerjee and Kane [46], and Xu *et al.* [47] used a set of thrusters to control the retrieval dynamics. In this active control scheme, the thrusters are placed at the subsatellite end to help reduce the motion and speed up the retrieval process. The thrusters provide control forces in both transverse and longitudinal directions.

(c) Offset control strategy

It has been shown that, when the tether length is small the thruster augmented control is quite effective; however firing of thrusters in the vicinity of the shuttle or space platform is considered undesirable due to plume impingement, safety and other considerations. To overcome this difficulty the "offset control strategy" was proposed by Modi, Lakshmanan and Misra [48]. Here, the point of attachment of the tether at the platform is moved to control the tether swing. The coupling of the offset acceleration and tether swing makes this control strategy a success. In their study, Modi *et al.* considered a 3-dimensional rigid model without any shift in the centre of mass. The results obtained from the numerical simulation were verified by a ground based experimental set-up. From the comparison between numerical and experimental results, they concluded the control strategy to be quite promising for shorter tethers. Because of relative advantages and disadvantages of different schemes, a desirable solution would be to use a hybrid strategy, where the offset control is implemented at shorter lengths while the thruster, tension or length rate

control scheme is used for longer tethers [49].

1.2.3 Control algorithms

An important factor which needs careful attention is the methodology used to obtain the control laws. In the pioneering work by Rupp [25], the feedback gains were selected to achieve an appropriate stiffness and damping in the closed-loop system. This approach is feasible only when the system dynamics is relatively simple, which is not the case in practice. Since then, linear and non-linear control laws have been developed by many investigators (for example [26]), where the control gains are obtained by trial and error.

Among the wide variety of control methodologies, the Linear Quadratic Regulator (LQR) has received considerable attention [44, 48, 49]. On the other hand, a feedback control law using the second method of Liapunov was used by Vadali and Kim [50, 51]. It was concluded that the tension control law is sufficient during fast deployment, however, thruster augmentation in the out-of-plane direction is required during the terminal phase of the retrieval [51]. The existence of limit cycles was avoided by the out-of-plane thrusting in conjunction with the tension control [50]. Monshi *et al.* [52] used the reel rate control law with nonlinear roll rate feedback, based on energy dissipation method. It was found to have better performance than that for the law developed using the Liapunov method. The study showed that the retrieval constant c ($c = l'/l$; l', nondimensionalized retrieval rate; l, instantaneous tether length), in case of an exponential retrieval, does not have a significant effect on limit cycle amplitude. As the retrieval rate increases the peak value of the pitch oscillation also increase. So the maximum retrieval rate is limited by a maximum allowable pitch angle. The limit cycle amplitude found in [52] is

quite close to that obtained by Vadali and Kim [50].

In the study by Liaw and Abed [53], tension control laws were established using the Hopf bifurcation theorem, which guarantees stability of the system during the stationkeeping mode. They also suggested a constant inplane angle control method which results in stable deployment but unstable retrieval. In this method, the instantaneous tether length is treated as an external control input, and the length rate is obtained as a function of some desired inplane equilibrium angle. The length rate expression required to control the system during deployment does not stabilize the retrieval dynamics.

Fleurisson *et al.* [54] designed an observer (Kalman filter) based controller to follow a predetermined retrieval length history. The length history was obtained to minimize a combination of final pitch angle, pitch rate at docking and total retrieval time. The control strategy used feedforward trajectories motivated by optimal control arguments. Optimal control procedure was employed to determine an invariant final approach path, or randezvous corridor, which the satellite must follow during the terminal phase to dock with the specified final conditions. The study focused only on the last 2 *km* of the retrieval.

In the study by Fujii *et al.* [55], the dynamics during deployment and retrieval is controlled by regulating the mission function, a positive definite quadratic function of the mission states. The desired value of the system states are referred to as the 'mission states'. For the closed-loop system, the non-dimensional time derivative of the mission function is set to be negative definite, guaranteeing stability of the system. Thus, the approach is quite similar to the Lyapunov's second method.

Onoda and Watanabe [56] as well as Fujii *et al.* [57] studied control of teth-

ered systems in the presence of atmospheric drag. Attitude control of the tethered systems after blocking of the attachment point has been explored by Grassi, *et al.* [58]. The offset control, as discussed before, is for regulating the attitude motion of the tether. However, this strategy can also be used for precise control of the subsatellite attitude, where the control moment can be generated by a combined effect of tether tension and the attachment point motion [59]. Numerous variations of the control algorithms discussed here are also reported in the literature.

Almost all the investigations reported so far deal with the control of attitude motion of the tether or the endbodies. Little attention has been directed towards the control of structural vibrations of the tether. Xu *et al.* [30, 47] addressed the problem of control of tether oscillations using length rate and thruster control. On the other hand, the study by Thornburg and Powell [60] considers the control of only transverse vibration in conjunction with the offset strategy.

As seen in this literature review, the models developed so far do not include the attachment point offset for a flexible tethered system capable of deployment and retrieval. The study in reference [60] incorporates the motion of the attachment point, of a flexible tether, along a line parallel to the end body's floor (i.e. motion along one bodyfixed axis), however, it does not include the most critical operational phases, deployment and retrieval. The tether is modelled as an arbitrary number of point masses connected by elastic members. Use of the lumped mass model for a continuum system may be appropriate for a preliminary study, however, any detailed analysis of the system needs the more accurate continuum model. With the offset motion restricted to be parallel to the subsatellite floor, the strategy is limited only to the control of transverse oscillations. Furthermore, the analysis does not account for the shift in the center of mass, an important parameter for long tethers during

deployment and retrieval maneuvers.

1.3 Scope of the Present Investigation

With this as background, the thesis aims at studying dynamics and control of two-body tethered systems, using a relatively general model, which is the fundamental requirement for their successful realization. Distinctive features of the model may be summarized as follows:

(i) A flexible tether, with arbitrary mass distribution and finite dimensional rigid end bodies, is taken to be in a general Keplerian orbit. The tether is treated as an elastic continuum during the system discretization.

(ii) Offset of the tether attachment point from the end body's center of mass and its time dependent variations are included in the formulation. This permits development of several offset control strategies. Furthermore, the formulation is amenable to thruster augmented active control and its hybrid synthesis with the offset control procedure.

(iii) The formulation accounts for time dependent variation of the tether length, thus permitting analysis of the tether performance during all the three operational phases of importance – deployment, stationkeeping and retrieval. The deployment/retrieval time histories are considered arbitrary.

(iv) Kinetic and potential energy expressions are obtained for the general three dimensional (i.e. in the orbital plane and out-of the orbital plane) motion of the system. However, the governing equations of motion and hence the study based on them are purposely confined to the inplane dynamics. This helped focus on more important aspects of the system performance which are governed by a large number of variables. Furthermore, some appreciation of

the coupling between the inplane and out-of-plane dynamics is already available through early studies (by the U.B.C. group and others) using simpler models.

(v) The formulation is based on the Lagrangian procedure which can account for both holonomic and nonholonomic constraints.

(vi) As can be expected the governing equations of motion are highly nonlinear, nonautonomous and coupled. Their decoupled, linearized forms are also obtained to facilitate the controller design.

(vii) Numerical integration codes for nonlinear and linear systems are so structured as to help isolate effects of design parameters on the system performance.

To begin with, kinematics and kinetics of the system, leading to a set of highly Coupled, Nonlinear and Nonautonomous (CNN) equations of motion, are discussed in Chapter 2. This is followed by a brief account of the numerical integration methodology as applied to the nonlinear as well as decoupled linearized system (Chapter 3). Validation of the formulation by energy check and comparison of frequencies with reported results in the literature are also included here. Chapter 4 focuses on the parametric dynamical study using the complete CNN set of equations. Objective is to assess effect of the system design parameters on its performance, and establish critical conditions leading to unacceptable response or instability. This sets the stage for an effective controller design.

As pointed out before, the governing equations of motion are coupled, nonlinear and nonautonomous. To assist in the controller design, rigid and flexible parts of the system are often (but not always) decoupled due to their widely separated

frequencies. However, it must be emphasized that the coupling between the rigid degrees of freedom, and among the flexible generalized coordinates, was retained. Two different control methodologies, linear eigenvalue assignment and the nonlinear Feedback Linearization Technique (FLT), in conjunction with the actuators in the form of offsets, thrusters and their combinations were used. Attitude controller was developed first (Chapter 5) followed by a composite attitude-vibration regulator design (Chapter 6). In all the cases, effectiveness of the controller was assessed through its application to the original nonlinear, nonautonomous and coupled system.

Finally, in Chapter 7, a ground based facility for studying dynamics of a tethered system as well as its control using the offset strategy is described. Experimental results are compared with numerically obtained simulation data.

The thesis ends with a summary of results and recommendations for future work. Figure 1-4 presents an overview of the research project.

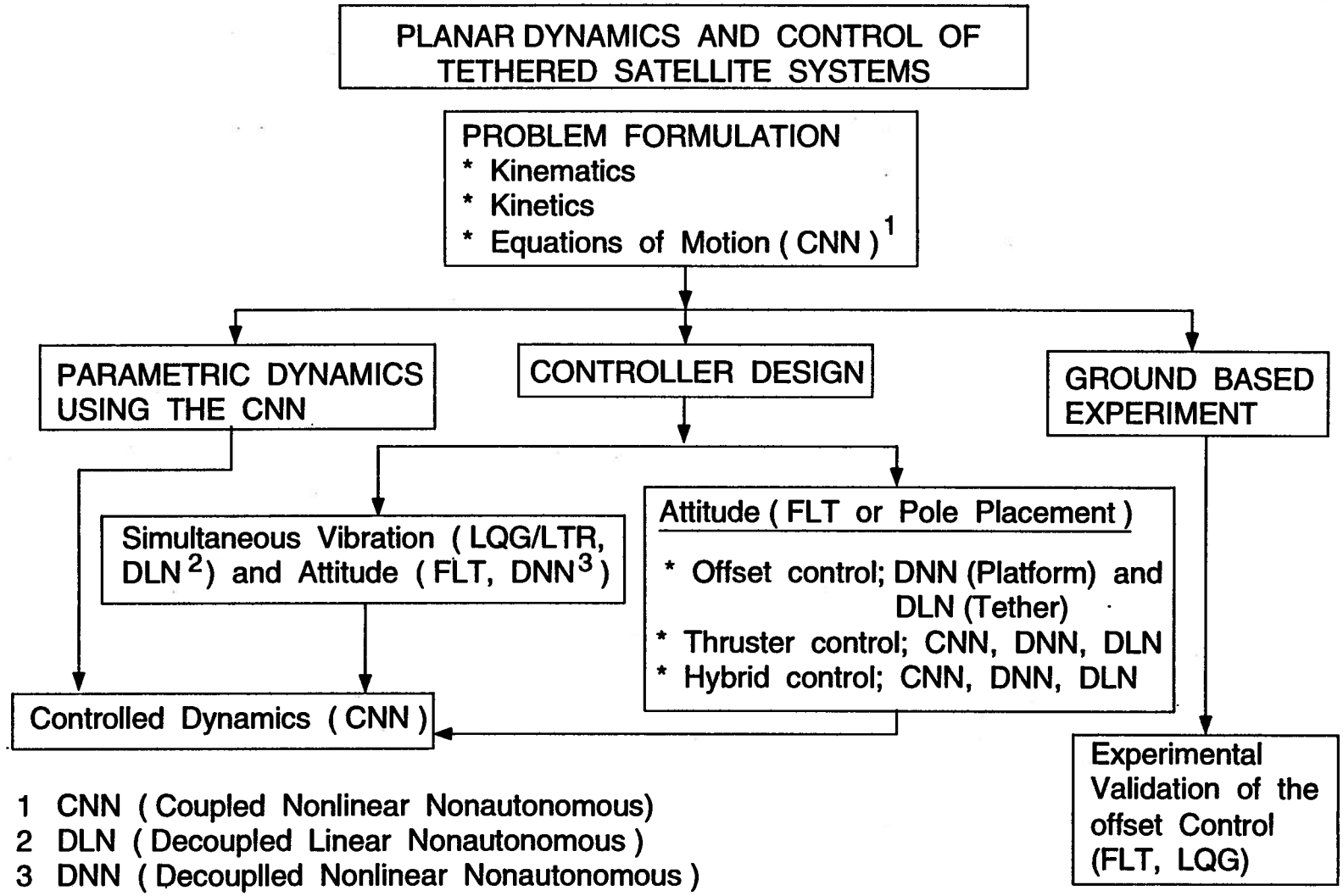

Figure 1-4 A schematic diagram showing the overview of the plan of study.

2. FORMULATION OF THE PROBLEM

2.1 Preliminary Remarks

Considerable thought was directed in arriving at a model of the complex tethered satellite system that would represent a logical step forward in understanding its dynamics and control. The model selected for study consists of a rigid platform connected by a flexible cable (tether) of finite mass density to a rigid subsatellite. The entire system is in an arbitrary Keplerian orbit and free to undergo librational as well as both longitudinal and transverse vibrations in the plane of the orbit. Furthermore, the tether can be deployed, retrieved or maintained at a constant length (stationkeeping). Deviation of the tether attachment from the platform center of mass is treated as a function of time permitting development of the offset control strategy. As in a practical situation, the platform based momentum wheels provide control torques for its attitude control. In addition, one may attempt to regulate the tether dynamics through an orthogonal set of thrusters at the subsatellite. Synthesis of the offset and thruster based strategies present interesting possibilities for a hybrid control design.

As pointed out before, in a typical mission under consideration, the tether may be deployed from a length of few meters to around 100 *km*. This results in a large change in the system inertia as well as a shift in the system center of mass with respect to a body fixed reference frame. Thus, a realistic model must account for the effect of shift in the center of mass on the system dynamics. The structural damping of the flexible tether is also an important parameter and hence included in the present formulation.

This chapter can be divided into three major sections: kinematics; kinetics; and equations of motion. System configuration and position of an elemental system mass in the inertial space are established first. This is followed by evaluation of the kinetic and potential energies of the system. Finally the governing equations of motion are derived using the Lagrangian procedure. The generalized forces due to active and passive control inputs are obtained using the principle of virtual work.

2.2 Kinematics of the System

2.2.1 Domains and reference coordinates

Four distinct domains can be established for the system described in Figure 2-1. Domain 'p' represents the rigid space platform. The frame F_p (X_p, Y_p, Z_p) is attached to the centre of mass of the platform with its axes along any arbitrary directions. Vectors described relative to this rotating frame are distinguished by the subscript 'p'. Mass of the platform is considered constant ($\dot{m}_p = 0$).

The tether involves two major domains. The domain 'o' consists of the offset mechanism and undeployed tether that is wrapped around a reel. In general, mass of the offset mechanism is expected to be quite small compared to the mass of the platform (Space Shuttle, Space Station). So, without any loss of generality, the offset mechanism is treated as a point mass and its location is expressed with respect to F_p by the vector $\bar{d}_p$. The mass of the offset mechanism is represented with subscript 'o'. As the tether is deployed or retrieved the mass of the spool, around which the tether is wound, changes. The deployed portion of the tether is flexible and belongs to the domain 't'. The frame F_t (X_t, Y_t, Z_t) has its origin at the point of attachment of the tether at the platform end. The Y_t-axis is along the undeformed length of the tether, i.e. the direction of tether in the absence of transverse deformation. The

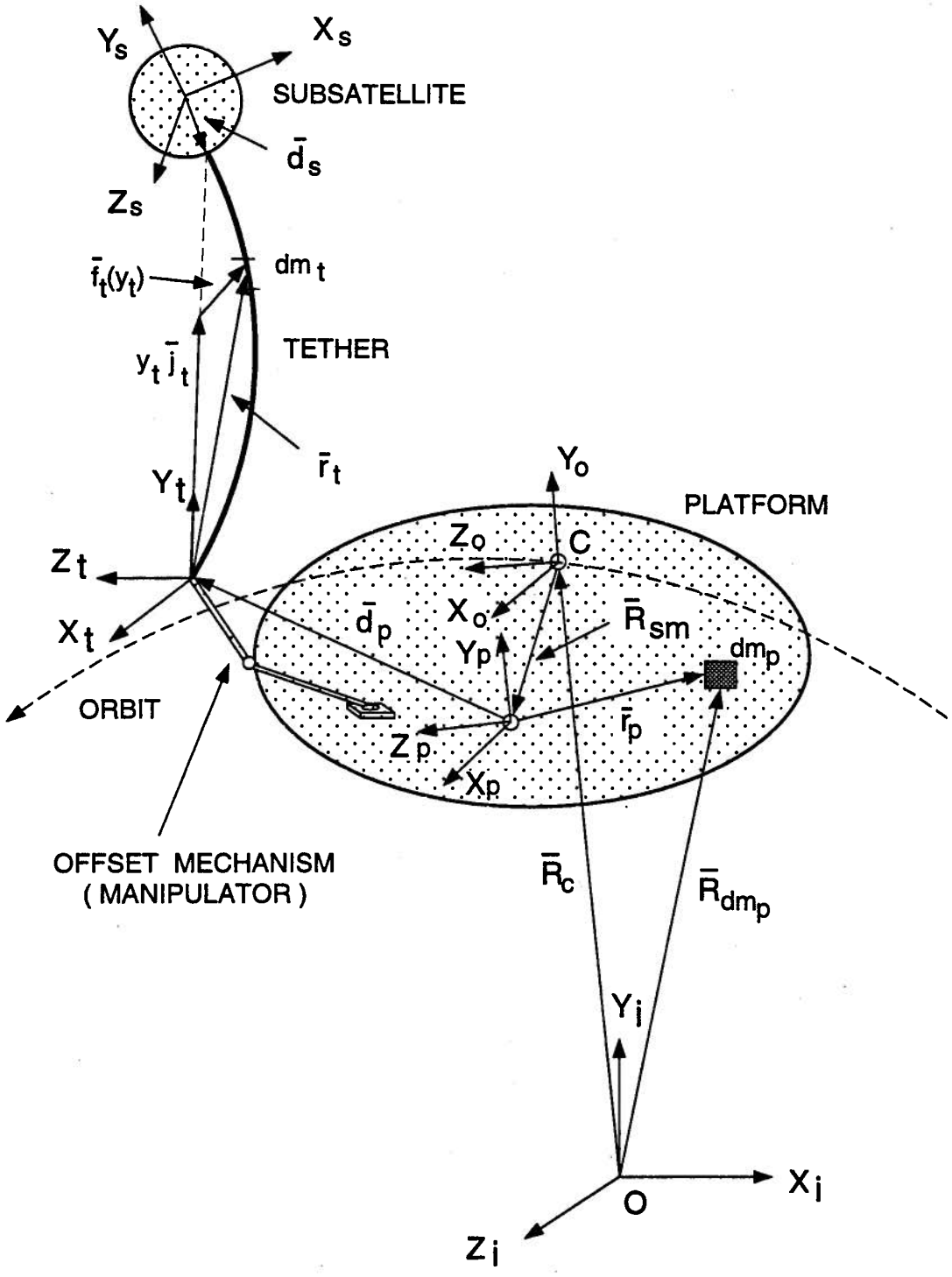

Figure 2-1 Domains and coordinate systems used in the formulation.

X_t-axis is so selected that, in absence of the out-of-plane motion, it is parallel to the orbit normal. The Z_t-axis completes the right-handed system. The mass of the deployed portion of the tether varies with time according to the deployment or retrieval rate. The total tether mass, composed of the deployed (domain 't') and undeployed (domain 'o') portions, is constant (i.e. $\dot{m}_t = -\dot{m}_o$).

Domain 's' consists of the rigid subsatellite attached to the end of the tether. The frame F_s (X_s, Y_s, Z_s) is used to describe its orientation in space. The origin of this frame is at the centre of mass of the subsatellite. Vectors measured relative to this rotating frame carry subscript 's'. Mass of the rigid subsatellite is constant $(\dot{m}_s = 0)$.

Two more reference frames are required to completely define the kinematics of a mass element in the system: the inertial frame F_I located at the centre of Earth; and the orbital frame F_o (X_o, Y_o, Z_o). The origin of the orbital frame is located at the instantaneous centre of mass of the system and follows a Keplerian orbit. The orbital frame is so oriented that the Y_o-axis is along the local vertical (the line joining the centre of Earth and instantaneous centre of mass of the system) and points away from Earth; the Z_o-axis is along the local horizontal (the line perpendicular to Y_o-axis and in the plane of the orbit) and points towards the direction of motion of the system; the X_o-axis is along the orbit normal and completes the right-handed triad.

2.2.2 Position vectors

With the reference frames selected, the position vector of an elemental system mass can be defined easily. As pointed out before, the instantaneous centre of mass of the system follows a Keplerian orbit. This is based on the assumption that the orbital motion is not affected by the librational (attitude) and vibrational motions

of the system [61–63]. The position vector to the mass element with respect to the inertial frame can be obtained by a set of vectors added in sequence. First of all, the position vector is defined with respect to the frame attached to the domain in which the mass element is located ($\bar{r}_i,\ i = p,t,s$). For bodies like the platform and subsatellite, $\bar{r}_p$ and $\bar{r}_s$ consist of only rigid components. But for the flexible tether, the position vector has contribution from two sources: rigid ($y_t\bar{j}_t$) and elastic deformation ($\bar{f}_t(y_t)$), i.e.

$$\bar{r}_t = y_t\bar{j}_t + \bar{f}_t(y_t),$$

where $\bar{j}_t$ is the unit vector along Y_t-axis, and y_t is the distance to the mass element from the origin of F_t. The position of the origin of the body fixed frames, $F_i,\ i = p,t,s$, is defined with respect to the orbital frame F_o by the vector $\bar{R}_i,\ i = p,t,s$. Finally, the origin of the orbital frame is defined with respect to the inertial frame by $\bar{R}_c$ (i.e. radius vector of the Keplerian orbit). With these notations, position of any elemental mass in the i^{th} domain with respect to inertial frame can be expressed as

$$\bar{R}_{\mathrm{d}m_i} = \bar{R}_c + \bar{R}_i + \bar{r}_i. \tag{2.1}$$

The vector $R_i,\ i = p,t,s$, can be expressed in terms of other vectors defined in the body fixed frames as:

$$\bar{R}_p = \bar{R}_{SM}; \tag{2.2}$$

$$\bar{R}_t = \bar{R}_{SM} + \bar{d}_p; \tag{2.3}$$

$$\bar{R}_s = \bar{R}_{SM} + \bar{d}_p + L\bar{j}_t + \bar{f}_t(L) - \bar{d}_s; \tag{2.4}$$

where:

$\bar{d}_p$ distance between origins of frames F_p and F_t expressed in F_p;

L undeformed length of the tether;

$\bar{j}_t$ unit vector along the Y_t-axis;

$\bar{f}_t(L)$ flexible deformation vector of the tether at a distance L from origin of F_t;

$\bar{d}_s$ offset of the tether attachment point at the subsatellite end and expressed in the frame F_s.

In Eqs.(2.3 and 2.4) all the terms on the right hand side are not independent. The vector $\bar{R}_{SM}$, the distance between origins of the frames F_o and F_p, represents the shift in the centre of mass and can be expressed in terms of other system variables. By taking the first moment of the masses about the instantaneous centre of mass and equating it to zero, it can be shown that

$$\bar{R}_{SM} = -\frac{1}{M}\Big\{(m_o + m_t + m_s)\bar{d}_p + m_s(L\bar{j}_t + \bar{f}_t(L) - \bar{d}_s) + \int_{m_t} \bar{r}_t \mathrm{d}m_t\Big\},$$

where:

M total mass of the system, $m_p + m_o + m_t + m_s$;

m_p mass of the platform;

m_o mass of the offset mechanism;

m_t mass of the tether, $\rho_t L$;

ρ_t mass of the tether per unit length;

m_s mass of the subsatellite.

It may be pointed out that the vectors defined above and in Eqs.(2.1-2.4) are not with reference to the same coordinate system. So, appropriate transformation matrices are used during vector operations.

2.2.3 Deformation vectors

Deformation at a point on the tether depends on its position and varies with time. At a given instant, it can be expressed as three orthogonal components u_t, v_t and w_t along X_t, Y_t and Z_t directions, respectively. The *assumed mode method* is used to discretize the deformations. The admissible functions are linearly independent and satisfy geometric boundary conditions [64]. In a system with constant length, the admissible functions may represent the mode shapes. But, in the present case, where the tether length changes over time, the concept of mode shape does not apply. However, an admissible function can be chosen to satisfy the geometric boundary conditions. Since the diameter of the tether is very small (a few mm), the admissible functions depend only on Y_t. So the tether deformations can be expressed as:

$$u_t(y_t, L, t) = \sum_{n=1}^{\infty} \Phi_n(y_t, L) A_n(t); \tag{2.5}$$

$$v_t(y_t, L, t) = \sum_{n=1}^{\infty} \Psi_n(y_t, L) B_n(t); \tag{2.6}$$

$$w_t(y_t, L, t) = \sum_{n=1}^{\infty} \Phi_n(y_t, L) C_n(t); \tag{2.7}$$

where:

$\Phi_n(y_t, L), \Psi_n(y_t, L)$ admissible functions for tether transverse and longitudinal deformations, respectively;

$A_n(t), B_n(t), C_n(t)$ generalized coordinates for out-of-plane transverse, longitudinal and inplane transverse deformations, respectively.

Theoretically, a complete set of admissible functions should include infinite

terms. Here the completeness implies that the energy of the discretized system is the same as the energy of the continuous system [64]. For most engineering systems, finite number of functions are sufficient to represent the dynamics. In the present study, the first N_l and N_t functions from the complete set are considered for representing the longitudinal and transverse deformations, respectively. Here N_l and N_t are arbitrary numbers. For the admissible functions, the kinematic boundary conditions dictate that the transverse deformations at the supported ends be zero, i.e.

$$u_t(0, L, t) = w_t(0, L, t) = u_t(L, L, t) = w_t(L, L, t) = 0; \tag{2.8}$$

and the longitudinal deformation at the boundary $y_t = 0$ is zero, i.e.

$$v_t(0, L, t) = 0. \tag{2.9}$$

At the subsatellite end ($y_t = L$), a dynamic boundary condition relating the stretch and static tension in the tether can be obtained [65]. Having defined the flexible deformations, elemental mass of the tether at any arbitrary unstretched distance y_t from the origin of F_t can be defined by the position vector

$$\bar{r}_t = u(y_t, L, t)\bar{i}_t + \Big(y_t + v(y_t, L, t)\Big)\bar{j}_t + w(y_t, L, t)\bar{k}_t. \tag{2.10}$$

The admissible functions for transverse oscillations of the tether correspond to those of a flexible string [65],

$$\Phi_n(y_t, L) = \sqrt{2}\sin\left(\frac{n\pi y_t}{L}\right), \qquad n = 1, 2, \cdots, N_t. \tag{2.11}$$

For the longitudinal deformation, the admissible functions can be chosen as the eigenfunction of a elastic tether supporting a point mass [29],

$$\Psi_n(y_t, L) = \sin\Big(\beta_n y_t/L\Big), \qquad n = 1, 2, \cdots, N_l, \tag{2.12}$$

where β_n is governed by the equation

$$\beta_n \tan(\beta_n) = \frac{\rho_t L}{m_s}, \qquad n = 1, 2, \cdots, N_l. \tag{2.13}$$

Alternatively, it can be taken as

$$\Psi_n(y_t, L) = \left(\frac{y_t}{L}\right)^{2n-1}, \qquad n = 1, 2, \cdots, N_l, \tag{2.14}$$

which represents the vibration of a string with an end mass [36]. In the present thesis the latter form of the admissible function (Eq.2.14) is used for the numerical simulation.

2.2.4 Librational generalized coordinates

The generalized coordinates defining librational motion (rigid body motion) are identified here. The orientation of each frame, $F_i\,(i = p, t, s)$, is obtained relative to the orbital frame through three modified Eulerian rotations starting from the orbital frame. The sequence consist of:

- rotation of $F_o(X_o, Y_o, Z_o)$ by angle α_i about the X_o-axis resulting in (X_1, Y_1, Z_1);
- rotation of (X_1, Y_1, Z_1) by angle β_i about the Y_1-axis resulting in (X_2, Y_2, Z_2);
- rotation of (X_2, Y_2, Z_2) by angle γ_i about the Z_2-axis resulting in (X_i, Y_i, Z_i).

These sequences of Eulerian rotations are indicated in Figure 2-2. Figure 2-2(b) shows α_i rotation about X_o axis in Y_o, Z_o–plane. In case of the tether, two rotations α_t and γ_t are sufficient to describe its orientation in space (i.e. $\beta_t = 0$). Therefore the generalized coordinates for the librational degrees of freedom are: α_p; β_p; γ_p; α_t; γ_t (assuming the subsatellite and offset mechanism to be point masses).

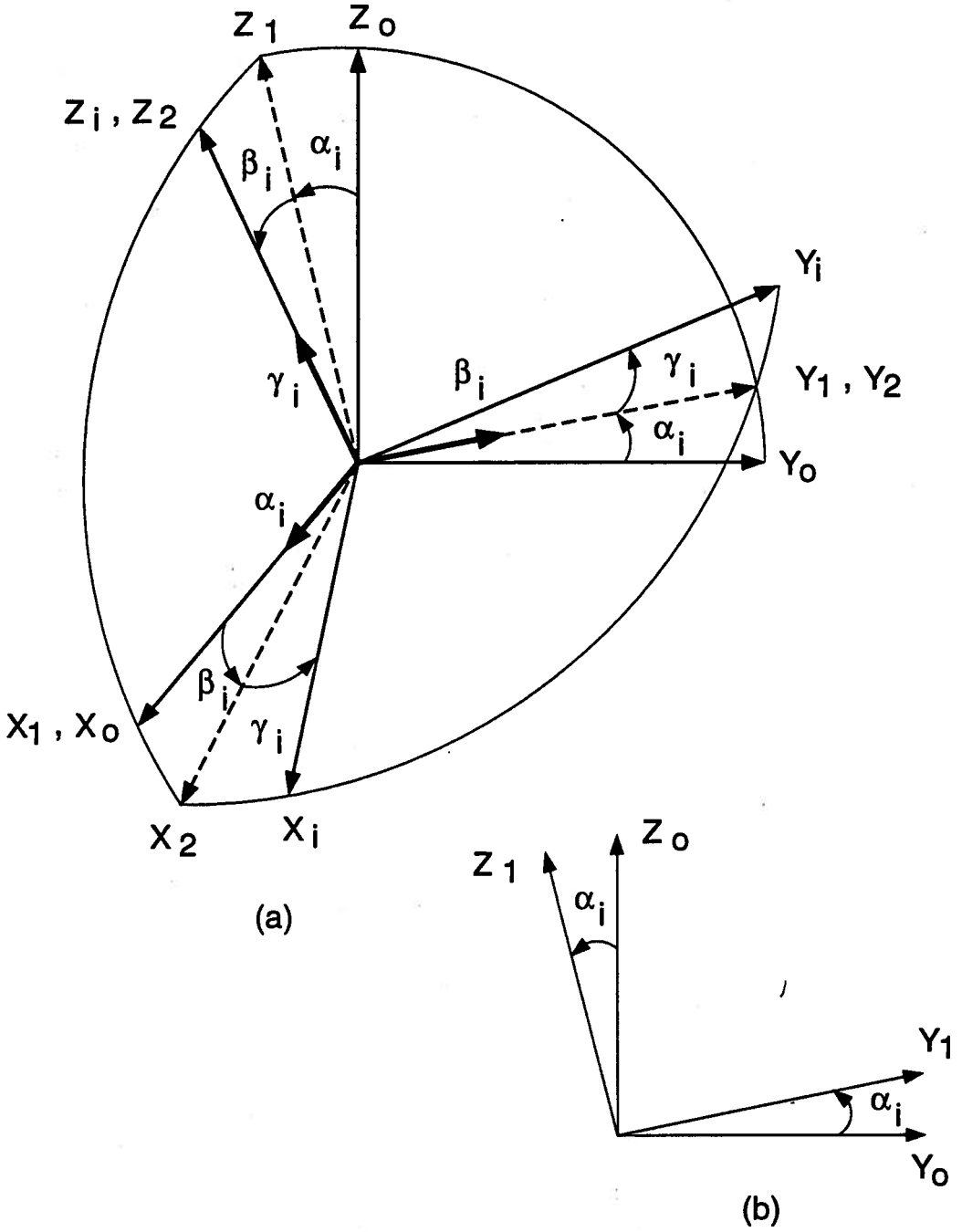

Figure 2-2 Diagrams showing relative orientations of two different frames: (a) sequence of Eulerian rotations; (b) rotation about the X_o-axis.

2.2.5 Angular velocity and direction cosine

Since the generalized coordinates are defined with respect to the intermediate frames of the Eulerian rotations, their derivatives are not the same as the inertial angular velocities expressed in frame F_i. Before relating derivatives of the Euler angles with the angular velocities, the following discussion on the vector transformation between the reference frames is appropriate.

The matrix which transforms a vector from the frame F_j to the frame F_i can be described by the equation

$$\{v_i\} = [T_{ij}]\{v_j\}, \tag{2.15}$$

where:

$\{v_i\}$ vector expressed in frame F_i;

$\{v_j\}$ vector expressed in frame F_j;

$[T_{ij}]$ transformation matrix relating (X_i, Y_i, Z_i) and (X_j, Y_j, Z_j).

The transformation matrix $[T_{ij}]$ has the following properties [66]:

$$[T_{ij}] = [T_{ik}][T_{k(k-1)}]\cdots[T_{21}][T_{1j}], \quad \forall \text{ integer } k\,; \tag{2.16}$$

$$[T_{ij}][T_{ji}] = [I]\,; \tag{2.17}$$

$$[T_{ij}] = [T_{ji}]^{-1} = [T_{ji}]^T. \tag{2.18}$$

Using Eq.(2.16), the angular velocity vector of the frame F_i can be obtained as

$$\{\omega_i\} = \begin{Bmatrix} \omega_{xi} \\ \omega_{yi} \\ \omega_{zi} \end{Bmatrix} = [T_{i2}][T_{21}][T_{1o}] \begin{Bmatrix} \dot{\theta} + \dot{\alpha}_t \\ 0 \\ 0 \end{Bmatrix}$$

$$+ [T_{i2}][T_{21}] \begin{Bmatrix} 0 \\ \dot{\beta}_t \\ 0 \end{Bmatrix} + [T_{i2}] \begin{Bmatrix} 0 \\ 0 \\ \dot{\gamma}_t \end{Bmatrix}$$

$$= \begin{Bmatrix} (\dot{\theta} + \dot{\alpha}_t)\cos(\beta_i)\cos(\gamma_i) + \dot{\beta}_i \sin(\gamma_i) \\ -(\dot{\theta} + \dot{\alpha}_t)\cos(\beta_i)\sin(\gamma_i) + \dot{\beta}_i \cos(\gamma_i) \\ (\dot{\theta} + \dot{\alpha}_t)\sin(\beta_i) + \dot{\gamma}_i \end{Bmatrix}, \qquad (2.19)$$

where: $\dot{\theta}$ is the orbital rotation rate; indices 1 and 2 in the transformation matrices refer to the intermediate frames in the Eulerian rotation sequence; and

$$T_{i2} = \begin{bmatrix} \cos(\gamma_i) & \sin(\gamma_i) & 0 \\ -\sin(\gamma_i) & \cos(\gamma_i) & 0 \\ 0 & 0 & 1 \end{bmatrix};$$

$$T_{21} = \begin{bmatrix} \cos(\beta_i) & 0 & -\sin(\beta_i) \\ 0 & 1 & 0 \\ \sin(\beta_i) & 0 & \cos(\beta_i) \end{bmatrix};$$

$$T_{1o} = \begin{bmatrix} 1 & 0 & 0 \\ 0 & \cos(\alpha_i) & \sin(\alpha_i) \\ 0 & -\sin(\alpha_i) & \cos(\alpha_i) \end{bmatrix}.$$

It is necessary to obtain the direction cosines $\{l_i\}$ of the frame F_i relative to the local vertical as they are needed in evaluation of the gravitational potential energy later:

$$\{l_i\} = \begin{Bmatrix} l_{x_i} \\ l_{y_i} \\ l_{z_i} \end{Bmatrix} = \begin{Bmatrix} \{i_i\} \cdot \{j_o\} \\ \{j_i\} \cdot \{j_o\} \\ \{k_i\} \cdot \{j_o\} \end{Bmatrix}$$

$$= [T_{i2}][T_{21}][T_{1o}] \begin{Bmatrix} 0 \\ 1 \\ 0 \end{Bmatrix}$$

$$= \begin{Bmatrix} \sin(\alpha_i)\sin(\beta_i)\cos(\gamma_i) + \cos(\alpha_i)\sin(\gamma_i) \\ -\sin(\alpha_i)\sin(\beta_i)\sin(\gamma_i) + \cos(\alpha_i)\cos(\gamma_i) \\ -\sin(\alpha_i)\cos(\beta_i) \end{Bmatrix}, \qquad (2.20)$$

where $\{i_i\}, \{j_i\}, \{k_i\}$ are unit vectors along the X_i, Y_i, Z_i axes, respectively; and $\{j_o\}$ is the unit vector along the Y_o-axis.

2.3 Kinetics

2.3.1 Kinetic energy

The inertial velocity of any elemental mass in the i^{th} domain can be obtained by differentiating Eq.(2.1). In the following development, a bar over a character to represent a vector quantity is dropped and replaced by brackets. The matrices are enclosed by square brackets. With these notations, the velocity of an elemental mass in the i^{th} domain becomes

$$\{\dot{R}_{\mathrm{d}m_i}\}_{F_I} = \{\dot{R}_c\}_{F_I} + \{\dot{R}_i\}_{F_I} + \{\dot{r}_i\} + \{\omega_i\} \times \{r_i\}. \tag{2.21}$$

Here, the terms with subscript F_I refer to velocities with respect to the inertial frame while those without any subscript are with reference to the local frames. The kinetic energy of the elemental mass (Figure 2-1) can be expressed as

$$T_{\mathrm{d}m_i} = \frac{1}{2}\{\dot{R}_{\mathrm{d}m_i}\}_{F_I} \cdot \{\dot{R}_{\mathrm{d}m_i}\}_{F_I} \mathrm{d}m_i. \tag{2.22}$$

The energy of the i^{th} body (T_i) can be obtained by integrating the above equation over the mass of the body. The kinetic energy of the entire system (T) is the sum of the energies of the individual domains,

$$\begin{aligned} T &= \sum_{i=p,t,s} T_i \\ &= \sum_{i=p,t,s} \frac{1}{2} \int_{m_i} \{\dot{R}_{\mathrm{d}m_i}\} \cdot \{\dot{R}_{\mathrm{d}m_i}\} \mathrm{d}m_i, \end{aligned} \tag{2.23}$$

where m_i is the mass of the domain i. Substituting Eq.(2.21) in Eq.(2.23) and after some algebraic manipulations, the total kinetic energy of the system can be written as

$$T = \frac{1}{2} M \{\dot{R}_c\}_{F_I} \cdot \{\dot{R}_c\}_{F_I} + \frac{1}{2} M \{\dot{R}_{SM}\}_{F_I} \cdot \{\dot{R}_{SM}\}_{F_I}$$

$$
\begin{aligned}
&+\frac{1}{2}(m_o+m_t+m_s)\{\dot{d}_p\}_{F_I}\cdot\{\dot{d}_p\}_{F_I}\\
&+\frac{1}{2}m_s\Big\{\{\dot{d}_s\}_{F_I}-\{\dot{f}_t(L)\}_{F_I}\Big\}\cdot\Big\{\{\dot{d}_s\}_{F_I}-\{\dot{f}_t(L)\}_{F_I}\Big\}+\frac{1}{2}\sum_{i=p,t,s}\{\omega_i\}^T[I_i]\{\omega_i\}\\
&+\frac{1}{2}\int_{m_t}\{\dot{r}_t\}\cdot\{\dot{r}_t\}\mathrm{d}m_t+\int_{m_t}\{\dot{r}_t\}\cdot\Big\{\{\omega_t\}\times\{r_t\}\Big\}\mathrm{d}m_t\\
&+\frac{1}{2}m_s\left(\left\{\frac{d}{dt}\{Lj_t\}\right\}_{F_I}\cdot\left\{\frac{d}{dt}\{Lj_t\}\right\}_{F_I}\right)\\
&-m_s\left(\left\{\frac{d}{dt}\{Lj_t\}\right\}_{F_I}\cdot\Big\{\{\dot{d}_s\}_{F_I}-\{\dot{f}_t(L)\}_{F_I}\Big\}\right)\\
&+\{\dot{R}_{SM}\}_{F_I}\cdot\Big\{(m_o+m_t+m_s)\{\dot{d}_p\}_{F_I}+\int_{m_t}\Big\{\ \{\dot{r}_t\}+\{\omega_t\}\times\{r_t\}\ \Big\}\mathrm{d}m_t\\
&\qquad+m_s\Big\{\frac{d}{dt}\{Lj_t\}\Big\}_{F_I}-m_s\Big\{\{\dot{d}_s\}_{F_I}-\{\dot{f}_t(L)\}_{F_I}\Big\}\Big\}\\
&+\{\dot{d}_p\}_{F_I}\cdot\Big\{\int_{m_t}\Big\{\ \{\dot{r}_t\}+\{\omega_t\}\times\{r_t\}\ \Big\}\mathrm{d}m_t\\
&\qquad+m_s\Big\{\frac{d}{dt}\{Lj_t\}\Big\}_{F_I}-m_s\Big\{\{\dot{d}_s\}_{F_I}+\{\dot{f}_t(L)\}_{F_I}\Big\}\Big\}. \qquad (2.24)
\end{aligned}
$$

For conciseness, the kinetic energy is expressed as products of vectors and matrices. Note, the kinetic energy expression accounts for 3-dimensional rotation of the platform, tether and subsatellite, as well as flexibility of the tether. For the particular case where the system dynamics is confined to the orbital plane, the kinetic energy expression reduces to

$$
\begin{aligned}
T=\ &\frac{1}{2}M\{\dot{R}_c\}^T_{F_I}\{\dot{R}_c\}_{F_I}+\{\dot{R}_{SM}\}^T_{F_I}\Big\{\frac{1}{2}M\{\dot{R}_{SM}\}_{F_I}+\{\dot{R}_m\}\Big\}\\
&+\frac{1}{2}\sum_{i=p,t}\{\omega_i\}^T[I_i]\{\omega_i\}+\frac{1}{2}(m_s+\rho_tL)\dot{L}^2+\frac{1}{2}m_sL^2\omega_{tx}^2+\frac{1}{2}m_a\{\dot{d}_p\}^T\{\dot{d}_p\}\\
&+m_a\omega_{px}\{\dot{d}_p\}^T[U_k]\{d_p\}+\frac{1}{2}m_a\omega_{px}^2\{d_p\}^T[U_k]^T[U_k]\{d_p\}\\
&+\{\dot{d}_p\}^T[T_{tp}]^T\{K_1\}+\omega_{px}\{d_p\}^T[U_k]^T[T_{tp}]^T\{K_1\}\\
&+\{\dot{d}_p\}^T[T_{tp}]^T[K_2]\{\dot{X}\}+\omega_{px}\{d_p\}^T[U_k]^T[T_{tp}]^T[K_2]\{\dot{X}\}\cdot
\end{aligned}
$$

$$+\{\dot{d}_p\}^T[T_{tp}]^T[K_3]\{X\}+\omega_{px}\{d_p\}^T[U_k]^T[T_{tp}]^T[K_3]\{X\}$$
$$+\{\dot{X}\}^T[K_4]\{\dot{X}\}+\{\dot{X}\}^T[K_5]\{X\}$$
$$+\{X\}^T[K_6]\{X\}+\{K_7\}\{\dot{X}\}+\{K_8\}\{X\}, \tag{2.25}$$

where :

$$m_a = m_o + \rho_t L + m_s;$$
$$\{\dot{R}_m\} = m_a\Big\{\{\dot{d}_p\}+\{\omega_p\}\times\{d_p\}\Big\}+\int_{m_t}\Big\{\{\dot{r}_t\}+\{\omega_t\}\times\{r_t\}\Big\}\mathrm{d}m_t$$
$$+ m_s\Big\{\Big\{\frac{d}{dt}\{Lj_t\}\Big\}_{F_I}+\{\dot{f}_t(L)\}_{F_I}\Big\};$$
$$\{X\}=\begin{Bmatrix}\{B\}\\{C}\end{Bmatrix},\quad \{\dot{X}\}=\begin{Bmatrix}\{\dot{B}\}\\{\dot{C}}\end{Bmatrix}, \text{and are expressed with respect to } F_t;$$
$$\{\dot{d}_p\} = \text{velocity of the offset point in the frame } F_p;$$
$$\{B\}=\{B_i\}_{i=1}^{N_l};\quad \{C\}=\{C_i\}_{i=1}^{N_t}.$$

Here, N_l and N_t are the number of generalized coordinates for longitudinal and inplane transverse vibrations, respectively. $\{K_1\}$, $[K_2]$, $\cdots$, $\{K_8\}$ are defined in Appendix-I. In the above energy expression (Eq.2.25), the first term represents the orbital kinetic energy; the second accounts for the shift in the centre of mass; while the rest of the terms arise from librational and vibrational motions of the system.

2.3.2 Gravitational potential energy

As in the case of the kinetic energy, the total gravitational potential energy is the sum of the energies of the individual domains. The gravitational potential energy for an elemental mass $\mathrm{d}m_i$ can be written as

$$dU_{G_i} = -\frac{GM_e}{|\bar{R}_{\mathrm{d}m_i}|}\mathrm{d}m_i. \tag{2.26}$$

Using the binomial expansion with truncation of the series after the second degree terms, the potential energy for the i^{th} domain can be written as

$$U_{G_i} = -\frac{GM_e m_i}{R_c} + \frac{GM_e}{2R_c^3}\int_{m_i}\Big(\{R_i\}\cdot\{R_i\} - 3\Big(\{j_o\}\cdot\{R_i\}\Big)^2\Big)\mathrm{d}m_i,$$

where :

G universal gravitational constant;

M_e mass of Earth;

R_c magnitude of the orbital radius;

m_i mass of the i^{th} domain;

$\{j_o\}$ unit vector along the Y_o-axis (local vertical);

and $\{R_i\}$ as defined in Eqs.(2.3, 2.4). The gravitational potential energy for the entire system can now be written as

$$\begin{aligned}
U_G = &-\frac{GM_eM}{R_c} + \frac{GM_e}{2R_c^3}\Big(M\Big(\{R_{SM}\}\cdot\{R_{SM}\} - 3(\{j_o\}\cdot\{R_{SM}\})^2\Big)\\
&+ m_a\Big(2\{R_{SM}\}\cdot\{d_p\} + \{d_p\}\cdot\{d_p\} - 6(\{j_o\}\cdot\{R_{SM}\})(\{j_o\}\cdot\{d_p\})\\
&\qquad - 3(\{j_o\}\cdot\{d_p\})^2\Big)\\
&+ m_s\Big(\{Lj_t\}\cdot\{Lj_t\} + 2\{Lj_t\}\cdot\{f_t(L)\} + \{f_t(L)\}\cdot\{f_t(L)\}\Big)\\
&+ 2m_s\Big\{\{R_{SM}\} + \{d_p\}\Big\}\cdot\Big\{\{Lj_t\} + \{f_t(L)\}\Big\}\\
&- 3m_s\Big(\{j_o\}\cdot\{Lj_t\}\Big)\Big(\{j_o\}\cdot\{Lj_t\} + 2\{j_o\}\cdot\{R_{SM}\}\\
&+ 2\{j_o\}\cdot\{d_p\} + 2\{j_o\}\cdot\{f_t(L)\}\Big)\\
&- 3m_s\Big(\{j_o\}\cdot\{f_t(L)\}\Big)\Big(\{j_o\}\cdot\{f_t(L)\} + 2\{j_o\}\cdot\{R_{SM}\} + 2\{j_o\}\cdot\{d_p\}\Big)\\
&+ 2\Big\{\{R_{SM}\} + \{d_p\} - 3\Big(\{j_o\}\cdot\{d_p\} + \{j_o\}\cdot\{R_{SM}\}\Big)\{j_o\}\Big\}\cdot\Big\{\int_{m_t}\{r_t\}\mathrm{d}m_t\Big\}\\
&- \sum_{i=p,t,s}\Big(tr[I_i] - 3\{l_i\}^T[I_i]\{l_i\}\Big)\Big).
\end{aligned} \tag{2.27}$$

Here the first term represents potential energy of the system treated as a point mass. The rest of the terms are due to the system's finite dimension. The potential energy expression when simplified and expressed in matrix notation for the planar case has the form

$$\begin{aligned} U_G = & -\frac{GM_eM}{R_c} + \frac{GM_e}{2R_c^3}\Big(\{R_{SM}\}^T[P_1]\{R_{SM}\} + \{d_p\}^T[P_2]\{d_p\} \\ & + 2\{R_{SM}\}^T[P_2]\{d_p\} + \{X\}^T[P_3]\{R_{SM}+d_p\} \\ & + \{X\}^T\{P_4\} + \{X\}^T[P_5]\{X\} + \{P_6\}^T\{R_{SM}+d_p\} \\ & + m_sL^2(1-3\hat{V}_{to}) - \sum_{i=p,t}\Big(tr[I_i] - 3\{l_i\}^T[I_i]\{l_i\}\Big)\Big), \end{aligned} \tag{2.28}$$

where :

$[I_i]$ inertia dyadic of the domain i with respect to F_i (Appendix-I) ;

$\{l_i\}$ direction cosine of the Y_o-axis (local vertical) with respect to the frame F_i;

and $[P_1]$, $[P_2]$, $\cdots$, $\{P_6\}$, and $\hat{V}_{to}$ are defined in Appendix-I. In Eq.(2.28), terms containing $\{R_{SM}\}$ account for the potential energy due to shift in the centre of mass.

2.3.3 Elastic potential energy

In the linear elastic theory of strings, it is generally assumed that the initial tension in the string is large enough and the transverse displacements cause negligible change in this tension. In a tethered orbiting system, the tension may be reasonably large for long tethers (length of the order of *kms*). But at shorter lengths, the tension is very low due to the weak gravity gradient force. In the extreme case when the length approaches zero, the tension tends to zero. Therefore the effect of transverse vibration on the tether tension, and hence on the elastic

oscillations can not be neglected.

The strain energy of the tether is based on the theory of vibrating string [67]. In order to account for interactions between the longitudinal and transverse modes, transverse displacement terms upto the second order are retained in the strain expression

$$\epsilon = \frac{\partial v_t}{\partial y_t} + \frac{1}{2}\left(\left(\frac{\partial u_t}{\partial y_t}\right)^2 + \left(\frac{\partial w_t}{\partial y_t}\right)^2\right),$$

where ϵ is the total strain in an elemental tether mass of volume $\mathrm{d}V_t$. Total strain energy of the tether can be written as

$$\begin{aligned} U_S &= \frac{1}{2}\int_{V_t} \sigma\epsilon \mathrm{d}V_t, \\ &= \frac{1}{2}EA\int_0^{L(t)} \left(\frac{\partial v_t}{\partial y_t} + \frac{1}{2}\left((\frac{\partial u_t}{\partial y_t})^2 + (\frac{\partial w_t}{\partial y_t})^2\right)\right)^2 \mathrm{d}y_t, \end{aligned} \tag{2.29}$$

where:

- σ stress in an elemental mass of volume $\mathrm{d}V_t$, $E\epsilon$;
- A area of cross-section of the tether;
- $L(t)$ unstretched tether length;
- V_t volume of the unstretched tether, $AL(t)$;
- E young's modulus of the tether material.

Substituting from Eqs.(2.6, 2.7) in Eq.(2.29), strain energy of the planar system can be obtained as

$$\begin{aligned} U_S =& \frac{EA}{2}\int_0^{L(t)} \left(\frac{\mathrm{d}\{F_\psi(y_t)\}^T}{\mathrm{d}y_t}\{B\}\right)^2 \mathrm{d}y_t + \frac{EA}{8}\int_0^{L(t)} \left(\frac{\mathrm{d}\{F_\phi(y_t)\}^T}{\mathrm{d}y_t}\{C\}\right)^4 \mathrm{d}y_t \\ &+ \frac{EA}{2}\int_0^{L(t)} \left(\frac{\mathrm{d}\{F_\psi(y_t)\}^T}{\mathrm{d}y_t}\{B\}\right)\left(\frac{\mathrm{d}\{F_\phi(y_t)\}^T}{\mathrm{d}y_t}\{C\}\right)^2 \mathrm{d}y_t. \end{aligned} \tag{2.30}$$

2.3.4 Dissipation energy

The energy dissipation during tether deformation can be accounted for through structural damping. Because of the complex mechanism of energy dissipation, the stress–strain relation does not correspond to the elastic case. The system exhibits the hysteresis phenomena during vibration. The area enclosed by the hysteresis curve indicates the energy dissipation. In engineering applications, it is commonly accounted for by considering the structural damping coefficient determined experimentally [68]. The structural damping can be expressed as an equivalent complex Young's modulus,

$$E^* = E + iE_I, \tag{2.31}$$

where the real part E is the Young's modulus without structural damping; the imaginary part E_I contributes to the structural damping; and $i = \sqrt{-1}$. Now the total stress can be written as

$$\sigma_t = E^*\epsilon = (E + iE_I)\epsilon = E(1 + i\eta)\epsilon,$$

where

$$\eta = \frac{E_I}{E} << 1. \tag{2.32}$$

If ϵ is harmonic with frequency ω_o,

$$i\epsilon = \frac{\dot{\epsilon}}{\omega_o} \tag{2.33}$$

and the total stress becomes

$$\sigma_t = E\left[\epsilon + \left(\frac{\eta}{\omega_o}\right)\dot{\epsilon}\right] = \sigma + \sigma_d, \tag{2.34}$$

where $\sigma = E\epsilon$ is the stress in absence of the structural damping; and $\sigma_d = E(\eta/\omega_o)\dot{\epsilon}$, is the stress causing energy dissipation.

The dissipation of energy can be expressed in terms of the Rayleigh's dissipation function [69],

$$W_d = \frac{1}{2}\int_{V_t} \sigma_d \dot{\epsilon} \mathrm{d}V_t$$
$$= \frac{EA\eta}{\omega_o}\int_0^L (\dot{\epsilon})^2 \mathrm{d}y_t. \tag{2.35}$$

2.4 Equations of Motion

Using the Lagrangian procedure, the governing equations of motion can be obtained from

$$\frac{\mathrm{d}}{\mathrm{d}t}\left(\frac{\partial T}{\partial \dot{q}}\right) - \frac{\partial T}{\partial q} + \frac{\partial U}{\partial q} + \frac{\partial W_d}{\partial \dot{q}} = Q_q, \tag{2.36}$$

where:

q vector of generalized coordinates;

Q_q vector of generalized forces corresponding to generalized coordinates q;

$U = U_G + U_S$.

The governing equations of motion account for:

(i) inplane rotation of platform and tether negotiating any arbitrary trajectory;

(ii) longitudinal and inplane transverse vibrations of the tether;

(iii) inplane (two dimensional) offset of the tether attachment point from the space platform's centre of mass;

(iv) effect of the controlled variation of the offset attachment point;

(v) influence of deployment and retrieval on the system dynamics;

(vi) effect of thrusters located at the subsatellite end and momentum gyros on the platform;

(vii) shift in the centre of mass due to rigid body librations and elastic deformations of the tether.

They would permit parametric response analysis of the system as well as aid in development of control strategies using thrusters, offsets and their hybrid combinations. In a compact form the equations of motion can be expressed as

$$[M(q,t)]\{\ddot{q}\} + \{F(q,\dot{q},t)\} = \{Q_q\}, \tag{2.37}$$

where:

$[M(q,t)]$ mass matrix (Appendix-II);

$\{F(q,\dot{q},t)\}$ nonlinear, nonautonomous terms accounting for gravitational, Coriolis and centrifugal forces (Appendix II);

$\{q\}$ vector of generalized coordinates, $\left\{\alpha_p,\ \alpha_t,\ \{B\}^T,\ \{C\}^T\right\}^T$;

α_p platform pitch angle;

α_t tether pitch angle;

$\{B\}$ vector of longitudinal elastic generalized coordinates;

$\{C\}$ vector of transverse elastic generalized coordinates;

$\{Q_q\}$ nonconservative generalized force vector.

2.5 Generalized Forces

The generalized force vector (Q_q) accounts for the effects of nonconservative external forces and moments due to active and passive control, and environmental disturbances. As mentioned before, the platform based momentum gyros provide control torque (M_{α_p}) about the platform axis X_p (Figure 2-3). As shown in the

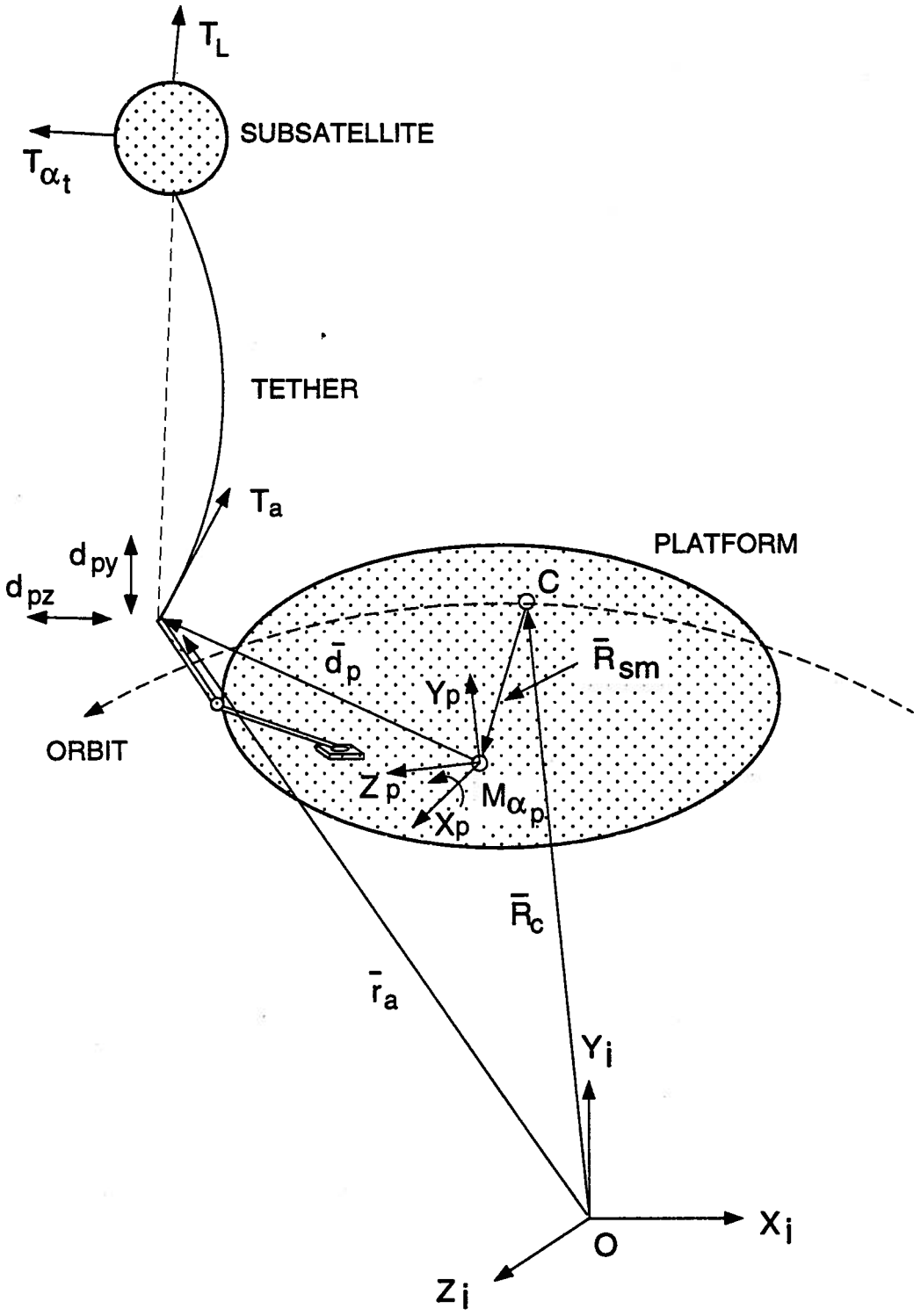

Figure 2-3 A schematic diagram of the Tethered Satellite System (TSS) showing different input variables.

figure, the tether swing can be controlled by manipulating an orthogonal set of thrusters (T_{α_t}, T_L) at the subsatellite, or the motion of the tether attachment point (d_{py}, d_{pz}) at the platform end. As discussed in Chapter 4, the control influence matrix for the offset strategy can be obtained from the coefficient of the offset acceleration in the equations of motion. However, for thruster control and platform pitch equation, it has to be obtained as the generalized force vector.

The generalized force vector, Q_q, can be evaluated using the principle of virtual work. Let $\bar{F}_1$, $\bar{F}_2$, $\cdots$, $\bar{F}_m$ are m external forces acting on the system at locations with position vectors $\bar{r}_1$, $\bar{r}_2$, $\cdots$, $\bar{r}_m$, respectively. The system has n generalized coordinates (q_1, q_2, $\cdots$, q_n). The position vectors are, in general, functions of q_i's. The virtual work, δW, by all the external forces can be expressed as

$$\begin{aligned}\delta W &= \sum_{i=1}^{m} \bar{F}_i \cdot \delta \bar{r}_i = \sum_{i=1}^{m} \bar{F}_i \cdot \left\{ \sum_{j=1}^{n} \frac{\partial \bar{r}_i}{\partial q_j} \delta q_j \right\} \\ &= \sum_{j=1}^{n} \left(\sum_{i=1}^{m} \bar{F}_i \cdot \frac{\partial \bar{r}_i}{\partial q_j} \right) \delta q_j = \sum_{j=1}^{n} Q_{q_j} \delta q_j, \end{aligned} \tag{2.38}$$

where

$$Q_{q_j} = \sum_{i=1}^{m} \bar{F}_i \cdot \frac{\partial \bar{r}_i}{\partial q_j} \tag{2.39}$$

is the generalized force corresponding to the generalized coordinate q_j. The external forces and moments acting on the system are:

M_x control moment acting on the platform about the X_p axis;

T_{α_t} thrust applied perpendicular to the tether line at the subsatellite end;

T_L control thrust along the undeformed tether applied at the subsatellite;

F_{dt} damping force perpendicular to the undeformed tether;

F_{dl} damping force along the tether line.

The transverse and longitudinal dampers are located at distances of Y_{dt} and Y_{dl} from the origin of F_t. Using Eq.(2.39), the generalized forces for the tether angle and elastic degrees of freedom can be obtained as:

$$Q_{\alpha_t} = T_{\alpha_t}\Big(L + \Big\{F_\psi(L)\Big\}^T\Big\{B\Big\}\Big) + F_{dt}\Big(Y_{dt} + \Big\{F_\psi(Y_{dt})\Big\}^T\Big\{B\Big\}\Big); \quad (2.40)$$

$$\Big\{Q_B\Big\} = T_L\Big\{F_\psi(L)\Big\} + F_{dl}\Big\{F_\psi(Y_{dl})\Big\}; \quad (2.41)$$

$$\Big\{Q_C\Big\} = F_{dt}\Big\{F_\phi(Y_{dt})\Big\}. \quad (2.42)$$

Since the tether can not transmit any moment or transverse force, the computation of Q_{α_p} needs special attention. To that end, rather than considering the external forces acting on the tether for virtual work computation, the equivalent tension ($\bar{T}_a$) at the platform end of the tether is employed. The tension $\bar{T}_a$ depends on T_{α_t}, T_L, F_{dt} and F_{dl}, and attitude angles of the tether and platform. T_{α_t} and F_{dt} are perpendicular to the undeformed tether and hence their contribution to $\bar{T}_a$ can be neglected. This results in

$$\bar{T}_a \approx (T_L + F_{dl})\Big\{\bar{j}_t\Big\}.$$

The generalized force for α_p can now be obtained from

$$Q_{\alpha_p} = M_x + \{\bar{T}_a\} \cdot \left\{\frac{\partial \bar{r}_a}{\partial \alpha_p}\right\},$$

where $\bar{r}_a$ is the position vector of the tether attachment point on the platform. After appropriate transformation of vectors and expanding the dot product it can be shown that

$$Q_{\alpha_p} = M_x + (T_L + F_{dl})\Big(D_{ty}\sin(\alpha) - D_{tz}\cos(\alpha)\Big), \quad (2.43)$$

where:

$$\alpha = \alpha_t - \alpha_p;$$

$$D_{ty} = R_{SM_y} + d_{py};$$

$$D_{tz} = R_{SM_z} + d_{pz}.$$

2.6 Summary

A general set of kinetic and potential energy expressions are obtained for a platform based tethered satellite system undergoing three-dimensional dynamics. These expressions are used to obtain, through the Lagrangian procedure, governing equations of motion for the system dynamics confined to the plane of the orbit. The highly nonlinear, nonautonomous and coupled equations of motion are extremely lengthy even in the matrix notation. They account for a shift in the center of mass, time dependent variation of the tether attachment point at the platform, as well as deployment and retrieval of the tether. The structural damping is modelled through Rayleigh's dissipation function. The generalized force vector representing effects of external forces is evaluated using the principle of virtual work. The relatively general formulation can implement the offset and thruster control strategies to regulate both the rigid and flexible dynamics of the tether with the platform attitude motion controlled by momentum gyros.

3. COMPUTER IMPLEMENTATION

3.1 Preliminary Remarks

The governing equations of motion developed in the last chapter were integrated numerically to study the dynamics and control of the tethered systems. The computer code is quite lengthy ($\approx$ 6200 lines), mainly due to the highly time varying nature of the system dynamics and moving tether attachment point. Moreover, the frequencies of attitude and elastic degrees of freedom are widely separated with a closely packed spectrum for the flexible system. The stiff characteristic of the system, which may present problems during numerical solution, demanded special attention. It was desirable to explore several different approaches to arrive at an efficient controller design. To that end, it was necessary to evolve a flexible program structure that would permit varied simulations with a few parameter changes in the input file. Of course, the program should be easy to debug and efficient to run.

This chapter begins with discussion on the numerical algorithm and program structure developed. Next, validity of the equations of motion and the computer code are assessed by two different methods: conservation of total energy; and comparison of frequency spectra for a particular case of the linear system as reported in the literature. The chapter ends with a summary of salient features of the numerical code.

3.2 Numerical Implementation

Integration algorithm

A computer program is written to numerically solve the governing equations of motion of the tethered satellite system. The second order ordinary differential

equations representing the system dynamics are rearranged as first order equations to this end. The system dynamics as represented in Eq.(2.37) can be expressed as

$$\ddot{q} = [M(q,t)]^{-1}\Big\{Q_q - F(q,\dot{q},t)\Big\}. \tag{3.1}$$

Defining

$$y = \begin{Bmatrix} q \\ \dot{q} \end{Bmatrix},$$

the above relation can be rearranged as

$$\dot{y} = \begin{Bmatrix} \dot{q} \\ [M(q,t)]^{-1}\Big\{Q_q - F(q,\dot{q},t)\Big\} \end{Bmatrix}, \tag{3.2}$$

which is a set of $2N$ first order equations. Here N is the dimension of the generalized coordinate vector $\{q\}$. The IMSL:DGEAR subroutine is used to integrate the above equation. The main advantage of this method is the automatic adjustment of the iteration step–size for stiff systems with error check in each iteration cycle [70]. The subroutine uses Gear's predictor-corrector algorithm [71].

Program structure

The flowchart showing the structure of the program to simulate both uncontrolled and controlled dynamics of the system is presented in Figure 3-1. The program starts with initialization of the system parameters and generalized coordinates. Special program parameters are introduced to identify the type of controller used in the simulation. The initialization is achieved by reading the input file. In each integration time-step, the generalized coordinates, length and offset variables are written into the output files. The main program calls the integration subroutine DGEAR which in turn calls the subprogram FCN. The system dynamics as expressed in Eq.(3.2) is computed by this subroutine. In case of controlled simulation, the actuator inputs are obtained from the subroutine CONTROL. Details of

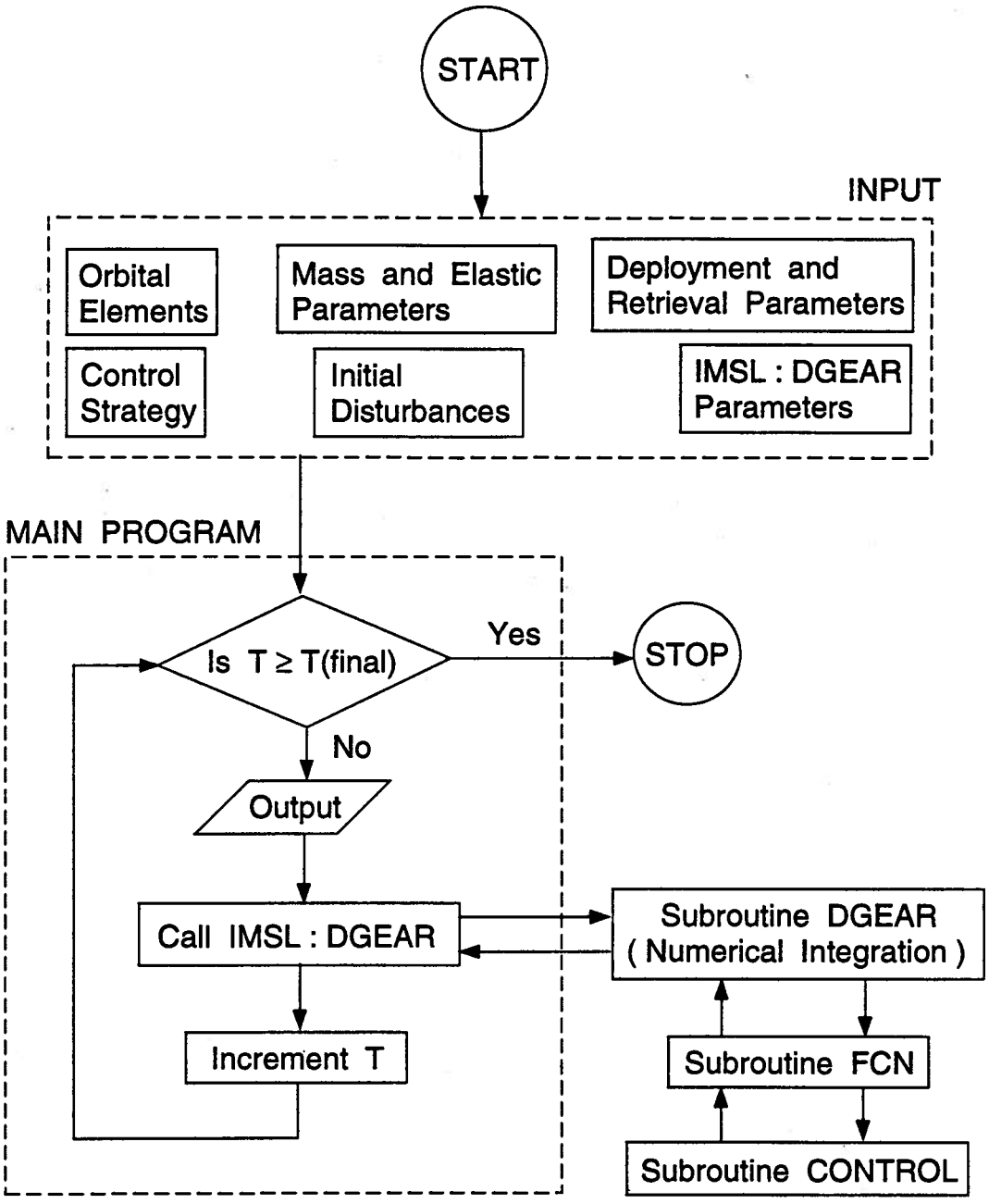

Figure 3-1 Flowchart showing the structure of the main program.

the subroutines are given below.

Subroutine FCN

This subroutine computes the mass matrix and the nonlinear terms to formulate the vector $\dot{y}$, Eq.(3.2), required by the integration subprogram (DGEAR). As shown in the flowchart (Figure 3-2), this subroutine calls a number of subprograms (such as KINETIC, POTENTIAL, etc.) which perform certain specific computation (e.g. computation of modal integrals used in Kinetic and potential energy expressions). This feature makes the program easy to debug. The velocity and acceleration of the tether deployment/retrieval maneuver are calculated by the subprogram LENGTH. Based on the specified parameters, the subprogram OFFSET computes the velocity and acceleration profiles for the specified offset motion. These two subroutines define the system maneuvers. Next, the modal integrals and other matrices used in the formulation (Appendix–I) are evaluated using the subprograms KINETIC and POTENTIAL. As explained in Chapter 2, some intermediate matrices are defined for concise presentation of the governing equations of motion. The matrices appearing in the potential and kinetic energy expressions are evaluated through the subprograms SP and SK, respectively. The matrices used in the potential energy equation are

$$[P_1],\ [P_2],\ [P_3],\ [P_4],\ [P_5],\ \{P_6\},$$

and those used in kinetic energy expression are

$$\{K_1\},\ [K_2],\ [K_3],\ [K_4],\ [K_5],\ [K_6],\ \{K_7\},\ \{K_8\}.$$

The contribution of the terms containing the inertia matrix (Appendix I) of the tether is computed by the subroutine INERTIA. The contribution of the strain

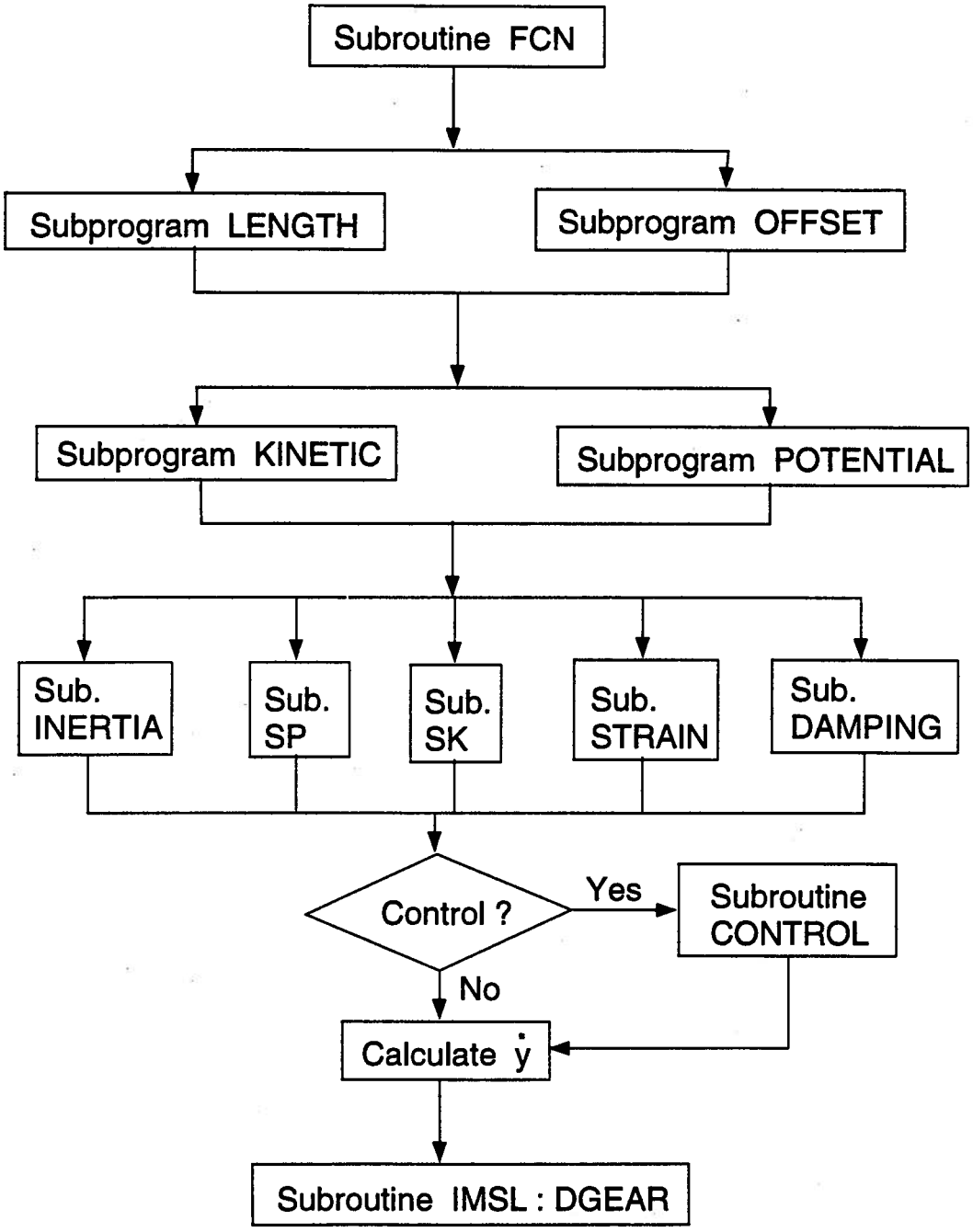

Figure 3-2 Structure of the subroutine FCN to evaluate the first order differential equations required by the integration subroutine.

energy and structural damping are estimated in subprograms STRAIN and DAMPING, respectively.

The above subprograms completely define all the terms required to evaluate the governing equations of the system. Depending on the specified control parameters, the system inputs are established and the vector $\dot{y}$ computed. This value is used by the integration subroutine DGEAR for the numerical solution.

Subroutine CONTROL

The system inputs required to regulate the dynamics are computed by the subroutine CONTROL (Figure 3-3). This subroutine selects the appropriate controller design subprogram for either offset or thruster strategy. The subprogram for offset control obtains the system model and then designs the controller. In the thruster based regulator, three different models can be used for the controller design. Once the model is selected, the procedure is the same as in the offset strategy. The control inputs are computed and returned to the subroutine FCN.

3.3 Formulation Verification

Once the computer program is developed to integrate the equations of motion, the next logical step is to validate the formulation as well as the numerical code. Two different approaches are used to this end. In the first place, total energy is computed for conservative configurations of the system. In the second approach, natural frequencies of the linear system are compared with those reported in the literature. As can be expected, numerical results for the model selected for study are not available. One is forced to be content with validation through comparison of a few simplified cases.

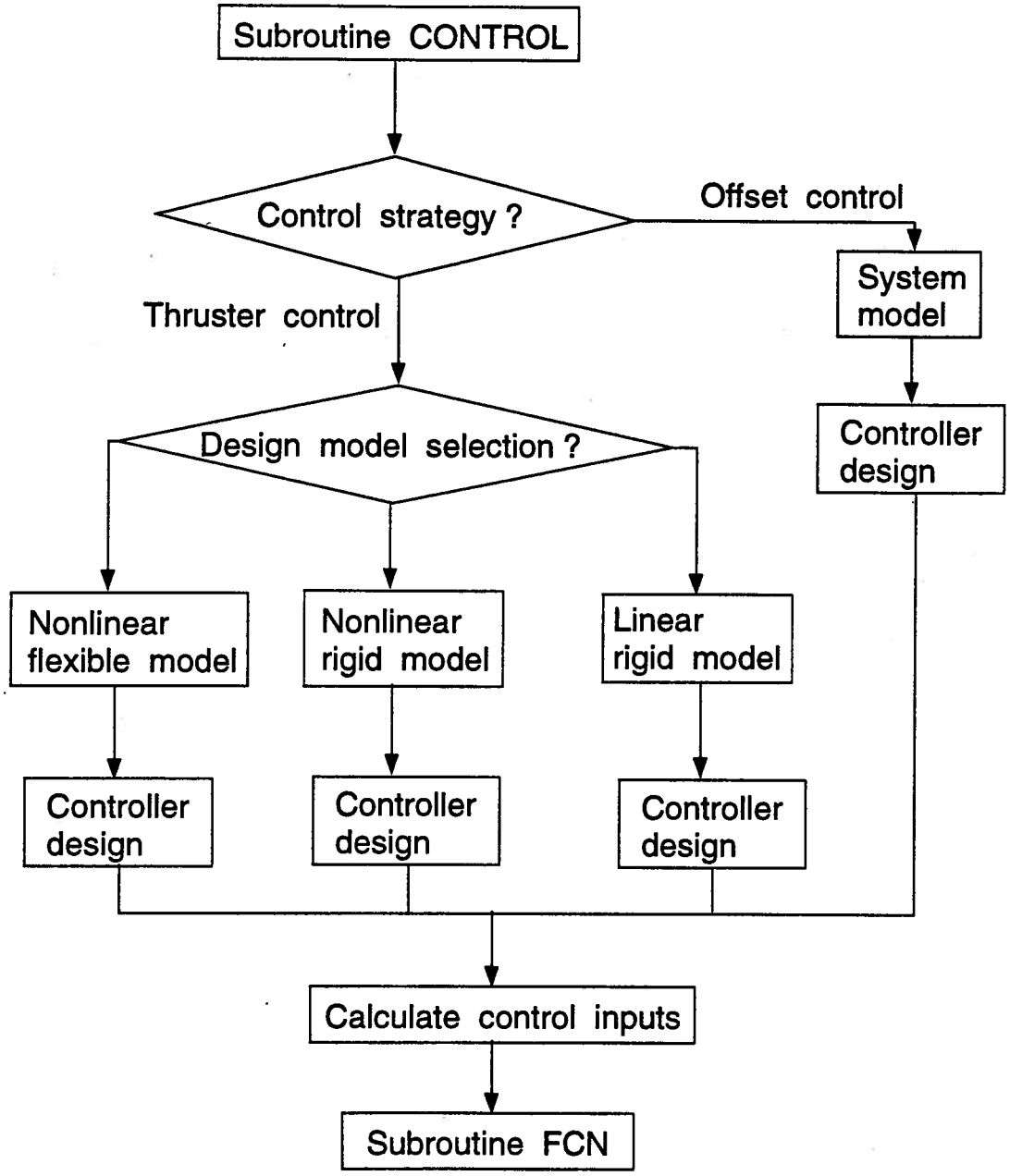

Figure 3-3 Flowchart for the subprogram CONTROL to compute actuation inputs.

3.3.1 Energy conservation

In the study of the attitude dynamics of spacecraft, the effect of attitude dynamics on the orbital motion is very small [61, 62, 63]. Therefore, it is a normal practice to consider the satellite to be moving in a Keplerian orbit. This assumption does not affect the results of an attitude dynamic study. However, it imposes an additional constraint and makes the system nonconservative. So, the attitude and the orbital motions are decoupled and the governing equations representing uncoupled attitude dynamics, which is a conservative system, is used for energy calculation. The inertia and elastic parameters considered in the analysis are the same as those used for the dynamic simulation (Chapter 4).

With zero structural damping, the variations in kinetic, potential and total energies from the reference values are plotted in Figure 3-4. The energies at the beginning of the simulation are considered as the reference values. Figure 3-4(a) shows results for the stationkeeping at a tether length of 20 km and zero offset where as Figure 3-4(b) is for $L = 5$ km and an offset of 1 m along the the local horizontal. In both the simulations, initial disturbances of 0.5^o is given to the tether attitude (α_t) and the platform pitch angle (α_p). Initial conditions of 12 m and 0.8 m are given to the longitudinal oscillation (B_1) of the tether for $L = 20$ km and 5 km, respectively. For the tether transverse vibration, the disturbance levels are taken as 1 m and 0.01 m for $L = 20$ and 5 km, respectively. As expected for a conservative system, change in the total energy remains zero and there is a continuous exchange between the potential and kinetic energies in both the simulations. Similar results were obtained for other lengths and offset positions of the tether. In all the cases conservative nature of the system was found to be preserved. It should be recognized that during deployment/retrieval and movement of the tether attachment point,

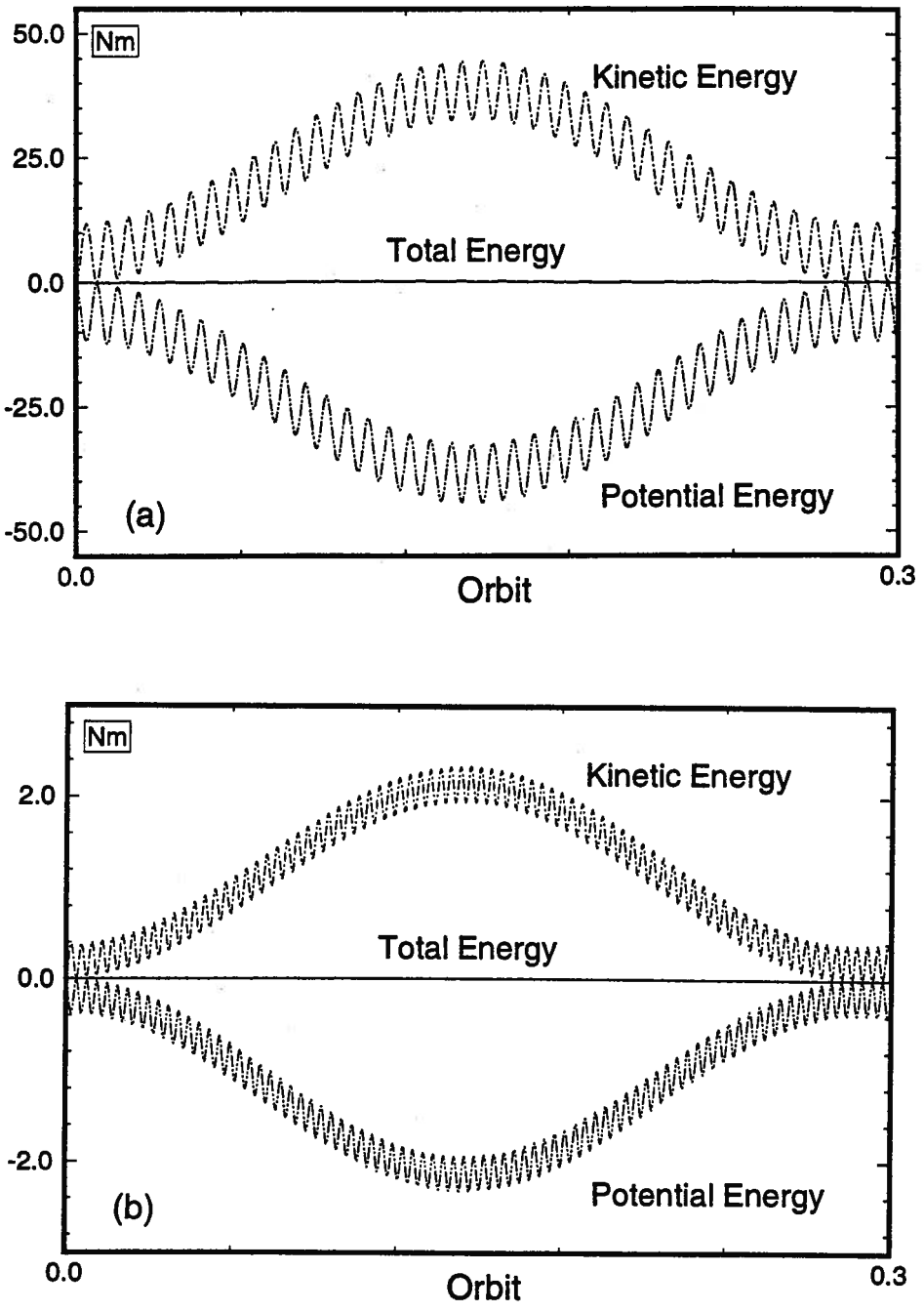

Figure 3-4 Figure showing variations of kinetic, potential (gravitational plus elastic) and total energies of the system during the stationkeeping phase: (a)$L = 20\ km$, $d_{py} = d_{pz} = 0$; (b) $L = 5\ km$, $d_{py} = 1\ m$, $d_{pz} = 0$.

there is energy input to the system. So the system is no longer conservative and the energy check can not be applied.

3.3.2 Eigenvalue comparison

In this case, linear models were obtained for decoupled rigid and flexible subsystems by neglecting the second and higher order terms and making appropriate substitution for the trigonometric terms. These linearized equations of motion for the rigid and flexible subsystems are given in Appendices III and IV, respectively. The frequencies of the system are calculated and compared with the results reported by Keshmiri and Misra [34], and Pasca and Pignataro [72]. In ref.[34], the number of elastic modes of a tether in each direction is limited to two. The higher frequencies of the system are obtained by using what authors call the *semi-bead model*, where the tether is divided into a number of smaller segments and negligible masses are placed at the connection points. Ref.[72] analyzes a system consisting of an elastic continuum tether with mass, and orbiter and subsatellite represented as point masses. The linearized equations of motion are solved by means of a perturbation technique.

The present analysis, which models the tether as a flexible string using the *assumed mode* method, can include any arbitrary number of modes in both the longitudinal and transverse directions. The eigenvalues are computed for the same mass and geometric parameters as in the references. The governing equations are linearized about the static equilibrium position which is zero for the rigid and transverse flexible modes. The equilibrium value for the first longitudinal mode is 100 m and 3.6 m for tether lengths (L) of 100 km and 20 km, respectively. The normalized frequencies are compared in Tables 3.1 and 3.2. The mass and elastic parameters

considered for the frequency computation are indicated in the tables.

Table 3.1 Inplane dimensionless natural frequencies ($\omega/\dot{\theta}$) of a 2-body system ($L = 100\ km$, $m_p = 10^5\ kg$, $m_s = 500\ kg$, $\rho_t = 5.76\ kg/km$, $EA = 2.8 \times 10^5\ N$).

Mode	Present Study	Ref.[34]	Ref.[72]	Type
1	1.732	1.731	1.794	Lib.
2	5.958	6.388	6.905	Tran.
3	11.917	12.059	12.457	Tran.
4	17.876	17.879	18.269	Tran.
5	23.835	23.742	24.142	Tran.
6	29.794	29.627	–	Tran.
7	35.753	35.528	–	Tran.
8	41.712	41.445	–	Tran.
9	47.670	47.383	–	Tran.
10	53.627	53.344	53.807	Tran.
11	54.266	54.541	54.559	Long.
12	59.589	59.337	59.758	Tran.

In the tables, ω is the frequency of the system; $\dot{\theta}$, the orbital frequency; m_s, the subsatellite mass; ρ_t, the mass per unit length of the tether; E, the Young's modulus and A, the cross sectional area of the tether. The first column represents the mode number and the last column is the mode type, i.e. librational (Lib.), transverse (Tran.) or longitudinal (Long.).

Table 3.2 Inplane dimensionless natural frequencies ($\omega/\dot{\theta}$) of a 2-body system ($L = 20\ km$, $m_p = \infty$, $m_s = 576\ kg$, $\rho_t = 5.76\ kg/km$, $EA = 2.8 \times 10^5\ N$).

Mode	Present Study	Ref.[34]	Ref.[72]	Type
1	1.732	1.732	1.733	Lib.
2	12.640	12.777	12.780	Tran.
3	25.281	25.245	25.241	Tran.
4	37.922	37.795	37.771	Tran.
5	50.563	50.369	50.319	Tran.

The minor differences between the present results and those of ref.[34] are of the same order in both the cases. The discrepancies may be attributed to the different formulation methods used. The larger differences for $L = 100\ km$ is due to a parameter $\gamma = \rho_t L/m_s$ defined in ref.[72], which plays an important role. γ has a smaller value in Table 3.2 than in the previous case. As pointed out by the authors, their results are more accurate for smaller γ, hence the correlation is better in Table 3.2.

Frequencies of the systems with different platform and subsatellite masses are shown in Table 3.3. The discrepancy between the present results and those of Ref.[34] follow the same trend as before. Since γ has a reasonable value, the results are in better agreement with those of Ref.[72]. Results for three cases are reported here with different end masses. One case is close to the TSS configuration where the platform mass is $10^5\ kg$ and the subsatellite mass is 500 kg. Other two cases are for equal end masses. As shown in Table 3.3, the frequencies are the highest with the largest end masses ($m_p = m_s = 10^5\ kg$) and the lowest for the smallest end masses ($m_p = m_s = 500\ kg$).

Note, the results of the linearized system match quite well with the reported data although the three studies use different methods to determine frequencies of the system. Furthermore, the results are in close agreement for different tether lengths as well as different masses of the endbodies. This with the conservation of total energy test provides considerable confidence in the validity of the governing equations of motion and the numerical code developed for their integration.

Table 3.3 Comparison of natural frequencies of a tethered two-body system with different end masses ($L = 20\ km$, $\rho_t = 5.76\ kg/km$, $EA = 2.8 \times 10^5\ N$).

Mode	Present Study	Ref.[34]	Ref.[72]	Type
$m_p = 10^5\ kg, m_s = 500\ kg$				
1	1.732	1.732	1.738	Lib.
2	11.917	11.956	11.993	Tran.
3	23.835	23.578	23.644	Tran.
4	35.753	35.286	35.368	Tran.
5	47.671	47.019	47.112	Tran.
$m_p = m_s = 10^5\ kg$				
1	1.732	1.715	1.728	Lib.
2	10.028	14.432	–	Tran.
3	113.453	113.430	113,385	Tran.
4	226.908	227.023	226.736	Tran.
5	340.364	340.934	340.095	Tran.
6	453.813	455.167	453.455	Tran.
$m_p = m_s = 500\ kg$				
1	1.732	1.732	1.742	Lib.
2	8.294	8.486	8.341	Tran.
3	16.588	16.507	16.191	Tran.
4	24.883	24.637	24.155	Tran.
5	33.178	32.799	32.142	Tran.

3.4 Summary

The governing equations of motion for the tethered satellite system are integrated numerically using the IMSL:DGEAR subroutine. The computer program is developed in a structured manner to reduce debugging and running time. The numerical code is validated by two methods: the total energy check for conservative systems; and comparison of frequencies with those reported in the literature. The excellent correlation provide confidence in the simulation model and the numerical code developed for its dynamical response and control studies.

4. DYNAMIC SIMULATION

4.1 Preliminary Remarks

Understanding of the system dynamics is fundamental to the design and development of any engineering system. Furthermore, design of an appropriate controller requires appreciation of the system performance under a wide variety of operating conditions to guard against the possible instability. To that end, the governing equations of motion of the tethered satellite system are numerically integrated and the system's dynamical response studied for different parameter values and operating conditions.

A major concern in the operation of tethered systems is the dynamical behaviour during deployment and retrieval phases. In modelling of a flexible system, the number of modes used for discretization is important. The model developed here can include an arbitrary number of modes for both the transverse and longitudinal vibration of the tether. An acceptable number of modes for the analysis of the system is arrived at through comparison of simulation results including higher modes. This chapter focuses on results of a parametric study carried out by systematic variations of the tether length (L), offset of the tether attachment point (d_{py} and d_{pz}), Young's modulus of the tether (E), density of the tether material (ρ_t) and mass of the payload (m_s).

4.2 Deployment and Retrieval Schemes

Before proceeding with the parametric analysis of the system dynamics, some remarks on the deployment and retrieval time histories used in the study

would be appropriate. The deployment is carried out with an exponential-constant-exponential velocity profile. Let L_1 and L_2 are the lengths where the velocity ($\dot{L}$) profile changes from exponential to constant and from constant to exponential character, respectively. The deployment velocity profile is characterized by the following relations:

$$\dot{L} = c_d L, \qquad L_o \leq L < L_1; \tag{4.1}$$

$$= c_d L_1, \qquad L_1 \leq L < L_2; \tag{4.2}$$

$$= c_d(L_1 + L_2 - L), \qquad L_2 \leq L \leq L_f; \tag{4.3}$$

where L_o and L_f are the initial and final tether lengths, and c_d is the proportionality constant. The above equations can be integrated to obtain the length expression:

$$L = L_o e^{c_d(t-t_o)}, \qquad L_o \leq L < L_1; \tag{4.4}$$

$$= L_1 + c_d L_1(t - t_1), \qquad L_1 \leq L < L_2; \tag{4.5}$$

$$= L_1 + L_2 - L_1 e^{-c_d(t-t_2)}, \qquad L_2 \leq L \leq L_f, \tag{4.6}$$

where t_1 and t_2 are the time instants when the tether length is L_1 and L_2, respectively, starting from the beginning of deployment. Given the initial time t_o, final time t_f, L_o, L_f, L_1 and L_2, the proportionality constant can be obtained as

$$c_d = \left(\frac{1}{t_f - t_o}\right)\left\{ln\left(\frac{L_1}{L_o}\right) + \left(\frac{L_2 - L_1}{L_1}\right) - ln\left(\frac{L_1 + L_2 - L_f}{L_1}\right)\right\}. \tag{4.7}$$

Similarly, expressions for the retrieval profile are

$$\dot{L} = c_r L; \tag{4.8}$$

$$\text{and} \qquad L = L_o e^{c_r(t-t_o)}, \tag{4.9}$$

where L_o and t_o are the tether length and time, respectively, at the beginning of

the retrieval phase. The proportionality constant, c_r, now has the form

$$c_r = \left(\frac{1}{t_f - t_o}\right) ln\left(\frac{L_f}{L_o}\right). \tag{4.10}$$

At times, particularly with the offset control in a hybrid scheme, only the exponential velocity profile is used. The corresponding length expressions for such deployment scheme are similar to the retrieval expressions with appropriate initial and final parameters.

4.3 Simulation Results and Discussion

The parametric study was rather comprehensive, however, for conciseness, only a few typical results are reported here to help establish the trends in the dynamic behaviour. The inertia and elastic parameters considered in the analysis are:

I_p = Inertia matrix of the platform,

$$\begin{bmatrix} 8,646,050 & -8,135 & 328,108 \\ -8,135 & 1,091,430 & 27,116 \\ 328,108 & 27,116 & 8,286,760 \end{bmatrix} kg\text{-}m^2;$$

m_p = mass of the platform, $90,000\ kg$;

m_o = mass of the offset mechanism, $10\ kg$;

ρ_t = mass of the tether per unit length, $4.9 \times 10^{-3}\ kg/m$;

m_s = mass of the subsatellite, $500\ kg$;

$EA = 61,645\ N$.

The system negotiates a circular trajectory with a period of 90.3 minutes. In the simulation, the X_p-axis is oriented parallel to the orbit normal (X_o). The platform

pitch, α_p, is the angle between the Y_p-axis and the local vertical (i.e. Y_o-axis). Similarly, X_t is parallel to X_o and the tether pitch is the angle between Y_t and the local vertical. The longitudinal and lateral elastic deformations of the tether are measured with respect to the frame F_t.

The structural damping considered in the simulation corresponds to a damping ratio (ξ) of 0.5% based on the first natural frequency of the longitudinal oscillation of the tether. Computation of dissipative terms due to the structural damping requires the values of the parameters η and ω_o (Section 2.3.4). Here ω_o is considered as the frequency of the 1^{st} longitudinal mode (B_1) which can be computed from the equivalent stiffness and mass of the decoupled system,

$$\omega_o = \sqrt{\frac{k_b}{m_b}},$$

where:

$$k_b = \frac{\ddot{L}}{2} C_{k_3}(1,1) + \frac{\dot{L}}{2} \dot{C}_{k_3}(1,1) + \omega_{t_x} \dot{H}_{k_4}(1,1) - 2K_6(1,1)$$
$$+ \omega_{t_x}^2 I_{b_1}(1,1) + 2\mu P_5(1,1) - 4\mu I_{b_1}(1,1) + EA \int_0^L \left(\frac{\partial \Psi_1}{\partial y_t} \right)^2 \mathrm{d}y_t;$$
$$m_b = 2K_4(1,1).$$

The structural damping parameter η can be obtained from the damping ratio ξ,

$$\eta = \frac{2\xi\omega_o^2 m_b}{EA \int_0^L \left(\frac{\partial \Psi_1}{\partial y_t} \right)^2 \mathrm{d}y_t} \quad .$$

The matrices used in the above expressions are defined in Appendix I.

4.3.1 Number of modes for discretization

In the modelling of a flexible system using the *assumed mode method*, the

system is complete in the sense that the energy of the mathematical model converges to the true energy when the number of modes approaches infinite [64]. However, in reality, one can employ only a finite number of modes. Fortunately, for most physical systems, it has been observed that only a few modes can represent the system dynamics with considerable degree of accuracy. The model with the first three transverse and the first two longitudinal modes are considered to be reasonably accurate. The disturbance induced relative amplitudes of different modes were used as a basis for selecting the acceptable number of modes.

Simulations are carried out for two tether lengths. Figure 4-1 shows the response of the system with a tether length of 20 km and initial conditions as shown in the diagram. As expected, for the stationkeeping case, the rigid degrees of freedom (i.e. α_p and α_t) exhibit pure oscillatory motion. The first and second longitudinal modes (B_1 and B_2) show high frequency decaying oscillation due to the structural damping, which has a stronger effect on the second mode (B_2). Modulation of the B_2 response is due to its coupling with the first longitudinal mode. Note, an initial disturbance of 10 m is given to the first transverse mode (C_1). With zero specified offset ($D_{py} = D_{pz} = 0$) of the tether attachment point, the tether dynamics is not coupled with the platform motion. Therefore C_1 has a pure oscillatory motion with zero mean. As the structural damping has only the second order effect on the transverse tether vibration, the responses in the higher modes, C_2 and C_3, are also non-decaying. As apparent from the α_t response, there is very small coupling between the attitude and flexible motion of the tether even for a length of 20 km. The modulation of the second and third transverse modes (C_2 and C_3) is due to the coupling between the flexible degrees of freedom.

The important aspect of this simulation is the relative magnitudes repre-

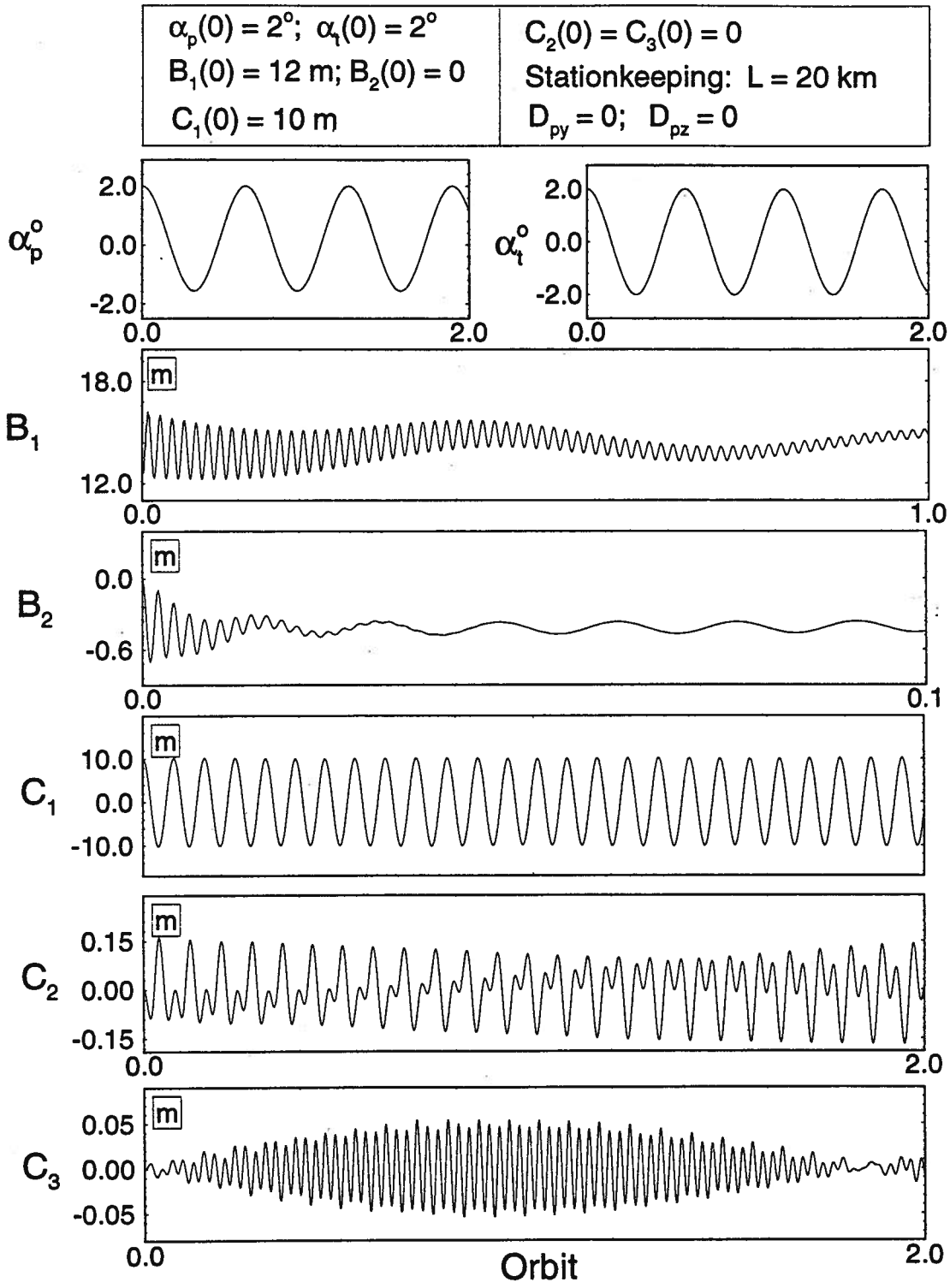

Figure 4-1 Dynamic response of the system with the higher modes included in the discretization of the system.

senting the energy content of the higher modes. A comparison for the longitudinal modes shows that the amplitude of B_2 is an order of magnitude lower than that of B_1. Moreover, the vibration of the second longitudinal mode decays in about 0.02 *orbit* as compared to one *orbit* for the first mode. As mentioned before, the sustained oscillation of B_2 is due to its coupling with the B_1 response. So the energy content of the second longitudinal mode would be very small compared to that of the first one. Similar conclusion can also be made for the transverse modes. The amplitude of the first transverse mode (C_1) is higher by at least one order of magnitude from that of C_2, and two orders of magnitude from that of the C_3 response. Thus the energy content in the higher modes of the tether vibration is minimal.

Similar conclusion can be arrived at from the simulation results for a tether length of 10 *km* (Figure 4-2). Unlike the previous case, now the modulation of the third transverse mode is quite prominent, although the amplitude is rather small. The beat phenomenon is due to the weak coupling between the attitude and flexible motions through a shift in the center of mass. Note, in this case the differences between the fundamental and the higher modes are more than two orders of magnitude.

From these two sample cases, it can be concluded that the energy content in the higher modes is relatively small. Therefore, in the subsequent dynamics and attitude control studies, only the first longitudinal and transverse modes are considered.

4.3.2 Tether length

To facilitate comparison of results, a reference case is established for a tether length of 5 *km* and zero offset along both the local horizontal and local vertical direc-

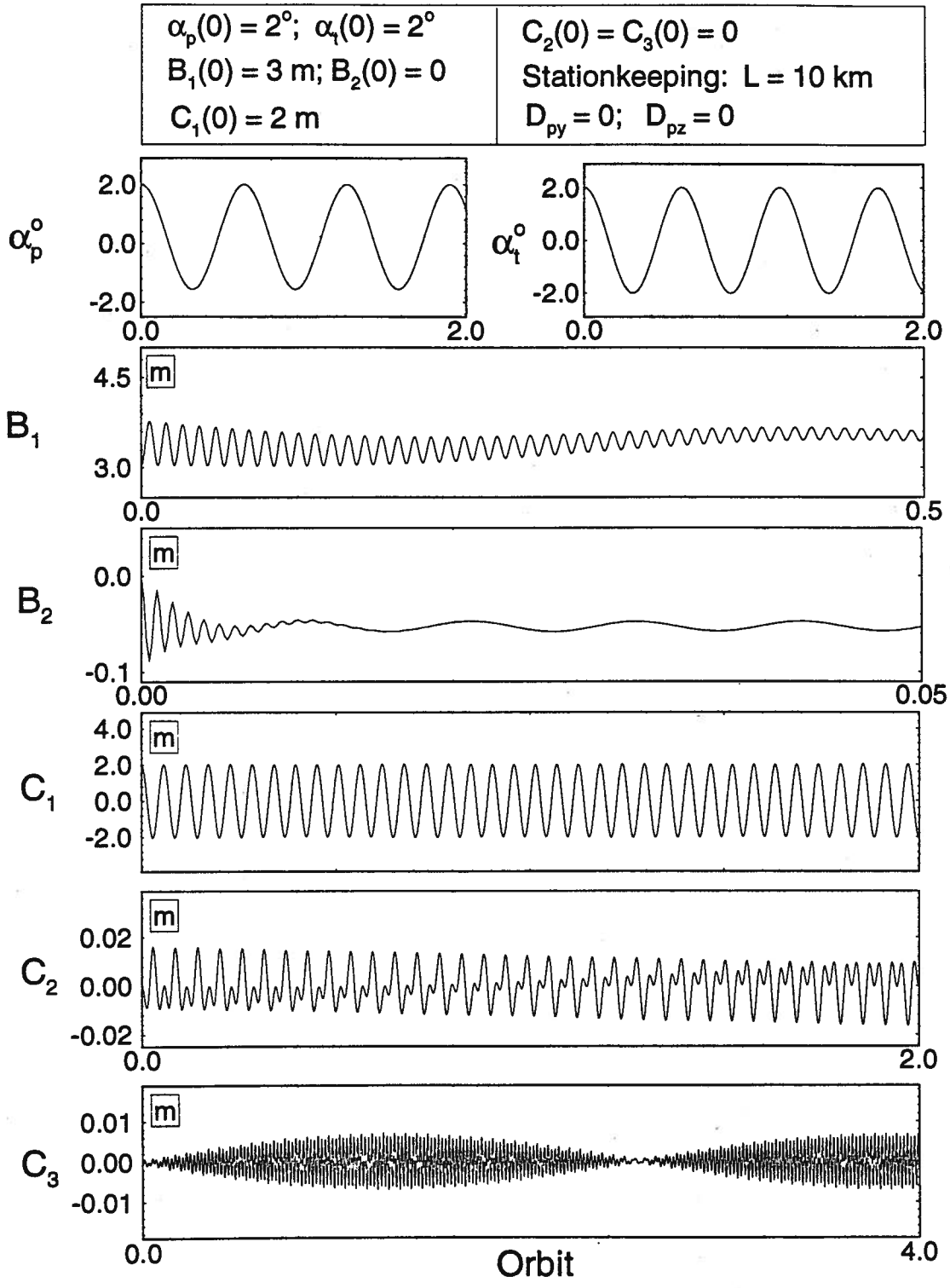

Figure 4-2 System response for a shorter tether with higher modes included in the flexibility modelling.

tions. In the reference case (Figure 4-3), the rigid body rotations of the tether (α_t) and the platform (α_p) are essentially unaffected by the tether flexibility. For zero offset it is expected that the platform dynamics is not coupled with the tether motion and hence free from its dynamical behaviour. The tether rotation is negligibly affected by its flexibility dynamics. As apparent from the figure, the longitudinal flexible response (B_1) consists of two frequencies. The lower frequency is due to the coupling between the rigid body motion of the tether (α_t) and the flexible dynamics, whereas the higher frequency corresponds to the flexibility itself. The high frequency component of B_1 decays due to the structural damping in the tether. The structural damping has a second order effect on the transverse tether vibration. So the C_1 response has an essentially constant amplitude. For zero offset, as expected, the transverse vibration (C_1) is not coupled with other degrees of freedom.

The response of the system with a smaller tether length ($L = 50\ m$) is shown in Figure 4-4. As in the reference case, the longitudinal mode contains two frequencies. But the higher frequency of oscillation increases from 0.025 Hz (corresponding to the reference case) to 0.249 Hz when the length decreases to 50 m. For $L = 50\ km$ (Figure 4-5), the higher frequency decreases to 0.0073 Hz. There was also a change in the frequency of transverse vibration (C_1) from 0.0045 Hz for the reference case to 0.0448 Hz for $L = 50m$ and to 0.0014 Hz for $L = 50\ km$. The stiffness of the tether, which is inversely proportional to its length, increases as the length decreases and hence results in a higher frequency of oscillation for a shorter tether.

Figure 4-6 shows the effect of the flexible tether on the rigid body dynamics for a length of 500 m. Simulation is carried out with zero initial condition for the tether attitude motion. α_t response has a high frequency component due to it

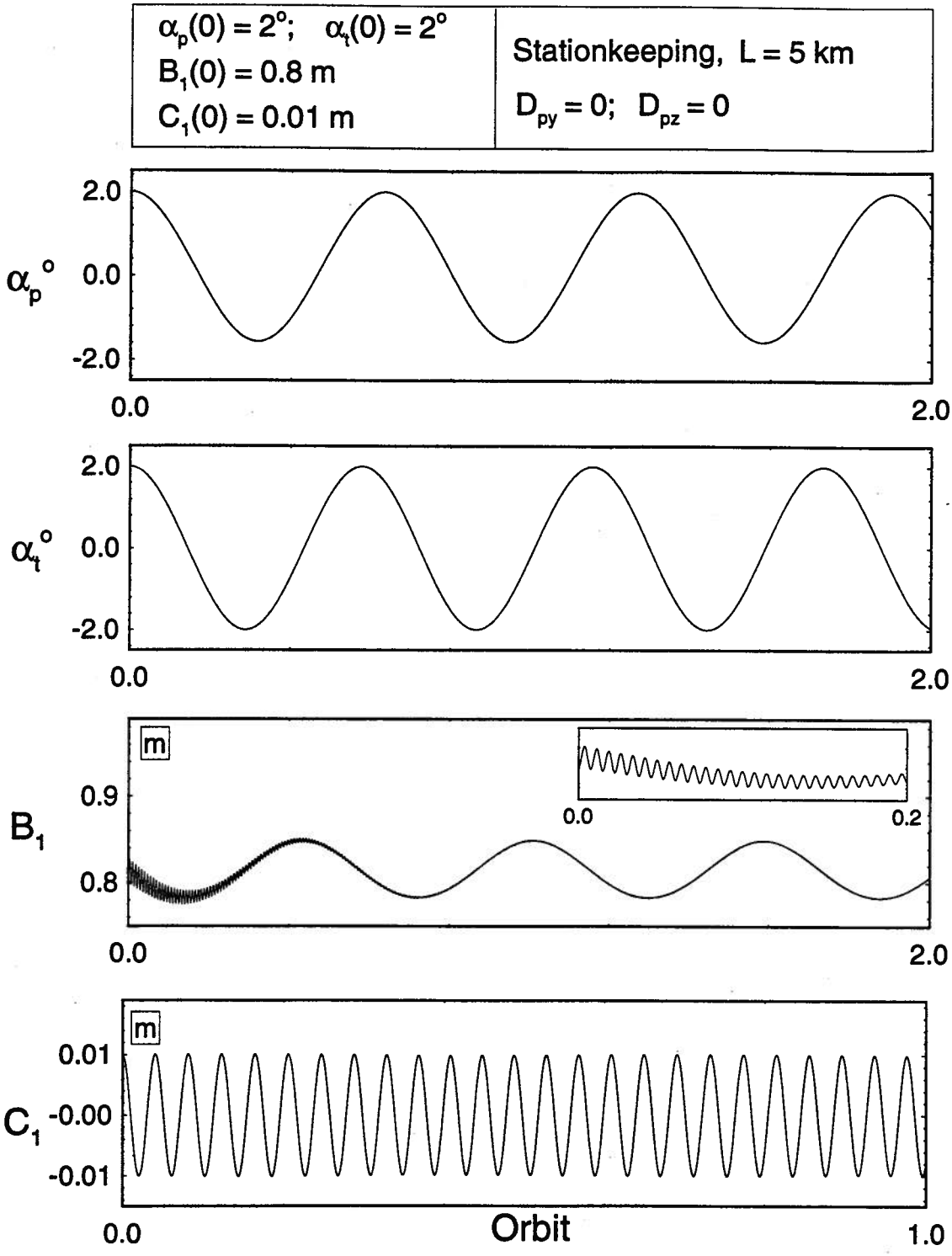

Figure 4-3 Dynamical response of the tethered satellite system in the reference configuration with the offset set to zero.

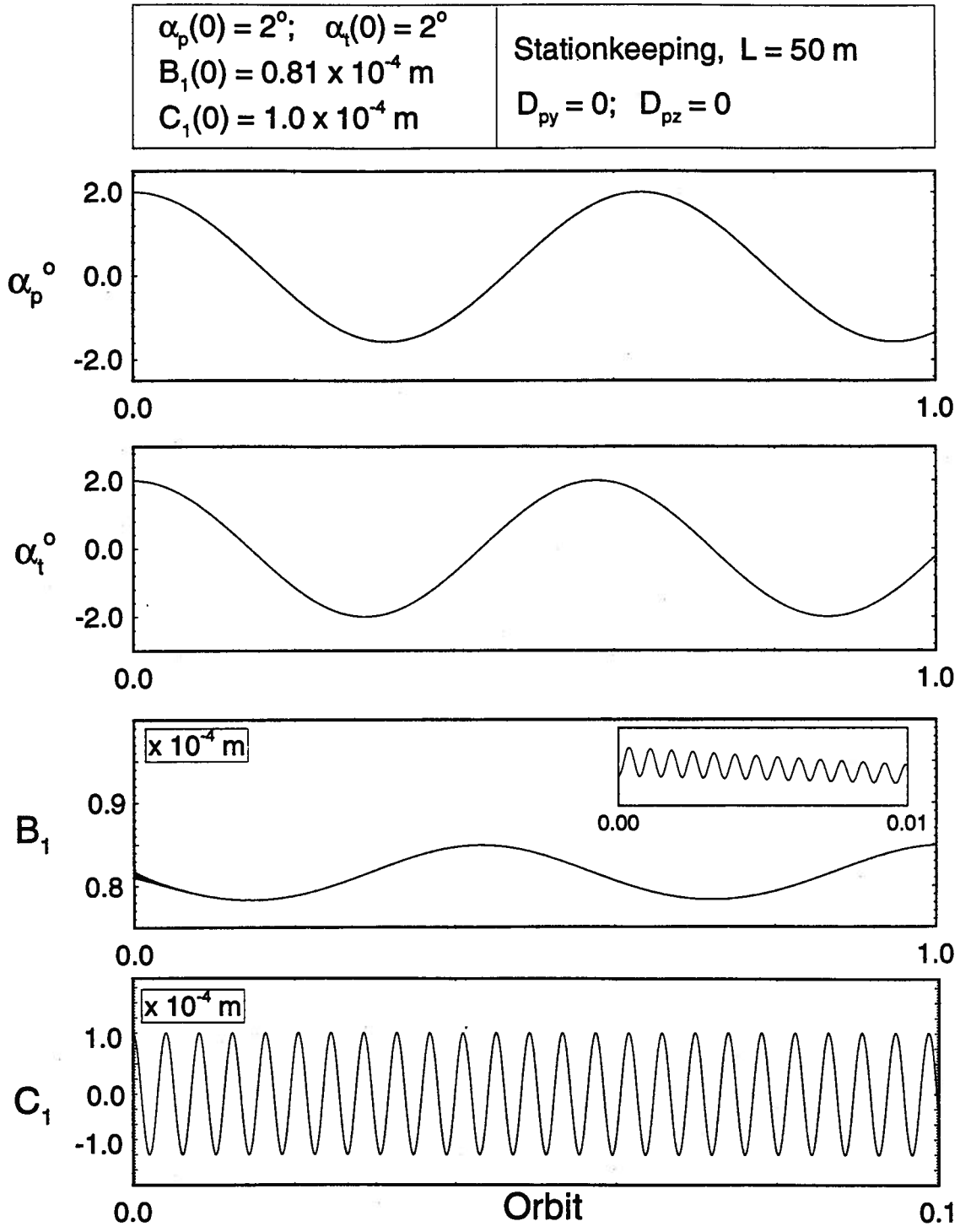

Figure 4-4 Response results showing the effect of decreasing the tether length on the system dynamics.

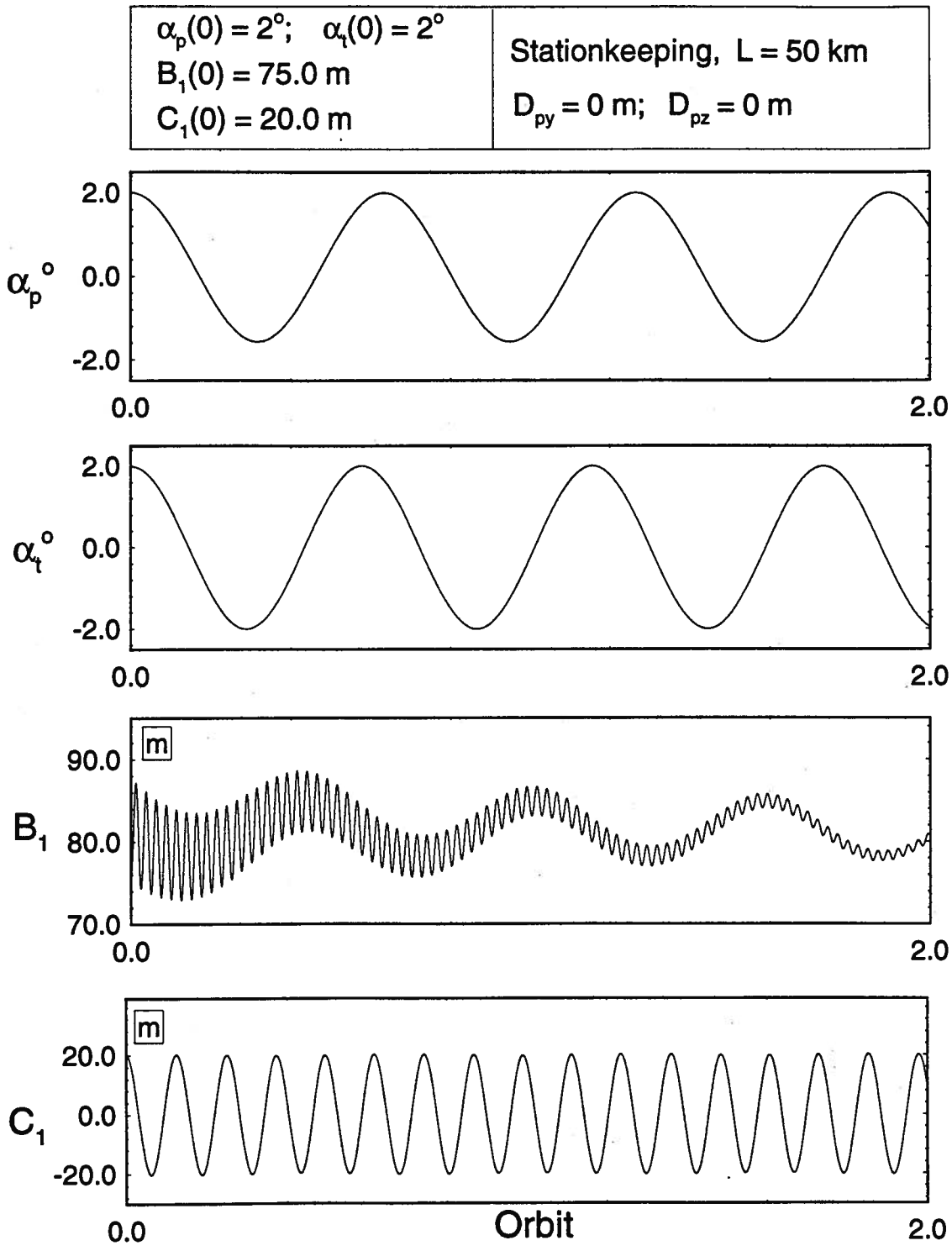

Figure 4-5 Plots showing the effect of increasing the tether length on the system dyanmcis.

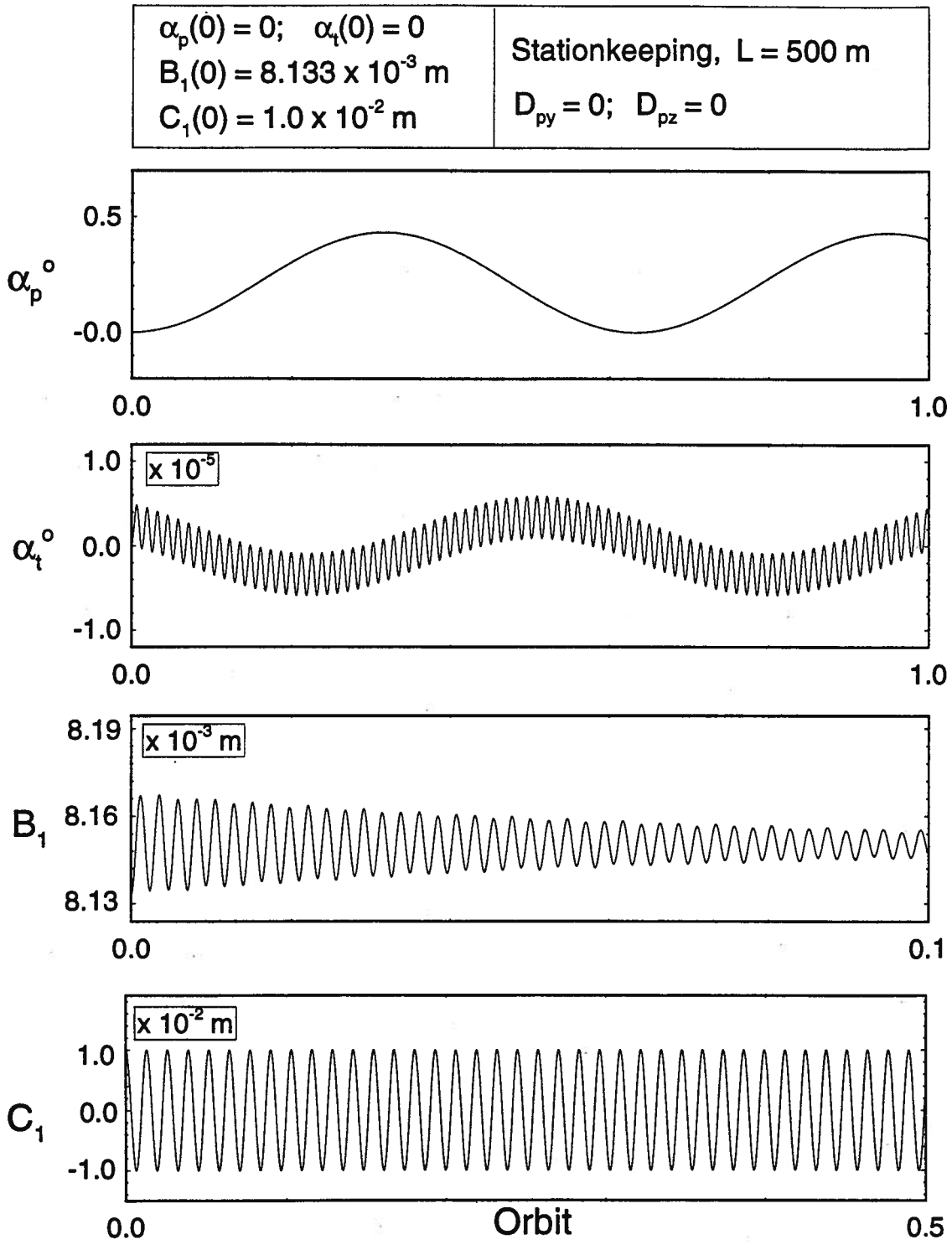

Figure 4-6 System response during stationkeeping showing the effect of flexibility on the tether attitude motion.

coupling with transverse tether oscillation (C_1). But the amplitude of oscillation is of the order of 10^{-5} degree, which can be considered negligible in practical applications.

4.3.3 Offset of the tether attachment point

Effect of the tether attachment point offset was found to be quite significant. It couples the platform dynamics with the tether degrees of freedom. The offset along different directions, i.e. local horizontal and local vertical, was found to have different coupling effects. Thus motion of the tether attachment point, which is required during the offset control, adds extra complexities to the system dynamics. Figure 4-7 shows the system response during the offset motion from the center of mass of the platform by 2 m in 120 s along the local vertical while D_{pz} is held fixed at zero. As shown in the figure, D_{py} is varied according to a sinusoidal acceleration profile. The tether pitch (α_t) and longitudinal elastic mode (B_1) are unaffected by the offset motion, while the platform pitch response (α_p) shows amplitude modulations. The amplitude of the transverse vibration (C_1) reaches around 0.08 m during the offset motion and remains at that value subsequently. Note, here the response reaches a higher value than the initial disturbance of 0.01 m.

Response results were also obtained for an offset motion from zero to 2 m in 120 s along the local horizontal (Figure 4-8). In this case there is strong coupling between the platform and tether dynamics. Particularly, the platform oscillates at much lower frequency and about a mean orientation at -90^o as compared to the local horizontal position in Figure 4-7. The C_1 response is modulated due to the coupling with the platform dynamics. The other degrees of freedom behave as before.

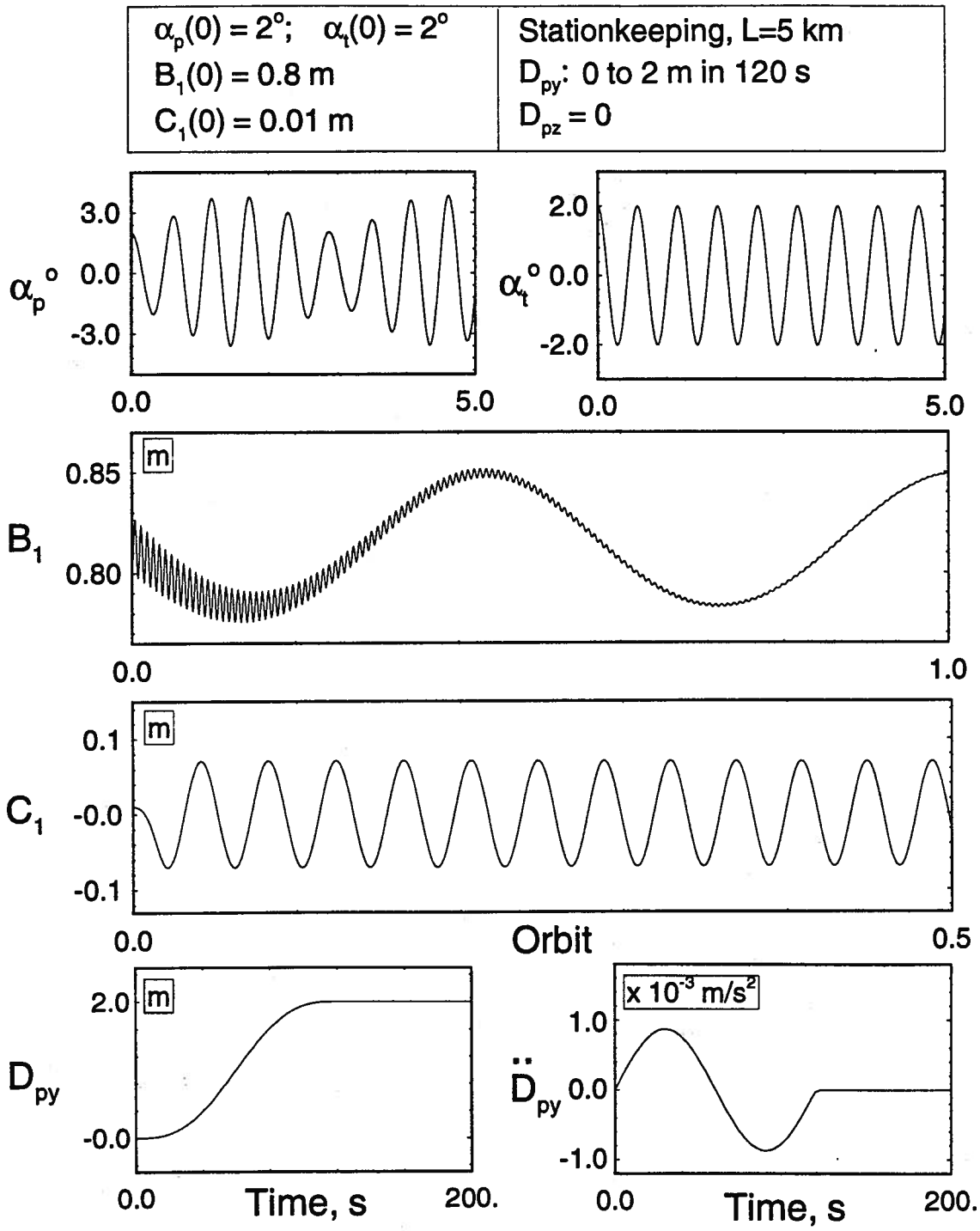

Figure 4-7 Simulation results during offset motion along the local vertical with the offset along the local horizontal fixed at zero.

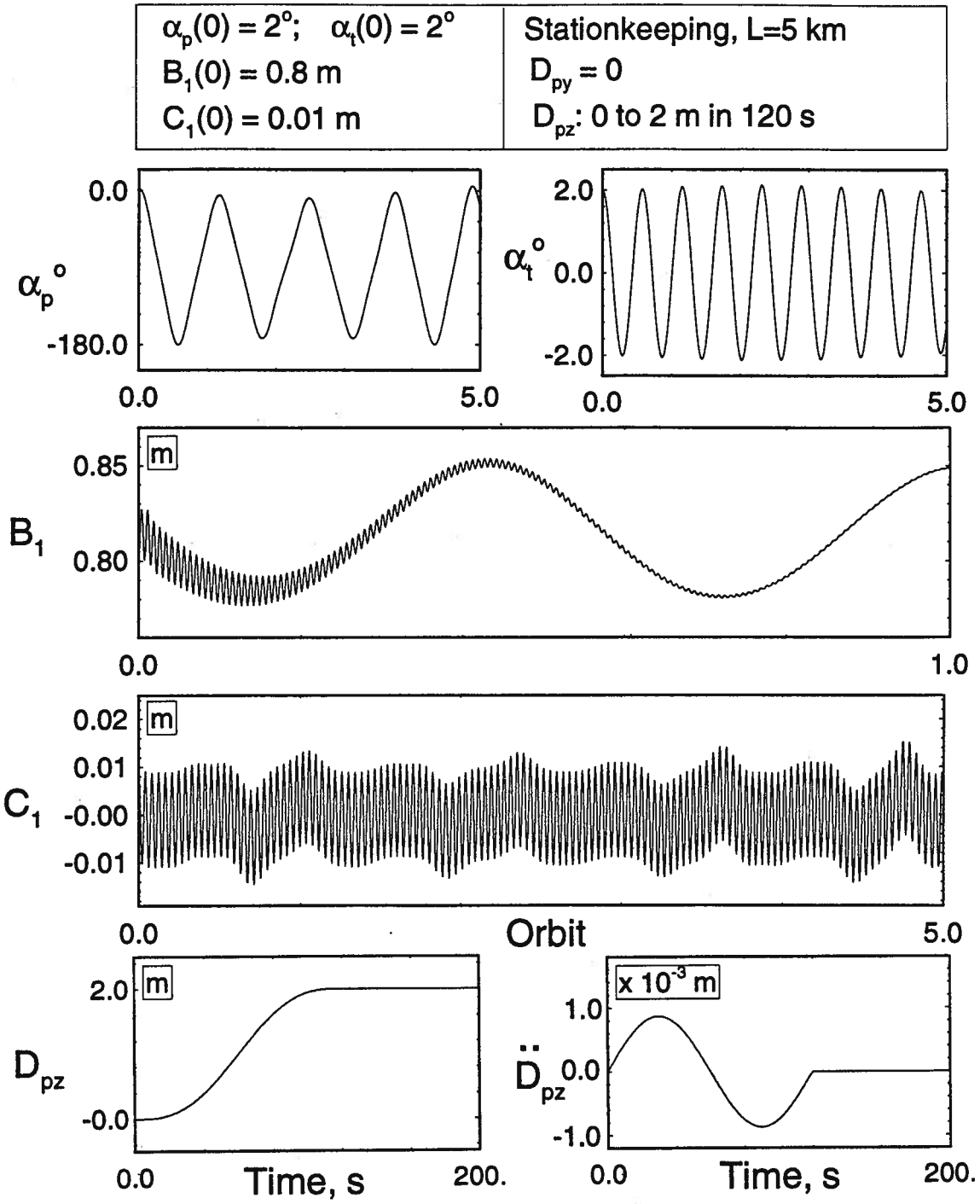

Figure 4-8 System response showing the effect of offset motion along the local horizontal.

When a fixed offset is given along both the local horizontal (D_{py}) and the local vertical (D_{pz}) directions (Figure 4-9), there is a strong modulation of the α_p response like that shown in Figure 4-7 but the frequency is not modulated as indicated in Figure 4-8. As shown in Figure 4-9, the transverse vibration (C_1) has a regular amplitude modulations due to the coupling with the platform pitch motion, however, The tether attitude and the longitudinal flexible modes are unaffected by the offsets.

4.3.4 Tether mass and elasticity

The flexible motion of the tether is significantly dependent on the mass and elastic properties of the material. The two flexible characteristics which are most affected by the change in mass and elastic stiffness are: static deformation of the tether; and the frequency of both the transverse and the longitudinal vibrations. To understand these effects, studies were undertaken with different mass densities and elastic stiffnesses for the stationkeeping phase at a tether length of 5 km. A decrease in the linear mass density (ρ_t) from 4.9 $\times$ 10^{-3} kg/m (corresponding to the reference case) to 1.0 $\times$ 10^{-3} kg/m does not significantly affect the longitudinal response (Figure 4-10). However, the frequency of the transverse elastic mode is increased from 0.0045 Hz, corresponding to the reference case (Figure 4-3), to 0.01 Hz. The platform and tether attitude responses are not affected by the change in the tether mass.

There is an increase in the static elongation of the tether from around 0.81 m to 0.88 m when the linear mass density is increased to 25 $\times$ 10^{-3} kg/m from the reference value of 4.9 $\times$ 10^{-3} kg/m. As shown in Figure 4-11, the most significant change is observed in the frequency of the transverse vibration mode (C_1), which

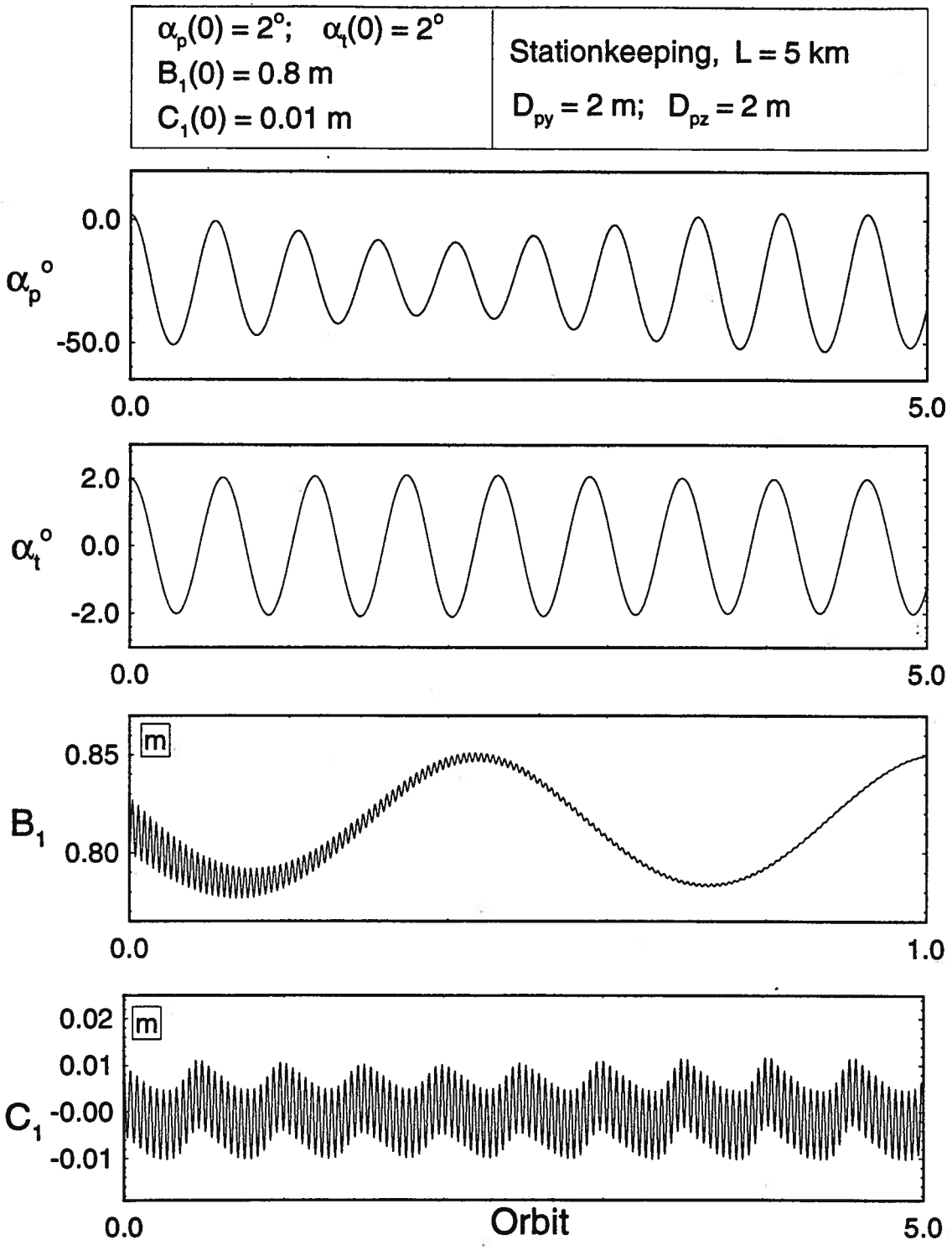

Figure 4-9 Dynamical response of the system with fixed offsets along both the local horizontal and local vertical directions.

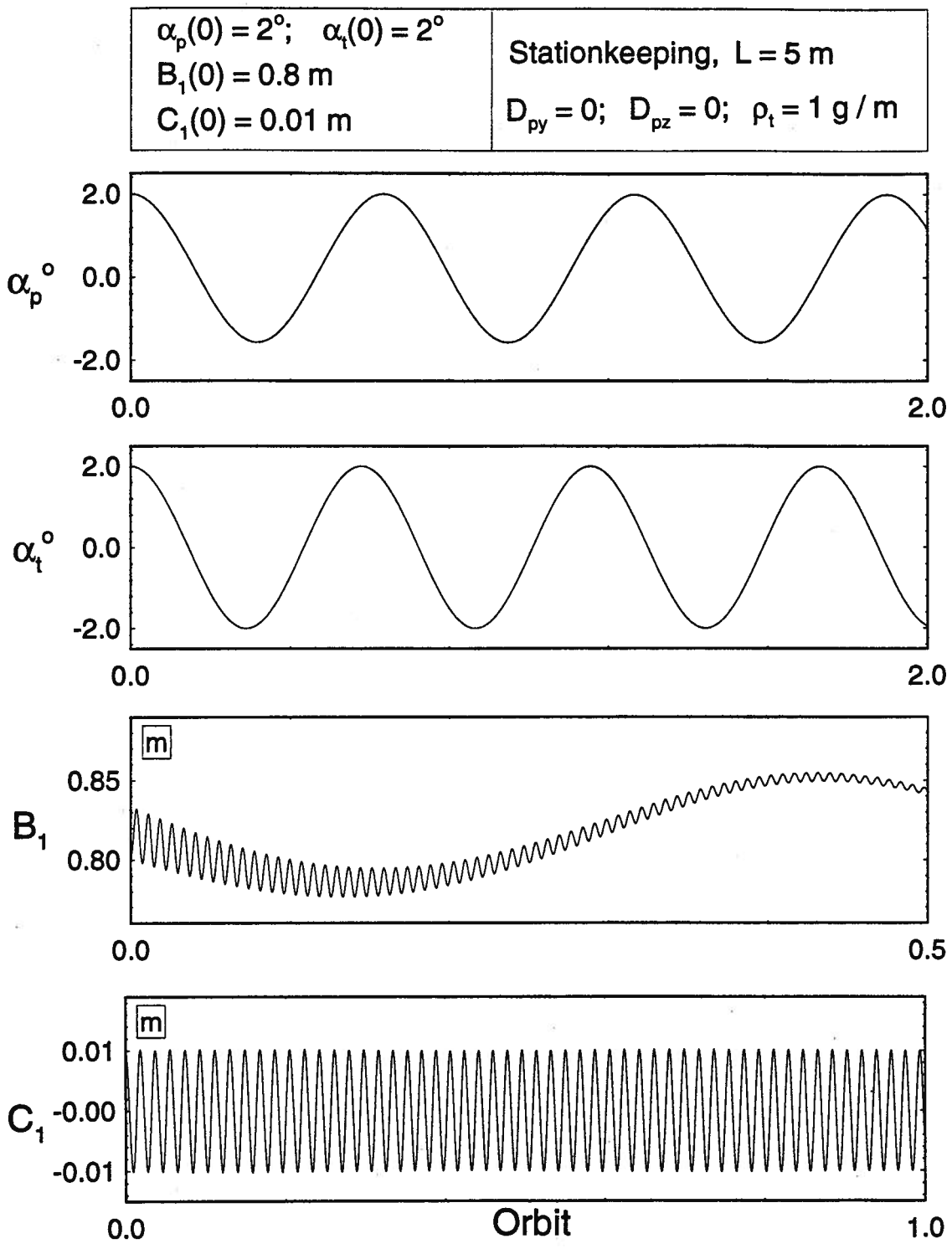

Figure 4-10 Plots showing the effect of decreasing the tether mass per unit length on the system response.

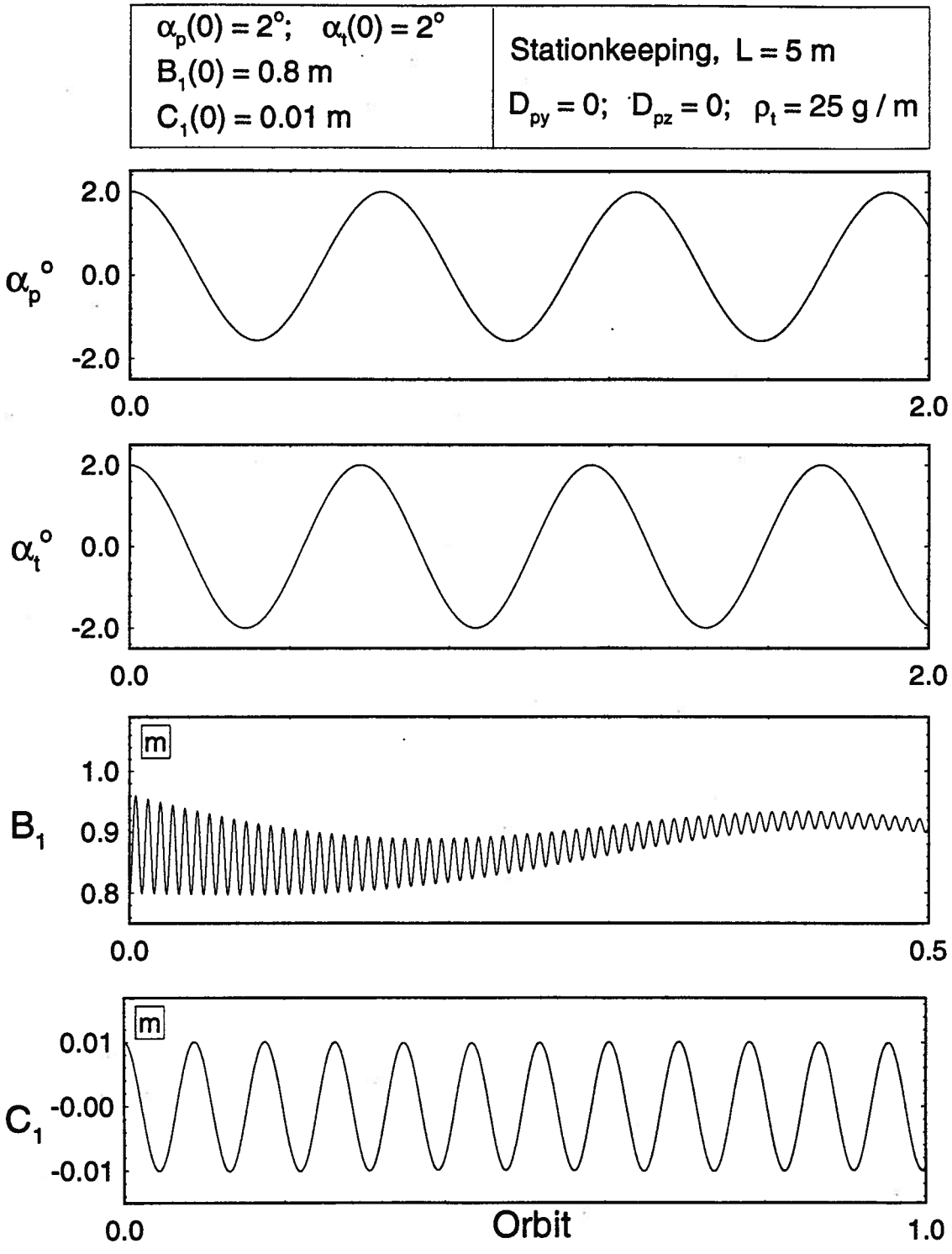

Figure 4-11 System response with an increase in the mass per unit length of the tether.

is decreased to 0.0021 Hz from the reference value of 0.0045 Hz. The rigid body responses are essentially unchanged.

The response of the system with a decrease in the the elastic stiffness (EA) to 40,000 N from the reference value of 61,645 N, is shown in Figure 4-12. As expected, with the reduced stiffness the static elongation of the tether increased to 1.27 m compared to 0.81 m for the reference case (Figure 4-3). The frequency of the longitudinal vibration (B_1) is also reduced to 0.02 Hz from the reference value of 0.0249 Hz. The change in stiffness has only a small influence on the transverse oscillation (C_1) of the tether. For a system with an increase in the elastic stiffness of the tether (Figure 4-13), the trends are as expected. Now, the frequency of B_1 is increased to 0.0282 Hz from the reference value of 0.0249 Hz. As before, the transverse vibrations exhibit insignificant change from the reference response.

4.3.5 Subsatellite mass

The mass of the subsatellite (m_s) is an important parameter affecting, particularly, flexible dynamics of the tethered satellite systems. The tether tension is mainly governed by the subsatellite mass and length profile during deployment/retrieval which, in turn, affects the elastic response of the system. The system behaviour with a decrease in the end mass to 50 kg and its increase to 5,000 kg from the reference value of 500 kg, is shown in Figures 4-14 and 4-15, respectively. For $m_s = 50$ kg (Figure 4-14), frequency of the longitudinal oscillation increased to 0.0733 Hz from the reference value of 0.0249 Hz (Figure 4-3). This can be explained by modelling the longitudinal oscillation by a spring–mass system which has a frequency inversely proportional to square root of the end mass. However, the frequency of the transverse vibration, which is proportional to square root of the tether tension

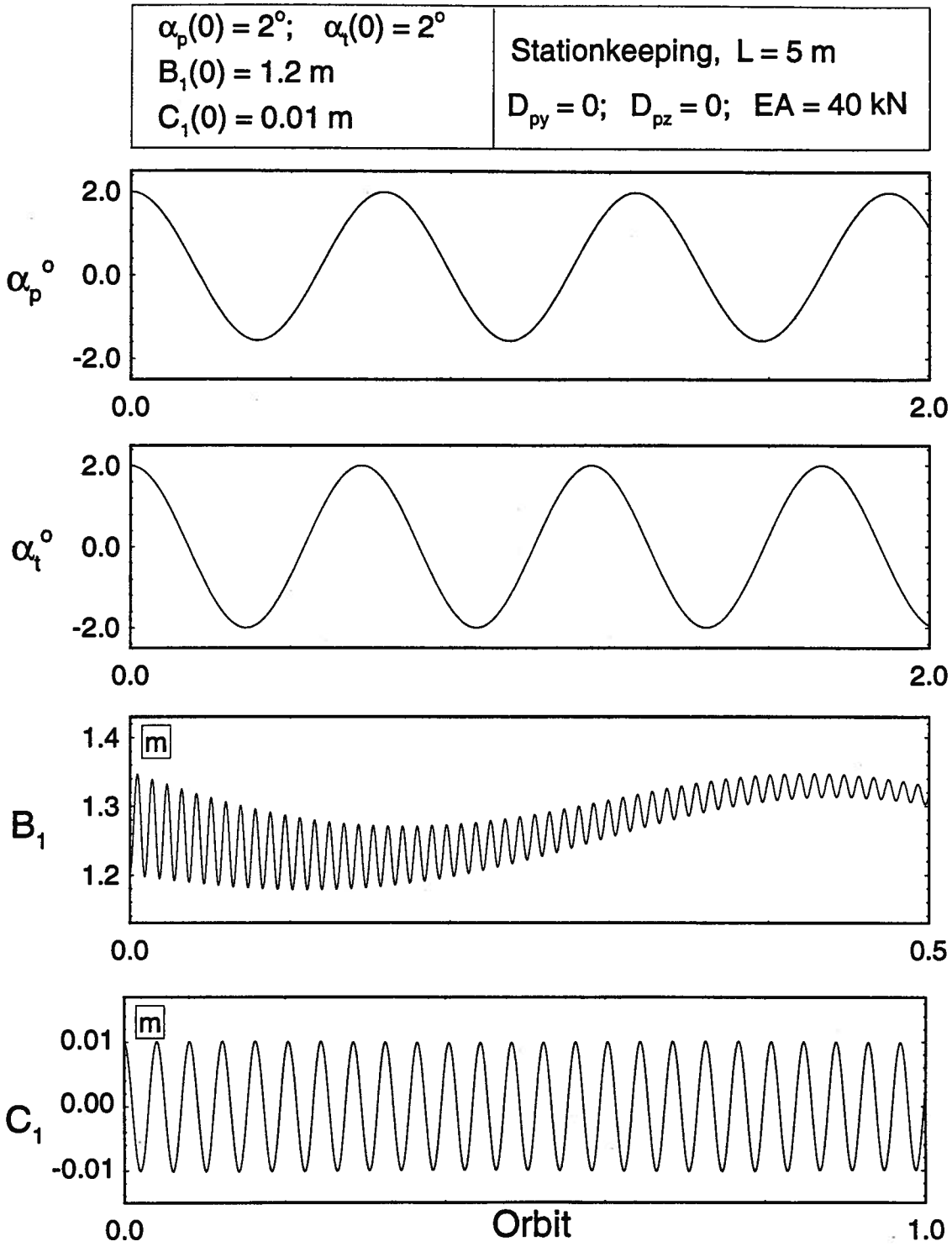

Figure 4-12 Diagram showing the effect of decreasing the elastic stiffness.

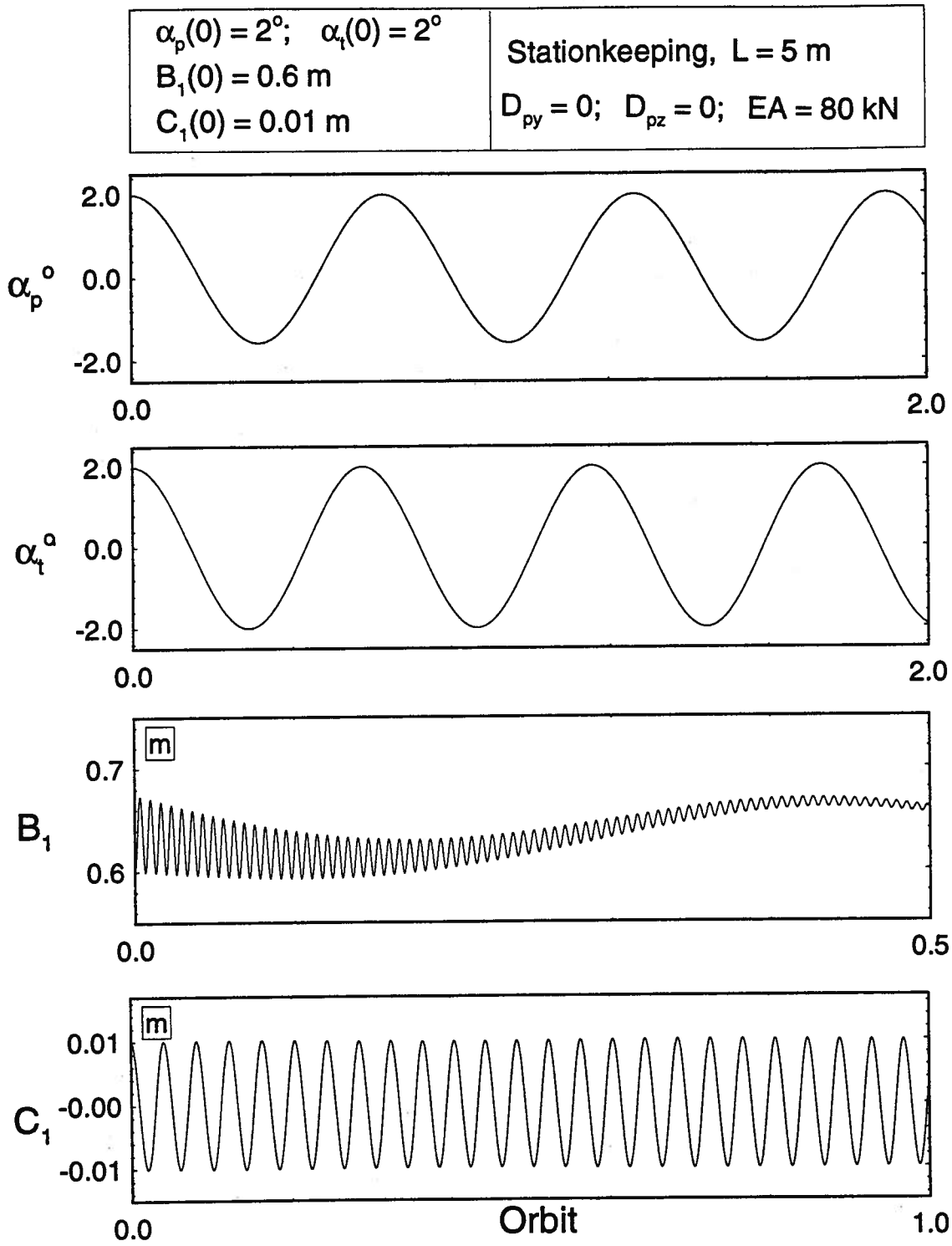

Figure 4-13 Response of the system with an increase in the elastic stiffness.

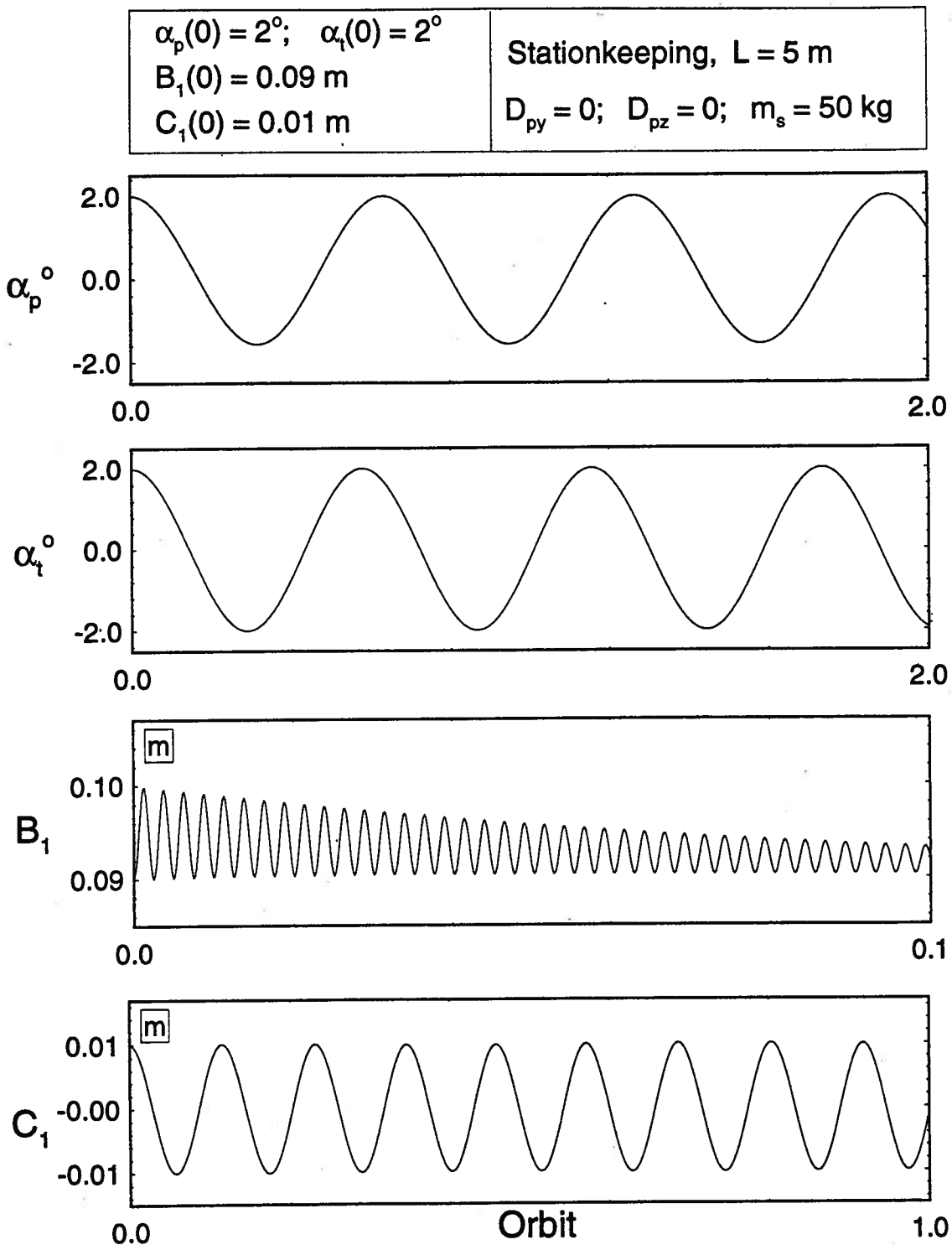

Figure 4-14 Response results showing the effect of decreasing the subsatellite mass.

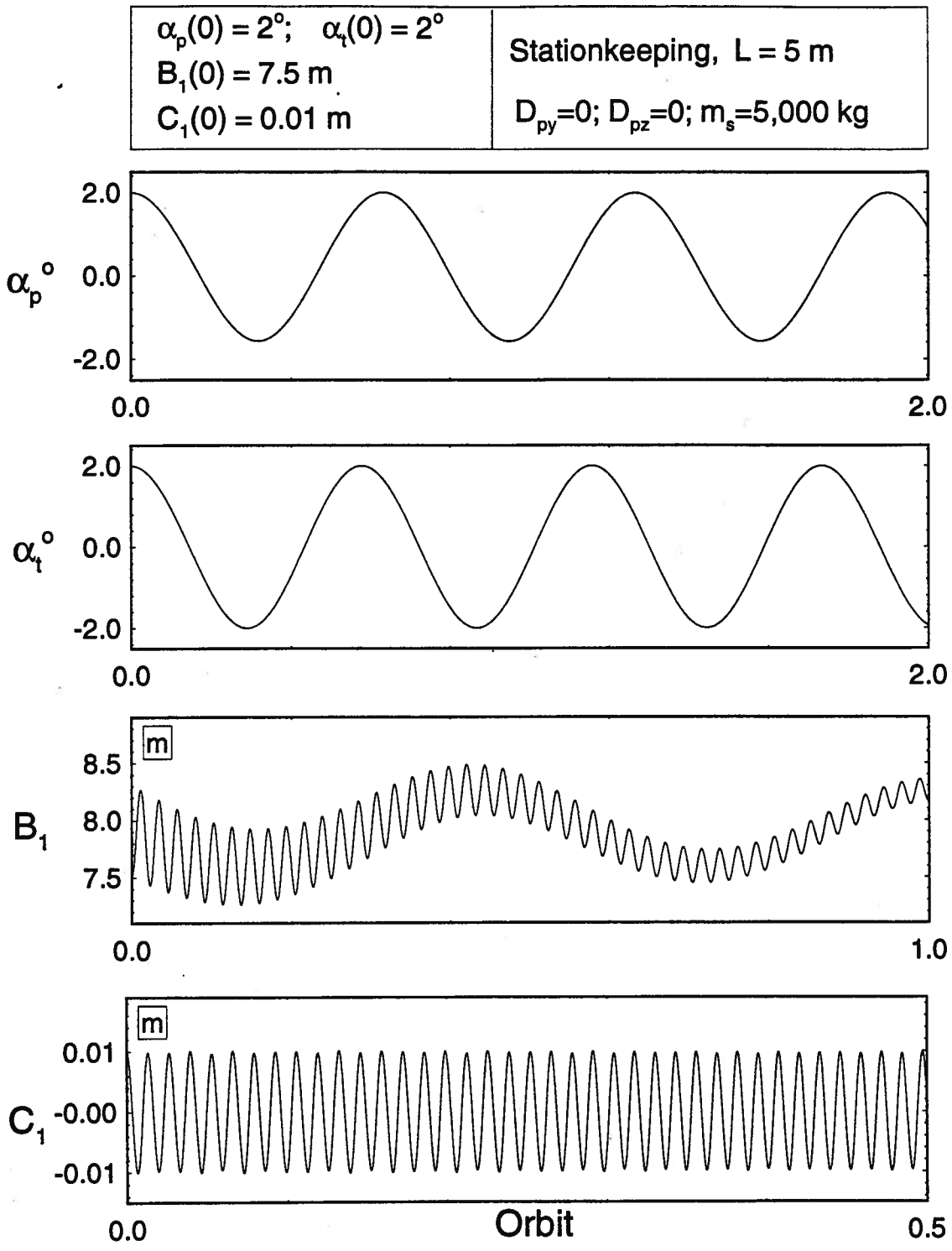

Figure 4-15 System response with an increase in the subsatellite mass.

[73] (tension is higher for a larger subsatellite mass), has a lower value of 0.0016 Hz as compared to 0.0045 Hz in the reference case. On the other hand, for an increase in the subsatellite mass to 5,000 kg, the frequency of longitudinal oscillation reduced to 0.0081 Hz and that of the transverse vibration increased to 0.014 Hz. It is interesting to note that the frequencies of the transverse and longitudinal oscillations change in opposite directions (i.e. one decreases and the other increases) for a change in the subsatellite mass. As expected, the static elongation of the tether is more for higher subsatellite mass.

4.3.6 Deployment and retrieval

From the dynamics point of view, deployment and retrieval are the critical phases in a tether mission. As pointed out before, the retrieval dynamics is an inherently unstable operation where as the deployment can be unstable if the velocity exceeds a certain critical value. Figure 4-16 shows the dynamic response during deployment of the subsatellite from a tether length of 200 m to 20 km in 3 $orbits$. An exponential- constant-exponential velocity profile is employed for the deployment. The deployment parameters are obtained from Eqs.(4.4-4.7). The velocity profile switches from the exponential to constant at a tether length of 2.5 km and the second switch, from constant to exponential, occurs at 18 km ($L_1 = 2.5$ km and $L_2 = 18$ km). As shown in the figure, even with a zero initial condition, the tether pitch (α_t) grows to -30^o during the initial phase of the tether deployment. Subsequently, it slowly decreases and oscillates between $\pm 2^o$ after the deployment is over. This growth in the amplitude of α_t is mainly due to the Coriolis force caused by the interaction between the orbital and deployment velocities. For zero offset, there is no coupling between the platform and the tether dynamics. Therefore, α_p oscillates between 0 and 0.5^o. The mean value of 0.25^o is caused by the nonzero product

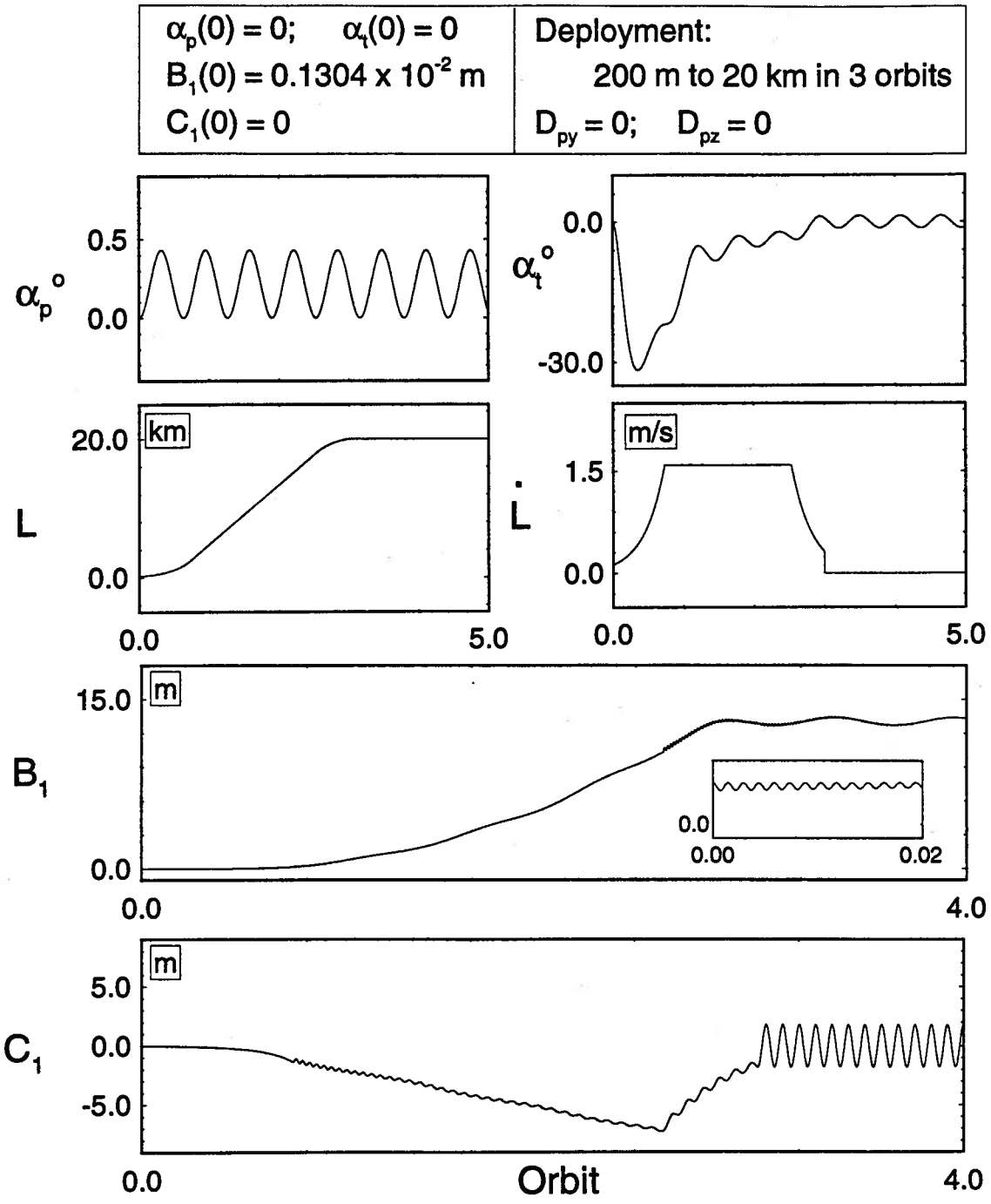

Figure 4-16 Response of the system during deployment of the subsatellite using an exponential-constant-exponential velocity profile.

of inertia about the Y_p, Z_p axes ($I_{p_{yz}} \neq 0$). As expected, the mean value of the longitudinal oscillations, which is the static elongation of the tether, increases with the length. As shown in the inset of the B_1 plot, the deformation of the tether is greater than zero implying that the tether tension is positive. Since tension in the tether is small at the beginning of the deployment, it is critical to use appropriate acceleration profile for deployment because higher acceleration may cause slackness (i.e. negative tension) in the tether. If the first switch in the velocity profile occurred at 800 m ($L_1 = 800$ m) instead at 2.5 km, B_1 became negative at the beginning of the deployment and the tether was slack (plot not shown). Because of the Coriolis force, C_1 increases to -7 m even without any initial disturbance. In the terminal exponential deployment phase, C_1 decreases because of the decrease in the velocity ($\dot{L}$). After the deployment is over C_1 oscillates with a constant amplitude about the zero mean value.

The system response for retrieval from $L = 20$ km to 200 m in 4 *orbits* with an exponential velocity profile is shown in Figure 4-17. The Coriolis force during the retrieval made the tether pitch (α_t) unstable. Since the offset in the simulation is taken to be zero, the platform attitude angle is not affected by the tether motion. As expected, the tether elongation (B_1) decreased with the length. As the length decreased, frequencies of the elastic modes (B_1 and C_1) increased as expected. The instability in the system excited the transverse mode (C_1), which grew to ± 50 m. The magnitude of the retrieval velocity, and hence the Coriolis force, decreases with the tether length. This, along with the increase in the stiffness, led to the decrease in the amplitude of C_1 towards the end of the retrieval. However, at the beginning of the retrieval the instability due to the Coriolis force is stronger resulting in an increase in the transverse amplitude. The instability also excited the longitudinal oscillations resulting in negative B_1, i.e. the slack tether.

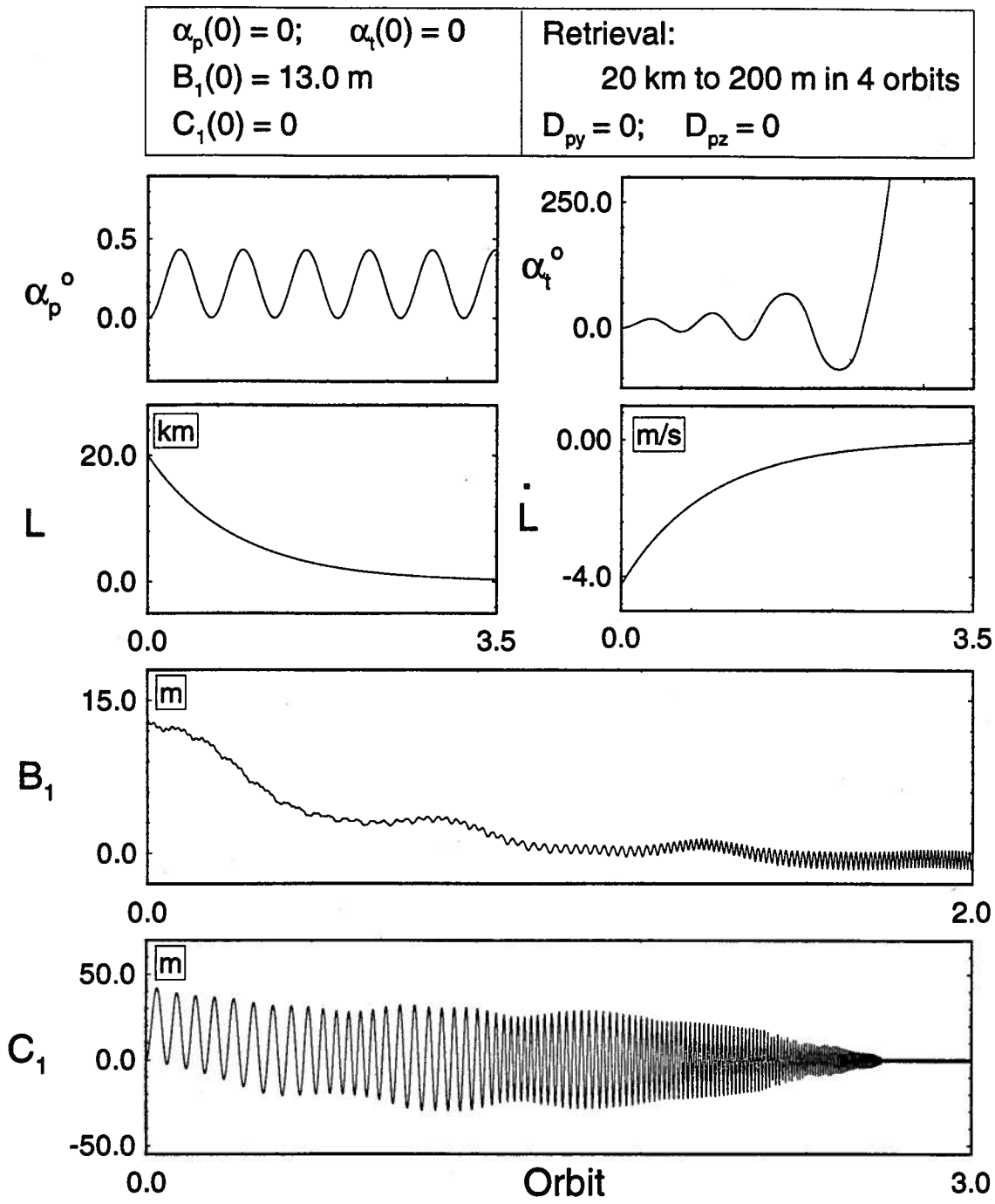

Figure 4-17 System response during exponential retrieval of the subsatellite. Note instability of the system in rigid (α_t) as well as flexible (B_1) degrees of freedom.

4.3.7 Shift in the center of mass

In a typical mission the length of the tether can vary from zero to 20 km. Experiments involving 100 km long tether are in the planning stage. Obviously, this would result in an extremely wide shift in the center of mass of the system. Figure 4-18 shows plots for the shift in the center of mass of the system during deployment, stationkeeping and retrieval for a maximum tether length of 20 km. As expected, at the beginning of deployment ($L = 200\ m$), the shift in the center of mass is small (Figure 4-18 a). The shift along the local vertical (R_{py}) increases with the tether length and, at the end of the deployment, R_{py} becomes more than 120 m, which is 0.6 % of the tether length. The shift along the local horizontal (R_{pz}) is mainly due to the tether libration. Though the tether pitch is large at the beginning of the deployment (Figure 4-16), because of a smaller length, R_{pz} variations remain essentially the same. As shown in Figure 4-16, there is a change in the mean value of α_t as the deployment terminates. This effect can be easily seen in a change in the amplitude of R_{pz} at the end of deployment.

Figure 4-18(b) shows the response during stationkeeping at $L = 20\ km$. The coupling between the attitude motion of the tether and platform results in a beat response for both R_{py} and R_{pz}. R_{py} variations are confined to one side of -121.26 m, where as R_{pz} oscillates about the zero mean. As expected, R_{py} decreases with the tether length during retrieval (Figure 4-18 c). The retrieval is carried out from a tether length of 20 km to 200 m in 4 *orbits* with an exponential velocity profile. The tether pitch (α_t) being unstable, there is no specific pattern to the shift in the center of mass. Though α_t becomes very large during the retrieval, R_{pz} does not increase beyond $-25\ m$. This is due to the fact that an increase in the tether attitude angle is associated with a decrease in the tether length. The combined effect of these two

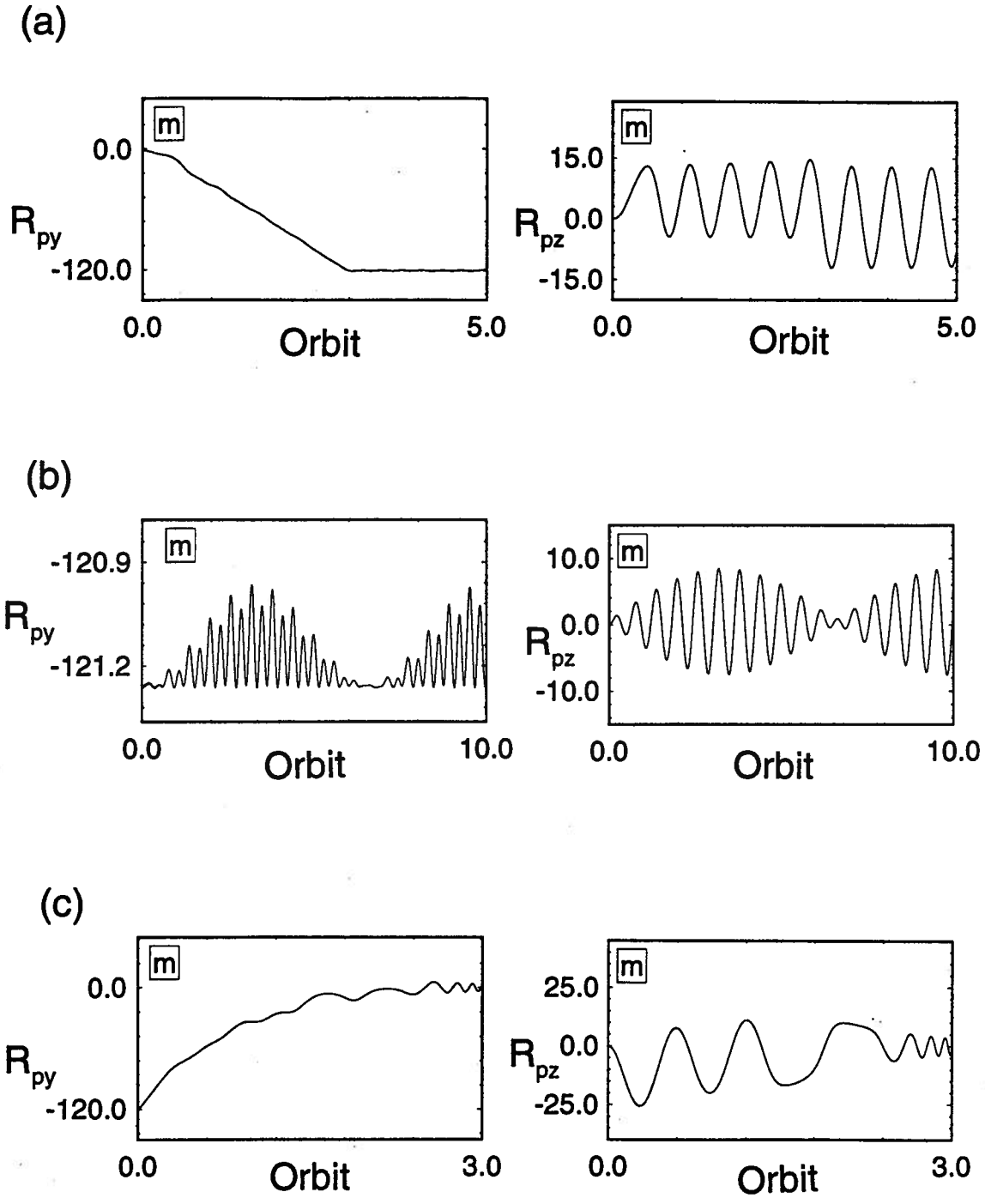

Figure 4-18 Plots showing shift in the center of mass during three different phases of the system operation:(a) deployment; (b) stationkeeping; and (c) retrieval. Total deployed length is 20 *km*.

factors limits any increase in R_{pz} beyond a certain value.

4.4 Concluding Remarks

Results of a comprehensive parametric study suggest the following:

(i) Higher modes carry insignificant amount of energy.

(ii) In absence of the tether attachment point offset, tether flexibility has little effect on the rigid body dynamics.

(iii) Offset of the tether attachment point couples the platform dynamics with the tether degrees of freedom.

(iv) Flexible dynamics of the tether is substantially affected by the mass and elastic properties of the tether material. In particular, they affect static deflection of the tether, and frequency of both transverse and longitudinal oscillations.

(v) The tension of the tether is primarily governed by the subsatellite mass and length of the tether and, in turn, affects its natural frequencies.

(vi) Deployment and retrieval represent critical phases in a tethered mission. Depending on the deployment/retrieval rate, the system is susceptible to instability and the tether may become slack.

(vii) There can be significant shift in the system center of mass during deployment, stationkeeping and retrieval.

5. ATTITUDE CONTROL

5.1 Preliminary Remarks

The instability during retrieval, large amplitude swinging motion at the time of deployment and undesirable performance in the stationkeeping phase would demand some active control strategy for a successful tether mission. Depending on the mission requirements, the objective of the controller is to regulate the attitude and/or flexible motion of the system. The design and implementation of the attitude controller is addressed in this chapter.

As mentioned in Chapter 1, in the past, control of tethered systems has been approached through three different strategies: tension or length rate control; thruster control; and offset strategy. The tension or length rate control scheme depends on the differential gravity field, and hence is ineffective at shorter tether lengths. Although the thruster based control procedure is unaffected by the length of the tether, it is not advisable to use thrusters in the vicinity of the space platform due to plume impingement and safety considerations. Therefore, the offset control strategy is the most effective choice for shorter tethers. The offset motion required for controlling the tether attitude dynamics increases with the length and hence the applicability of this strategy is limited by the space available to move the tether attachment point on the platform.

The advantages associated with the three control strategies over different lengths lead to a hybrid scheme where the offset method can be used for shorter tethers and thruster or tension based approaches can be applied at longer lengths. Such a hybrid strategy was originally used by Modi *et al.*[49] for a rigid tethered

system. In this thesis, the hybrid strategy is extended to a system with flexible tether. The thruster augmented active control is used here to regulate the attitude dynamics for longer tethers.

The dominant feature, which governs the system characteristics, is the time varying length of the tether. If the time dependent variation of the system parameters is relatively small, the Linear Time Invariant (LTI) robust control techniques can be used to regulate the dynamics with the parameter variations treated as uncertainties. But, in the present situation, the length of the tether varies from few meters to 20 km, and hence the robust LTI controller will not be effective. There are mainly four different approaches to control such highly time varying systems:

- gain scheduling control;
- adaptive/self-tuning control;
- simultaneous control of multiple plants;
- control based on the Feedback Linearization Technique (FLT).

In the gain scheduling approach, a number of LTI controllers are designed for different operating conditions and are stored on-board. In the real time operation, the controller selects and implements the appropriate gains corresponding to an operating condition. The major difficulties with these controllers are the design and storage of the controller gains for a number of operating conditions. Any change in the mission objective may need redesign of the controllers for new operating points.

In the adaptive control, a simple system model is estimated from the knowledge of the system inputs and outputs. Based on the estimated model, the controller is designed and implemented in real time [74]. This approach has advantages for systems whose dynamics can not be modelled accurately.

Another alternative to these approaches is the simultaneous control of a number of LTI plants, over the entire range of parameter variation, by a single controller. Here, the time varying system is considered as a collection of controllable and observable LTI plants described by:

$$\dot{x}_i = A_i x_i + B_i u_i; \tag{5.1}$$

$$y_i = C_i x_i, \qquad i = 1, 2, \cdots, n_p; \tag{5.2}$$

where: x_i, y_i and u_i are the state, output and control input vectors, respectively; and A_i, B_i and C_i are the LTI matrices of appropriate dimensions. The index 'i' corresponds to the i^{th} plant and n_p is the total number of plants. Considering the output feedback, the objective is to design a single controller, $u_i = -Ky_i, \quad i = 1, 2, \cdots, n_p$, so that all the plants are simultaneously controlled. The control can also be achieved by state or dynamic output feedback. Several algorithms to accomplish this objective have been reported in the literature [75–81].

In the FLT, the nonlinear and time varying dynamic equations are transformed into an LTI system by the nonlinear, time-varying feedback. Thus a single controller structure can regulate the highly time varying and nonlinear dynamics of the system. References [82-88] discuss detail mathematical background and design procedures for the feedback linearization control.

The FLT based controller is quite effective for systems which can be modelled accurately. The controller performance is sensitive to the modelling errors [89]. In the present study, attitude dynamics of the system can be modelled quite accurately and hence the FLT is selected for the controller design. In a general problem with feedback linearization, the control algorithm consists of three steps: transformation of the state space; control variable transformation making the system linear in the

new coordinate system; and control of the linear system in the new state space. The dimension of the transformed linear controllable system depends on its properties and type of the linearization procedure applied, such as the input-state or the input-output feedback linearization [83].

The attitude controller for shorter and longer tethers are designed using the offset and the thruster strategies, respectively. The following section discusses the design algorithm and implementation of the thruster based controller. The design and implementation issues related to the offset strategy are addressed in the next section. Finally, a hybrid control scheme is presented followed by some concluding remarks.

5.2 Thruster Control Using Dynamic Inversion

Selection of an acceptable design model is important in the development of a controller using the dynamic inversion. From the implementation point of view, it is advantageous to use a simpler model for the controller design. However, an approximate model may affect the system stability [89] and performance. In the present study an acceptable dynamic model for the controller design is obtained via numerical simulation. Three different models – complete nonlinear flexible, rigid nonlinear, and rigid linear – are selected for the controller design. Simulation results for each case are compared to arrive at an acceptable model.

5.2.1 Controller design algorithm

As pointed out before, the thruster control strategy is used to regulate the attitude motion of the longer tether, and momentum gyros control the platform pitch motion. The rigid body modes, i.e. α_p and α_t, are controlled actively through

feedback and the flexible degrees of freedom are regulated by passive dampers. The control of the flexible generalized coordinates becomes important particularly during retrieval when the elastic modes are unstable. The controller for the rigid degrees of freedom is designed using the inverse control procedure, which is a special case of the Feedback Linearization Technique (FLT). In case of the thruster control, the system is already in the canonical form. So only control transformation is necessary for linearization of the system.

The system model for the controller design can be expressed in the form

$$M_s \ \ddot{q}_s + F_s = Q_s, \tag{5.3}$$

where: M_s is the mass matrix; F_s is the vector of nonlinear terms; and q_s and Q_s are the vectors of generalized coordinates and forces, respectively. If the number of independent control inputs in Q_s is the same as the dimension of q_s, the above system can be transformed into a linear time invariant form by the generalized force vector

$$Q_s = M_s v + F_s. \tag{5.4}$$

This transforms Eq.(5.3) into a linear form of

$$\ddot{q}_s = v. \tag{5.5}$$

Here v is the new control input required to regulate the transformed decoupled linear system. A linear control theory can be used to design the control input. In the present study, v is chosen in such a way that the error ($e = q_s - q_{s_d}$) dynamics has poles at desired locations in the s-plane. This is accomplished by

$$v = \ddot{q}_{s_d} + K_v(\dot{q}_{s_d} - \dot{q}_s) + K_p(q_{s_d} - q_s), \tag{5.6}$$

which results in the error equation

$$\ddot{e} + K_v\dot{e} + K_p e = 0. \tag{5.7}$$

Here K_v and K_p are the diagonal matrices of velocity and position feedback gains, respectively, and q_{s_d}, $\dot{q}_{s_d}$ and $\ddot{q}_{s_d}$ represent the desired trajectory. The controller expression in Eq.(5.4) is referred to as *the primary controller* while that in Eq.(5.6) is called *the secondary controller.*

The next step in the controller design is to decide an acceptable structure for M_s, F_s and Q_s for the system model in Eq.(5.3). As mentioned before: nonlinear flexible; nonlinear rigid; and linear rigid models are used for the controller design. The linear and nonlinear rigid models are in a form which can directly be used for the controller design. But the nonlinear flexible model has a different form. However, it can be transformed to have the required structure as follows.

The system under consideration has the form

$$M(q,t)\ \ddot{q} + F(q,\dot{q},t) = Q_q, \tag{5.8}$$

where: q and Q_q are vectors of the generalized coordinates and forces, respectively; $M(q,t)$ is the nonlinear time varying mass matrix; and $F(q,\dot{q},t)$ is the vector containing nonlinear gravitational, Coriolis and centrifugal terms. Here the dimension of q is more than the number of independent control inputs in Q_q. Let q_r and q_f denote the components of q; F_r and F_f the components of $F(q,\dot{q},t)$; and Q_{q_r} and Q_{q_f} the components of Q_q corresponding to the rigid and flexible modes, respectively. Here Q_{q_r} represents the generalized forces due to the control inputs, and Q_{q_f} corresponds to the generalized forces due to the passive dampers in the system.

Partitioning the mass matrix appropriately, the above equation can be rewritten as

$$\begin{bmatrix} M_{rr} & M_{rf} \\ M_{fr} & M_{ff} \end{bmatrix} \begin{Bmatrix} \ddot{q}_r \\ \ddot{q}_f \end{Bmatrix} + \begin{Bmatrix} F_r \\ F_f \end{Bmatrix} = \begin{Bmatrix} Q_{qr} \\ Q_{qf} \end{Bmatrix}. \tag{5.9}$$

Here: $q_r = \{\alpha_p,\ \alpha_t\}^T$; $q_f = \{B_1,\ B_2, \cdots, B_{N_l},\ C_1,\ C_2, \cdots, C_{N_t}\}^T$; and N_t and N_l represent the number of flexible modes in transverse and longitudinal directions, respectively. If the controller is to be designed based on the rigid model of the system, M_{rf} and the flexibility terms from M_{rr}, F_r and Q_{qr} are neglected and the resulting rigid body (q_r) equation can be used to design the controller using Eqs.(5.4) and (5.6). But if the effect of flexibility on the rigid modes is to be accounted for by the controller, the equations of motion for the rigid degrees of freedom (q_r) can be obtained as [84]

$$M_s\ \ddot{q}_r + F_s = Q_{qr}, \tag{5.10}$$

where:

$$M_s = M_{rr} - M_{rf} M_{ff}^{-1} M_{fr};$$

$$\text{and} \quad F_s = F_r + M_{rf} M_{ff}^{-1} (-F_f + Q_{qf}).$$

Eqs.(5.4) and (5.6) can be used to design the controller for this system.

In the implementation of this control strategy, the submatrices of M and F are to be computed, which need the knowledge of the flexible system model and the flexible generalized coordinates. Using the *assumed mode method* to discretize the elastic deformations, the dynamic model can be obtained with a considerable degree of accuracy. The problems associated with the observation of the flexible modes and their resolution is a subject in itself. Here, it is assumed that the flexible generalized coordinates are available for the control purpose.

5.2.2 Control with the knowledge of complete dynamics

The system model considered for the controller design includes all the nonlinear time varying terms including the effect of tether flexibility (Eq. 5.10). The controller is designed using the dynamic inversion (Eqs. 5.4 and 5.6) and implemented on the complete nonlinear flexible model of the system (Eq. 5.8). The numerical values for the system parameters considered in the simulation are the same as those used for the dynamic study in Chapter 4. Only the first longitudinal (B_1) and lateral (C_1) modes are considered in the simulation, however, the program developed can incorporate an arbitrary number of modes in both directions.

Figure 5-1 shows controlled response of the system during the stationkeeping phase at a tether length of $20km$. Since the dynamics of the rigid system is exactly cancelled by the controller, the platform pitch (α_p) and tether swing (α_t) behave as required. The desired performance specifications for the closed loop system are characterized by the rise and settling times, which are 0.1τ and 0.4τ, respectively, for both the platform and tether librations. Here τ is the orbital period. The thrust (T_{α_t}) requirement is quite small for an initial disturbance of 2^o in the tether pitch (α_t). The nonzero mean value of M_x is required to regulate α_p about zero which is not its equilibrium value, and to cancel the extra moment on the platform due to a nonzero offset. The control inputs (M_x and T_{α_t}) cancel the effect of flexible dynamics on the rigid degrees of freedom. This introduces the high frequency component in the time histories of M_x and T_{α_t}. The coupling between the rigid and flexible generalized coordinates excites the transverse vibration (C_1) even in absence of any initial disturbance. As expected, the longitudinal elastic mode decays due to the structural damping.

The controlled response during deployment from $L = 200m$ to $20km$ in 3

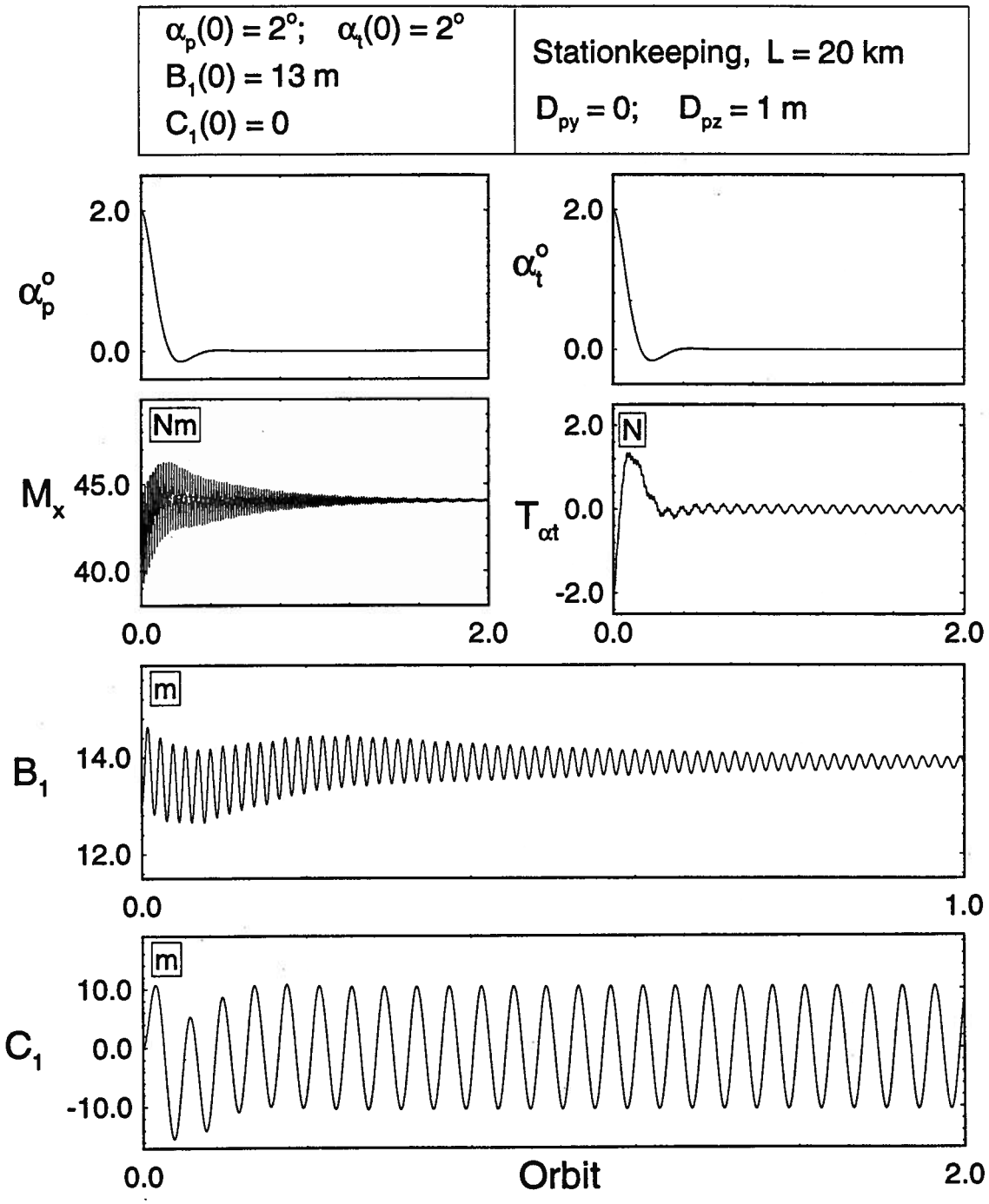

Figure 5-1 Controlled response of the system during the stationkeeping phase.

orbits is shown in Figure 5-2. An exponential-constant-exponential velocity profile is used for the deployment. The first switch from exponential to constant velocity occurs at $L = 2.5\ km$ and the second switch takes place at $L = 18\ km$. The behaviour of the rigid modes, α_p and α_t, is similar to the stationkeeping case. It is interesting to note the similarity between the deployment velocity ($\dot{L}$) and control thrust (T_{α_t}) profile governed by the Coriolis force. The moment M_x is very small due to zero offset of the tether attachment point from the platform center of mass ($D_{py} = D_{pz} = 0$). As expected, elongation of the tether (B_1) increases with the length. With the present deployment profile, inset within the B_1-plot shows the tether elongation at the beginning of deployment to be greater than zero. Sometimes, if the deployment acceleration is high, tether may become slack. The response of the transverse flexible mode (C_1) is governed by two effects: change in the tether tension due to the deployment acceleration profile; and the Coriolis force effects due to the deployment velocity.

The rigid body dynamics during the retrieval is controlled quite successfully (Figure 5-3). However, it is important to recognize the unstable dynamics of the flexible subsystem. The uncontrolled longitudinal elastic mode (B_1) becomes negative implying that the tether is slack. The amplitude of C_1 response also becomes very high ($\pm 80m$) due to the Coriolis force. The retrieval is carried out with an exponential velocity profile (Chapter 4). As the velocity decreases the effect of the Coriolis force becomes small. Furthermore, frequencies of the flexible degrees of freedom increase with a decrease in the tether length. The decay in the amplitudes of B_1 and C_1 responses after certain time during retrieval is due to the combined effect of the tether length, changing Coriolis effect and structural damping. The

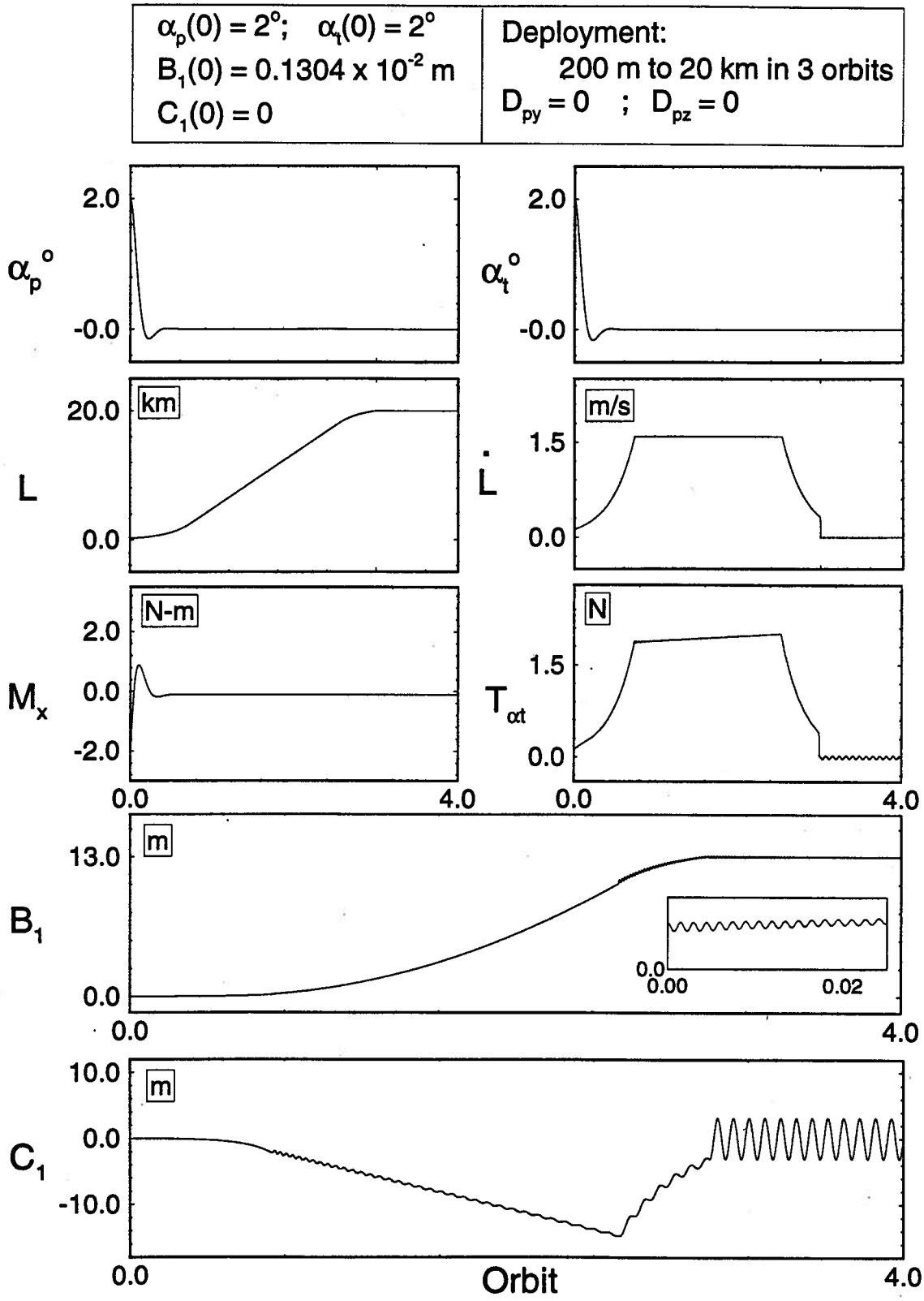

Figure 5-2 System response during controlled deployment with an exponential-constant-exponential velocity profile.

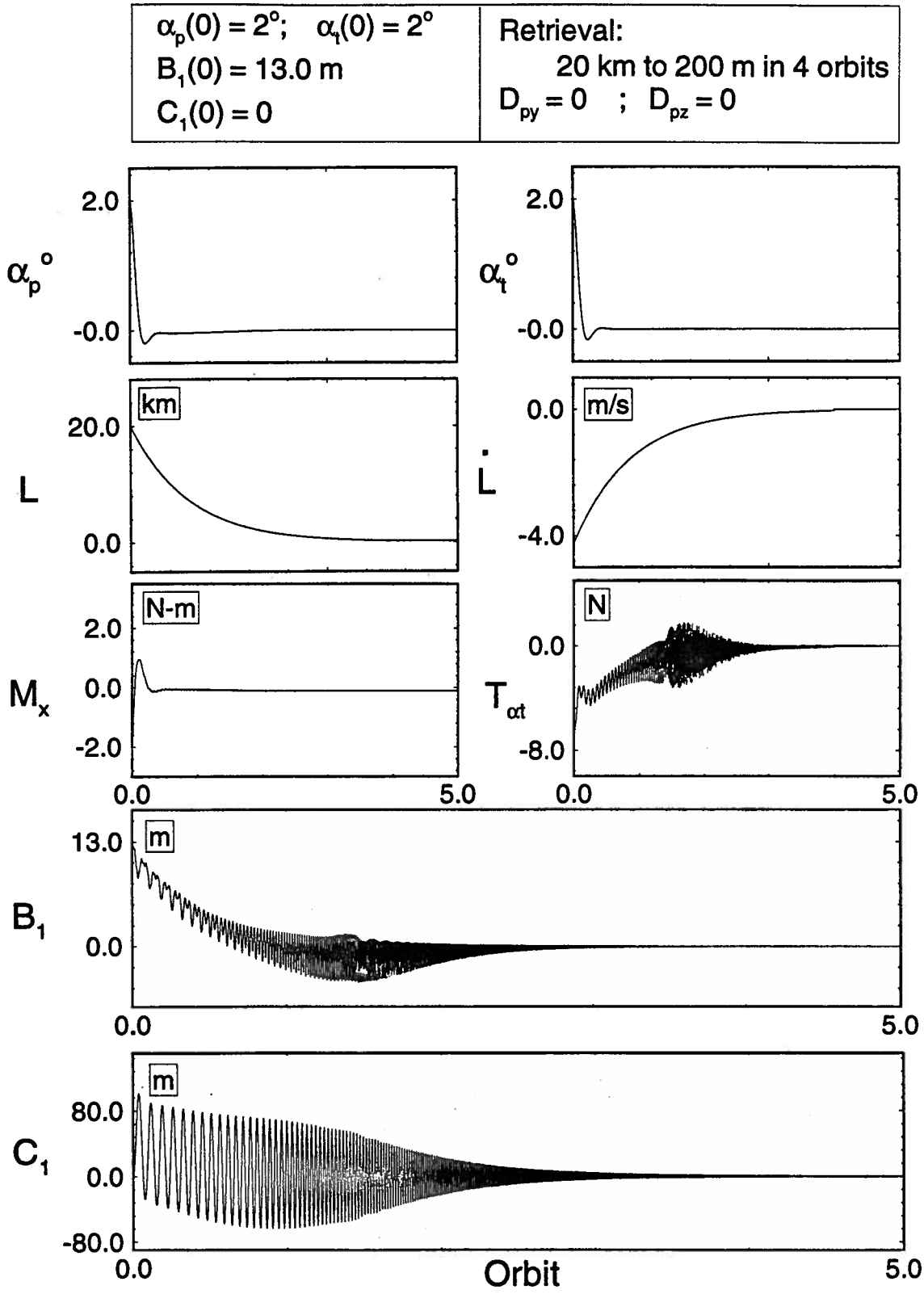

Figure 5-3 . Controlled response during the exponential retrieval without a passive damper.

control thrust cancels effects of the flexible dynamics on the rigid modes resulting in the high frequency oscillations of T_{α_t}.

In the present study, the unstable dynamics of the flexible degrees of freedom is controlled only by passive dampers. Passive dampers are provided for both the transverse and longitudinal oscillations. The transverse damper (damping coefficient = 0.03 Ns/m) is placed at the middle point of the tether and the longitudinal damper (damping coefficient = 1.5 Ns/m) is located at the subsatellite. The magnitude of the damping coefficients considered in the simulation are within the practically achievable range [90]. The results for controlled retrieval with passive dampers are presented in Figure 5-4. The rigid body responses are the same as the previous case without damper. However, the flexible responses (B_1 and C_1) now settle to their equilibrium values rather quickly. Note, the magnitude of B_1 is always greater than zero implying that the tether has positive tension.

5.2.3 Inverse control using simplified models

The controller design in the last section is based on the complete nonlinear model of the system. The implementation of this controller needs knowledge of all the flexible modes, which are difficult to obtain, and requires considerable amount of the real time computational effort. These limitations may make the controller difficult to implement. Therefore, to obtain a readily implementable controller, two simplified models are considered here. The results of the uncontrolled dynamic simulation (Chapter 4) serves as the guideline in selecting the simplified model. As seen in Figure 4-6, the rigid body responses are not significantly affected by the tether flexibility. Since objective of the attitude controller is to regulate the rigid body modes, the nonlinear rigid body model is considered for the controller design.

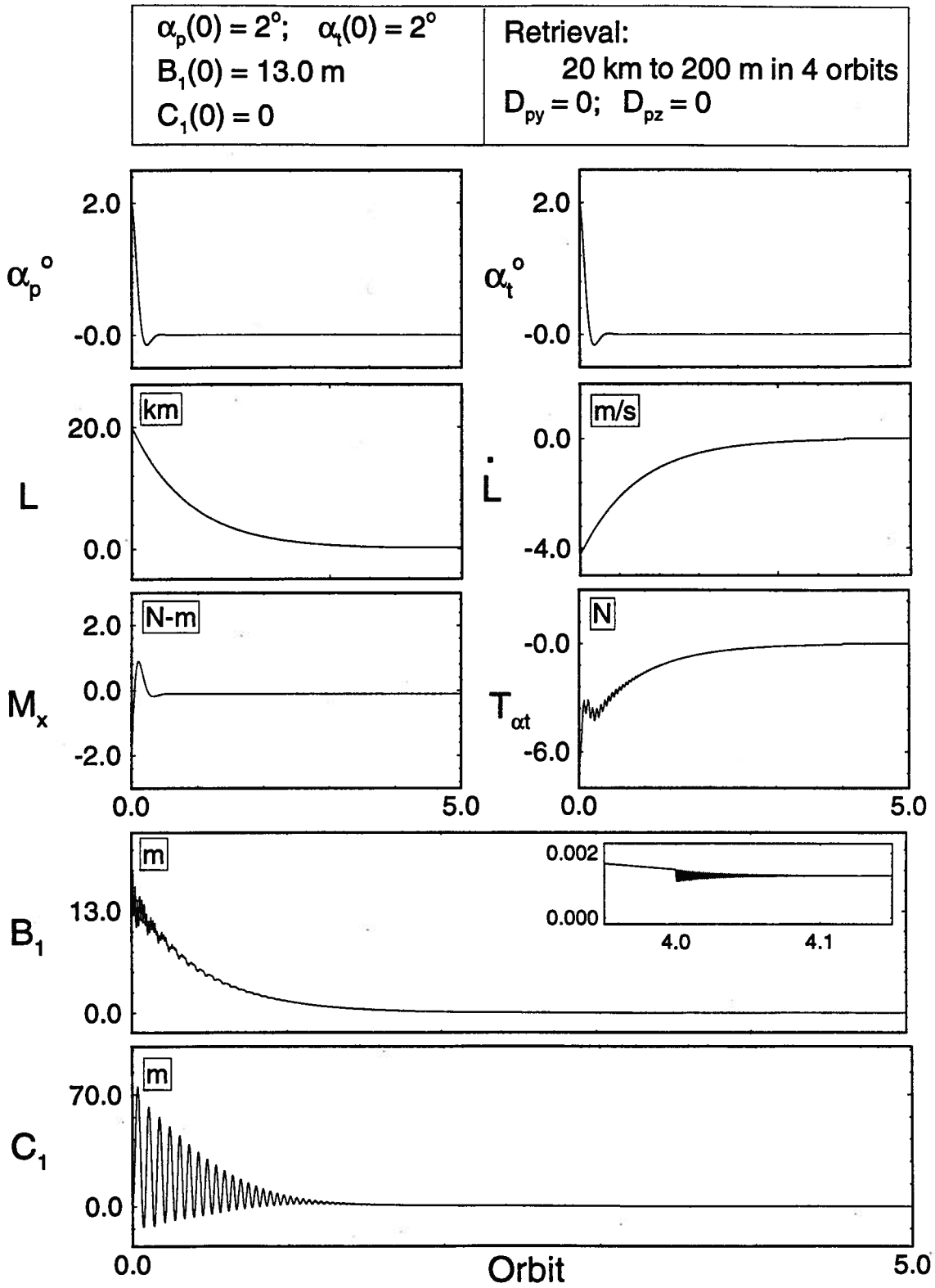

Figure 5-4 System response during the controlled retrieval with passive dampers. Note, the flexible modes are controlled quite effectively keeping the tether tension positive.

The governing equations of motion can now be expressed as

$$\begin{bmatrix} M_{11} & M_{12} \\ M_{21} & M_{22} \end{bmatrix} \begin{Bmatrix} \ddot{\alpha}_p \\ \ddot{\alpha}_t \end{Bmatrix} + \begin{Bmatrix} F_1 \\ F_2 \end{Bmatrix} = \begin{Bmatrix} M_x \\ LT_{\alpha_t} \end{Bmatrix}, \tag{5.11}$$

where the coefficients are defined in Appendix III. This system is in the canonical form and hence Eqs.(5.4 and 5.6) can be used directly to design the controller. The other simplified model considered for the design corresponds to the rigid linear system, which can be expressed as

$$\begin{bmatrix} ML_{11} & ML_{12} \\ ML_{21} & ML_{22} \end{bmatrix} \begin{Bmatrix} \ddot{\alpha}_p \\ \ddot{\alpha}_t \end{Bmatrix} + \begin{bmatrix} GL_{11} & GL_{12} \\ GL_{21} & GL_{22} \end{bmatrix} \begin{Bmatrix} \dot{\alpha}_p \\ \dot{\alpha}_t \end{Bmatrix} + \begin{bmatrix} KL_{11} & KL_{12} \\ KL_{21} & KL_{22} \end{bmatrix} \begin{Bmatrix} \alpha_p \\ \alpha_t \end{Bmatrix} + \begin{Bmatrix} PL_1 \\ PL_2 \end{Bmatrix} = \begin{Bmatrix} M_x \\ LT_{\alpha_t} \end{Bmatrix}, \tag{5.12}$$

with the coefficients defined in Appendix III. This controller is also designed using Eqs.(5.4 and 5.6). The controllers, designed by dynamic inversion using simplified models, are implemented on the complete nonlinear flexible system. Figure 5-5 shows the system response during stationkeeping with the controller based on the nonlinear rigid model. As expected, α_p and α_t settle to the desired value in about 0.5 *orbit*. Note, in the present case, the control inputs do not cancel the effect of flexibility on the rigid modes. Therefore the high frequency components of M_x and T_{α_t} have much lower amplitudes than those in Figure 5-1. As can be seen from the inset of α_t-plot, due to the coupling between C_1 and α_t, the tether pitch has a high frequency component with very small amplitude. These oscillations slowly decay due to active control and, in turn, decease the amplitude of C_1 through coupling effects.

As shown in Figure 5-5, the controller based on the rigid nonlinear model results in a steady state error in the platform pitch (α_p). An outer Proportional-Integral (PI) controller loop is used to take care of this error. With this, the primary

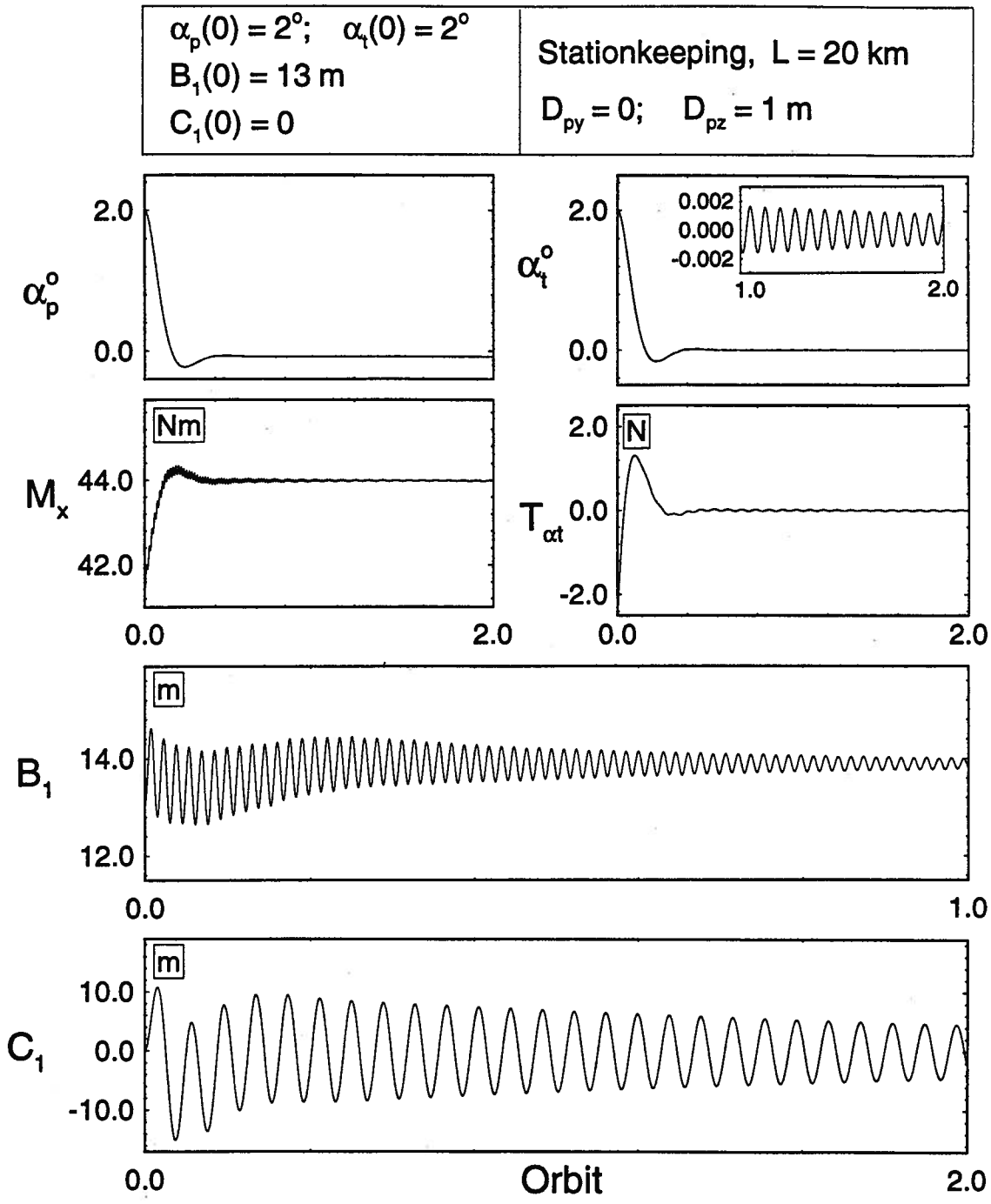

Figure 5-5 System response during stationkeeping using the rigid nonlinear model for the controller design.

controller of Eq.(5.4) becomes

$$Q_s = M_s v + F_s + \left\{ \begin{array}{c} K_{p_T}(\alpha_p - \alpha p_d) + K_{I_T} \int_0^t (\alpha_p - \alpha_{p_d}) \mathrm{d}t \\ 0 \end{array} \right\}, \qquad (5.13)$$

where K_{p_T} and K_{I_T} are the proportional and integral gains, 2.0 and 0.05, respectively. The response of the system with the PI-controller is presented in Figure 5-6. Note, the steady state error in the platform pitch response is reduced to zero. The other responses remain essentially unchanged.

The response of the controlled system during deployment, with dynamic inversion, using rigid nonlinear model is shown in Figure 5-7. The deployment velocity profile is the same as in Figure 5-2. Comparing Figures 5-2 and 5-7, it can be concluded that the system dynamics is virtually identical except for two effects: amplitude of the steady state oscillations of the control thrust (T_{α_t}) is very small; and the C_1 response decays slowly with the controller based on the rigid nonlinear model. In Figure 5-7, the controller does not cancel the effect of flexibility on the rigid model. It leads to a smaller fluctuation of T_{α_t} as compared to that in Figure 5-2. The tether transverse oscillation (C_1) decays slowly due to its coupling with the α_t response which has a small diminishing amplitude. Similarly, response of the system with the controller based on the rigid linear model (Eq. 5.12) was found to be almost identical to that in Figure 5-7. Thus the controllers based on the rigid nonlinear and rigid linear models lead to essentially the same performance during deployment.

The simplified linear and nonlinear models of the rigid system were also used to design the controller for regulating the attitude motion during retrieval. Response of the system with the controller based on the rigid nonlinear model and in presence of passive dampers is shown in Figure 5-8. The dampers used here are the same

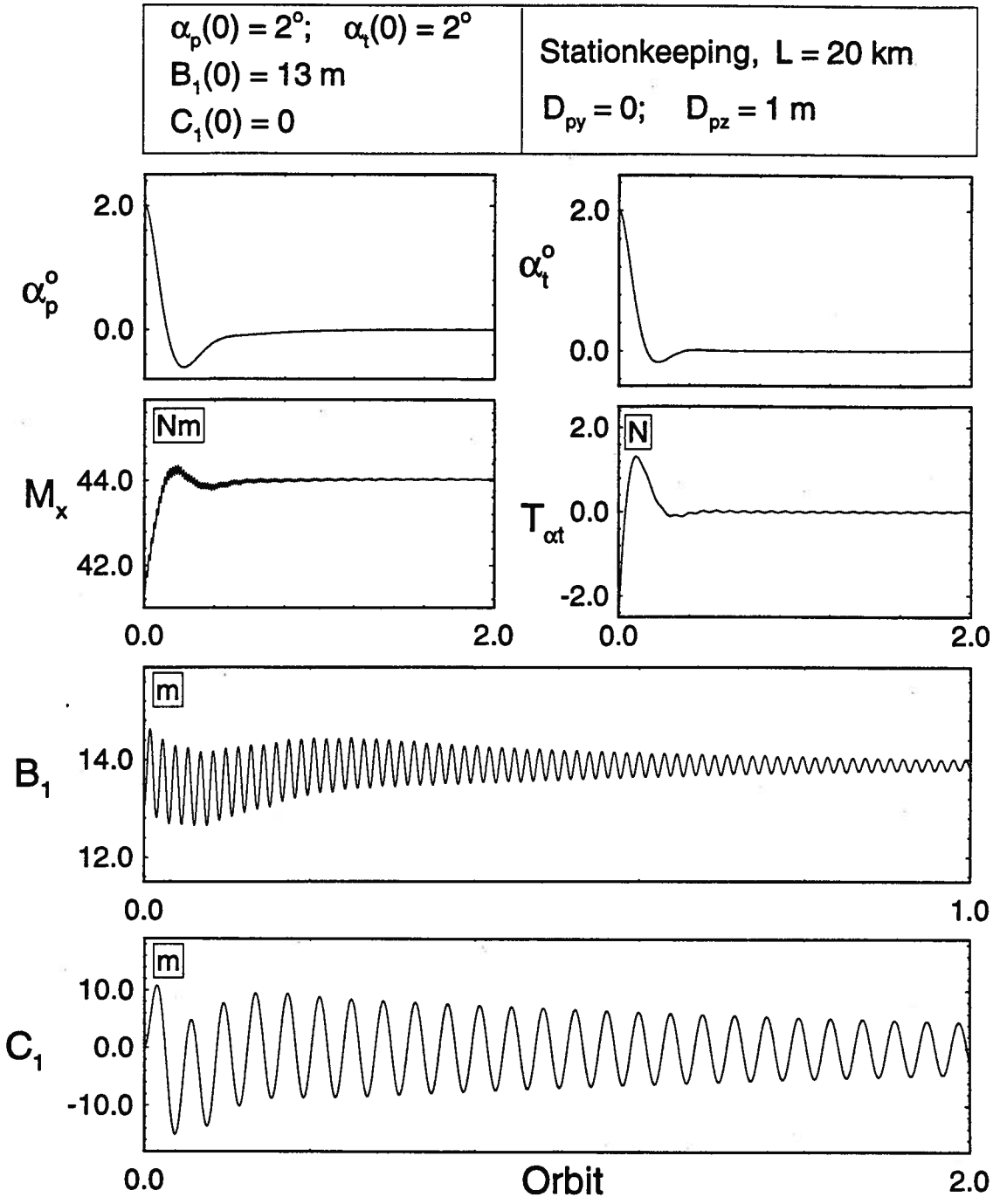

Figure 5-6 System behaviour during stationkeeping with the outer PI control loop and the FLT employing the rigid nonlinear model.

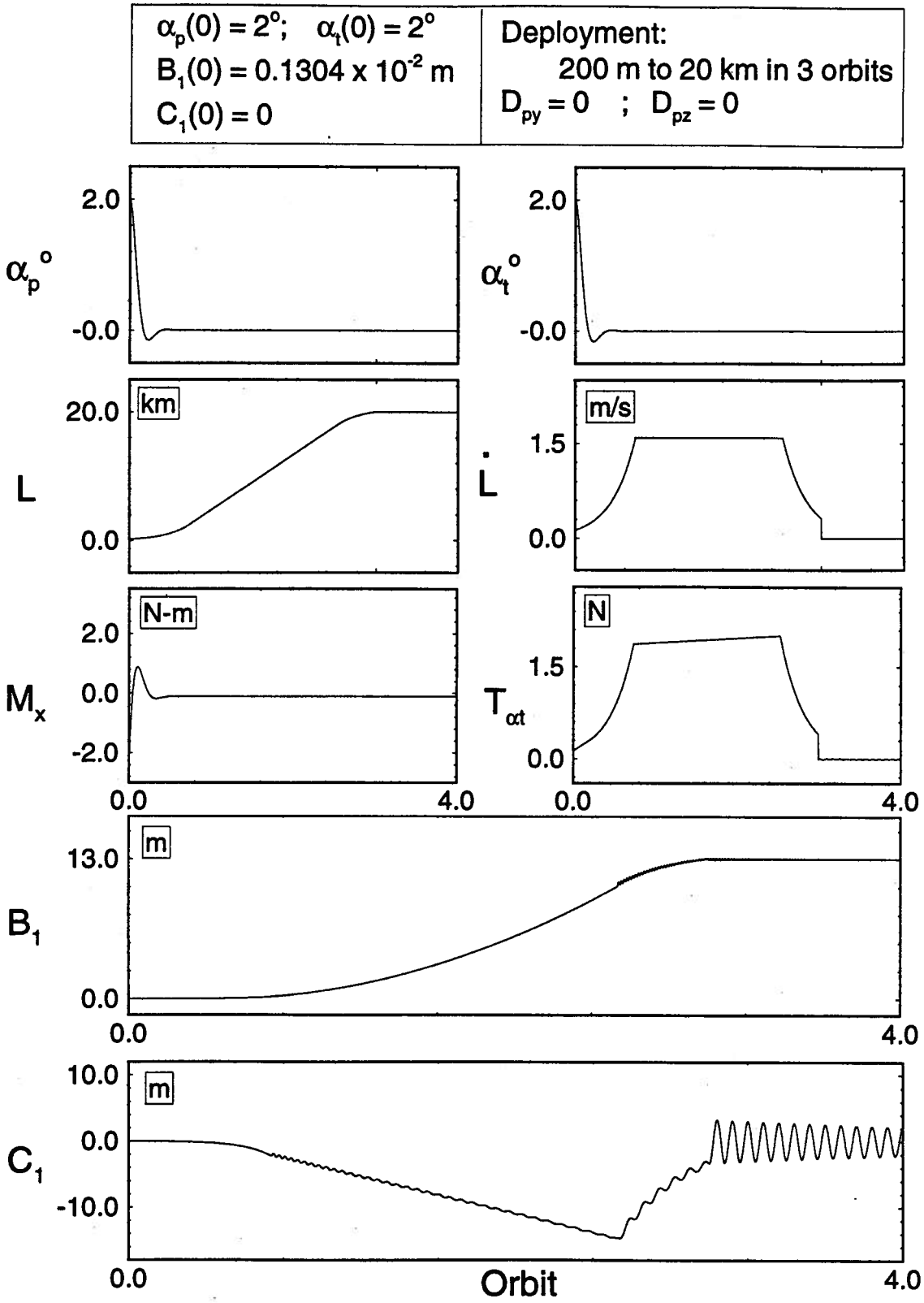

Figure 5-7 Deployment dynamics with the controller based on the rigid non-linear model.

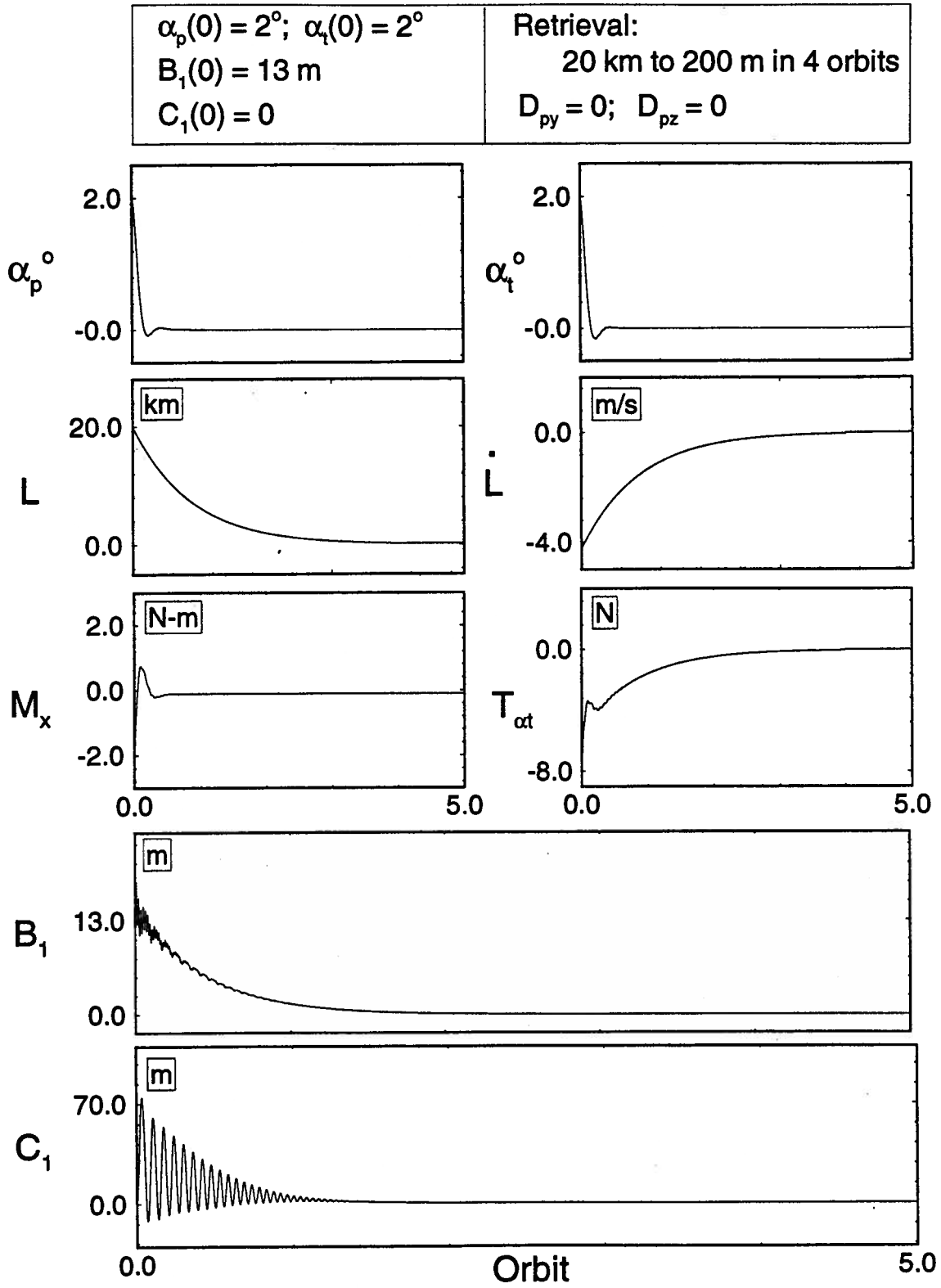

Figure 5-8 Controlled response during exponential retrieval of the subsatellite. The controller is designed using the rigid nonlinear model and applied in presence of passive dampers.

as those for the simulation in Figure 5-4. A comparison of results in Figures 5-4 and 5-8 shows similar behaviour except for reduced T_{α_t} fluctuations in the present case. Similar trends were observed with the controller based on the rigid linear model. Identical observations can be made for the controller design aimed at the stationkeeping case.

5.2.4 Comments on the controller design models

As seen in the previous section, the controllers based on the complete flexible nonlinear, rigid nonlinear, and rigid linear models result in very similar system performance. Hence, the computational time may serve as an important criterion in selection of the model. To that end, the controlled dynamics was assessed over five *orbits* with a time–step of 1 s. This corresponds to the situation where the controller can be implemented as a sampled data system with a step–size of 1 s. The computational time with the controller design based on different models are compared in Table 5-1 for stationkeeping, deployment and retrieval phases.

Table 5.1 Comparison of the time (s) required by the controllers using different design models.

	Nonlinear Flexible Model	Nonlinear Rigid Model	Linear Rigid Model
Stationkeeping	402.6	67.6	70.4
Deployment	5195.1	68.1	71.6
Retrieval	5332.2	68.4	71.7

Each computation loop involves calculation of the control inputs, and recording of the system output as well as input values in a file. Calculations for the stationkeeping case correspond to $L = 20\ km$. Deployment is carried out from a tether

length of 200 m to 20 km in 3 *orbits* using an exponential-constant-exponential velocity profile with the switch over at tether lengths of 2.5 km and 18 km. During retrieval, the tether length decreases from 20 km to 200 m in 4 *orbits* with an exponential velocity profile. The study was carried out on a SUN Sparc-2 workstation.

As expected, in all the three modes of tether operation, the controller based on the nonlinear flexible model demands the maximum computational effort. The controller based on the rigid nonlinear model takes the minimum time. In the linear rigid model, the equations are linearized about an arbitrary reference trajectory. So the governing equations involve more algebraic and trigonometric operations than the rigid nonlinear case. This results in a longer computational effort for the controller based on the rigid linear model as compared to the rigid nonlinear case. As seen in the previous section, the system performance with the different controller is essentially similar. So the controller based on the rigid nonlinear system is preferred. Of course, it should be recognized that irrespective of the system model chosen for the controller design, its effectiveness is assessed through application to the nonlinear, nonautonomous and coupled flexible system.

5.3 Offset Control using the Feedback Linearization Technique

As mentioned before, because of practical limitations, it is advantageous to use the offset strategy for attitude control when the tether length is small. This section presents the design procedure and simulation results for the offset control of a class of tethered systems. The Feedback Linearization Technique (FLT) is used to design the controller for this highly time varying tether dynamics.

5.3.1 Mathematical background

For two vector fields f and g on $\mathbf{R^n}$, the Lie bracket $[f,g]$ is a vector field defined by [83]

$$[f,g] = \frac{\partial g}{\partial x} f - \frac{\partial f}{\partial x} g,$$

where $\partial f/\partial x$ and $\partial g/\partial x$ are the Jacobians. It is also denoted by $ad_f^1(g)$, and by induction

$$ad_f^k(g) = [f,\ ad_f^{k-1}(g)],$$

with $ad_f^o(g) = g$. A set of vector fields $\Delta(x) = \{x_1, \cdots, x_m\}$ is said to be *involutive* if there are scalar fields α_{ijk} such that

$$[x_i,\ x_j] = \sum_{k=1}^{m} \alpha_{ijk} x_k,$$

or in other words $[x_i,\ x_j] \in \Delta(x)$. It is called *completely integrable* if for every point, assuming $x_1, \cdots, x_m$ are linearly independent, there exists an m-dimensional manifold M in $\mathbf{R^n}$ such that at each point of M the tangent space of M is spanned by $x_1, \cdots, x_m$.

Let $h : \mathbf{R^n} \to \mathbf{R}$ be a scalar field. The gradient of h, denoted by $\mathrm{d}h$, is a row vector field

$$\left(\frac{\partial h}{\partial x_1}, \cdots, \frac{\partial h}{\partial x_n}\right)$$

on $\mathbf{R^n}$. A set of scalar fields are linearly independent if their gradients are a linearly independent set of row vector fields. For a scalar field h and a vector field $f = (f_1, \cdots, f_n)^T$, the dual product of $\mathrm{d}h$ and f, denoted by $\langle \mathrm{d}h, f \rangle$,is a scalar field defined by

$$\langle \mathrm{d}h, f \rangle = \frac{\partial h}{\partial x_1} f_1 + \cdots + \frac{\partial h}{\partial x_n} f_n.$$

The feedback equivalence for control systems is based on three operations

[86]: coordinate transformation in the state space; coordinate transformation in the control space; and feedback. For linear systems, with the operations defined in a linear fashion, it is well known that every single input system which is time invariant and controllable is feedback equivalent to the canonical form

$$\frac{\mathrm{d}}{\mathrm{dt}}\begin{Bmatrix} z_1 \\ \vdots \\ z_{n-1} \\ z_n \end{Bmatrix} = \begin{Bmatrix} z_2 \\ \vdots \\ z_n \\ 0 \end{Bmatrix} + \begin{Bmatrix} 0 \\ \vdots \\ 0 \\ 1 \end{Bmatrix} v. \tag{5.14}$$

Any nonlinear system which is feedback equivalent to the above form is called *linear equivalent.*

Theorem 1 (Su, 1982 [86]): A system $\dot{x} = \tilde{f}(x,u)$ is a linear equivalent *if and only if*

(i) $\tilde{f}(x,u) = f(x) + g(x)\phi(x,u)$ where $f(0) = 0$, $\phi(0,0) = 0$ and $\partial\phi/\partial u \neq 0$;

(ii) the vectors $g,\ ad_f^1(g), \cdots, ad_f^{n-1}(g)$ span $\mathbf{R^n}$ about the origin;

(iii) the set of vector fields $\{g,\ ad_f^1(g), \cdots, ad_f^{n-2}(g)\}$ is involutive. □

For systems satisfying the above theorem, the state transformation $z = T(x) = \{T_1, \cdots, T_n\}^T$ required for linearization can be obtained from the following conditions:

$$\langle \mathrm{d}T_1, ad_f^i(g)\rangle = 0, \quad i = 0, 1, \cdots, n-2; \tag{5.15}$$

$$\langle \mathrm{d}T_1, ad_f^{n-1}(g)\rangle \neq 0; \tag{5.16}$$

$$\frac{\mathrm{d}}{\mathrm{d}t}\begin{Bmatrix} T_1 \\ \vdots \\ T_{n-1} \\ T_n \end{Bmatrix} = \begin{Bmatrix} T_2 \\ \vdots \\ T_n \\ 0 \end{Bmatrix} + \begin{Bmatrix} 0 \\ \vdots \\ 0 \\ \sum_{j=1}^n \frac{\partial T_n}{\partial x_j}\Big(f_j(x) + g_j(x)\phi(x,u)\Big) \end{Bmatrix}. \tag{5.17}$$

Eqs. (5.15) and (5.16) can be used to get the function T_1. The complete transfor-

mation, $z = T(x)$, can be obtained from Eq.(5.17). If $\phi(x,u)$ is selected as

$$\phi(x,u) = \frac{v - P(x)}{Q(x)}, \tag{5.18}$$

where:

$$P(x) = \sum_{j=1}^{n} \frac{\partial T_n}{\partial x_j} f_j(x);$$

$$\text{and} \quad Q(x) = \sum_{j=1}^{n} \frac{\partial T_n}{\partial x_j} g_j(x);$$

Eq.(5.17) acquires the same canonical form as that of Eq.(5.14).

The expression for $\phi(x,u)$, Eq.(5.18), which transforms the system into the canonical form, is referred to as the *primary controller*. Now the task is to design a feedback controller (called the *secondary controller*) to generate the control input, v, so that the transformed states $z_1, \cdots, z_n$ and hence the original states $x_1, \cdots, x_n$ follow the desired trajectory. This can be achieved by using the linear time invariant control procedure.

5.3.2 Design of the controller

The purpose of the attitude controller is to regulate the rigid body rotations of the platform and tether. The dominant characteristic, which governs the system dynamics, is the time varying length of the tether during deployment and retrieval. As discussed in the previous section, the controller based on the rigid model of the system gives almost the same performance as that obtained using the flexible nonlinear model. Furthermore, as shown in Chapter 4, the tether response is not significantly coupled with the platform dynamics; however, for a nonzero offset, the platform attitude is strongly affected by the tether motion. Therefore the controller for the tether dynamics is designed based on the rigid model decoupled from the platform motion. On the other hand, the model for the platform controller includes

the effect of tether libration.

As shown in the thruster control case (Section 5.2), performance of the system with the controllers based on linear and nonlinear rigid models is almost identical. Therefore, it is sufficient to consider only the linear model for design of the tether controller. The rigid body equation for the tether dynamics, decoupled from the platform motion, is linearized about the quasi-equilibrium trajectory ($\bar{\alpha}_t$) and the specified offset motion. The total offset position, $\{d_p\}$, is the sum of the specified value, $\{D_p\}$, and the controller coordinate $\{D\}$. The resulting dynamic equations for the controller design are:

$$m_{\alpha p}(\alpha_p, x, t)\ddot{\alpha}_p + f_{\alpha p}(\alpha_p, \dot{\alpha}_p, x, \dot{x}, t) = Q_{\alpha p}; \tag{5.19}$$

$$\ddot{\alpha}_t = a_1\alpha_t + a_2 D_z + a_3\dot{\alpha}_t + a_4\dot{D}_z + b + c\ddot{D}_z, \tag{5.20}$$

where

$$x = \{\alpha_t,\ D_z,\ \dot{\alpha}_t,\ \dot{D}_z\}^T.$$

Here D_z is the z-component of $\{D\}$ which is the offset along the local horizontal required by the controller. The coefficients of Eqs.(5.19) and (5.20) are defined in Appendix III.

The equilibrium value for the platform pitch angle ($\bar{\alpha}_p$) is specified by the mission requirement, and the quasi-equilibrium angle for the tether pitch rotation ($\bar{\alpha}_t$) is given by

$$\begin{aligned}\Big\{m_1\ddot{\theta}D_{pz} + m_1(\dot{\theta}^2 - 2\mu)D_{py} + 6\mu m_1(D_{py} - D_{pz}\bar{\alpha}_p) + 6\mu m_{\alpha_t}\Big\}\bar{\alpha}_t \\ = m_1\ddot{\theta}(-D_{py} + D_{pz}\bar{\alpha}_p) - m_{\alpha_t}\ddot{\theta} - \dot{m}_{\alpha_t}\dot{\theta} \\ + m_1(\dot{\theta}^2 - 2\mu)(D_{py}\bar{\alpha}_p + D_{pz}).\end{aligned} \tag{5.21}$$

Here D_{py} and D_{pz} represent the 'y' and 'z' components, respectively, of the vector $\{D_p\}$ and other coefficients are defined in Appendix III. In Eq.(5.20), the acceleration of the tether attachment point along the local horizontal ($\ddot{D}_z$) is used to control the tether swing. Since it is necessary to regulate the position and velocity of the tether attachment point, the dynamic model for the tether pitch is augmented by the identity

$$\ddot{D}_z = u_t. \tag{5.22}$$

The alternate method to control the offset motion is to include the physical behaviour of the offset mechanism into the system dynamics. It should be pointed out that the time constant of the offset mechanism is usually much smaller than that of the tether libration. Hence the use of Eq.(5.22) to regulate the offset motion does not affect the implementation of the control strategy.

The governing equation for the platform dynamics (Eq. 5.19) is already in the canonical form. Therefore, only the control variable transformation is required to linearize the system. The structure of the primary controller which accomplishes the linearization is

$$Q_{\alpha_p} = m_{\alpha_p}(\alpha_p, x, t)v_p + f_{\alpha_p}(\alpha_p, \dot{\alpha}_p, x, \dot{x}, t). \tag{5.23}$$

The secondary control input, v_p, which asymptotically drives the error ($e = \alpha_p - \alpha_{p_d}$) dynamics to zero, can be expressed as

$$v_p = k_{p_1}(\alpha_{p_d} - \alpha_p) + k_{p_2}(\dot{\alpha}_{p_d} - \dot{\alpha}_p) + \ddot{\alpha}_{p_d}, \tag{5.24}$$

where: k_{p_1} and k_{p_2} are coefficients of the desired closed loop polynomial for the error dynamics; and α_{p_d}, $\dot{\alpha}_{p_d}$, $\ddot{\alpha}_{p_d}$ represent the desired trajectory. Now the error

equation becomes

$$\ddot{e} + k_{p_2}\dot{e} + k_{p_1}e = 0.$$

The model used for the tether controller design, Eqs.(5.20) and (5.22), can be represented by

$$\dot{x} = f(x,t) + g(x,t)u_t, \tag{5.25}$$

where:

$$f(x,t) = \begin{Bmatrix} x_3 \\ x_4 \\ a_1x_1 + a_2x_2 + a_3x_3 + a_4x_4 + b \\ 0 \end{Bmatrix};$$

$$\text{and} \quad g(x,t) = \begin{Bmatrix} 0 \\ 0 \\ c \\ 1 \end{Bmatrix}.$$

In general, the coefficients in Eq.(5.25) are time varying. The transformation of this system to time invariant canonical form can be obtained using the algorithm of Hunt and Su [91]. However, in the present case, the coefficients of the tether dynamics are slowly time varying parameters and hence a quasi-static approach is sufficient to achieve the objective. This results in a quasi-static controller structure which transforms the system into the canonical form. The functions $f(x)$ and $g(x)$ satisfy the conditions in Theorem 1, and hence the system is feedback equivalent. The state transformation, which maps the system into the canonical form, is

$$z = T(x) = [t_{ij}]x, \tag{5.26}$$

where:

$$t_{11} = a_2 + a_1c + a_3(a_4 + a_3c);$$

$$t_{12} = -c(a_2 + a_1c) + a_4(a_4 + a_3c);$$

$$t_{13} = -a_4 - a_3c;$$

$$t_{14} = c(a_4 + a_3 c);$$

and for $i = 2, 3, 4$

$$t_{i1} = a_1 t_{(i-1)3};$$

$$t_{i2} = a_2 t_{(i-1)3};$$

$$t_{i3} = t_{(i-1)1} + a_3 t_{(i-1)3};$$

$$t_{i4} = t_{(i-1)2} + a_4 t_{(i-1)3}.$$

The structure of the transformed system is similar to Eq.(5.14), where the primary controller has the form

$$u_t = \frac{v_t - P(x)}{Q(x)}, \tag{5.27}$$

with:

$$P(x) = a_1 t_{43} x_1 + a_2 t_{43} x_2 + (t_{41} + a_3 t_{43}) x_3 + (t_{42} + a_4 t_{43}) x_4;$$

$$Q(x) = c t_{43} + t_{44}.$$

The secondary controller for the system is designed to place the closed loop eigenvalues at some desired locations. This leads to the following expression for the transformed control input v_t,

$$v_t = k_{t_1}(z_1 - z_{1_d}) + k_{t_2}(z_2 - z_{2_d}) + k_{t_3}(z_3 - z_{3_d}) + k_{t_4}(z_4 - z_{4_d}), \tag{5.28}$$

where k_{t_i} and z_{i_d}, $i = 1, \cdots, 4$, are the coefficients of the desired closed loop polynomial and the desired values for z_i, respectively. z_{i_d} can be computed from Eq.(5.26) with the knowledge of the desired x. The structure of the tether pitch controller is shown in Figure 5-9.

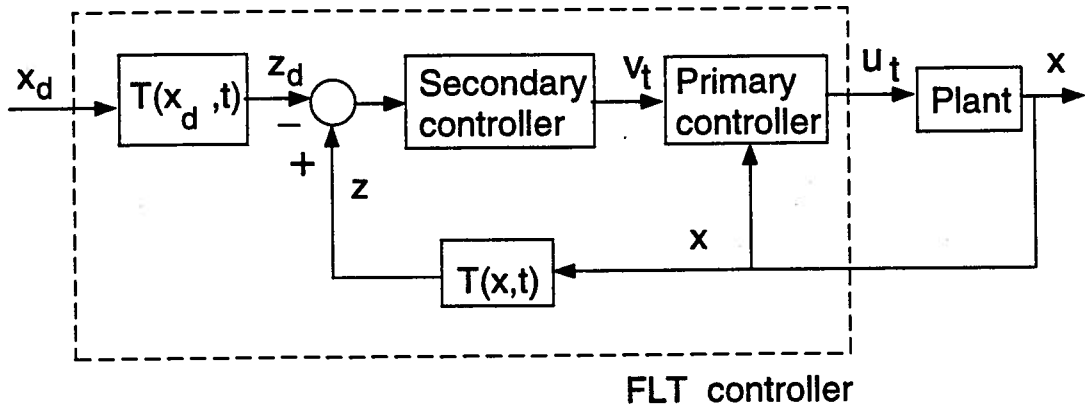

Figure 5-9 Schematic diagram of the closed-loop tether dynamics with the FLT based controller.

5.3.3 Results and discussion

The controller designed for the platform and tether pitch angles are implemented on the complete flexible and nonlinear model. As mentioned before, the offset control strategy has advantages at shorter tether lengths. In this section, controlled response results are presented for operations with a maximum tether length of 200 m. The inertia and elastic parameters are the same as those used in the dynamic simulation of Chapter 4. One possible drawback of the inverse control procedure may be its lack of robustness against the model uncertainty [89]. To assess this aspect, intentional modelling error was introduced by neglecting the shift in the center of mass terms from the controller model, but retaining the corresponding terms in the simulation model.

The desired system performance is characterized by the settling and rise times. The settling times for platform, tether and offset motion are 0.4 τ, 0.8τ and 0.82τ, respectively. The rise times are 0.1τ and 0.15τ for the platform and offset

motions, respectively. The rise times for the tether libration are 0.2τ, 0.16τ and 0.18τ during deployment, stationkeeping and retrieval, respectively. Here τ is the orbital period. The maximum allowable offset is taken as $\pm 15m$.

Figure 5-10 shows the controlled performance of the system for stationkeeping at $L = 200\ m$ with the modelling error in the controller design. Though the rigid modes are stabilized to some steady state values, the performance of the system is not satisfactory. The desired steady state values for α_p and d_{pz} are 0 and 1 m, respectively, which are not achieved by the controller. Moreover, the α_t and d_{pz} response is quite oscillatory. The moment required to control α_p, i.e. M_x, is also oscillatory because of the coupling between the platform and the tether dynamics caused by a nonzero offset.

When the shift in the center of mass terms are included in the controller model, the oscillatory nature of α_t and d_{pz} responses is reduced substantially and the steady state value of α_p become zero (Figure 5-11). The steady state value of d_{pz} is still less than the required magnitude of 1 m. An outer Proportional-Integral (PI) loop was introduced to reduce this steady state error. With this, the structure of the tether primary controller becomes

$$u_t = \frac{v_t - P(x)}{Q(x)} + K_{p_o}(d_{pz} - D_{pz}) + K_{I_o}\int_0^t (d_{pz} - D_{pz})\mathrm{d}t, \qquad (5.29)$$

where K_{p_o} and K_{I_o} are the proportional and integral gains, respectively. The secondary control input v_t is obtained as before using Eq.(5.28). In the present simulation, the gains are: $K_{p_o} = 1.0 \times 10^{-6}$ and $K_{I_o} = -1.5 \times 10^{-9}$. The schematic diagram of the controllers with the integral loop is shown in Figure 5-12 and response of the system is presented in Figure 5-13. Now, the steady state offset is 1.0 m. Note, the offset requirement is a little higher than the previous case, however

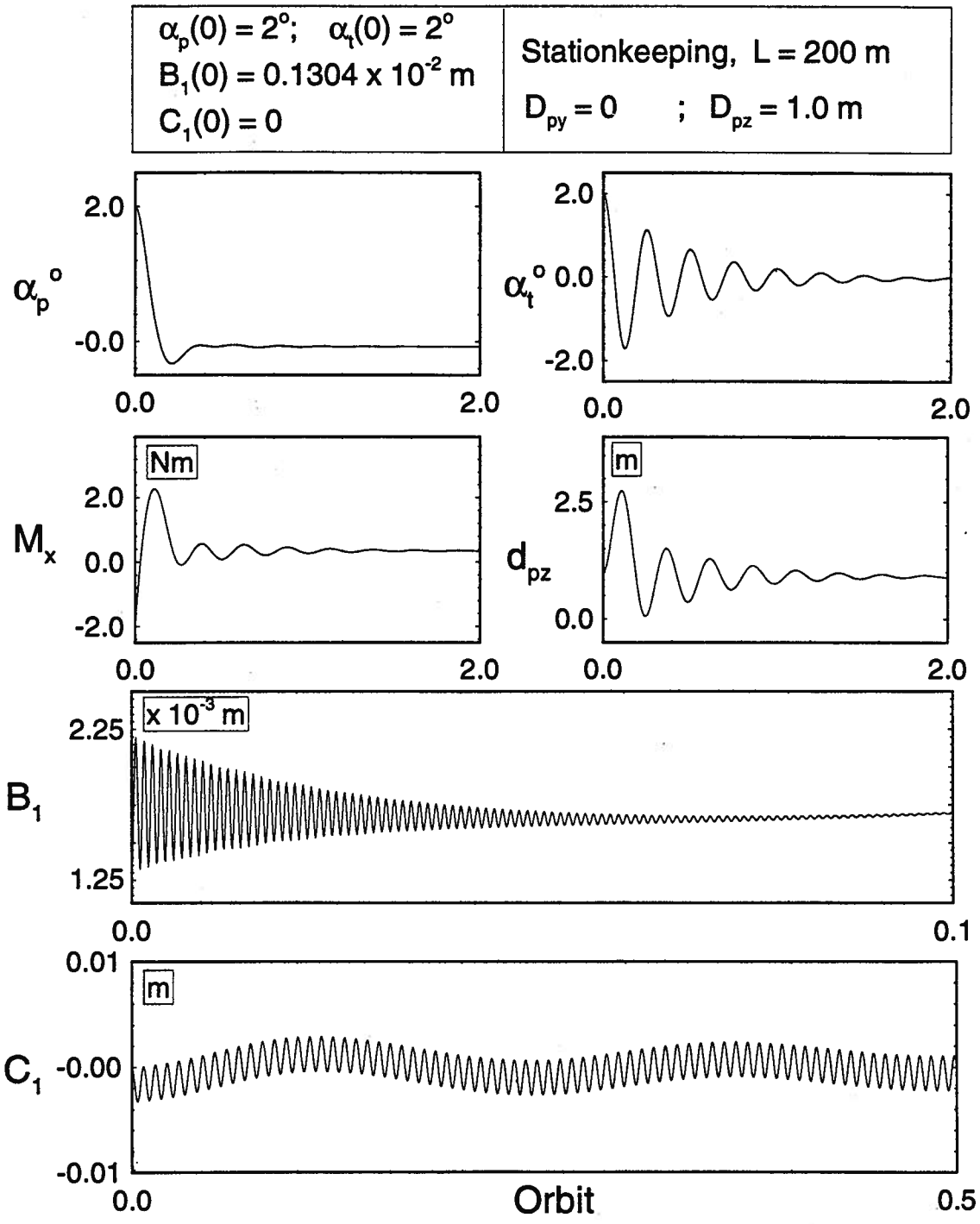

Figure 5-10 Controlled response in presence of the modelling error introduced by neglecting the shift in the center of mass terms during the controller design.

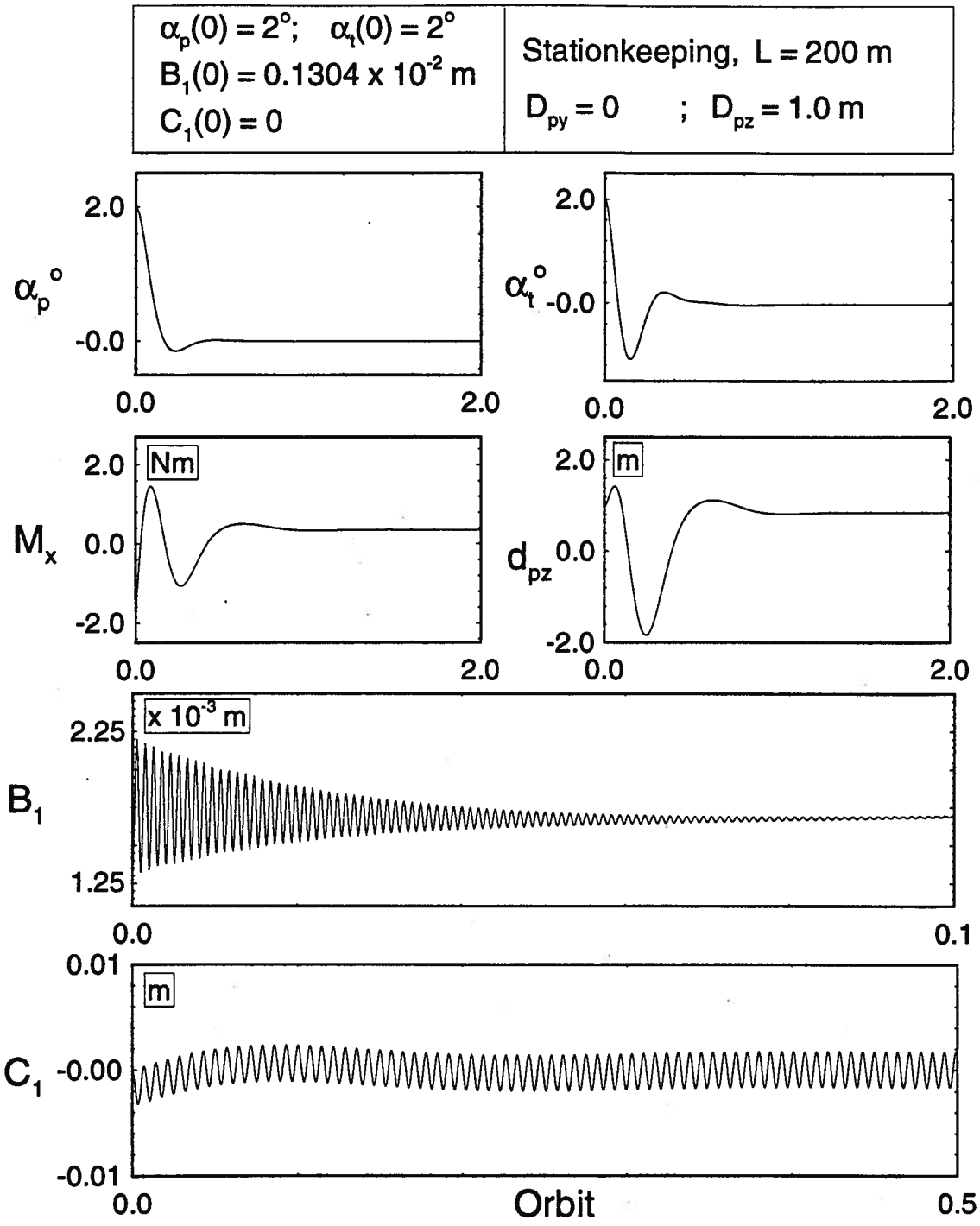

Figure 5-11 System response with the shift in the center of mass included in the controller design model.

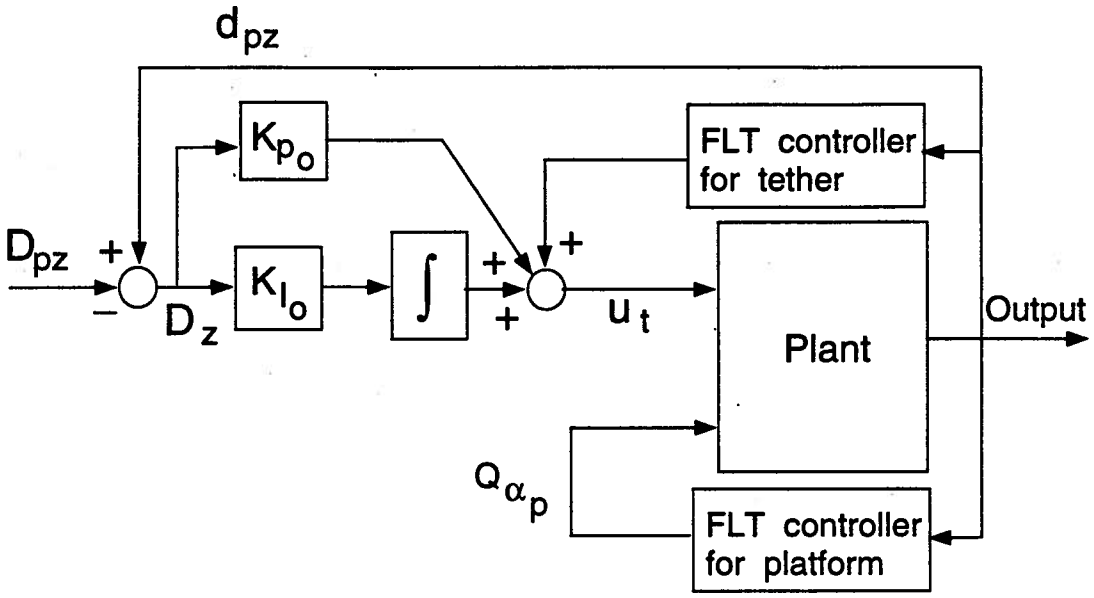

Figure 5-12 Schematic diagram of the closed-loop system with the outer PI control loop for the tether dynamics.

the response is substantially improved. The longitudinal oscillation (B_1) decays due to the structural damping in the tether. Although the transverse vibrational degree of freedom is not subjected to any initial disturbance, the offset motion during the control excites the C_1 response resulting in a small amplitude oscillation.

Response results were also obtained for the controlled deployment of the subsatellite from a tether length (L) of 50 m to 200 m in one *orbit* (Figure 5-14). An exponential-constant-exponential velocity profile was used for the deployment. The first switching of the velocity from exponential to constant profile occurs at $L = 80$ m and the second switching is at $L = 180$ m. The controller used in this case includes the outer PI loop for the tether dynamics with the gains as mentioned before. As shown in Figure 5-14, the platform pitch angle is controlled quite successfully. The

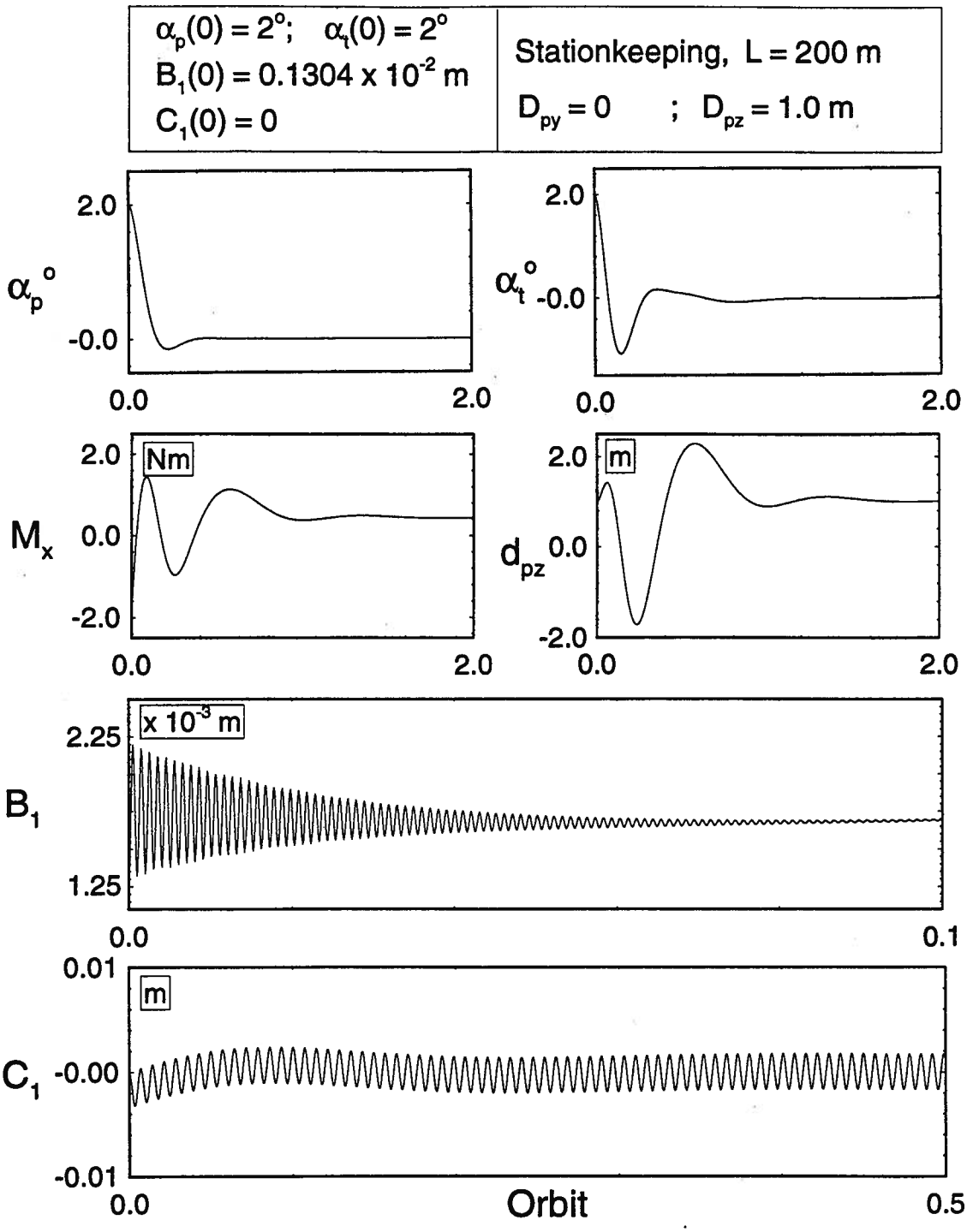

Figure 5-13 System response in presence of the outer PI control loop.

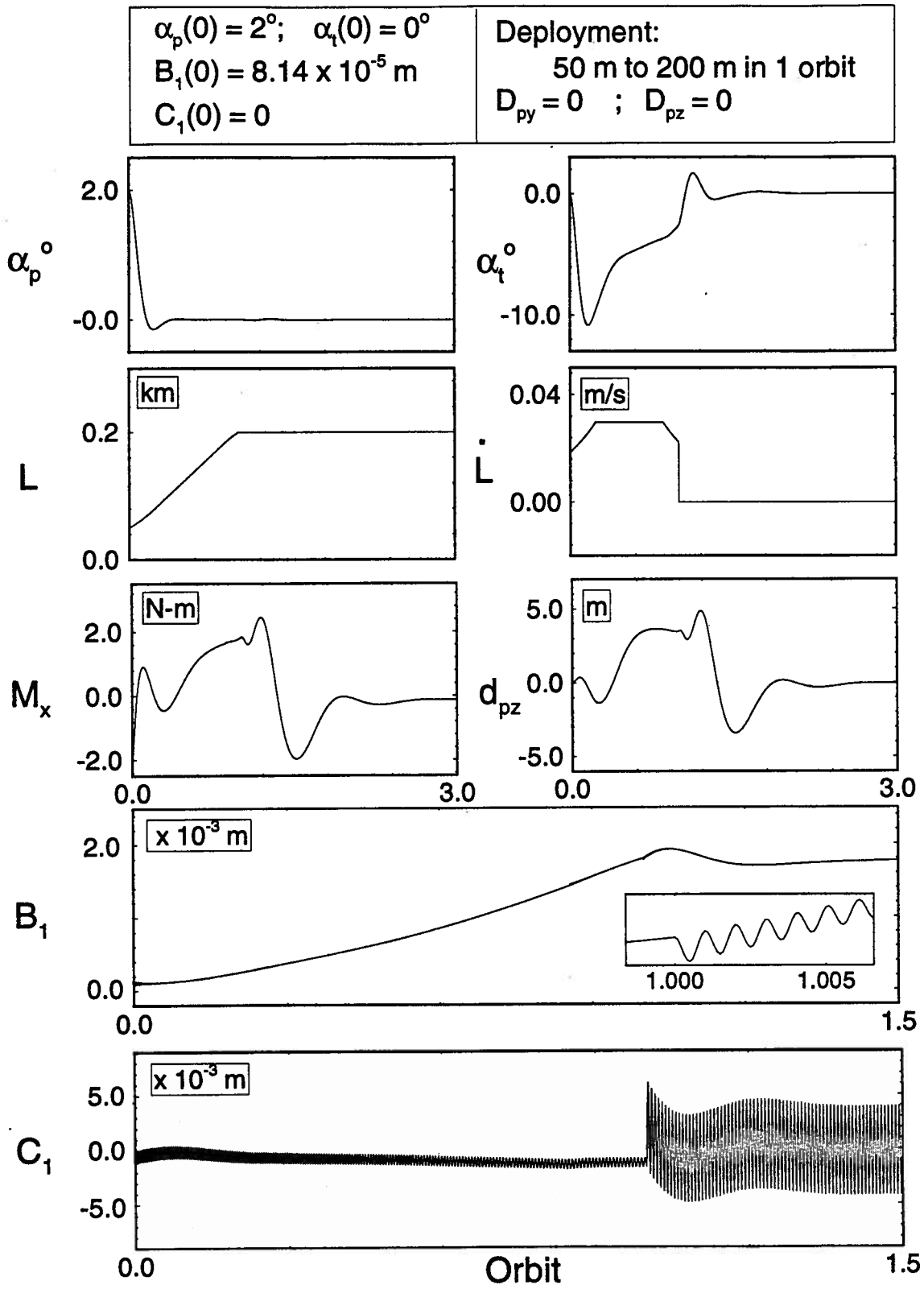

Figure 5-14 Controlled response of the system during deployment. The offset control strategy in conjunction with the Feedback Linearization Technique (FLT) is used.

tether pitch (α_t) is controlled about the quasi-equilibrium trajectory as defined by Eq.(5.21). After deployment, α_t settles to zero. The total offset motion required is within ± 5 m, which is much less than the limiting value of ± 15 m. The control moment M_x cancels the coupling between the tether and platform dynamics, and drives α_p towards its desired value. The coupling between the tether and platform dynamics is due to the offset (d_{pz}). This leads to similarity between the moment (M_x) and d_{pz} time histories. The nonzero steady state value of M_x is needed to stabilize α_p about zero, which is not its equilibrium state.

As expected, the mean value of the longitudinal oscillations increase with the tether length. Note, frequency of the transverse vibrations decrease as the tether length increases. Effect of the Coriolis force during deployment is stabilizing and keeps amplitude of the transverse oscillations quite small, however the mean value of C_1 is not zero. In the post–deployment phase, amplitude of the transverse oscillations increase with zero mean. Simulations were also carried out for several other deployment rates (0.7 and 1.5 *orbit*, plots not shown). As can be expected, the maximum offset requirement was found to be higher (± 7 m) for the faster deployment in 0.7 *orbit* and lower (± 3 m) for the slower deployment rate.

The controlled response of the system during the exponential retrieval from a tether length of 200 m to 50 m in 1 *orbit* is shown in Figure 5-15. The generalized coordinate for the transverse vibration (C_1) grows to around 0.02 m even when it is not excited initially, i.e. $C_1(0) = 0$. The initial disturbance in the first longitudinal mode (B_1) decays quite rapidly due to the structural damping, however a small amplitude oscillation persists due to coupling with the transverse vibration (inset in B_1 plot). In the present case the destabilizing Coriolis force is not enough to make the tether slack (i.e. $B_1 < 0$). The platform pitch (α_p) response settles to zero

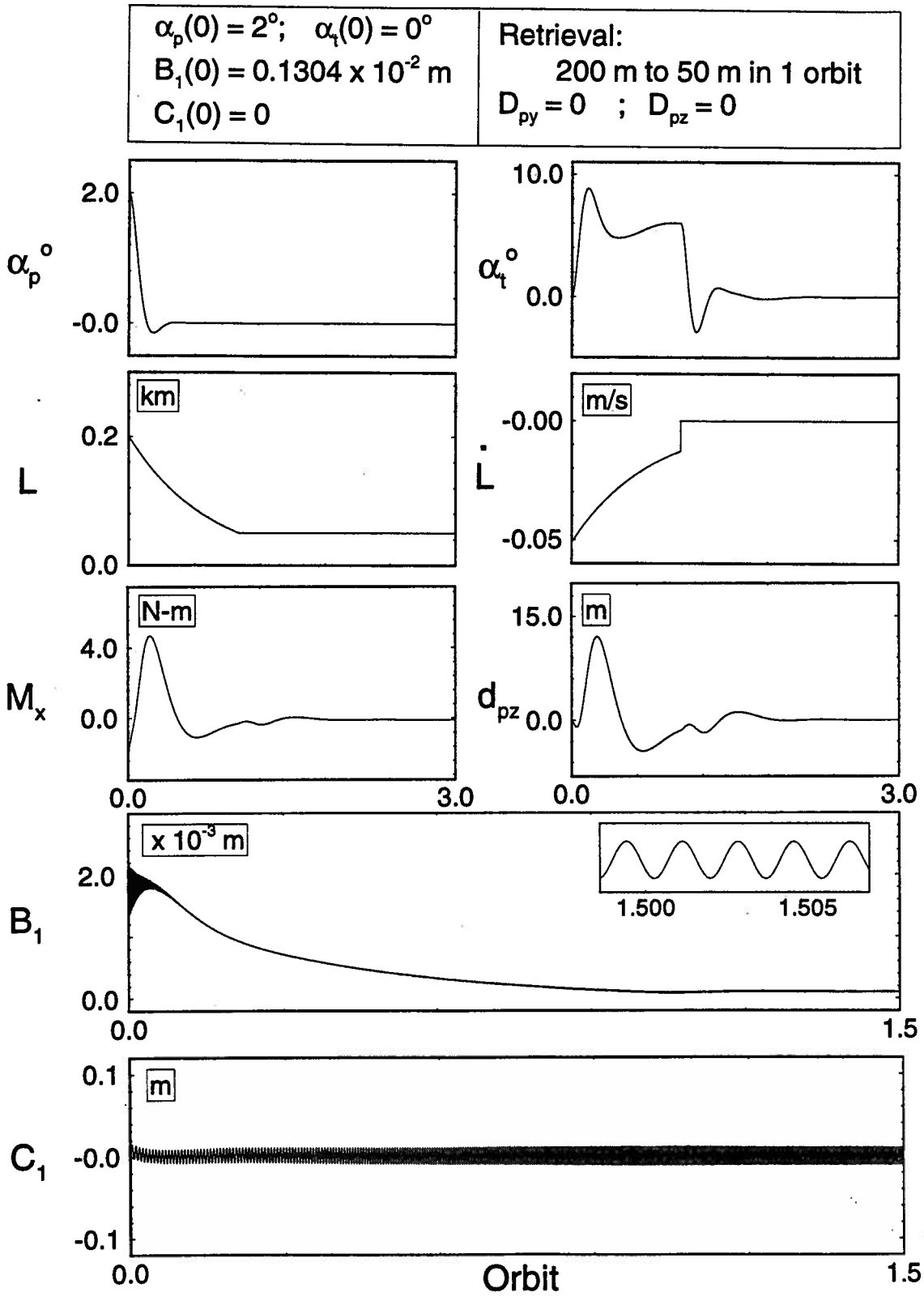

Figure 5-15 System response during controlled retrieval with an exponential velocity profile.

within 0.4 *orbit* while the tether pitch (α_t) is stabilized about the quasi-equilibrium trajectory, which is zero after the retrieval. The moment (M_x) required to control α_p is only 4 Nm. The offset position required to control the tether swing is between $+12$ m and -5 m, which is within the limit of ± 15 m used in the present study. As in the case of deployment, simulation results were also obtained for several retrieval times (results not shown). As anticipated, the maximum offset required to regulate the tether swing was larger for a faster retrieval.

5.4 Attitude Control using Hybrid Strategy

As discussed earlier, thruster and tension control schemes have disadvantages at shorter tether lengths which leaves the offset strategy as an efficient alternative. This section presents simulation results of a tethered system implementing a hybrid control scheme. The controller design procedures are the same as those described earlier. In the study, the offset strategy is used for tether lengths less than 200 m and the thruster control law is applied for longer (> 200 m) tethers. The thruster control strategy is based on the rigid nonlinear model of the system.

Response of the system during controlled deployment from 50 m to 20 km using this hybrid strategy is shown in Figure 5-16. Deployment from 50 m to 200 m is carried out in 1 *orbit* with an exponential velocity profile while the rest of the deployment (200 m to 20 km) is completed in 3 *orbits* with an exponential-constant-exponential velocity profile. In the second deployment stage, the first switch (from exponential to constant velocity profile) takes place at a tether length of 2.5 km and the second switch occurs at 18 km. The tether pitch is controlled about its quasi-equilibrium value during the first orbit. In this period, the maximum offset required along the local horizontal is within ± 3 m from the steady state value of 1

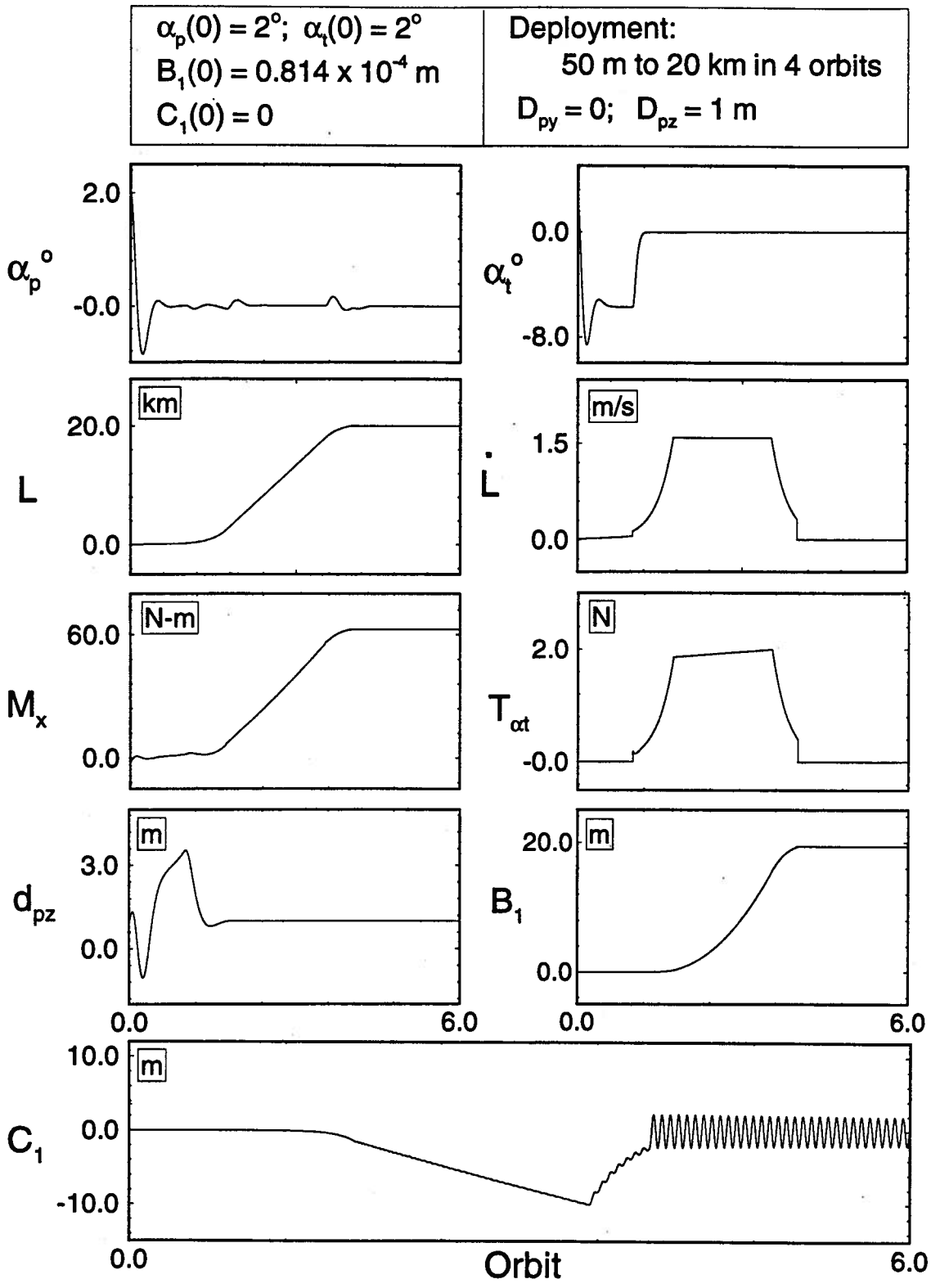

Figure 5-16 Controlled response during deployment using a hybrid strategy.

m. The nonzero steady state value of the offset leads to coupling between the tether and platform dynamics. This coupling exhibits through the small fluctuations in the α_p response. As observed earlier in the thruster control section (Sec. 5.2), the M_x and T_{α_t} profiles have similarity with the L and $\dot{L}$ responses, respectively.

The simulation results for retrieval from a tether length of 20 km to 50 m in 5 *orbits* is shown in Figure 5-17. An exponential velocity profile is used for the retrieval. The initial retrieval from 20 km to 200 m is carried out in 4 *orbits*. To limit the offset motion, the final stage of the retrieval from 200 m to 50 m is completed in 1 *orbit*. The instability of the flexible modes is controlled by passive dampers. As in the case of the thruster control, the damper for the longitudinal oscillation is located at the subsatellite and for the transverse vibration at the center of the tether. The damping coefficients for the longitudinal and transverse dampers are 1.5 and 0.03 Ns/m, respectively. The thruster control is used for retrieval upto 200 m, and the offset scheme for the rest of the retrieval as well as the subsequent stationkeeping. During the offset control, the tether pitch angle is regulated about the quasi-equilibrium trajectory (Eq.5.21). As in the case of deployment, M_x and T_{α_t} profiles are similar to the L and $\dot{L}$ trajectories, respectively. The offset excursions to control the unstable tether attitude during the retrieval range from -4 m to $+13$ m, a significantly large distance than that required during deployment. Of course, this is expected due to unstable character of the retrieval maneuver.

5.5 Gain Scheduling Control of the Attitude Dynamics

For a comparison between the FLT based regulator and a linear controller with gain scheduling, design of an attitude controller using the eigenvalue assignment algorithm was undertaken. This linear time invariant controllers were implemented

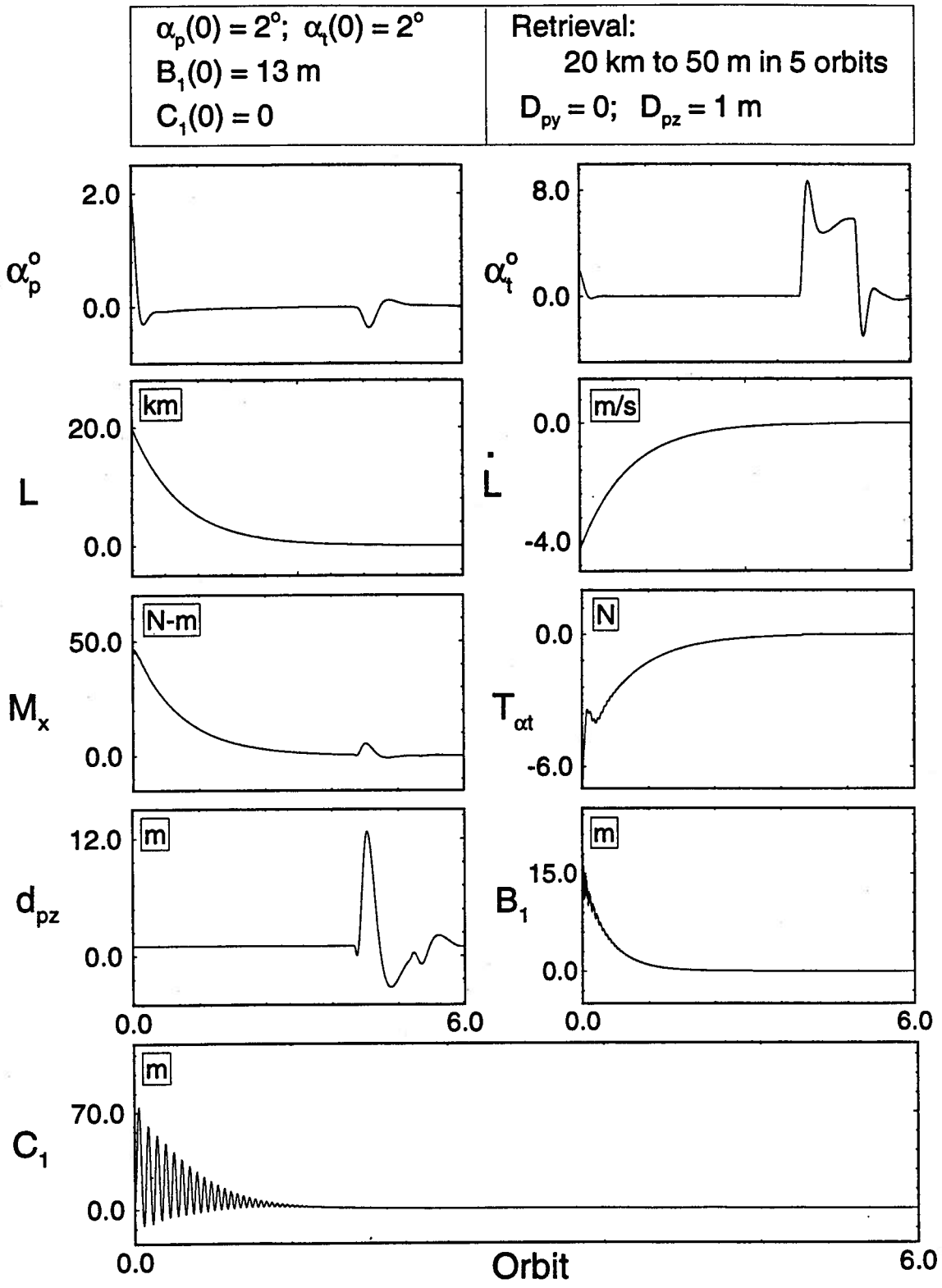

Figure 5-17 System response during retrieval with a hybrid control scheme.

on the time varying nonlinear plant in conjunction with the gain scheduling. The controllers were designed using the Graph Theoretic Approach. The detail mathematical background and the controller expressions are given in Appendix IV. Only a few typical results are presented here for comparison. Figure 5-18shows the station-keeping dynamics in presence of the thruster augmented active control. Note, the attitude degrees of freedom are controlled quite successfully. The control effort (M_x and T_{α_t}) requirements are rather modest. However, the system performance during retrieval with a fixed specified offset of 1 m along the local horizontal (D_{pz}=1 m) is not satisfactory (Figure 5-19). Particularly, the platform pitch response has a large overshoot of more than -5^o at the beginning of the retrieval. This is attributed to coupling, caused by a nonzero offset, between the tether and platform dynamics. The linear controller (with gain scheduling) takes some time to compensate for the coupling effect. Similar response was also observed during the retrieval maneuver of shorter tethers using the offset strategy (Figure 5-20). The performance of the system during a hybrid control is essentially the same. Comparison of these results with those presented in Figure 5-17, where the FLT based hybrid control is used to regulate the retrieval dynamics, clearly shows better performance of the FLT controller compared to the gain scheduling linear regulator.

5.6 Concluding Remarks

A controller based on the FLT is found to be adequate in regulating the highly time varying attitude dynamics of the TSS with a flexible tether. Two different strategies, thruster and offset control, are used for longer and shorter tethers, respectively. Three different system models (nonlinear flexible, nonlinear rigid, and linear rigid) are considered to arrive at an efficient FLT controller design. Results

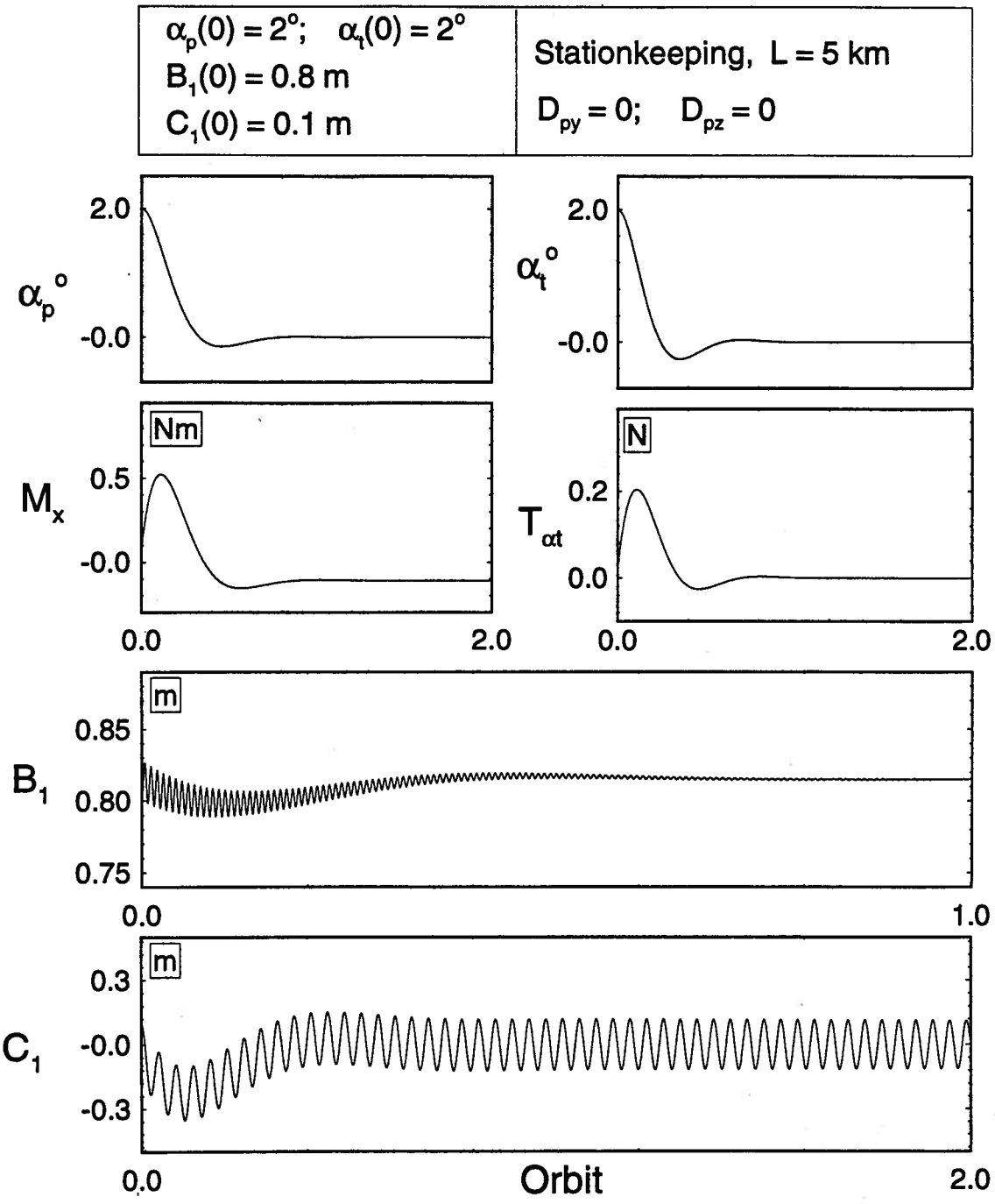

Figure 5-18 Controlled stationkeeping dynamics using the graph theoretic approach.

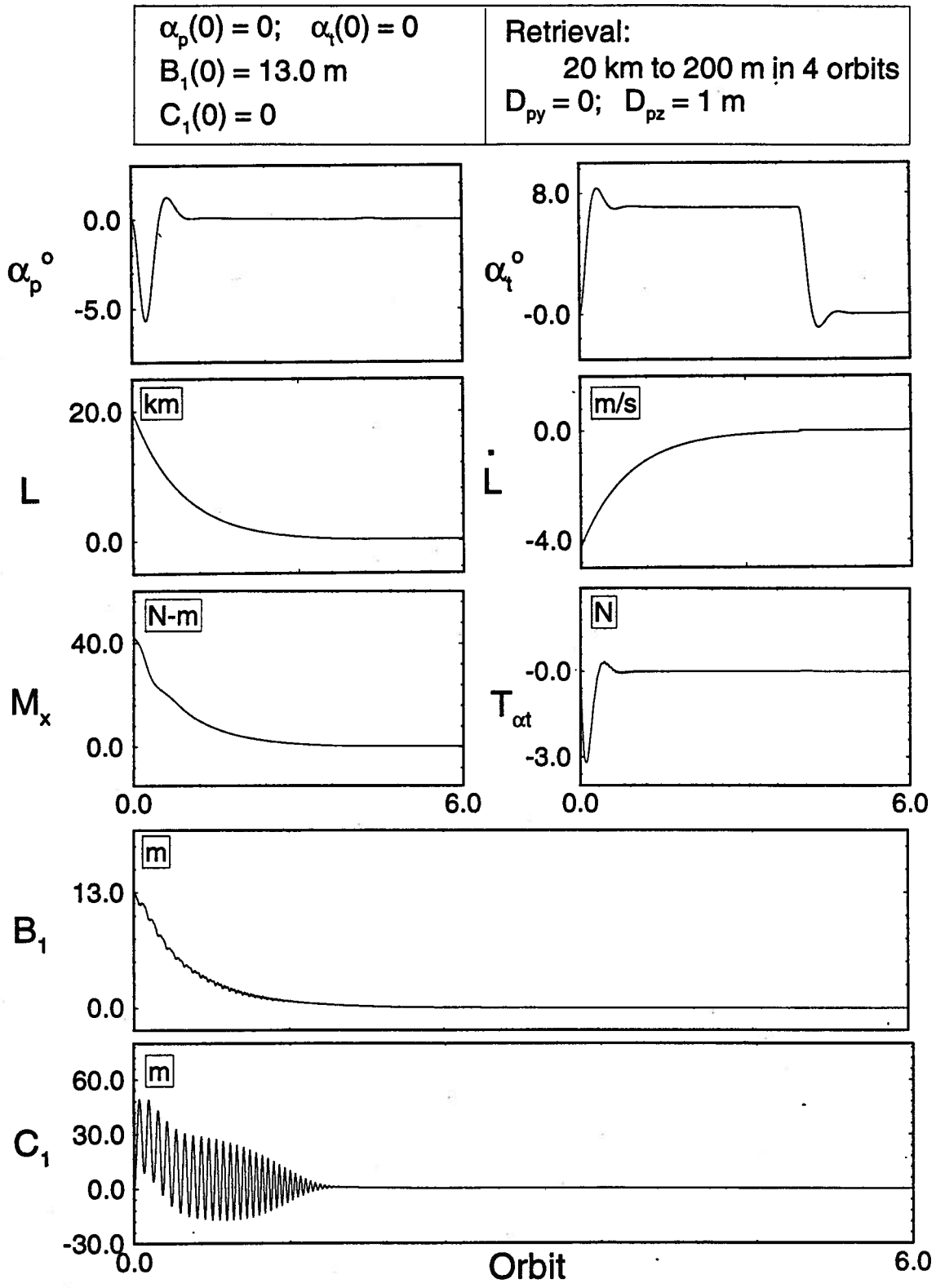

Figure 5-19 Gain scheduling control of the retrieval maneuver using the thruster augmented strategy.

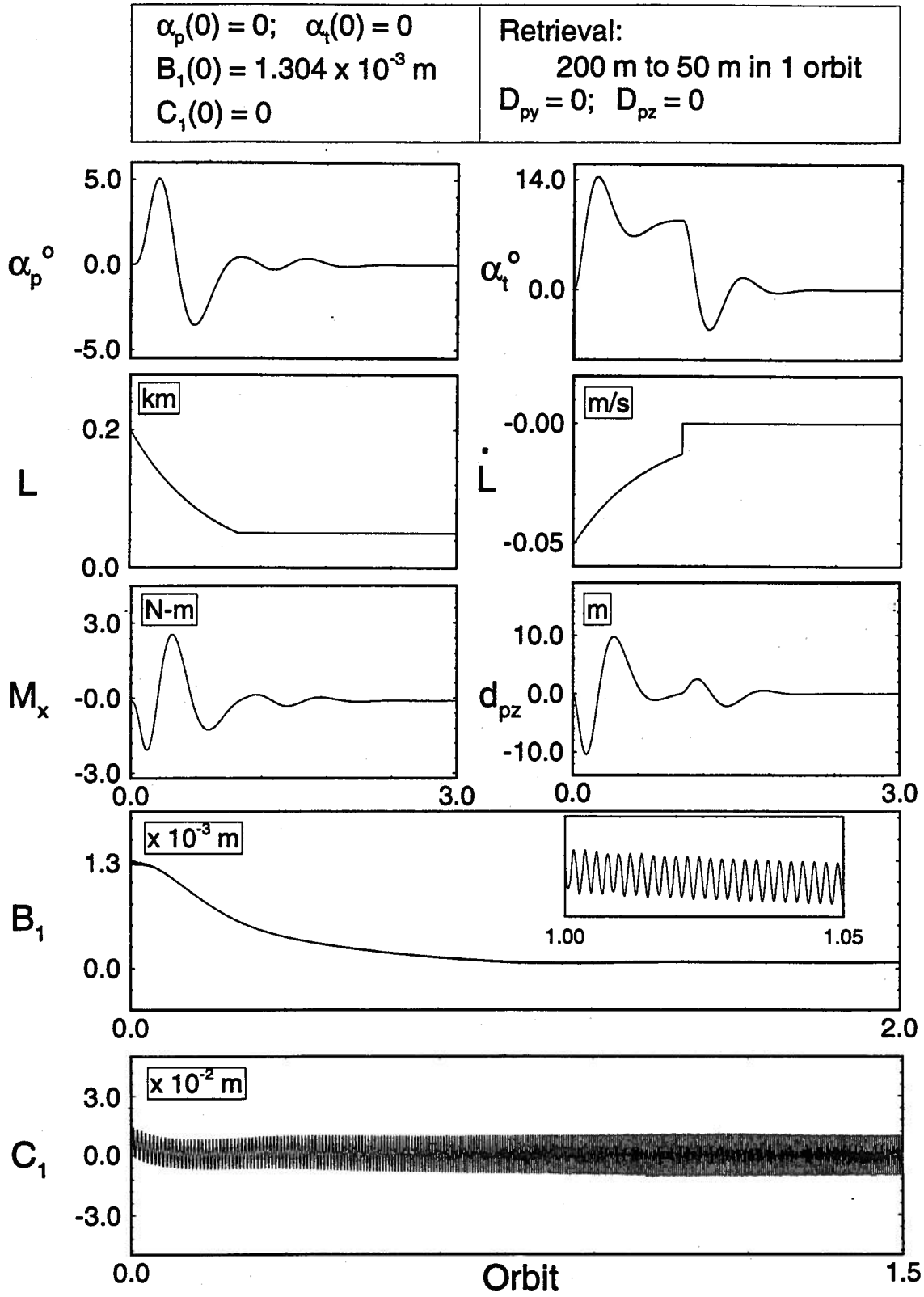

Figure 5-20 Offset control of the retrieval dynamics using the gain scheduling approach.

suggests that the rigid body model (either nonlinear or linear) is sufficient to develop an effective thruster based regulator with a PI control loop. The FLT based controller with an PI loop is also shown to be effective during the offset control. Both the offset and thruster strategies are also implemented in a hybrid fashion. The hybrid control strategy using the thruster control at longer tether lengths and the offset control for shorter tethers appears quite promising.

Linear time invariant regulators, designed using the graph theoretic approach and implemented through gain scheduling, though effective are not as efficient as the FLT based control system.

6. VIBRATION CONTROL OF THE TETHER

6.1 Preliminary Remarks

Tether missions involving controlled gravity environment or precise positioning of the subsatellite require regulation of the tether's vibratory motion. The tether may oscillate in both the longitudinal and transverse directions. The design and implementation of the controller to suppress tether vibrations is addressed in this chapter. The results presented here correspond to the stationkeeping situation where most of the mission objectives are carried out. Only the first longitudinal and transverse modes are controlled actively here as their energy content is dominant. The higher transverse modes constitute critically stable degrees of freedom. The tether vibrations can be controlled either by some active methods (if controllable and observable) or using passive dampers at appropriate locations. In the present study, a passive damper is used to control the higher transverse modes. The rigid degrees of freedom are regulated by thrusters and momentum gyros, and the transverse and longitudinal modes are governed by the offset strategy.

This chapter begins with some mathematical background for the controller design. This is followed by the system linearization. Finally design of the controller is undertaken which includes the choice of system inputs and outputs as well as some typical results showing its performance.

6.2 Mathematical Background

The nominal design model of a plant in the linear state space form can be

expressed as:

$$\dot{x} = A_o x + B_o u + \Gamma \xi; \tag{6.1a}$$

$$y = C_o x + \eta; \tag{6.1b}$$

where: $x \in \mathbf{R}^n$; $u \in \mathbf{R}^m$; $y \in \mathbf{R}^r$; $\xi \in \mathbf{R}^l$; and A_o, B_o, C_o and Γ are constant real matrices of appropriate dimensions. x, u and y are the state, control input and measured output vectors, respectively. ξ is the state noise vector and η is the measurement noise vector. These are *white noises* uncorrelated in time (but may be correlated with each other) with covariances

$$\mathrm{E}[\xi\xi^T] = \Xi \geq 0, \qquad \mathrm{E}[\eta\eta^T] = \Theta > 0, \qquad \text{and} \qquad \mathrm{E}[\xi\eta^T] = O,$$

where O is the null matrix of appropriate dimension. In the transfer function notation the system can be represented by

$$y = G(s)u + d + \eta, \tag{6.2}$$

where:

$$G(s) = C_o \Phi(s) B_o;$$

$$d = C_o \Phi(s) \Gamma \xi;$$

$$\text{and} \quad \Phi(s) = [sU - A_o]^{-1}.$$

Here, $G(s)$ is an $m \times r$ transfer function matrix and U is the unit matrix. The standard feedback configuration of the system is illustrated in Figure 6-1. It consists of an interconnected plant $G(s)$ and a compensator $F(s)$ forced by the command input r, measurement noise η and disturbance d.

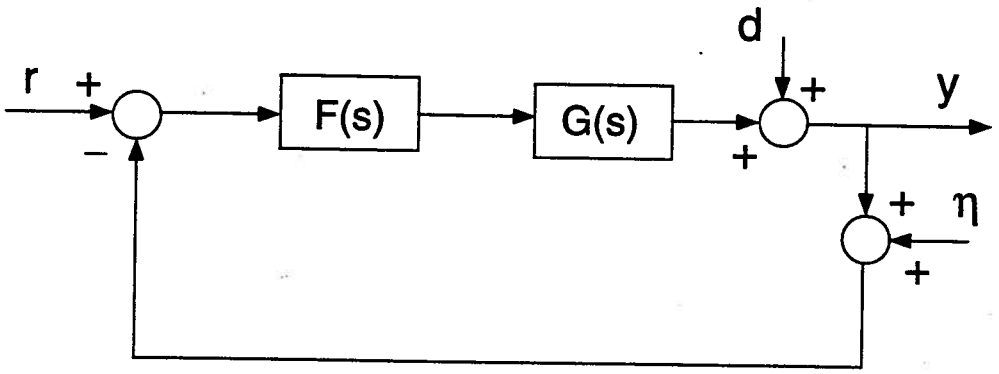

Figure 6-1 Standard feedback configuration.

6.2.1 Model uncertainty and robustness conditions

In reality, the true model of the system, $G'(s)$, is not the same as the nominal design model, $G(s)$. Hence, no nominal model can be considered complete without some assessment of its error, normally referred to as *model uncertainty*. The representation of these uncertainties varies primarily in terms of the amount of structure it contains. For example, the uncertainty caused by variation of certain parameters in the governing equations of motion is a highly structured representation. It typically arises from the use of linear incremental models, e.g. error in the moment of inertia of a spacecraft, variation in the satellite mass due to firing of thrusters, changes in the aerodynamic coefficients of an aircraft with flight environment and configuration, etc. In these cases, the extent of variation and any known relationship between the parameters can be expressed by confining them to appropriately defined subsets in the parameter space. An example of the less structured representation of uncertainty is the direct statement for the transfer function matrix of the model

such as

$$G'(jw) = G(jw) + \Delta G(jw) \tag{6.3a}$$

with

$$\bar{\sigma}[\Delta G(jw)] < l_a(w), \qquad \forall w \geq 0,$$

where: $l_a(\cdot)$ is a positive scalar function confining the matrix G' to the neighborhood of G with magnitude $l_a(w)$; and $\bar{\sigma}(\cdot)$ represents the maximum singular value of a matrix. The statement does not imply a mechanism or structure that gives rise to $\Delta G(jw)$. The uncertainty may be caused by parameter changes as above, or by neglected dynamics, or by some other unspecified effects. This is also referred to as *additive uncertainty*. The alternative statement has the multiplicative forms:

$$G'(jw) = [U + L_o(jw)]G(jw); \tag{6.3b}$$

or

$$G'(jw) = G(jw)[U + L_i(jw)], \tag{6.3c}$$

with

$$\bar{\sigma}[L_o(jw)] < l_{m_o}(w), \qquad \bar{\sigma}[L_i(jw)] < l_{m_i}(w), \qquad \forall w \geq 0,$$

where $l_{m_o}(\cdot)$ and $l_{m_i}(\cdot)$ are positive scalar functions; U is the unit matrix of appropriate dimensions with $L_o(jw)$ and $L_i(jw)$ representing *output and input multiplicative uncertainties*, respectively. The structure of the system with these uncertainties is shown in Figure 6-2.

The objective of the feedback design problem is to find a compensator $F(s)$ such that:

(i) the nominal feedback system, $GF[U + GF]^{-1}$, is stable;

(ii) the perturbed system, $G'F[U + G'F]^{-1}$, is stable for all possible G'; and

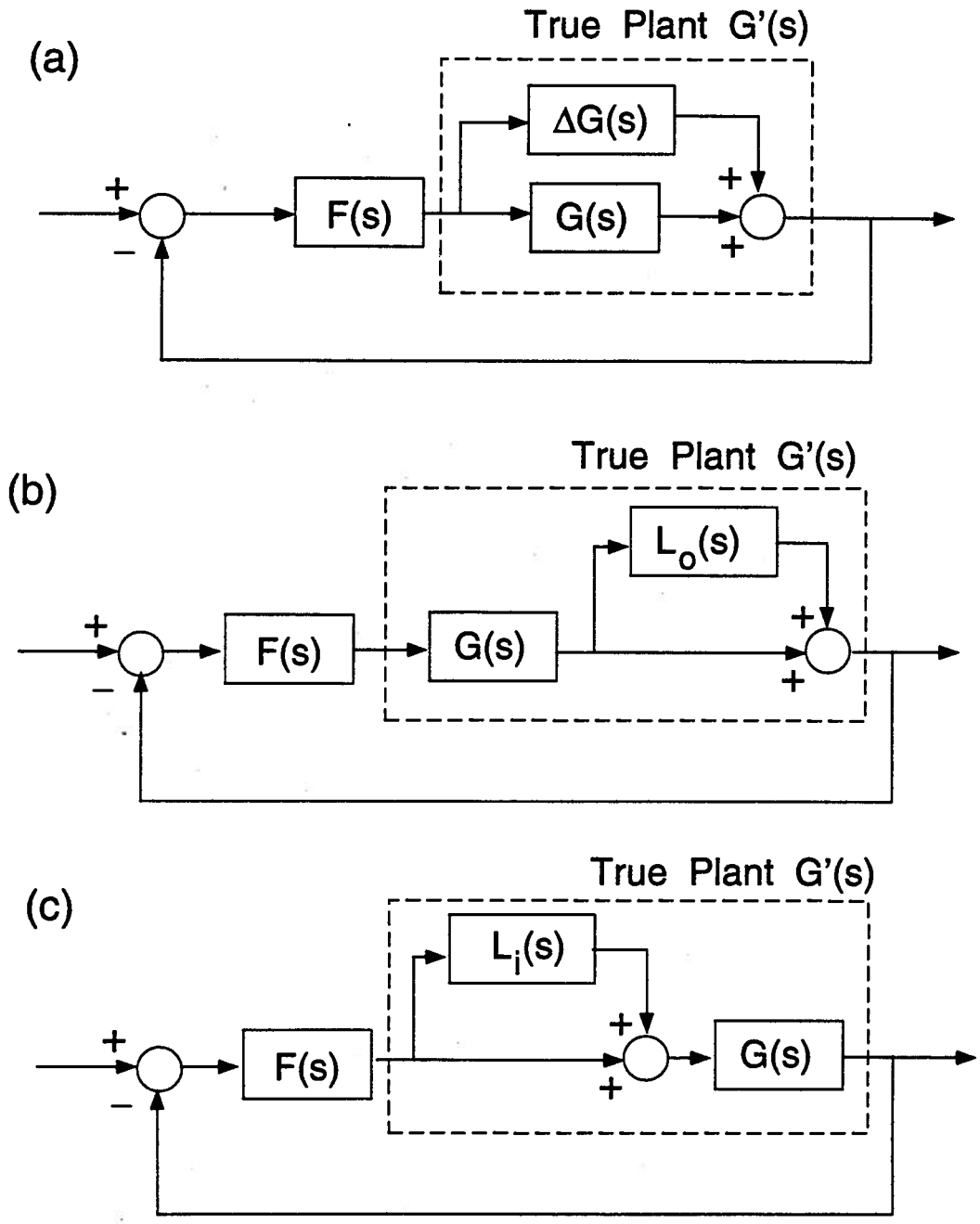

Figure 6-2 Diagram showing different unstructured uncertainties: (a) additive; (b) output multiplicative; and (c) input multiplicative.

(iii) performance objectives are satisfied for all possible G'.

The requirement (i) demands that the encirclement count of the map $det[U + GF(s)]$, evaluated on the standard Nyquist D-counter, be equal to the (negative) number of unstable open loop modes of $GF(s)$ [92]. As shown by Yuan and Stieber [93], for the additive uncertainty used in the present study, the closed loop system satisfies the stability robustness requirement (ii) iff

$$l_a(w) < \frac{1}{\bar{\sigma}[R(j\omega)]}, \tag{6.4}$$

where $[R(j\omega)] = F(j\omega)[U + G(j\omega)F(j\omega)]^{-1}$. Simillar conditions for other uncertainties can also be obatained [94].

6.2.2 LQG\LTR design procedure

Linear Quadratic Gaussian (LQG) procedure is a widely used approach for feedback design [95, 96]. The LQG controller is an ordinary finite dimensional LTI compensator with the internal structure as shown in Figure 6-3. It consists of a Kalman-Bucy Filter (KBF) which provides an estimate of the state, $\hat{x}$. The KBF gain, K_f, is given by [94]

$$K_f = P_f C_o^T \Theta^{-1}, \tag{6.5}$$

where P_f is the solution of the algebraic Riccati equation

$$P_f A_o^T + A_o P_f - P_f C_o^T \Theta^{-1} C_o P_f + \Gamma \Xi \Gamma^T = 0, \tag{6.6}$$

and $P_f = P_f^T \geq 0$. In general there are several solutions to Eq.(6.6), but only one of them is positive-semidefinite.

The state estimate, $\hat{x}$, is multiplied by the full-state Linear Quadratic Regulator (LQR) gain, K_c, to produce the control command which drives the plant and

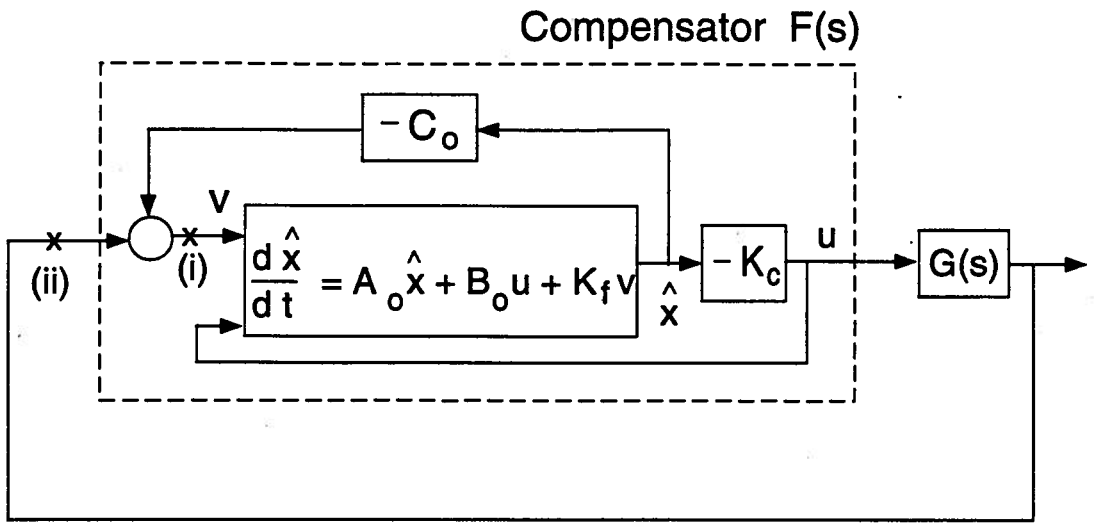

Figure 6-3 Closed-loop system with the LQG feedback controller.

also feed–backs internally to the KBF. The LQR gain K_c is obtained to minimize the cost function

$$J = \int_0^\infty (z^T Q z + u^T R u) \mathrm{d}t,$$

where: $z = Mx$ is some linear combination of the states; and $Q = Q^T \geq 0$, $R = R^T > 0$ are weighting matrices. The solution to this problem is

$$K_c = R^{-1} B_o^T P_c, \tag{6.7}$$

where P_c satisfies the algebraic Riccati equation

$$A_o^T P_c + P_c A_o - P_c B_o R^{-1} B_o^T P_c + M^T Q M = 0, \tag{6.8}$$

and $P_c = P_c^T \geq 0$.

Both the LQR and KBF loops have good robustness properties [97, 98]. Therefore, it may be expected that the LQG compensator would generally display acceptable robustness and performance. Unfortunately, it has been shown that the LQG designs can exhibit arbitrarily poor stability margins [99]. However, there are

procedures to design either LQR controller or KBF so that the full state-feedback properties are *recovered* at the output or input, respectively, of the plant [100]. For a square minimum phase plant, design for the Loop Transfer (function) Recovery (LTR) at the plant output consists of two steps:

(i) Design a KBF by manipulating the covariance matrices Ξ and Θ until a return ratio $C_o(sU - A_o)^{-1}K_f$ (i.e. the KBF loop transfer function) is obtained which would be satisfactory at the plant output (i.e. at the break point (i) in Figure 6-3).

(ii) The loop transfer function obtained by breaking the loop at point (ii) in Figure 6-3 is $GF(s)$, where $F(s)$ is the compensator transfer function. It can be made to approach $C_o(sU - A_o)^{-1}K_f$ pointwise in s by designing the LQR in accordance with a *sensitivity recovery* procedure due to Kwakernaak and Sivan [101]. To achieve this, synthesize an optimal state-feedback regulator by setting $Q = Q_o + qU$ and $R = R_o$ (or $Q = Q_o$ and $R = R_o + \rho U$), and increase q (reduce ρ) until the return ratio at the output of the compensated plant converges sufficiently close to $C_o(sU - A_o)^{-1}K_f$ over a large range of operational frequencies.

For non-square plants, the inputs and/or outputs can be redefined to make the system square and the LQG/LTR procedure can be applied to the modified plant (if it is observable and controllable). For non-minimum phase plants the recovery may be achievable at those frequencies at which the plant's response is very close to that of a minimum-phase plant, i.e. at frequencies which are small compared to the distance from the origin to any of the right-half plane zeros [94]. A simple strategy to use with the non–minimum phase plant is to follow the usual LTR procedure. If the right half-plane zeros lie well out side the required bandwidth, then adequate

recovery of the ideal characteristics would be achieved at all significant frequencies.

6.3 Controller Design and Implementation

The prime objective of the controller is to regulate longitudinal and transverse tether vibrations using the offset strategy with the attitude dynamics regulated by the thruster augmented active control. As explained earlier, only the first longitudinal and transverse modes are considered for the controller design. The LQG/LTR based procedure is used which can account for the model uncertainty due to the neglected dynamics.

6.3.1 Linear model of the flexible subsystem

The model is obtained by linearizing the decoupled equations of motion for the flexible subsystem about the equilibrium positions. The equilibrium position for the transverse vibrations is zero and for the longitudinal oscillations corresponds to the static deflection value. The linearized equations can be written as

$$M_z\ddot{Z} + G_z\dot{Z} + K_zZ + M_{dy}\ddot{d}_{py} + G_{dy}\dot{d}_{py} + K_{dy}d_{py} + M_{dz}\ddot{d}_{pz} + G_{dz}\dot{d}_{pz} + K_{dz}d_{pz} + P_z = Q_zT_L, \qquad (6.9)$$

where: $Z = \left\{\{B - B_{eq}\}^T,\ C^T\right\}^T$ is the flexible generalized coordinate vector; T_L, the control thrust along the undeformed tether line; d_{py} $(D_{py} + D_y)$ and d_{pz} $(D_{pz} + D_z)$, the offsets of the tether attachment point along the local vertical and local horizontal, respectively; D_{py} and D_{pz}, the specified offsets; and D_y and D_z, the offsets required by the controller. The expressions and numerical values of the coefficient matrices (for a system with 10 transverse and 2 longitudinal modes) are defined in Appendix V. The numerical values are for the system without any passive damping. Depending on the choice and controllability, the variables T_L, $\dot{D}_y$, $\dot{D}_z$,

$\ddot{D}_y$ and $\ddot{D}_z$ can be used as control inputs, either separately or in combinations.

The selection of outputs completes system characterization in the linear state-space form. It should be recognized that placement of sensors on the tether to measure vibrations is impractical due to small diameter (one to two mm) of the tether as well as its deployment and retrieval maneuvers. The objective of the controller is to suppress longitudinal as well as transverse vibrations using the offset control strategy. The output vector consists of: longitudinal deformation from the equilibrium value of the tether at $y_t = L$; slope of the tether due to transverse deformation at $y_t = 0$; and offset positions along the local vertical and horizontal; i.e.

$$y = \begin{Bmatrix} \left\{\psi_1(L),\ \cdots,\ \psi_{N_2}(L),\ 0,\ \cdots,\ 0\right\}\{Z\} \\ \left\{0,\ \cdots,\ 0,\ \left(\partial\Phi_1/\partial y_t\right)_{y_t=0},\ \cdots,\ \left(\partial\Phi_{N_1}/\partial y_t\right)_{y_t=0}\right\}\{Z\} \\ D_y \\ D_z \end{Bmatrix} \tag{6.10}$$

6.3.2 Design of the controller

In the nondimesional form, the lowest elastic and maximum attitude frequencies ($\omega/\dot{\theta}$) are 12.6 and 1.732, respectively. This separation of frequencies allows the controllers for the rigid and flexible subsystems to be designed based on the decoupled equations of motion. The rigid body controller was designed using the Feedback Linearization Technique (FLT) discussed in Section 5.2.3. Now, the controller for the flexible subsystem is designed by the LQG based approach. Here, the objective is to regulate both the longitudinal and transverse vibrations by the offset control strategy. As mentioned earlier, the 1^{st} transverse (C_1) and 1^{st} longitudinal (B_1)

modes are controlled. The nondimensional frequencies of C_1 and B_1 degrees of freedom are 12.6 and 65.5, respectively. Again, the frequency separation permits the design to be based on the decoupled C_1 and B_1 models. The control input for the B_1 model is the offset acceleration along the local vertical ($\ddot{D}_y$) and that for C_1 model is $\ddot{D}_z$ (offset acceleration along the local horizontal). The outputs are selected from Eq.(6.10). For the B_1 subsystem, the output vector is

$$y_b = \left\{ \begin{array}{c} \psi_1(L)Z_1 \\ \\ D_y \end{array} \right\}, \tag{6.11}$$

where $Z_1 = B_1 - B_{eq_1}$, and B_{eq_1} is the equilibrium (static deflection) value of the 1^{st} longitudinal mode (B_1). For the C_1 equation, the outputs are

$$y_c = \left\{ \begin{array}{c} \left(\partial\Phi_1/\partial y_t\right)_{y_t=0} C_1 \\ \\ D_z \end{array} \right\}. \tag{6.12}$$

Controller for the B_1 model, which is a two output and a single input system, is designed using the LQG/LTR method. The design approach is due to Doyle and Stein [100]. The controller matrices are obtained using the subroutines available in the Robust Control Toolbox of MATLAB [102]. This procedure requires the system to be square. The rectangular linear model for the B_1 dynamics is rendered square by defining the output as

$$y_b = \psi_1(L)Z_1 + D_y. \tag{6.13}$$

The system and control influence matrices are obtained consistent with the first mode assumption. With this modified output, the system is found to be controllable and observable. The controller design equations for the C_1 dynamics is obtained in a similar way. In this case, the LQG/LTR controller, obtained after redefining the output, does not give satisfactory performance. The degradation was attributed to the modified output and can be avoided by using the original input-output structure

in conjunction with the LQG design procedure. To regulate the offset motion, the design equations are augmented by the following identities:

$$\ddot{D}_y = u_b;$$

$$\text{and} \qquad \ddot{D}_z = u_c,$$

for B_1 and C_1 dynamics, respectively. The controller design models can be represented by:

$$\dot{x}_b = A_b x_b + B_b u_b; \tag{6.14a}$$

$$y_b = C_b x_b, \tag{6.14b}$$

and

$$\dot{x}_c = A_c x_c + B_c u_c; \tag{6.15a}$$

$$y_c = C_c x_c, \tag{6.15b}$$

where:

$$x_b = \{(B_1 - B_{eq_1}),\ \dot{B}_1,\ D_y,\ \dot{D}_y\}^T;$$

$$x_c = \{C_1,\ \dot{C}_1,\ D_z,\ \dot{D}_z\}^T;$$

with y_b and y_c given by Eqs.(6.13) and (6.12), respectively.

Here, the subscripts 'b' and 'c' refer to B_1 and C_1 dynamics, respectively. The dynamic feedback controllers have the form:

$$\dot{x}_{fb} = A_{fb}\ x_{fb} + B_{fb}\ y_b; \tag{6.16a}$$

$$u_b = C_{fb}\ x_{fb}, \tag{6.16b}$$

and

$$\dot{x}_{fc} = A_{fc}\ x_{fc} + B_{fc}\ y_c; \tag{6.17a}$$

$$u_c = C_{fc}\ x_{fc}, \tag{6.17b}$$

where x_{fb} and x_{fc} are the state vectors for the B_1 and C_1 controllers, respectively. The numerical values of the design model are obtained from the higher order model. The complete linear model, controller and weighting matrices are given in Appendix V. The data are for a tethered system during stationkeeping at $L = 20\ km$ with mass and elastic properties as given in Chapter 4. Next, the closed-loop eigenvalues for the linear flexible system were obtained to have some appreciation as to the controller's effectiveness. The eigenvalues of the open-loop and closed-loop systems are shown in Table 6.1.

Table 6.1 Comparison of the open-loop and closed-loop eigenvalues of the system.

Mode	Open-loop	Closed-loop
Trans. 1	0.0 ± 1.468e-2	− 9.880e-4 ± 1.463e-2
Trans. 2	0.0 ± 2.937e-2	0.0 ± 2.937e-2
Trans. 3	0.0 ± 4.405e-2	0.0 ± 4.406e-2
Trans. 4	0.0 ± 5.874e-2	0.0 ± 5.874e-2
Trans. 5	0.0 ± 7.342e-2	0.0 ± 7.343e-2
Long. 1	− 3.797e-4 ± 7.601e-2	− 1.144e-2 ± 7.614e-2
Trans. 6	0.0 ± 8.811e-2	0.0 ± 8.811e-2
Trans. 7	0.0 ± 1.028e-1	0.0 ± 1.028e-1
Trans. 8	0.0 ± 1.174e-1	0.0 ± 1.174e-1
Trans. 9	0.0 ± 1.321e-1	0.0 ± 1.321e-1
Trans. 10	0.0 ± 1.468e-1	0.0 ± 1.468e-1
Long. 2	− 2.267e-2 ± 5.870e-1	− 2.183e-2 ± 5.912e-1

Additional controller was designed for the model with a passive damper hav-

ing a damping coefficient (C_{dt}) of 0.2 Ns/m and located on the tether at a distance of 9.8 km from the platform. The damper was introduced to reduce the transverse vibrations. The controller design procedure is given in Figure 6-4. As before, the controller for the B_1-dynamics is designed by the LQG/LTR method and the C_1-controller is designed using the LQG algorithm. The attitude controller is obtained through the FLT procedure. The recovery of the return ratio at the plant output with the LQG/LTR controller for the B_1 dynamics is shown in Figure 6-5. The gain and phase of the return ratio approaches those of the KBF loop transfer function with an increase in the design parameter q. In the present case, the B_1 dynamics is a non-minimum phase system with zeros at $+0.045$ and -0.042. As mentioned before, the recovery in this class of plants is not guaranteed as apparent in Figure 6-5.

Finally, the robustness property of both the B_1 and C_1 controllers is checked against the additive model uncertainty $\Delta G(j\omega)$. Figure 6-6 compares the bound for $\Delta G(j\omega)$, i.e. $l_a(\omega)$, and the inverse of the maximum singular value of $R(j\omega) \triangleq F(j\omega)\Big(U + L(j\omega)\Big)^{-1}$, where: $L(j\omega) = G(j\omega)F(j\omega)$ is the loop transfer function; $F(j\omega)$ is the controller transfer function (both the controllers); $G(j\omega)$ is the openloop transfer function; and U is the unit matrix. As shown in the figure, the stability condition of Eq.(6.4) is satisfied. The structure of the closed-loop system, with controllers for rigid body dynamics as well as longitudinal and transverse vibrations, is shown in Figure 6-7.

6.3.3 Results and discussion

The controllers were implemented on the complete nonlinear system with two longitudinal and three transverse modes. Figure 6-8 shows the response of the

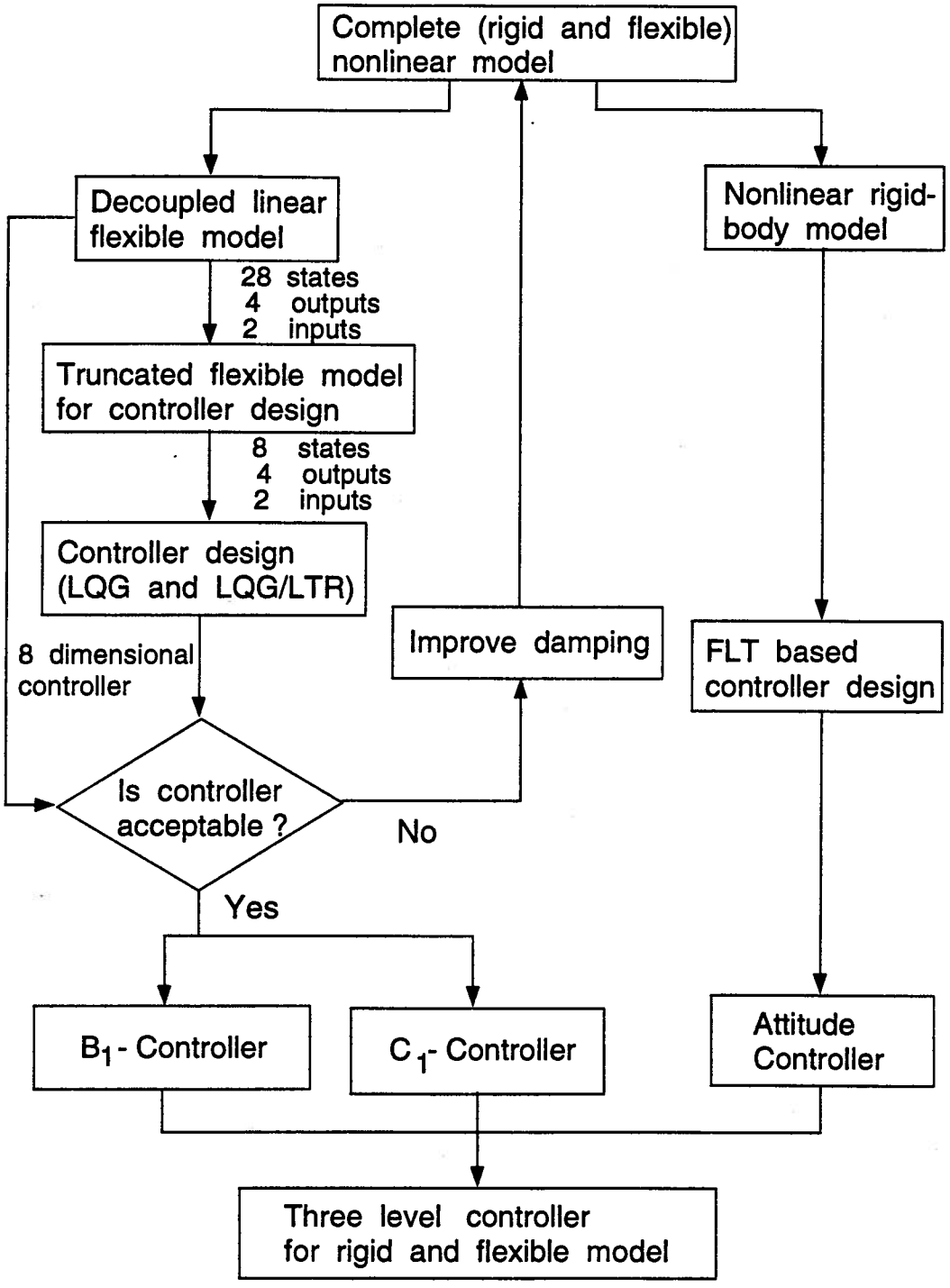

Figure 6-4 Flow chart for the controller design.

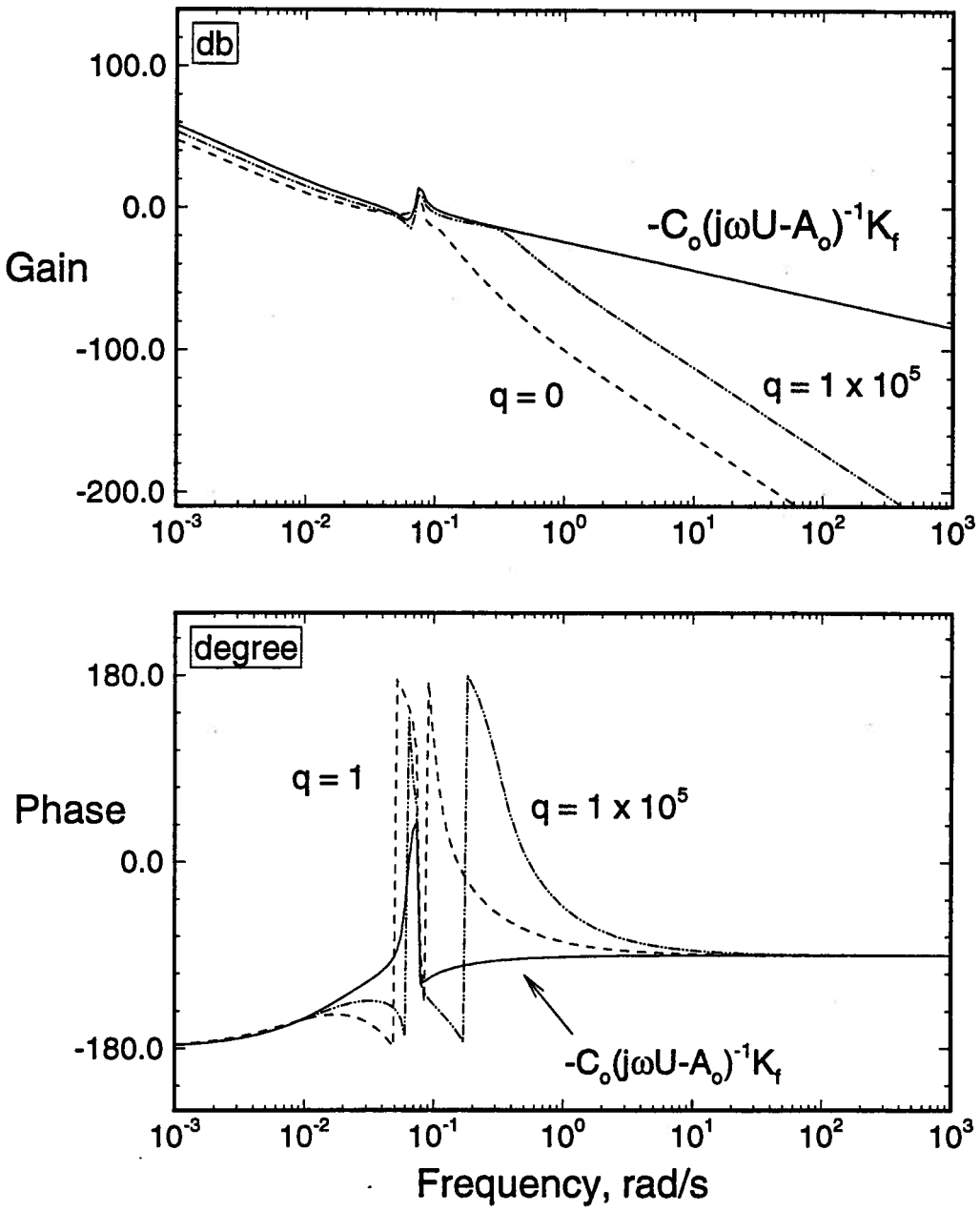

Figure 6-5 Comparison of gain and phase of the return ratio at the plant output with those of the KBF loop transfer function.

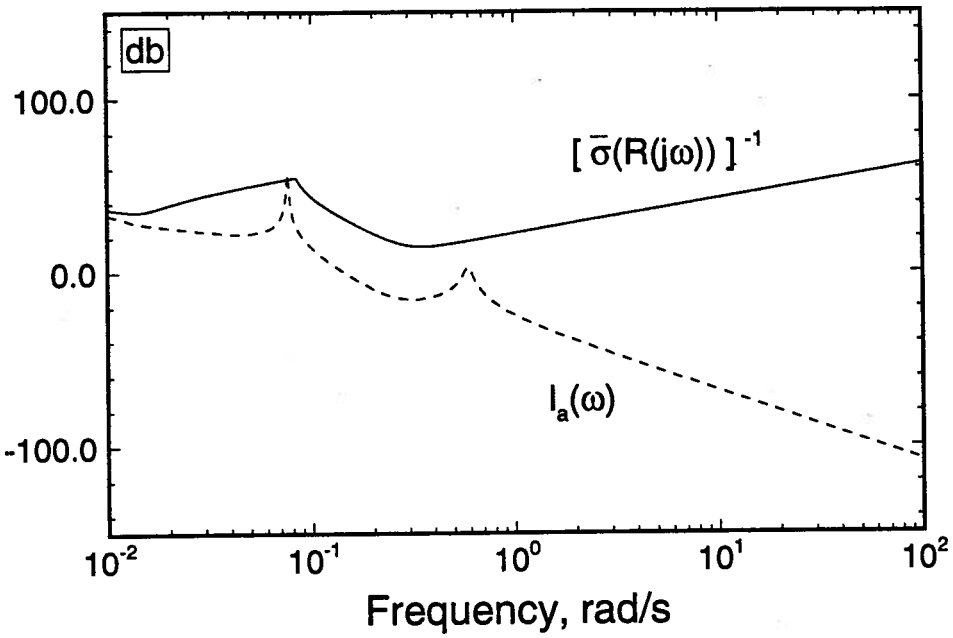

Figure 6-6 Robustness property of the vibration controller.

system without a passive damper and using a three level control structure for simultaneous regulation of flexible and rigid modes. The total longitudinal deformation, $v(L)$, is controlled about its equilibrium value of 13.896 m. As shown in Figure 6-8, it returns to the equilibrium value in less than 0.05 *orbit*. The initial specified offsets for this simulation was set at zero ($D_{py} = D_{pz} = 0.0$). The offset motion requirement for control of the flexible modes is much lower than $\pm$ 15 m limit set for regulation of the rigid degrees of freedom. The total offset motion along the local vertical (d_{py}) is less than $\pm$ 2 m. The first transverse mode settles to zero in around one *orbit*. The offset motion along the local horizontal (d_{pz}), required by the C_1-controller, is around $\pm$ 0.6 m. As discussed earlier, the platform motion is strongly coupled with the tether dynamics through d_{pz}. Since the FLT controller for the platform pitch (α_p) dynamics cancels all the coupling effects, the shape of

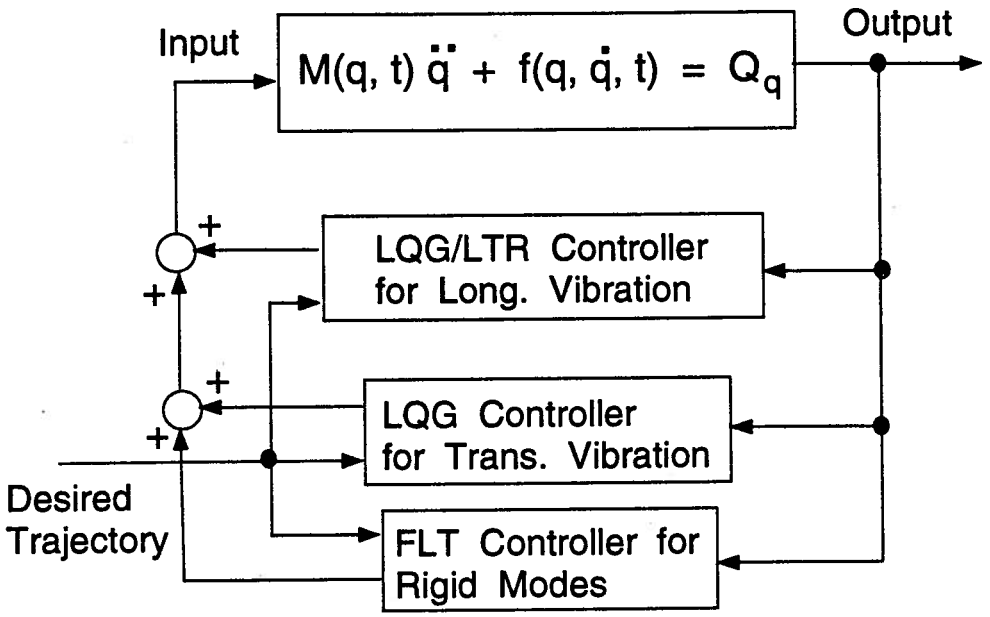

Figure 6-7 Three-level controller structure to regulate rigid as well as transverse and longitudinal flexible motions of the tether.

the moment (M_x) time history required to regulate α_p is similar to that of d_{pz}. The magnitude of M_x is well within the acceptable limit. The thrust (T_{α_t}) required to control the tether pitch (α_t) is also very low.

Figure 6-9 shows the response of the controlled system with a passive damper. The rigid body and longitudinal vibration responses are similar to those observed in the previous case. However, there is a substantial improvement in the transverse vibration responses, particularly in the C_1 and C_3 modes. There is a room for further improvement through optimum location of the damper.

From these simulations, it can be concluded that the tether vibrations in both longitudinal and transverse directions can be controlled effectively by the offset strategy. It is important to note that the offsets required to control the flexible modes

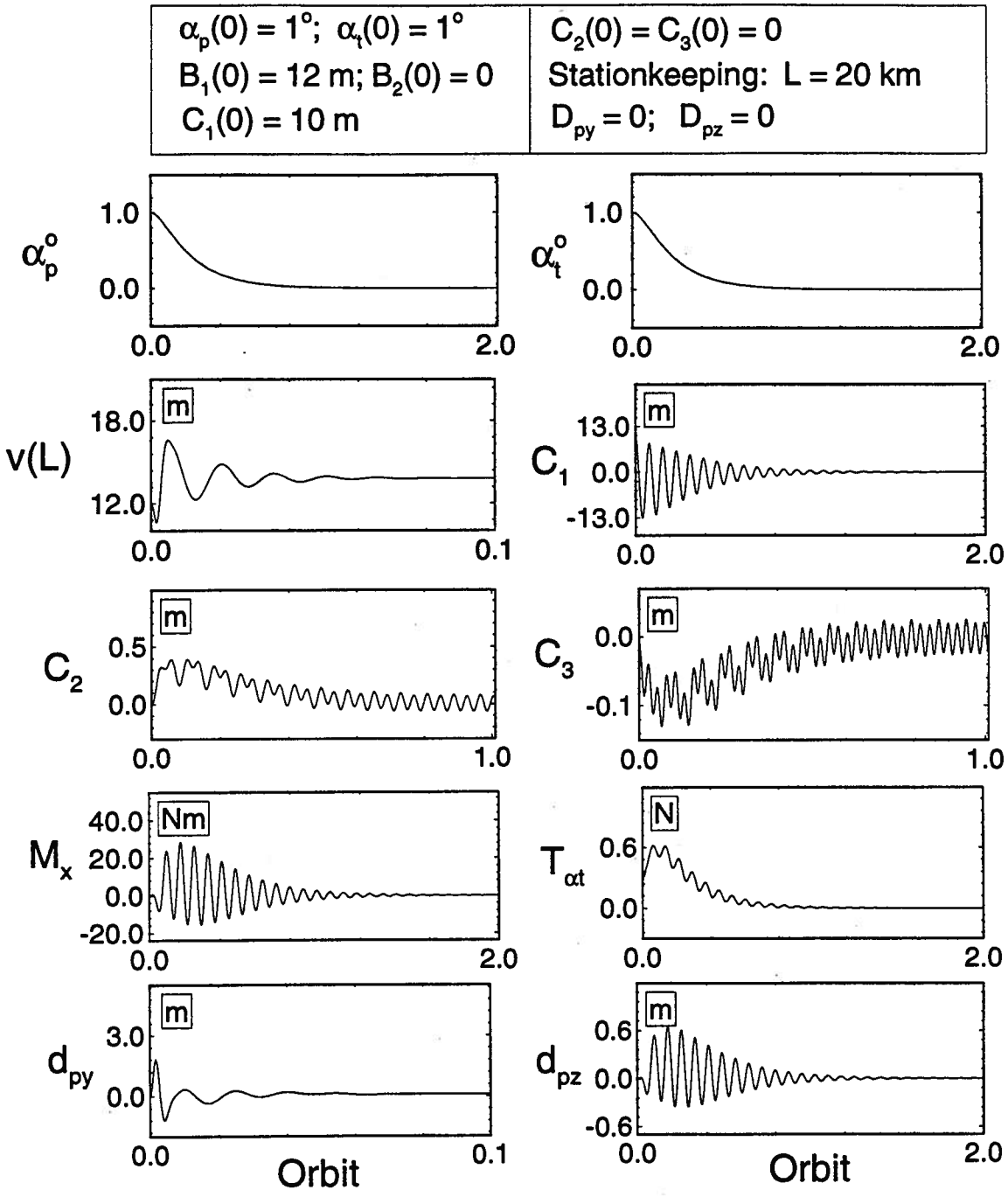

Figure 6-8 Response of the system using a three level controller in absence of a passive damper.

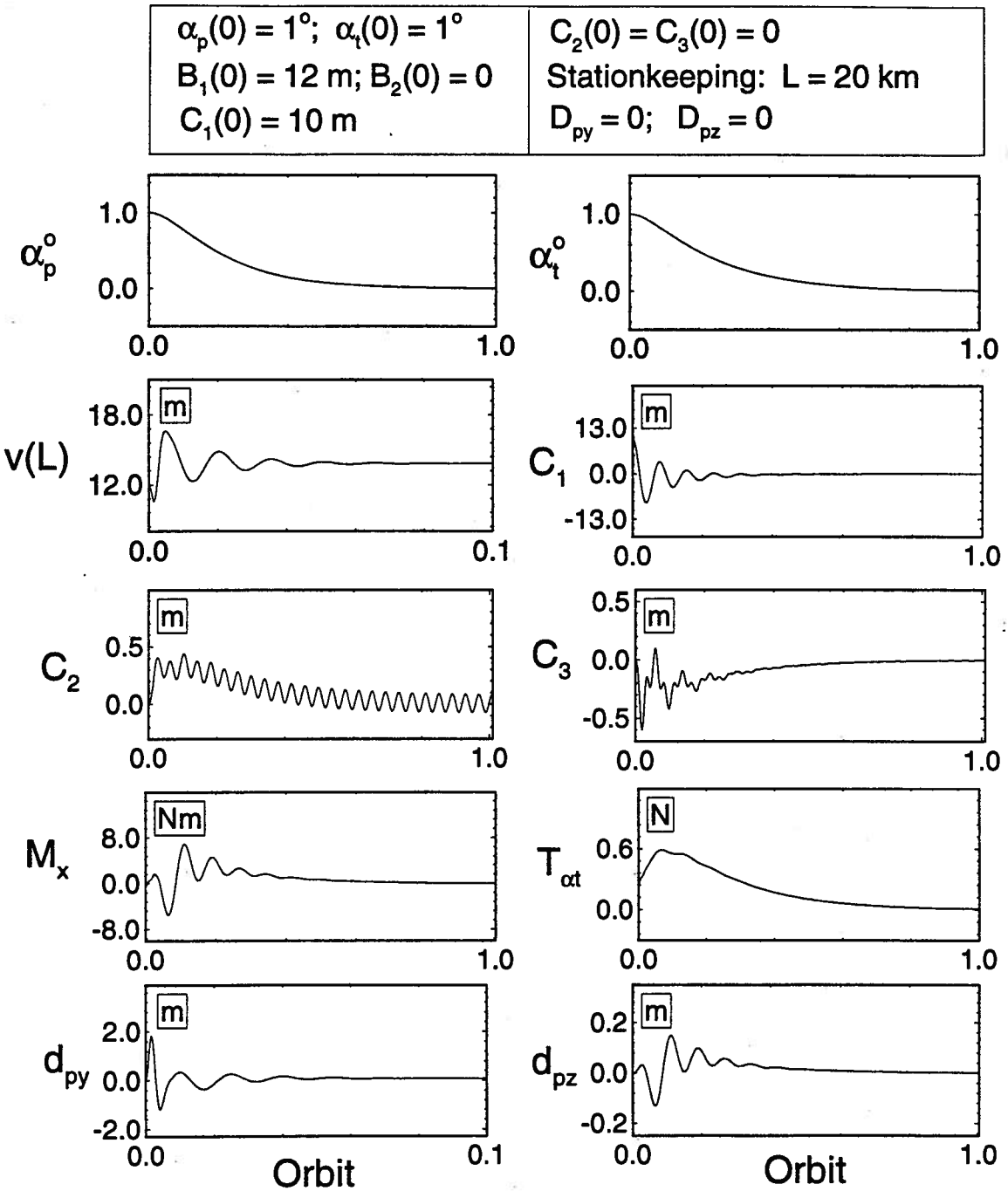

Figure 6-9 Controlled response of the system in presence of a passive damper.

are less than $\pm 2\ m$, which is small compared to the limit ($\pm 15\ m$) set for regulating the attitude motion.

6.4 Concluding Remarks

Issues involving the control of elastic motion of the tether using offset strategy were addressed in this chapter. To begin with a linear model of the flexible subsystem was obtained. Next, three controller loops were designed for simultaneous regulation of attitude as well as longitudinal and transverse flexible modes. The controllers for flexible modes were obtained using the LQG based approaches while the attitude controller employed the FLT algorithm. Offset accelerations along local horizontal and vertical were used as inputs for transverse and longitudinal modes, respectively, while the attitude motion was controlled through thrusters. Effectiveness of the controllers was assessed through its application to the complete nonlinear coupled system. From the simulation results it can be concluded that the procedure is quite effective in regulating, during stationkeeping, both the rigid and flexible degrees of freedom.

7. EXPERIMENTAL VERIFICATION

7.1 Preliminary Remarks

Since the first practical application of a tethered system in 1966 during the Gemini flight, several missions have been carried out to demonstrate the concept. As mentioned in Chapter 1, they include: a joint U.S.–Japan sounding rocket based Tethered Payload Experiment [TPE, 5]; U.S.A.–Italy TSS–1 (Tethered Satellite System–1) mission in August 1992 [6]; sounding rocket based OEDIPUS (Observation of Electrified Distributions in the Ionosperic Plasma–a Unique Strategy) experiment launched by the Canadian Space Agency in January 1989 [7]; and the most recent studies called SEDS–I and II [Small Expendable Deployment System, 8], launched in 1993 and 1994, respectively by NASA. Several ground based laboratory experiments have also been carried out to verify the tether dynamics and effectiveness of different attitude control strategies. Dynamical aspects of a spinning tethered system were explored by Jablonski *et al.* [103] and Tyc *et al.* [104] particularly with reference to the OEDIPUS–C experiment scheduled for lunch in December 1995.

Gwaltney and Greene [105] implemented a tension scheme by converting the control algorithm to a length rate law, for both inplane and out-of-plane dynamics, as well as accounting for the deployment and retrieval phases. The control scheme, with measured tension feedback, was investigated by Shoichi and Osamu [106]. A laboratory set–up, for studying the attitude control of the subsatellite using the offset strategy, has been developed by Kline -Schoder and Powell [59]. Effectiveness of the offset control strategy was verified by Modi *et al.* [48] using a ground based

experimental facility. An LQR type offset control algorithm was used to regulate tether librations during deployment, stationkeeping and retrieval. Using the modified facility to improve the sensor accuracy, the present study assesses effectiveness of the FLT and LQG control methodologies.

To begin with, the experimental set–up is described followed by details of the controller design and implementation procedure. Only a sample of typical results is presented to attest effectiveness of the two controllers. The chapter ends with some concluding remarks.

7.2 Laboratory Setup

The objective of the present experiment is to have some appreciation as to the effectiveness of the FLT and LQG based offset control schemes for regulating the attitude motion of the tether. The experimental setup consists of a spherical mass, representing the subsatellite, which can be deployed or retrieved from a carriage. The carriage, depicting the offset mechanism translating on a platform, can be moved in a horizontal plane. This permits time dependent displacement of the tether attachment point to implement the offset control strategy. A Nylon thread, 1 mm in diameter, connecting the subsatellite with the carriage, serves as tether. The tether can have a maximum length of 2.25 m. A larger platform with a height of 5 m to accommodate longer tethers has also been designed and constructed. Details of the dimensions and mass properties of the setup are given in Appendix-VI. The experimental apparatus consists of three main parts: the sensor; actuator; and controller.

7.2.1 Sensor

Role of the sensor is to measure the angular deviation of the tether from the

vertical position. To that end, a pair of optical potentiometers (S1 series Softpot, U.S. Digital Corp.) were used. The Softpot optical shaft encoder is a noncontacting rotary to digital converter. Useful for position feedback, it converts the real–time shaft angle, speed and direction into the Transistor–Transistor Logic (TTL) compatible two channel quadrature outputs plus a third channel index output. It utilizes a mylar disk, a metal shaft with bushing, and an LED. The unit operates from a single $+5\ V$ supply. Low friction ball bearing makes it suitable for motion control applications.

The output pulses are monitored by a counter circuit, which generates an eight bit digital signal. The counter output can directly be read by the data acquisition system (a commercially available card [107]). The resolution of the sensor depends on whether one or two potentiometer output channels are used in the counter. Two different resolutions, 0.25^o and 1^o, can be obtained with the present counter circuit. The index pulses are used to reset the counter to a reference value when the tether swings through the vertical position. This feature eliminates sensor drift that is normally associated with a resistance potentiometer. Attractive features of the system are : low friction in the bearing; no sensor drift; and accurate resolution to 0.25^o.

An important step in the sensor development was the design of a suitable mechanism to rotate the potentiometer shaft with the tether swing. The mechanism has to perform its task without interfering with the deployment/retrieval maneuvers and yet maintain the unavoidable friction at a low level. The design consists of a light, slotted, aluminum semi–ring as shown in Figure 7-1. The ring is so designed as to maintain dynamic balance during acceleration of the carriage. Any dynamic unbalance may introduce an inertia torque on the ring leading to an error in the

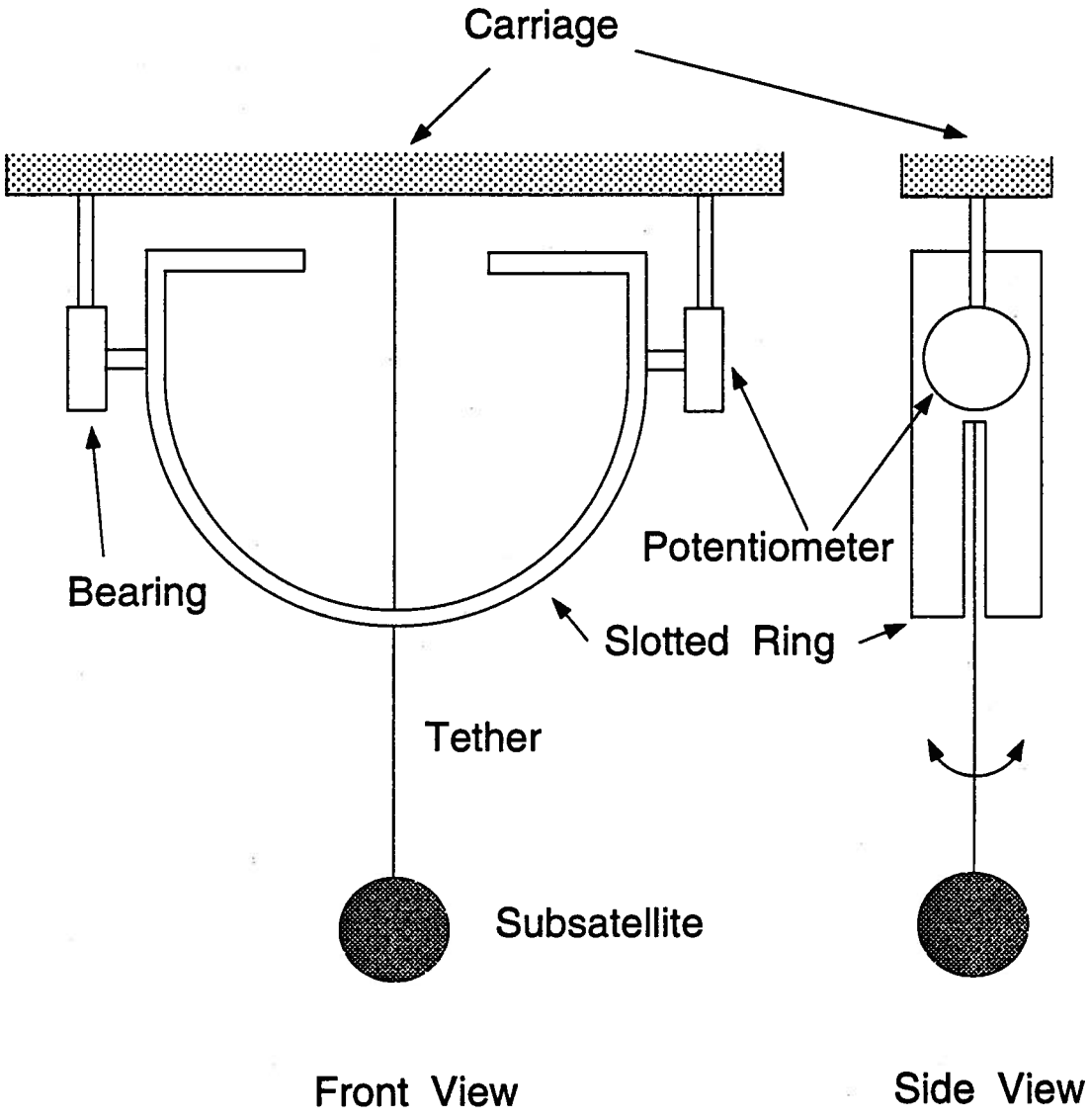

Figure 7-1 A device to measure the tether swing through rotation of the potentiometer shaft.

potentiometer reading . One side of the ring is connected to the potentiometer shaft while the other is supported by the bearing thus permitting it to rotate about a fixed axis. The tether passes through the slot in the ring permitting detection of the swinging motion even during deployment and retrieval. A pair of such semi–rings are used to measure the angles in two orthogonal planes.

7.2.2 Actuator

The actuation mechanism can be visualized as a large x-y table, where a carriage representing the tether attachment point traverses a horizontal plane (Figure 7-2). The motion of the carriage is controlled by a pair of stepper motors. The carriage carried a reel mechanism, driven by another stepper motor, to deploy or retrieve the tethered payload. All the three motors were commanded by a digital computer that implements the control strategy.

7.2.3 Controller

The controller was a 486/33 MHz IBM compatible personal computer. A typical control loop consists of sensing the tether angles, computation of the corrective control effort, transmitting actuation commands for moving the tether attachment point, and saving the required information into an output file. The stepper motor commands are sent through translators, which supply required voltage to the motors for each pulse received from the controller. The pulse train for the deployment/retrieval motor is generated by a commercially available card [108]. A trapezoidal velocity profile is selected for this maneuver. The pulses for the carriage motors are generated through the digital output port of the PCLabCard [107]. A linear velocity profile is chosen to implement the constant acceleration of the tether attachment point during each time–step. Photographs of the test facility are presented in Figures 7-3 to 7-6.

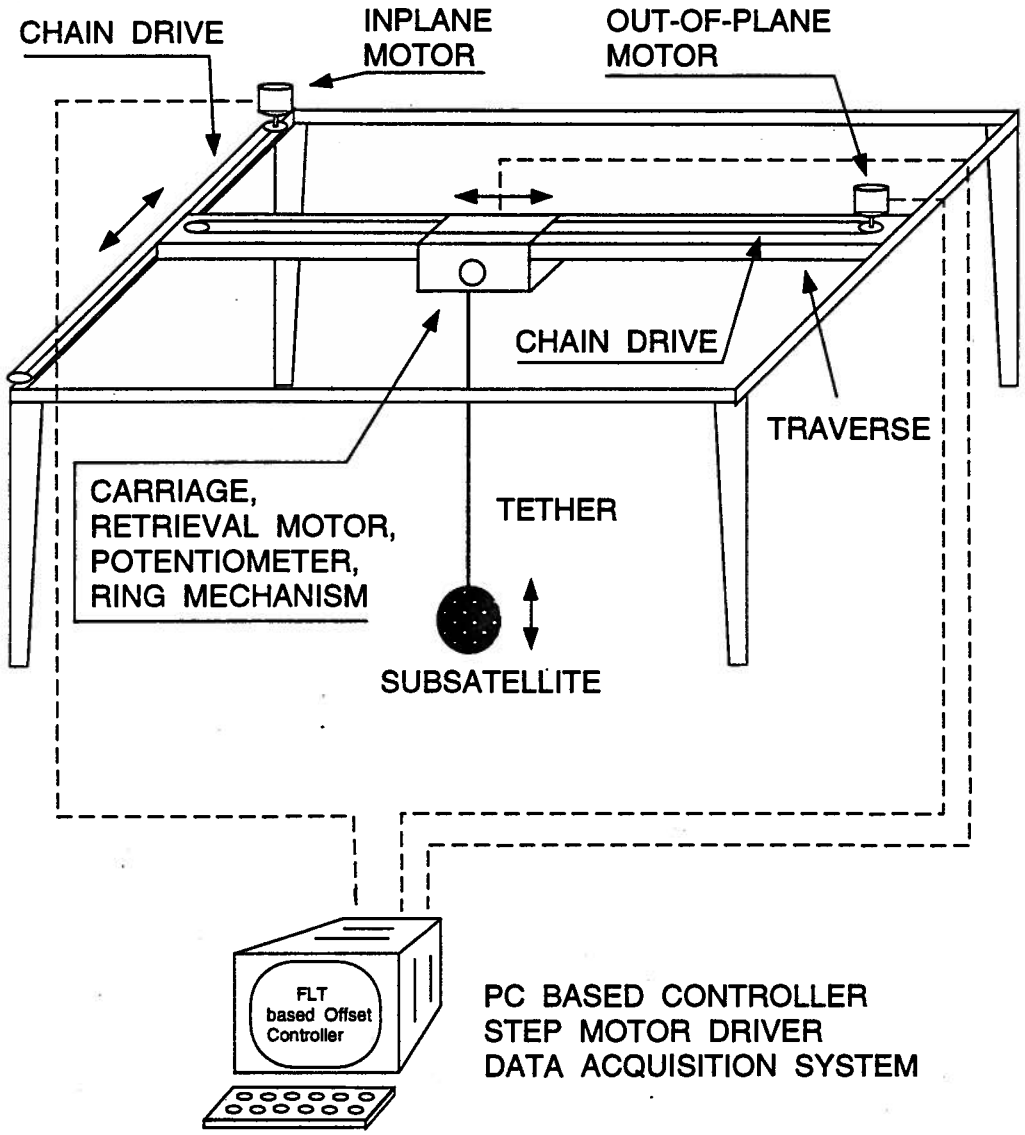

Figure 7-2 A schematic diagram of the experimental test-facility.

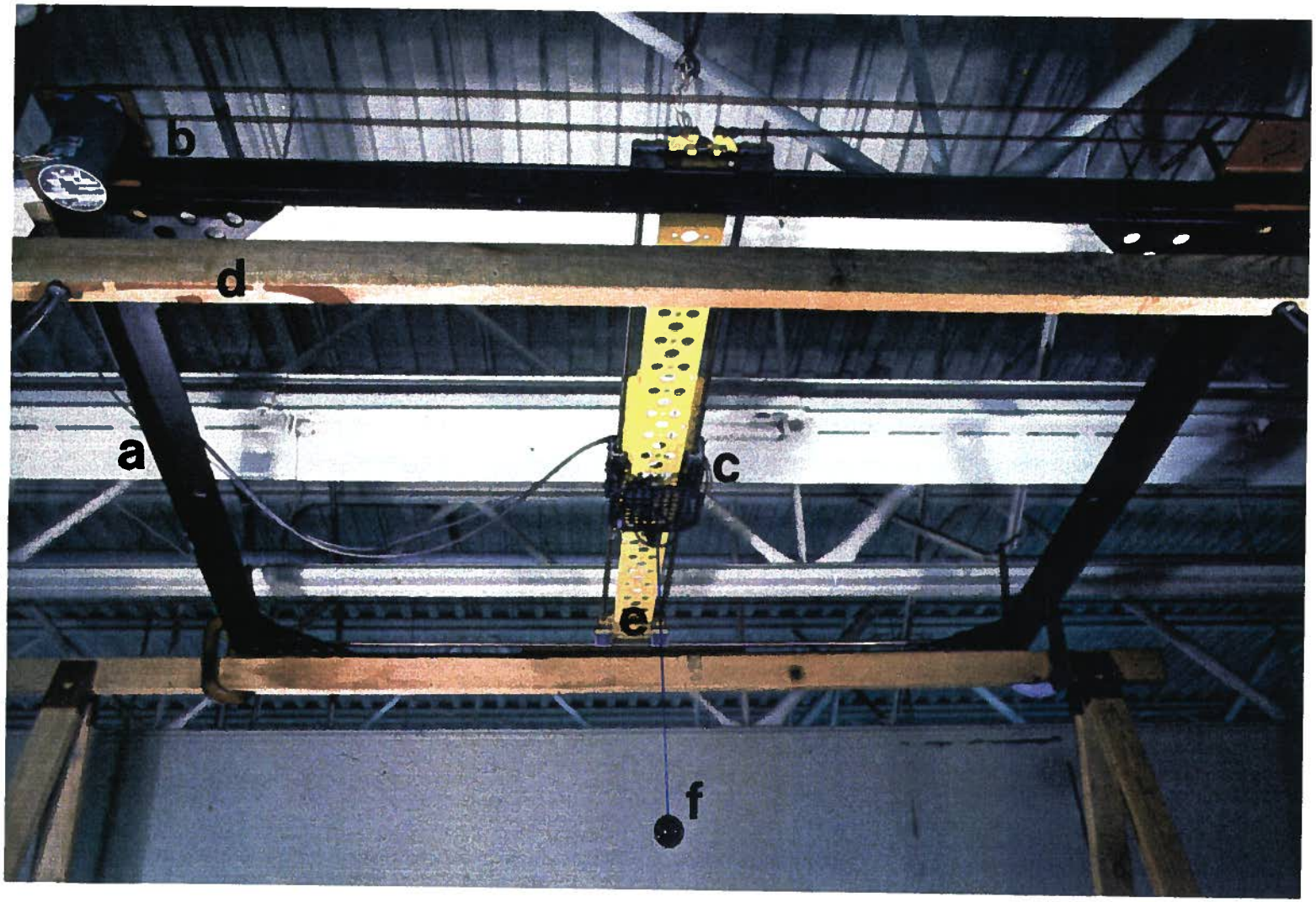

Figure 7.3 Photograph of the test-rig constructed to validate offset control strategy: (a) aluminum frame; (b) inplane motor; (c) carriage for out-of-plane motion; (d) wooden stand; (e) linear bearings; (f) tethered payload.

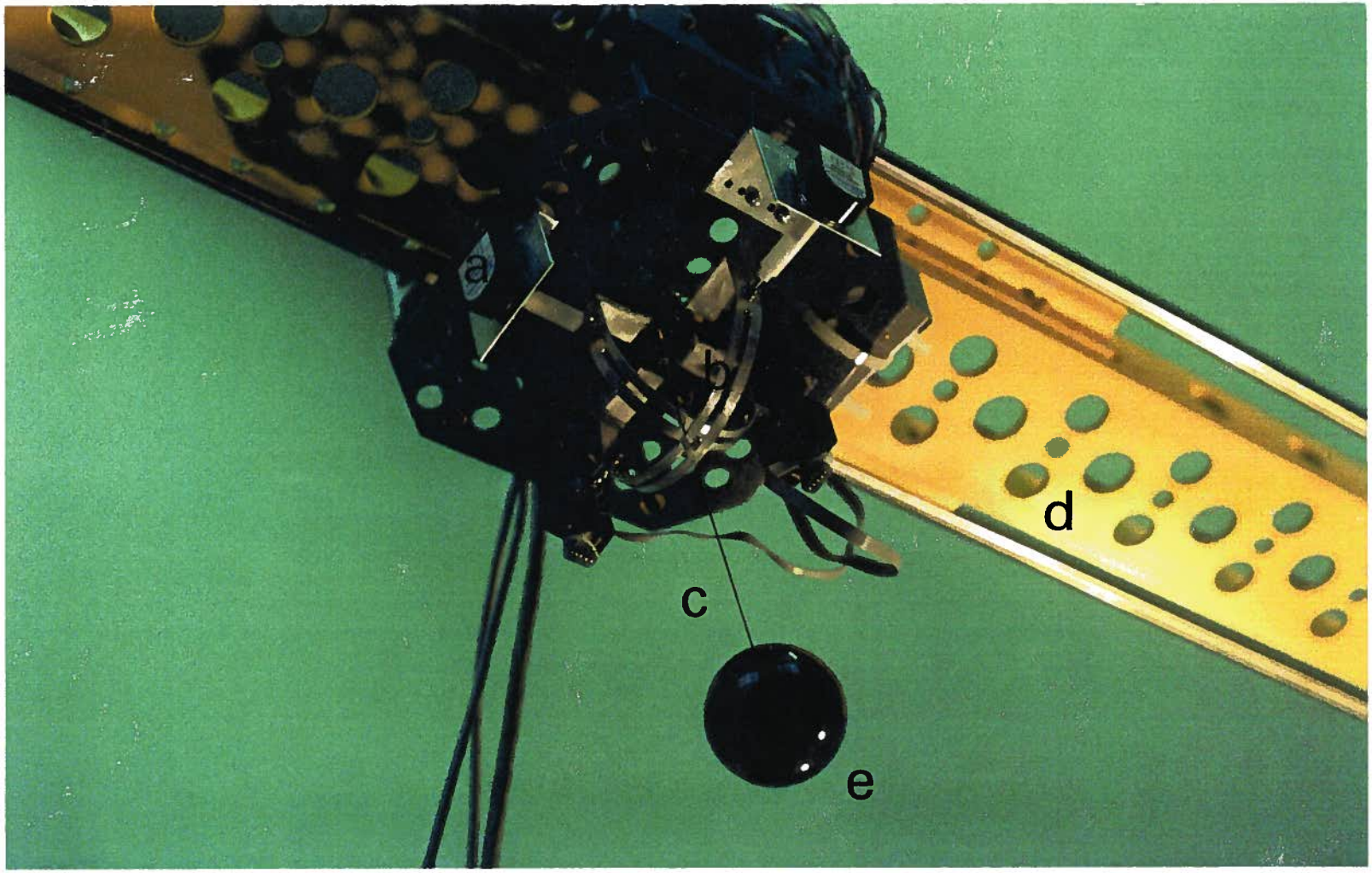

Figure 7.4 Carriage and sensor mechanism: (a) potentiometer on mounting bracket; (b) moveable aluminum semi–ring mechanism with slots for tether; (c) tether; (d) inplane traverse with linear bearings; (e) payload.

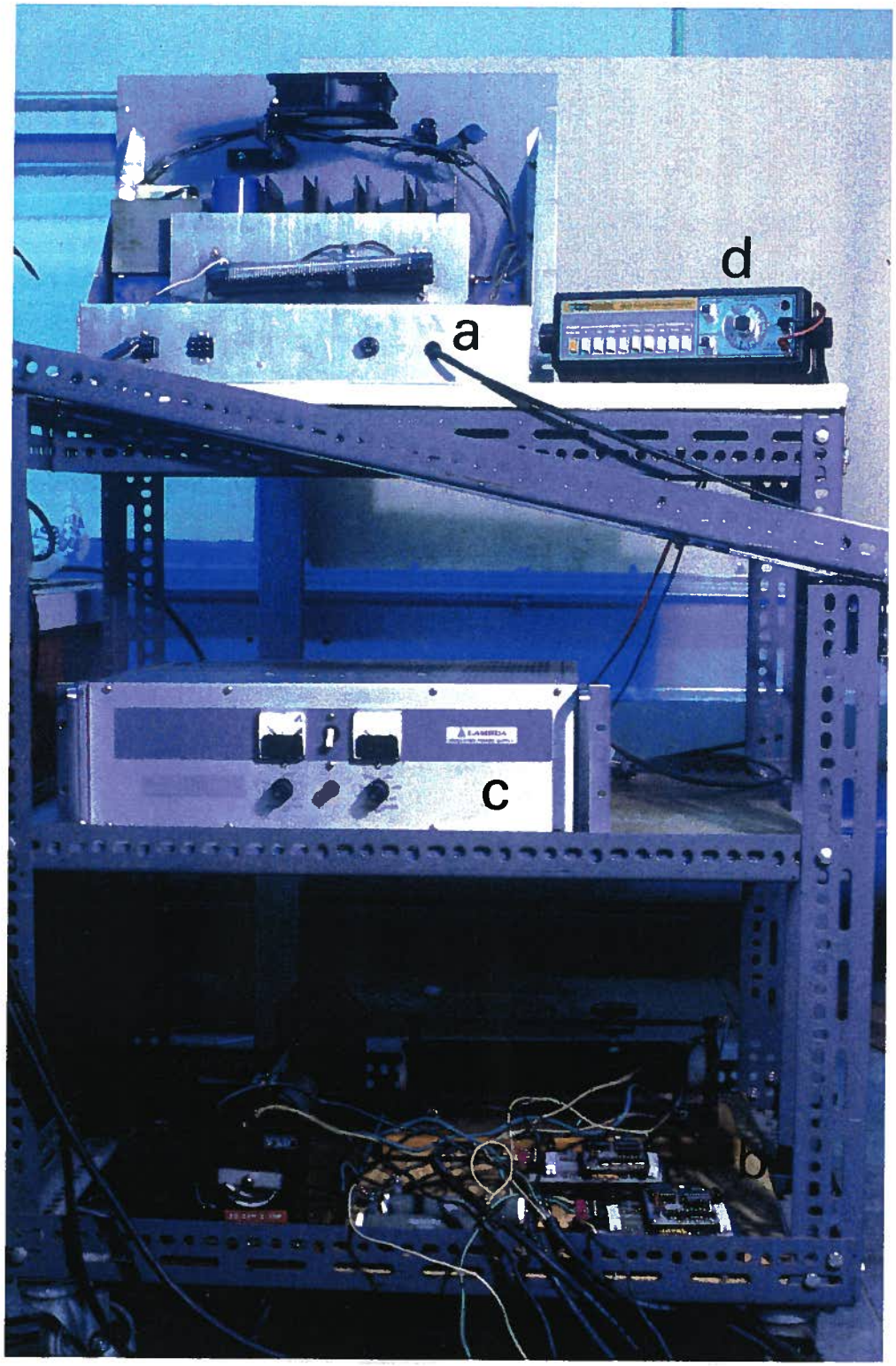

Figure 7-5 Digital hardware used in the experiment: (a) translator module, deployment and retrieval; (b) translator module, offset motions; (c) power supply; (d) function generator.

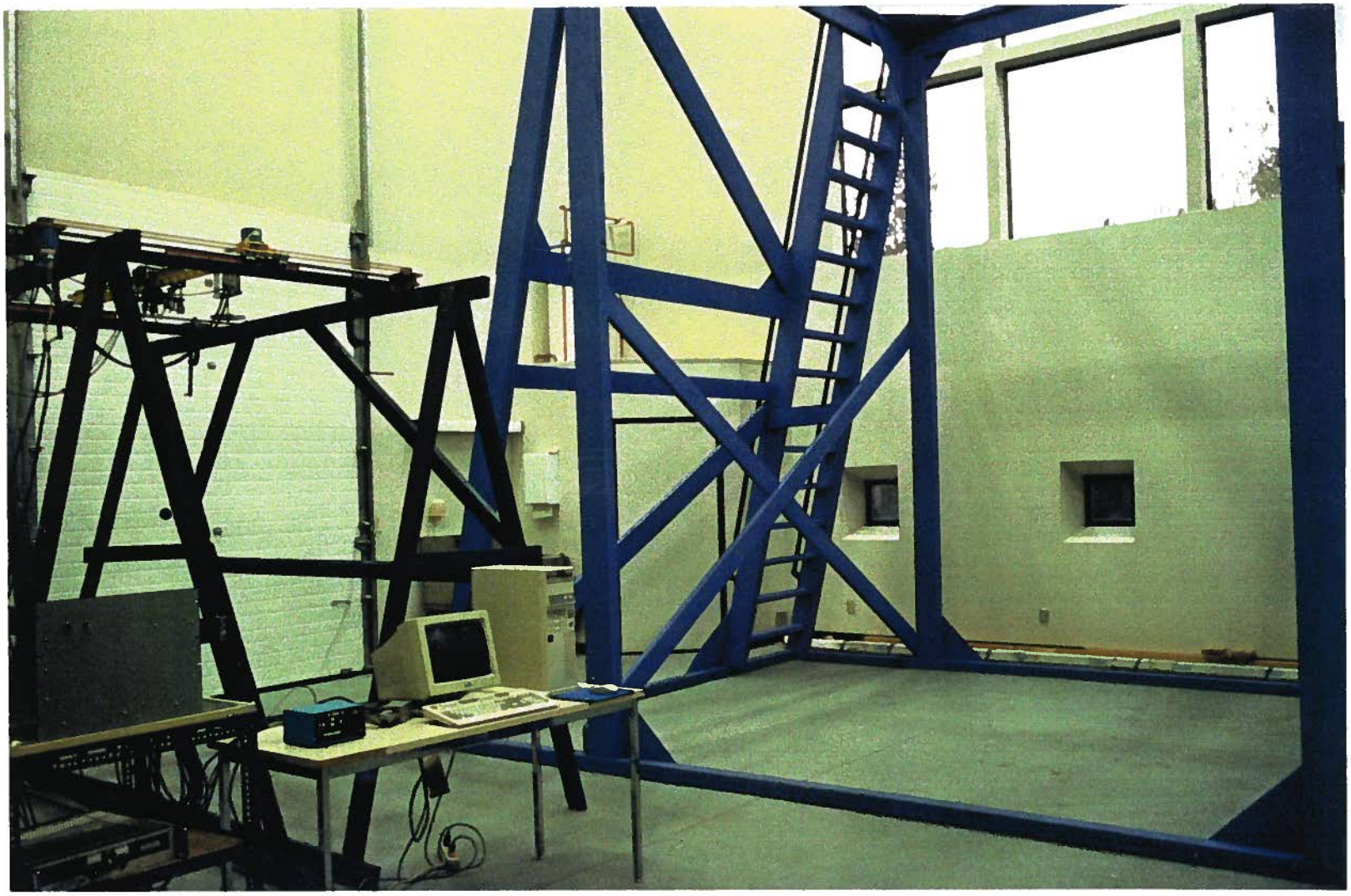

Figure 7.6 Photograph showing the recently constructed larger test–facility which can accomodate tethers upto 5 m in length. The present smaller set–up on which the experiments reported here were carried out can be seen in the foreground to the left.

7.3 Controller Design and Implementation

The equations governing dynamics of the laboratory model of the tethered satellite system were obtained. The linearized equations of motion can be written as:

$$\ddot{\alpha} = a_1\alpha + a_3\dot{\alpha} + c\ddot{d}_\alpha; \tag{7.1}$$

$$\ddot{\gamma} = a_1\gamma + a_3\dot{\gamma} + c\ddot{d}_\gamma, \tag{7.2}$$

where:

$$a_1 = -g/L; \quad a_3 = -2\dot{L}/L; \quad c = -1/L.$$

Here: L is the instantaneous tether length; g is the acceleration due to gravity; α and γ are the tether angles in two orthogonal vertical planes; and $\ddot{d}_\alpha$ and $\ddot{d}_\gamma$ are the accelerations of the offset point for controlling α and γ, respectively. The α and γ equations are independent of each other and hence the controllers can be designed separately. The controller design is based on the FLT and LQG procedures which are explained below.

7.3.1 FLT design

The procedure for the FLT controller design was outlined in Chapter 5. For the experimental model, it consists of state and control transformations:

$$z = T(x) = [t_{ij}]x; \tag{7.3}$$

$$u_t = \frac{v_t - P(x)}{Q(x)}; \tag{7.4}$$

where:

$$t_{11} = a_1c + a_3^2c;$$

$$t_{12} = -a_1 c^2 + a_3 c;$$

$$t_{13} = -a_3 c;$$

$$t_{14} = a_3 c^2;$$

and for $i = 2, 3, 4$

$$t_{i1} = a_1 t_{(i-1)3};$$

$$t_{i2} = 0;$$

$$t_{i3} = t_{(i-1)1} + a_3 t_{(i-1)3};$$

$$t_{i4} = t_{(i-1)2};$$

$$P(x) = a_1 t_{43} x_1 + a_2 t_{43} x_2 + (t_{41} + a_3 t_{43}) x_3 + (t_{42} + a_4 t_{43}) x_4;$$

$$Q(x) = c t_{43} + t_{44}.$$

The secondary controller, v_t, for the system is designed to place the closed loop eigenvalues at some desired locations. This leads to the following expression for v_t

$$v_t = k_{t_1}(z_1 - z_{1_d}) + k_{t_2}(z_2 - z_{2_d}) + k_{t_3}(z_3 - z_{3_d}) + k_{t_4}(z_4 - z_{4_d}), \qquad (7.5)$$

where: k_{t_i} and z_{i_d}, $i = 1, \cdots, 4$, are the coefficients of the required closed loop polynomial and the desired values for z_i, respectively.

Controllers for α and γ degrees of freedom are designed by considering x as $\{\alpha,\ d_\alpha,\ \dot{\alpha},\ \dot{d}_\alpha\}^T$ and $\{\gamma,\ d_\gamma,\ \dot{\gamma},\ \dot{d}_\gamma\}^T$, with u_t as $\ddot{d}_\alpha$ and $\ddot{d}_\gamma$, respectively. The coefficients of the desired closed loop polynomials correspond to rise–times of 0.5 and 0.6 s for tether and offset motions, respectively, and settling–times of 3.0 s for both the tether and offset motions.

7.3.2 LQG design

Considering the dynamics of α, the linear equations for the LQG controller design can be written as:

$$\dot{x}_\alpha = A_\alpha x_\alpha + b_\alpha u_\alpha; \tag{7.6a}$$

$$y_\alpha = C_\alpha x_\alpha, \tag{7.6b}$$

where:

$$x_\alpha = \{\alpha \;\; d_\alpha \;\; \dot{\alpha} \;\; \dot{d}_\alpha\}^T;$$

$$u_\alpha = \ddot{d}_\alpha;$$

$$A_\alpha = \begin{bmatrix} 0 & 0 & 1 & 0 \\ 0 & 0 & 0 & 1 \\ a_1 & 0 & a_3 & 0 \\ 0 & 0 & 0 & 0 \end{bmatrix}; \qquad b_\alpha = \begin{Bmatrix} 0 \\ 0 \\ c \\ 1 \end{Bmatrix};$$

$$y_\alpha = \{\alpha \;\; d_\alpha\}^T;$$

$$C_\alpha = \begin{bmatrix} 1 & 0 & 0 & 0 \\ 0 & 1 & 0 & 0 \end{bmatrix}.$$

The controller design (i.e. LQR gains and KBF matrices) is arrived at using the subprograms available in MATLAB. The weighting matrices considered in the design are:

$$Q = \begin{bmatrix} 50.0 & 0 & 0 & 0 \\ 0 & 2.0 & 0 & 0 \\ 0 & 0 & 1.0 & 0 \\ 0 & 0 & 0 & 0.1 \end{bmatrix}; \quad R = 1.0;$$

$$\Xi = \begin{bmatrix} 30.0 & 0 & 0 & 0 \\ 0 & 1.0 & 0 & 0 \\ 0 & 0 & 100.0 & 0 \\ 0 & 0 & 0 & 100.0 \end{bmatrix}; \quad \text{and} \quad \Theta = \begin{bmatrix} 1.0 & 0 \\ 0 & 1.0 \end{bmatrix}.$$

The continuous time LQG controller is implemented as a sampled data system. To that end, the dynamic controller equation is transformed into the discrete model,

which can be expressed as:

$$x_{f\alpha}(k+1) = A_{f\alpha}x_{f\alpha}(k) + B_{f\alpha}y_{\alpha}(k); \tag{7.7a}$$

$$u_{\alpha}(k) = C_{f\alpha}x_{f\alpha}(k). \tag{7.7b}$$

For $L = 1\ m$; $\dot{L} = 0$; and a sample time of $0.09\ s$, the controller matrices are:

$$A_{f\alpha} = \begin{bmatrix} 0.52214 & 0.00177 & 0.06212 & 0.00639 \\ 0.01194 & 0.62945 & 0.00585 & 0.06604 \\ -1.17623 & 0.01768 & 0.81021 & 0.15977 \\ 0.22942 & -0.74557 & 0.14336 & 0.80424 \end{bmatrix};$$

$$B_{f\alpha} = \begin{bmatrix} 0.43029 & 0.00243 \\ 0.00341 & 0.36614 \\ -0.03394 & 0.08718 \\ 0.11417 & 0.64020 \end{bmatrix}; \text{ and}$$

$$C_{f\alpha} = [5.49377 \quad -1.41421 \quad 1.73788 \quad -2.12424].$$

The controller for regulating γ is designed in a simillar way and leads to exactly the same design.

7.3.3 Controller implementation

The two controllers were implemented as sampled data systems with the zero order hold. The FLT compensator is described by algebraic equations. Therefore, the control inputs can be computed by Eqs.(7.3-7.5) at the sampling point. The LQG control inputs are calculated by the discrete time model given in Eq.(7.7).

As pointed out before, in the present experimental setup, stepper motors are used to move the tether attachment point. These motors are commanded to move to a specified position by providing required number of pulses in each time–step. Therefore, the acceleration requirement, i.e. the control input, is converted into a displacement requirement. The displacement can easily be converted into the num-

ber of pulses required, from the knowledge of pulses per revolution and parameters of the transmission mechanism (chain drive in the present case). The conversion of acceleration requirement to displacement is accomplished by integrating the acceleration profile, which is considered constant over a time–step. This leads to:

$$\dot{d}_\alpha(k+1) = \dot{d}_\alpha(k) + \ddot{d}_\alpha(k)\Delta t; \tag{7.8a}$$

$$d_\alpha(k+1) = d_\alpha(k) + \dot{d}_\alpha(k)\Delta t + \frac{1}{2}\ddot{d}_\alpha(k)(\Delta t)^2, \tag{7.8b}$$

where: $\dot{d}_\alpha(k)$ and $d_\alpha(k)$ are the magnitudes of $\dot{d}_\alpha$ and d_α at the k^{th} sampling point, respectively; and Δt is the sampling period.

In case of the LQG controller, the control input $\ddot{d}_\alpha(k)$ is directly computed from the knowledge of the system outputs $\alpha(k)$ and $d_\alpha(k)$. In the present study, $\alpha(k)$ is measured directly by the potentiometers and $d_\alpha(k)$ is obtained from Eq.(7.8b). For the FLT controller, in addition to these outputs, magnitudes of $\dot{\alpha}(k)$ and $\dot{d}_\alpha(k)$ are required. $\dot{d}_\alpha(k)$ can be computed using Eq.(7.8a). Since no sensor is used to measure $\dot{\alpha}$, backward finite difference method is used for its evaluation, i.e.

$$\dot{\alpha}(k) = \frac{\alpha(k) - \alpha(k-1)}{\Delta t}. \tag{7.9}$$

As the equations of motion for α and γ degrees of freedom are identical in form, the γ-controller can be implemented using exactly the same procedure.

The next important step in the controller implementation is the selection of the sampling time Δt. It has to be sufficiently large so that the computations required in the control loop can be completed in the time–step. In the present setup, the time required to complete a control loop, i.e. to perform sensing, computation, actuation and data storage is less than 5 ms. The sampling rate is based on the requirement that the sampling frequency should be higher than the Nyquist frequency.

For better performance of the system, the sampling time should be less than one sixth of the minimum period of the system [109], which is 1.45 s in the present case. From these considerations, the sampling time (Δt) is taken to be 90 ms.

The computer program to implement the controller was written in MicroSoft C language. The real time implementation starts with initialization of the system parameters and special purpose computer cards, and calibration of the potentiometers for reference vertical position. Application of a disturbance activates the control loop. Each loop consists of measurement of the angles; computation of the offset position, velocity and acceleration; checking the steady state and safety conditions; commanding the motors to move; writing the data into the output file; and updating the variables for the next time–step. The controller operation can be stopped by pressing an arbitrary key at any time. This can be used for emergency exit of the controller. The flow chart for the controller operation is shown in Figure 7-7.

7.4 Results and Discussion

The experimental validation of the offset strategy in conjunction with the FLT and LQG controllers provided considerable insight into the feasibility of the approach. The concept of controlling the attitude motion of a tether, using offset acceleration as the input, augmenting the tether dynamical equations with the identity $\ddot{d}_\alpha = u$, and providing both angle and offset variable feedback proved to be feasible. Small discrepancies observed between the experimental and numerical simulation results may be attributed to the following factors:

- Damping effects can not be completely eliminated in a real system. Here the contributions come from friction in the sensing mechanism (Figure 7-1), linear bearings of the carriage and aerodynamic effects.

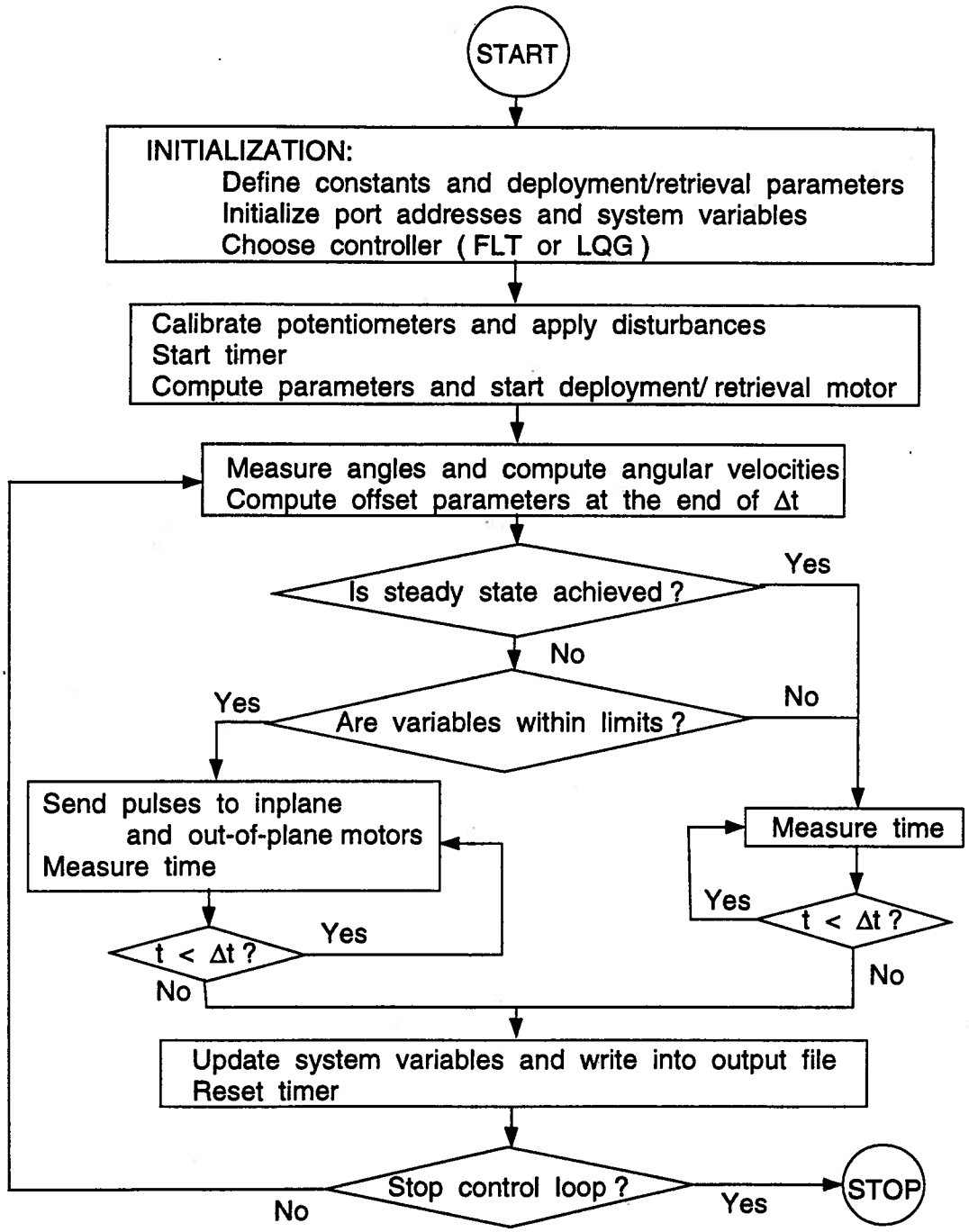

Figure 7-7 Flow chart showing the real time implementation of the attitude controller.

- The stepper motors are controlled in the open loop fashion. Therefore, any missing pulse can not be compensated by the controller.
- The step–size for the motors is 1.8^o. The required angular rotation of the motor in each time–step may not be a multiple of 1.8^o. This introduces error in the implementation of the controller.

Considerable amount of information was obtained through a series of carefully planned experiments. Only a sample of results is presented here. The system was purposely subjected to a very large disturbance of 10^o in both the directions (α and γ) to assess the controller's effectiveness under demanding situations. In practice, an external excitation would seldom result in motions larger than a few degrees. Performance of the FLT and LQG controllers is discussed in the following two subsections. The acceptable steady state error limits are set at $\pm$ 1 cm for offset positions and $\pm$ 0.5^o for the tether angles. The maximum allowable offset positions are limited to $\pm$ 20 cm.

7.4.1 FLT control

Figure 7-8(a) compares numerical and experimental results during the stationkeeping phase at a tether length of 0.5 m. The uncontrolled response is fairly well predicted by the numerical simulations, however, small attenuation is observed in the amplitude of the experimental response. As pointed out before, this may be attributed to friction in the ring mechanism used to measure the angles. Comparison of results during the controlled phase shows acceptable correlation. Note, the steady state errors are within the limits. The initial disturbance is damped within a very short time (< 4 s). The offset motions required to regulate α and γ are also within the specified limits.

Subsatellite and carriage positions during the controlled experiment are shown

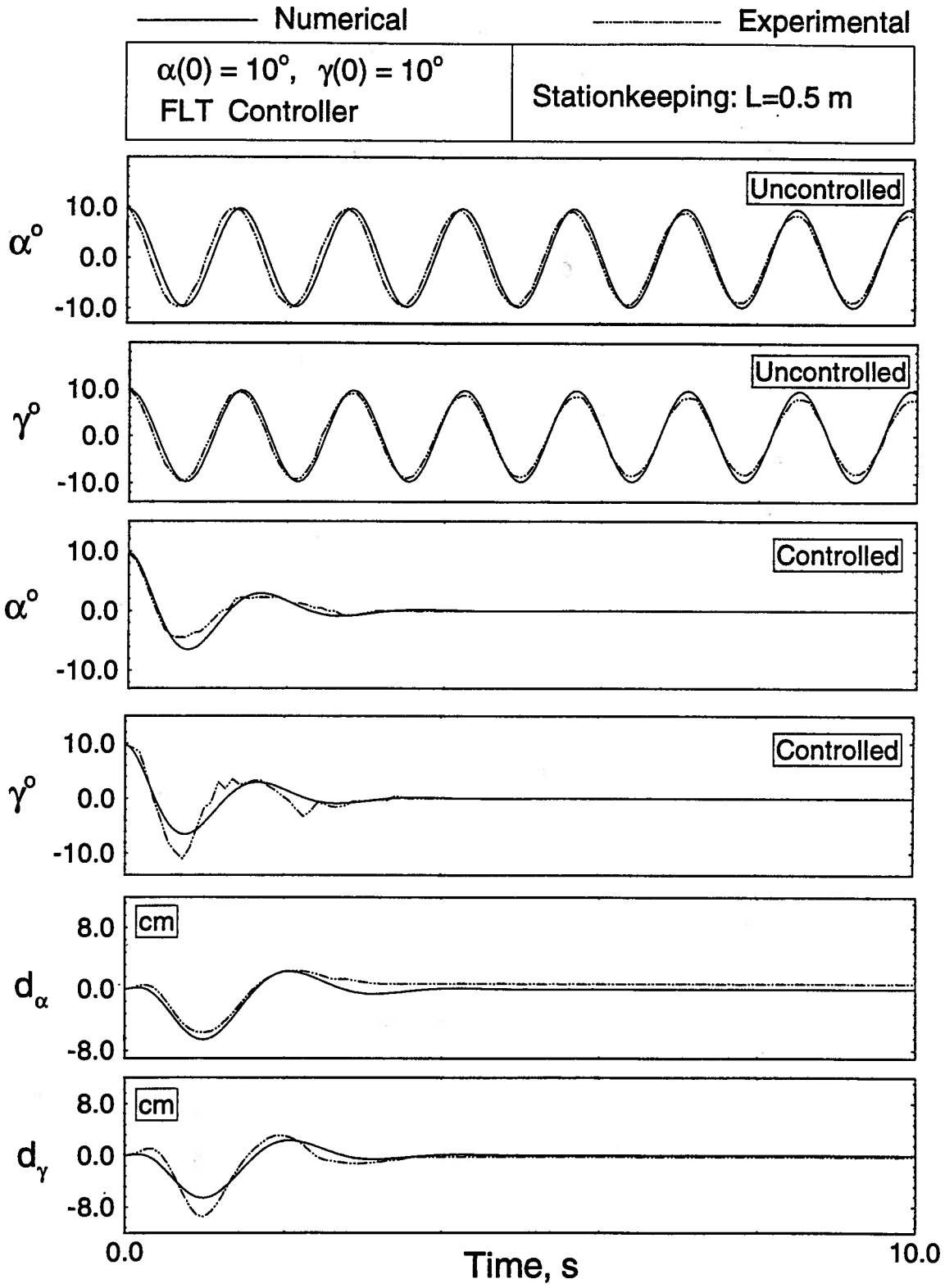

Figure 7-8 Plots showing the comparison between numerical and experimental response results during the stationkeeping phase: (a) uncontrolled and controlled system.

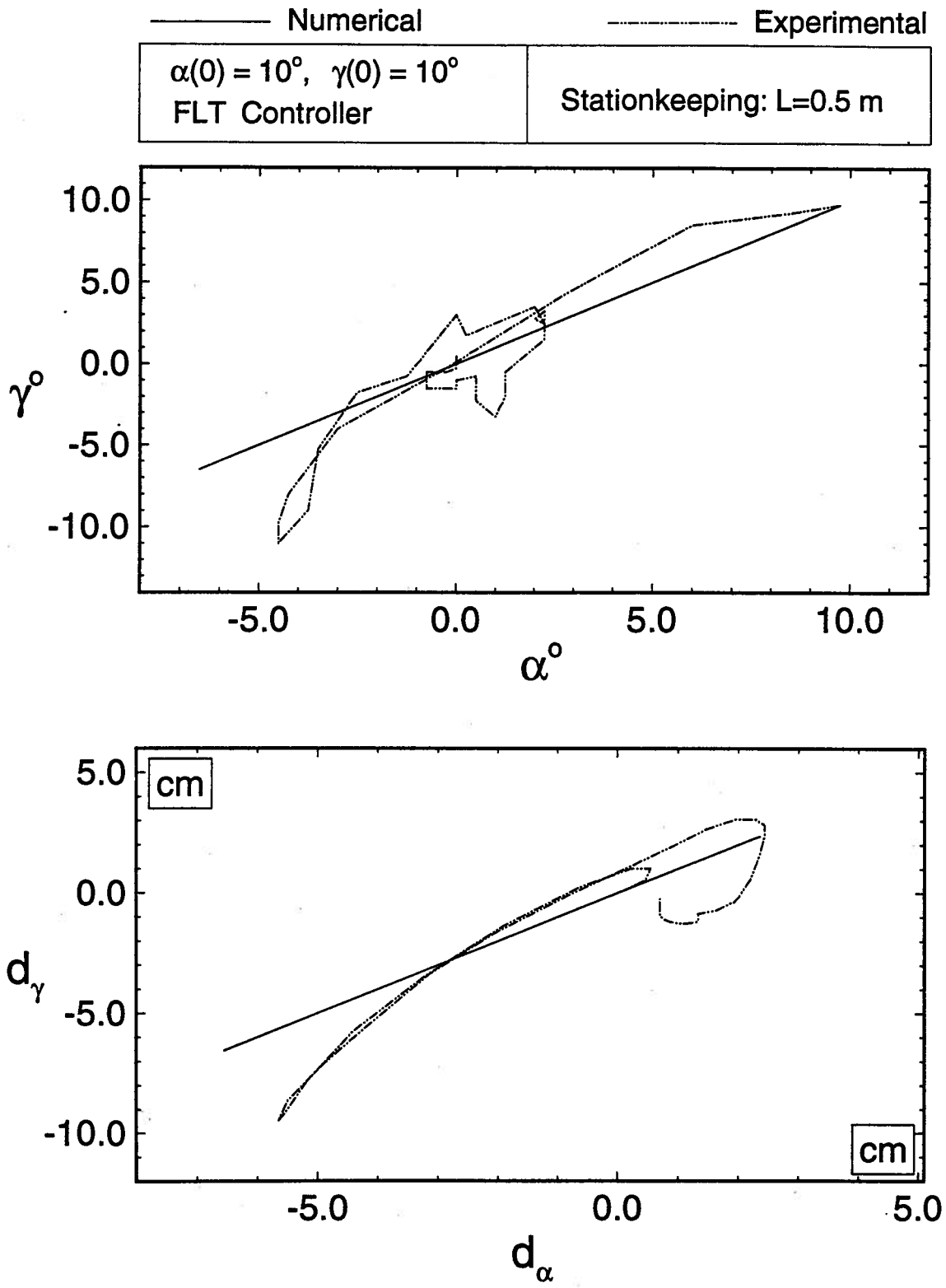

Figure 7-8 Plots showing the comparison between numerical and experimental response results during the stationkeeping phase: (b) subsatellite and carriage positions.

in Fig.7-8(b). The projection of the subsatellite position in a horizontal plane has two orthogonal components, $L \sin\alpha \cos\gamma$ and $L \sin\gamma \cos\alpha$. For small angles they may be represented, approximately, as $L\alpha$ and $L\gamma$. Therefore, γ vs. α plot represents the scaled position of the subsatellite projected on a horizontal plane. In the present simulations, disturbance is given to the angular positions only. Initially, librational velocities, as well as position and velocity of the carriage (tether attachment point)are zero. Under this situation, the subsatellite should oscillate in one plane during both the uncontrolled and controlled conditions. The numerical simulation (solid line in γ-α plot) substantiates this observation. The small discrepancy in the experimental results is again due to the sensor noise mentioned before. The plots for carriage position show similar trends.

Figure 7-9(a) shows response of the system during stationkeeping at a longer tether length of 1 m. The numerical and experimental responses for the uncontrolled as well as controlled system show excellent agreement. As expected, the frequency of angular motion is lower compared to that for $L = 0.5$ m. The offset motion required to regulate the inplane and out-of-plane librations is rather modest (within $+6$ cm and -4.5 cm). Experimental results for the subsatellite and carriage positions are quite close to the straight line predicted by the numerical simulation (Figure 7-9b). Similar trends continued even at a higher length of 2 m (Figure 7-10).

As emphasized earlier, retrieval is the most critical phase in the tether operation. To show effectiveness of the controller, two different retrieval rates are considered with maneuver completed in 15 s and 5 s. In each case, the tether length was reduced from 2 m to 0.5 m in accordance with a trapezoidal velocity profile. The velocity was linearly increased (constant acceleration) from zero to the maximum value in $0.1t_r$, held constant (zero acceleration) at the maximum value for

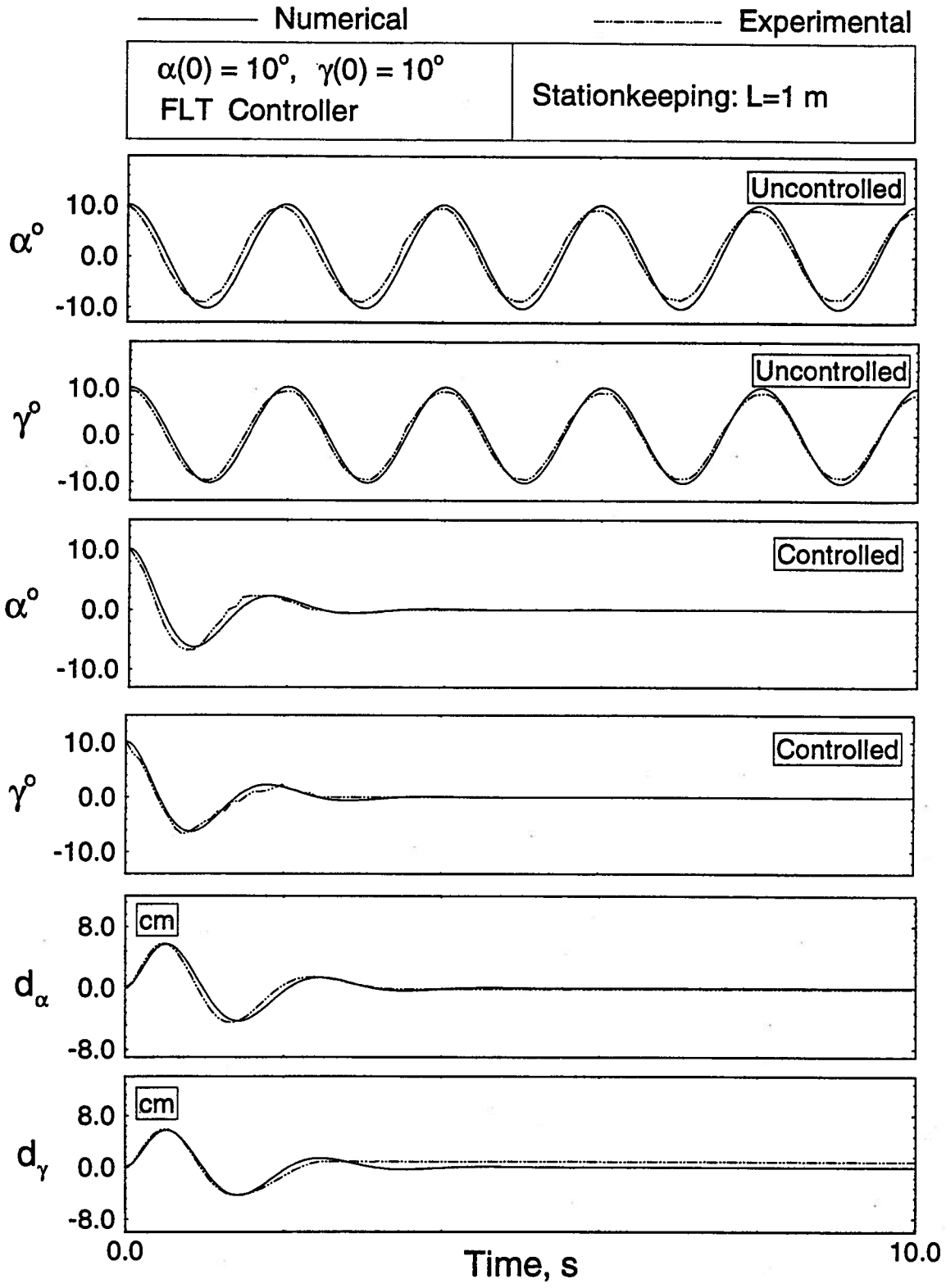

Figure 7-9 A comparative study between numerical and experimental results for the system during stationkeeping at 1 m: (a) uncontrolled and FLT controlled system.

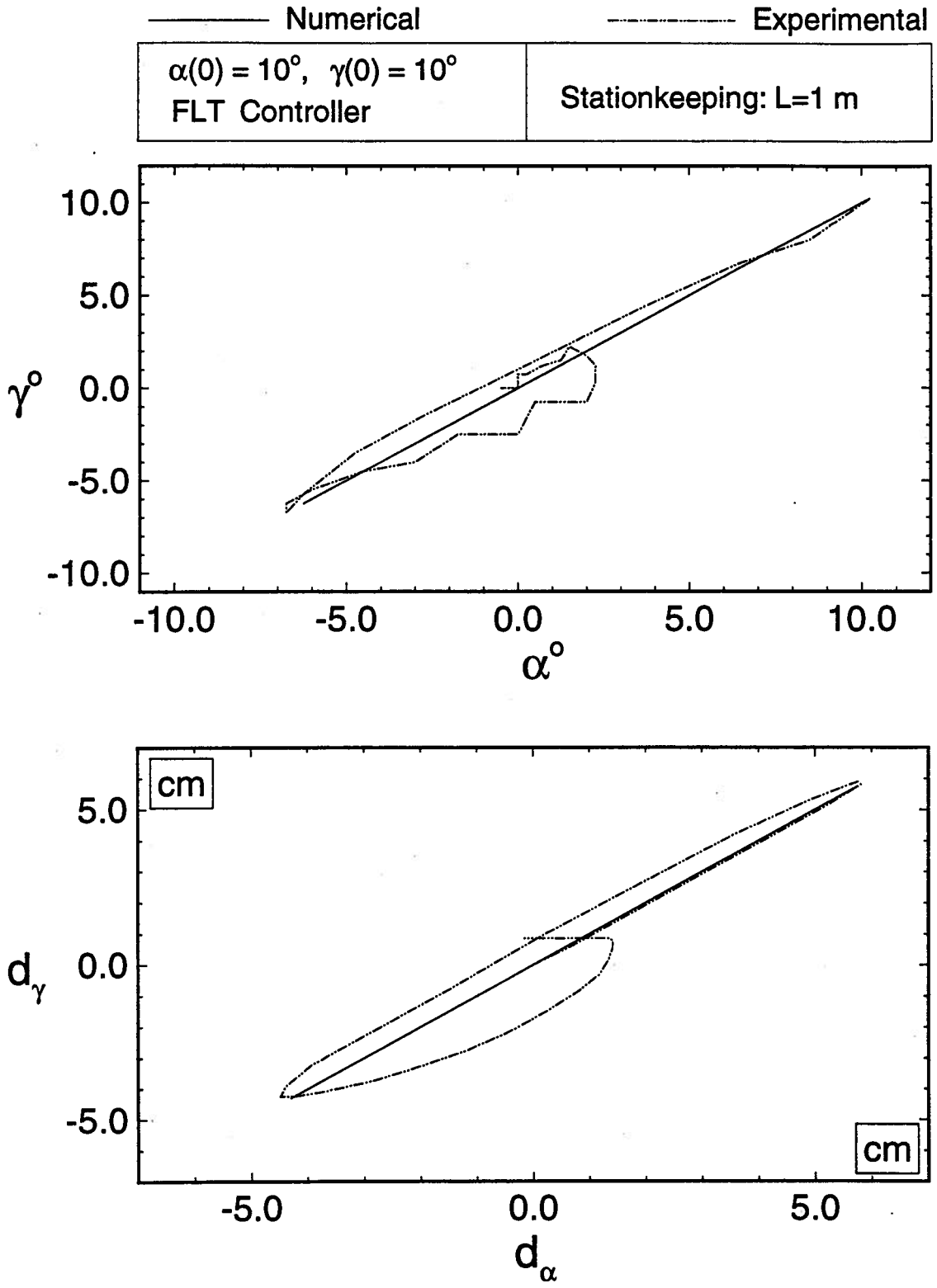

Figure 7-9 A comparative study between numerical and experimental results for the system during stationkeeping at 1 m: (b) subsatellite and carriage positions.

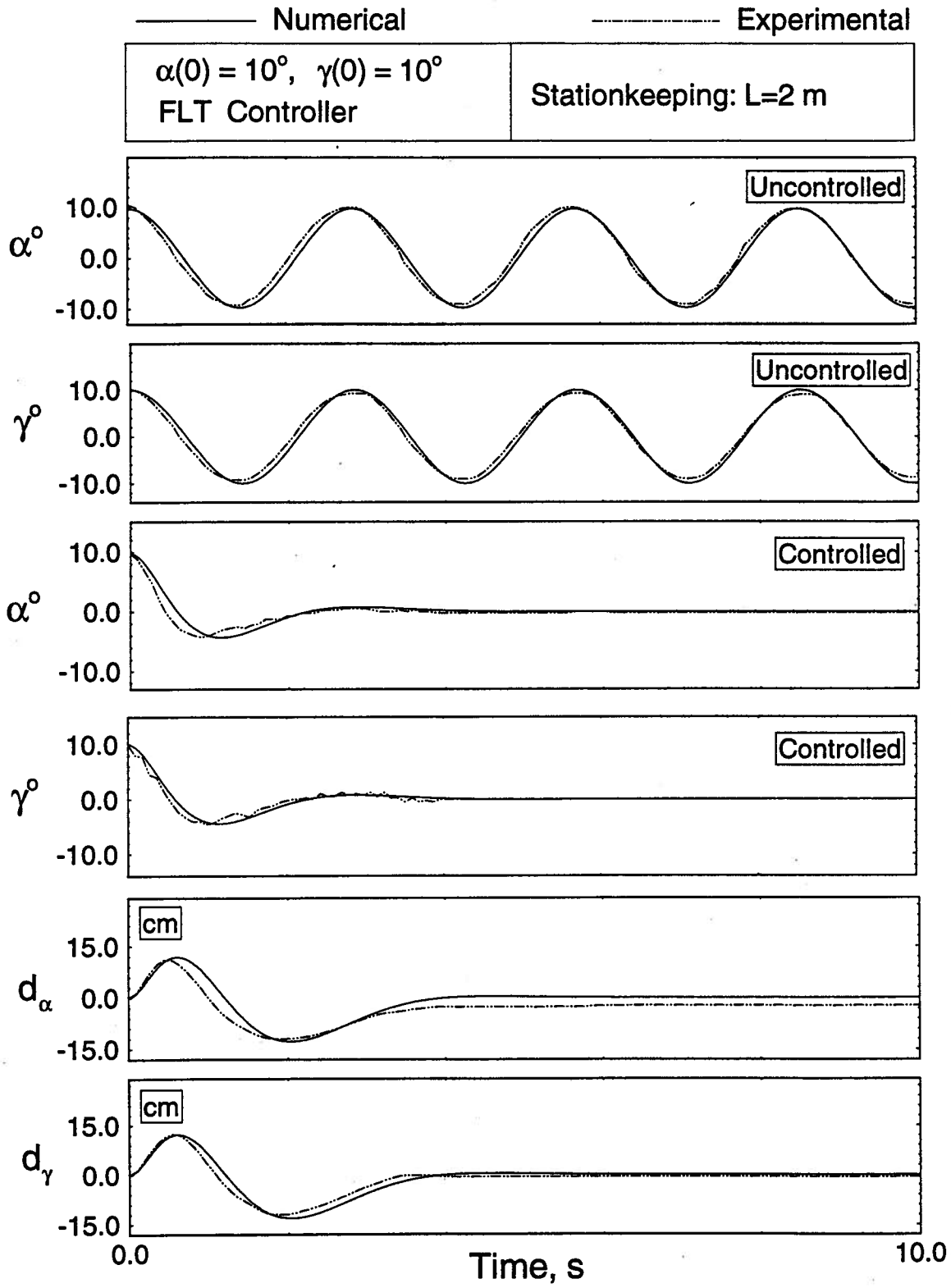

Figure 7-10 A comparative study between numerical and experimental results for the system during stationkeeping at 2 m: (a) uncontrolled and FLT controlled system.

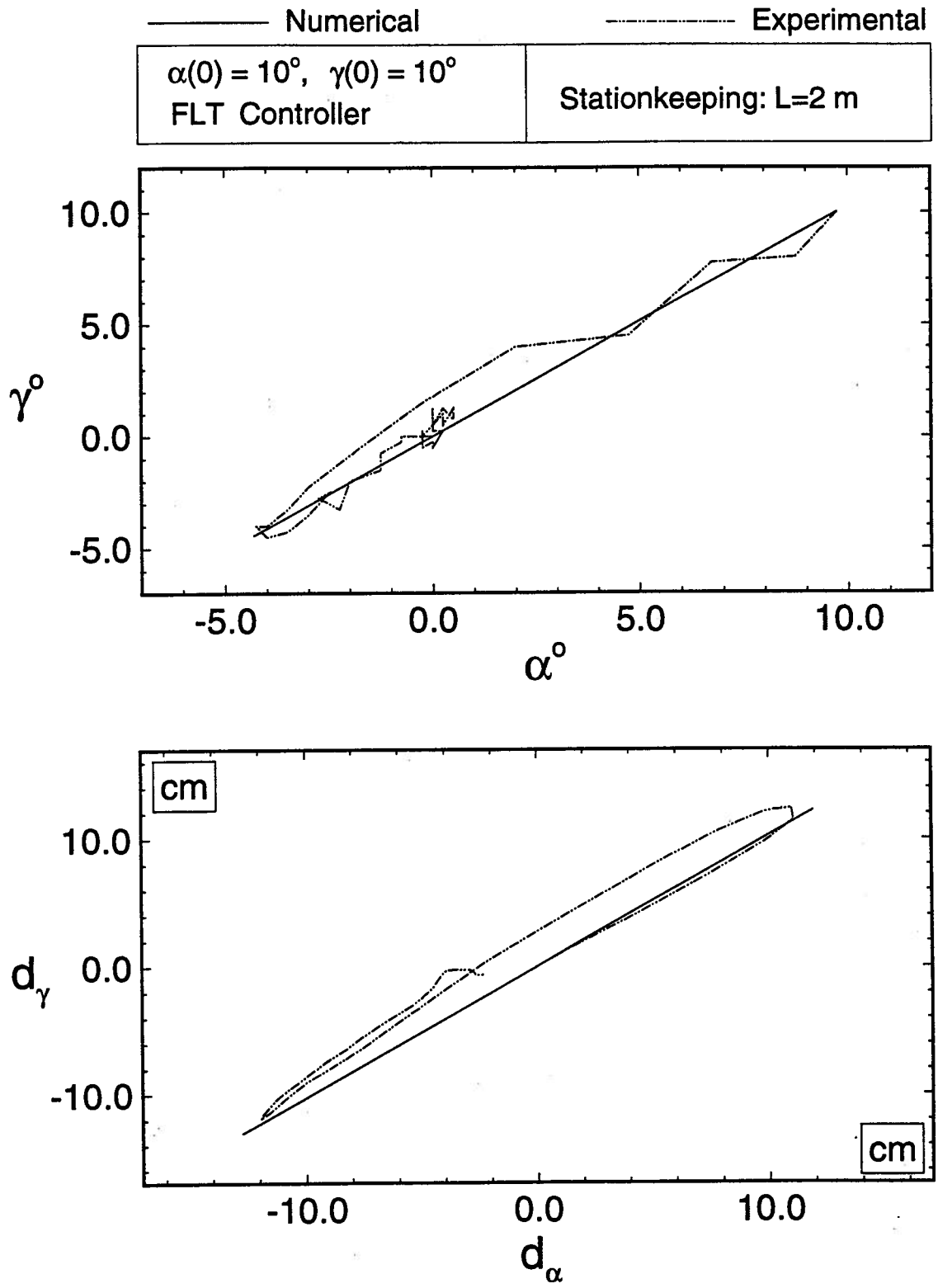

Figure 7-10 A comparative study between numerical and experimental results for the system during stationkeeping at 2 m: (b) subsatellite and carriage positions.

$0.8t_r$, and finally linearly reduced to zero in $0.1t_r$. Here t_r is the specified time to complete the retrieval. The maximum velocities are 0.11 m/s and 0.33 m/s for the retrieval times of 15 s and 5 s, respectively.

Figure 7-11(a) shows experimental response results for the retrieval completed in 15 s. As expected, with the tether length becoming smaller, inertia of the system reduces causing the tether oscillations to grow to conserve the system angular momentum. During the uncontrolled operation, the system response (α and γ) grows to a maximum amplitude of $\pm$ 29^o as the retrieval ends. Subsequently, the frictional damping causes the amplitudes to slightly diminish as expected. The offset procedure effectively controls the motion within 8 s, i.e. long before the retrieval is completed. Note, excursion of the tether attachment point is maintained within the specified limit of $\pm$ 20 cm. Even at a faster retrieval rate (t_r = 5 s), the offset strategy continues to be effective (Figure 7-11b).

7.4.2 LQG control

The offset controller, designed using the LQG algorithm (Section 7.3.2), was also implemented on the same tethered system. The uncontrolled and controlled responses, for the stationkeeping case at $L = 1m$, are compared in Figure 7-12(a). As before, the results show good agreement with the numerically predicated performance. The initial disturbance is damped within 5 s. Considering the frictional effects, the subsatellite and carriage positions also show good correlation with the numerically predicted results (Figure 7-12b).

The experimental results for the retrieval phase are presented in Figure 7-13. As before, a trapezoidal velocity profile was employed with the retrieval from 2 m to 0.5 m completed in 10 s. Instability of the uncontrolled system is shown rather dramatically. Gain scheduling was used during the retrieval phase with the gains

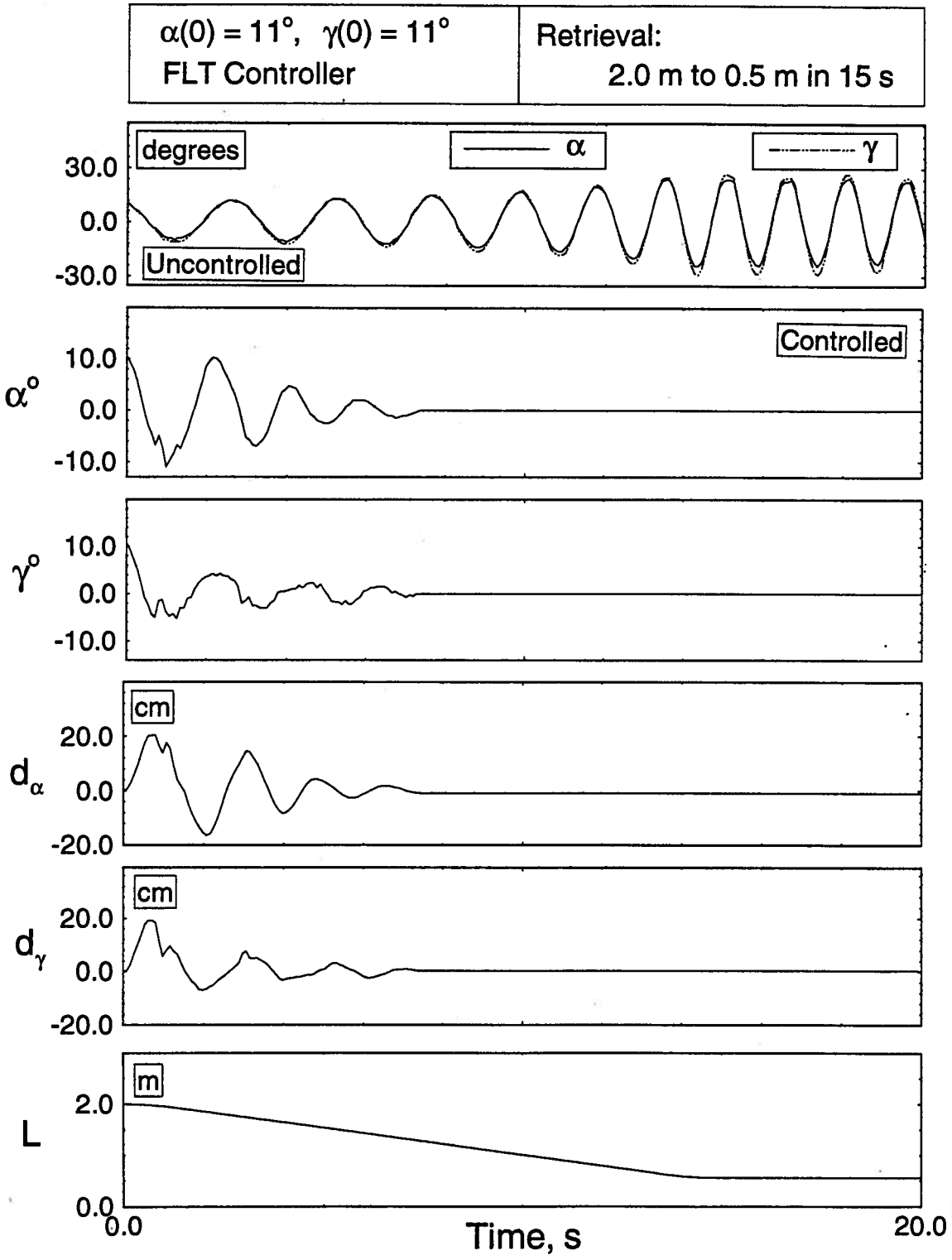

Figure 7-11 Uncontrolled and controlled experimental results for retrieval of the subsatellite: (a) retrieval time of 15s.

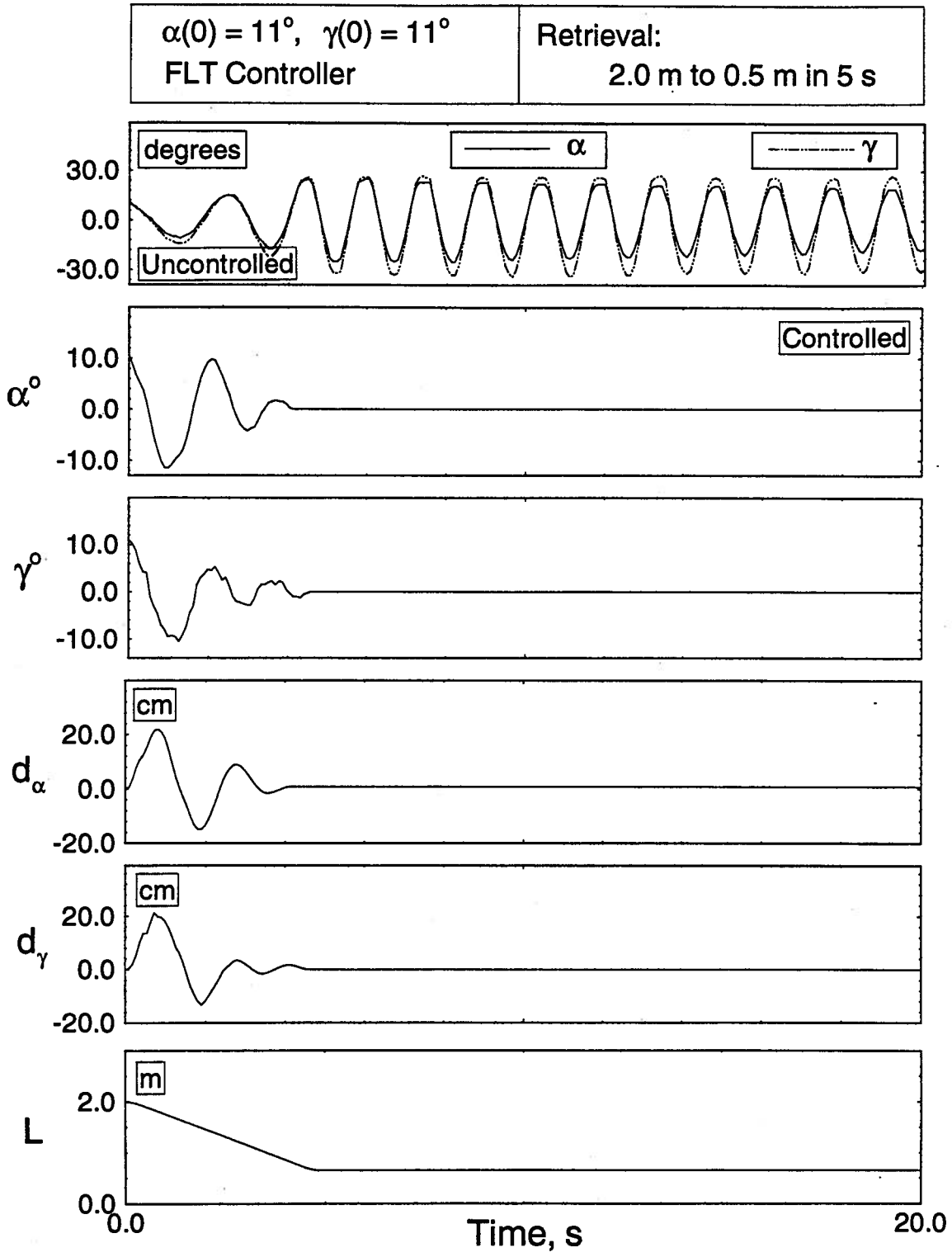

Figure 7-11 Uncontrolled and controlled experimental results for retrieval of the subsatellite: (b) faster retrieval in 5*s*.

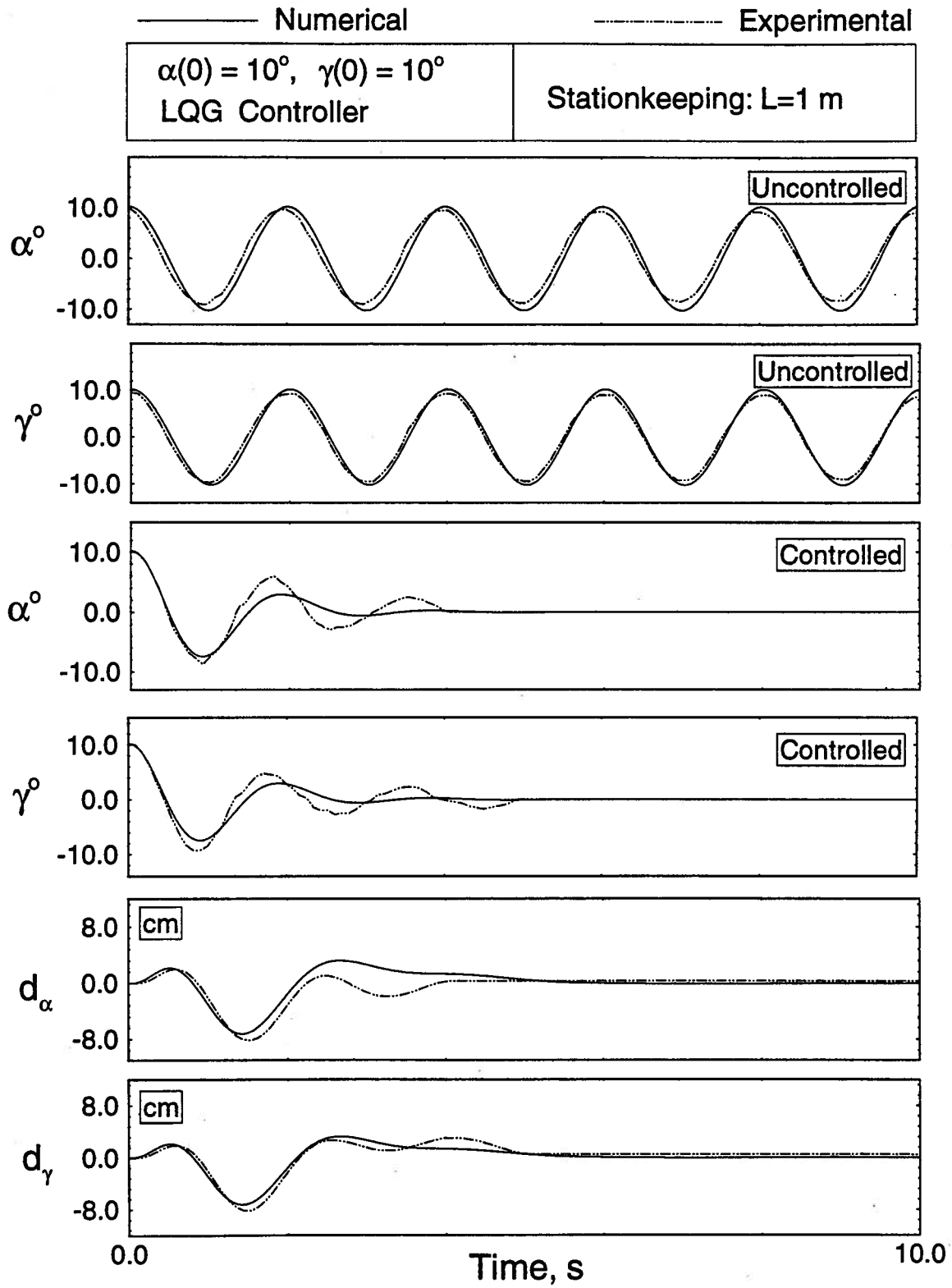

Figure 7-12 A comparative study with the LQG controller during stationkeeping at 1 m: (a) uncontrolled and controlled performance.

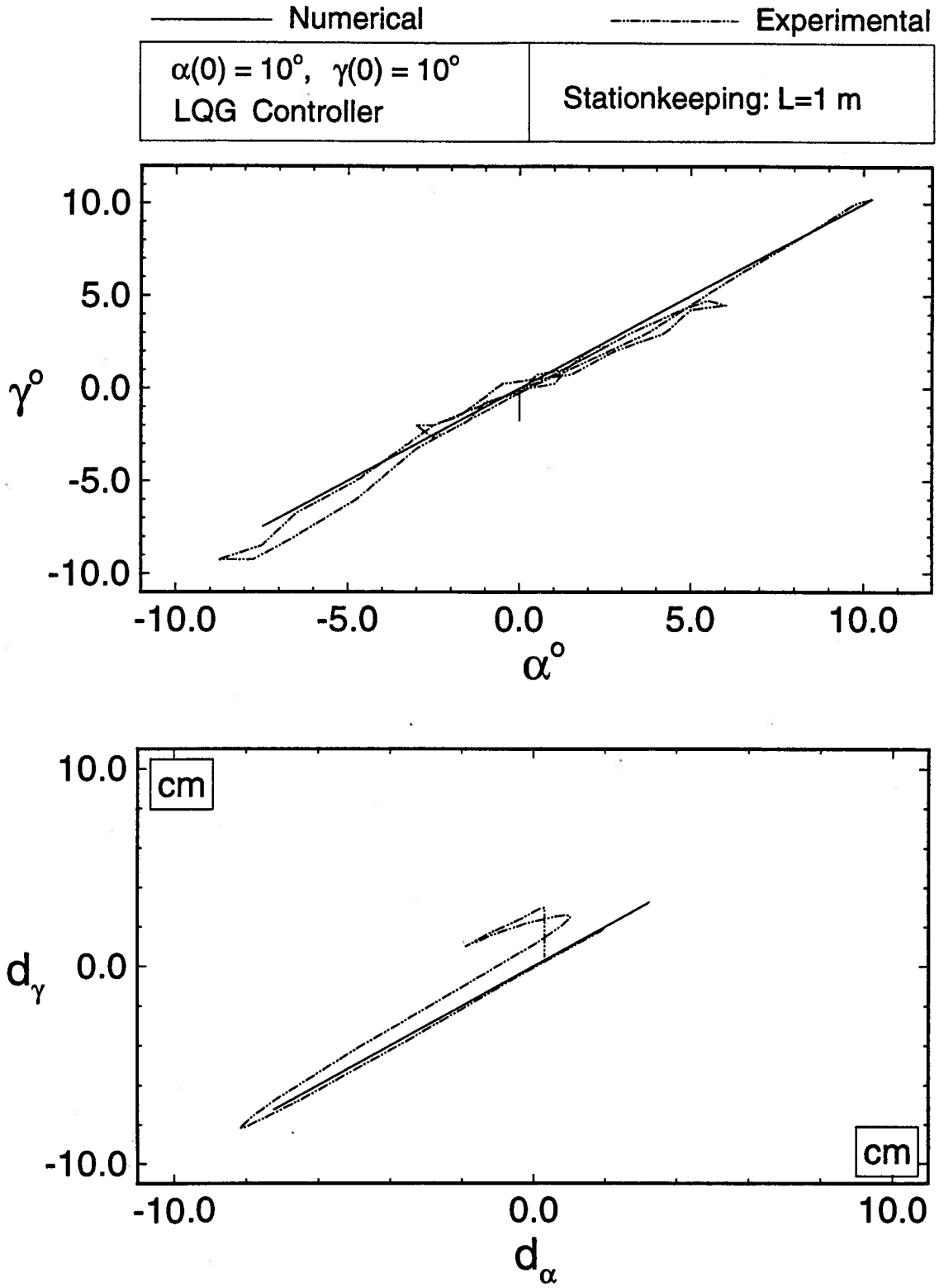

Figure 7-12 A comparative study with the LQG controller during stationkeeping at 1 m: (b) subsatellite and the tether attachment point positions.

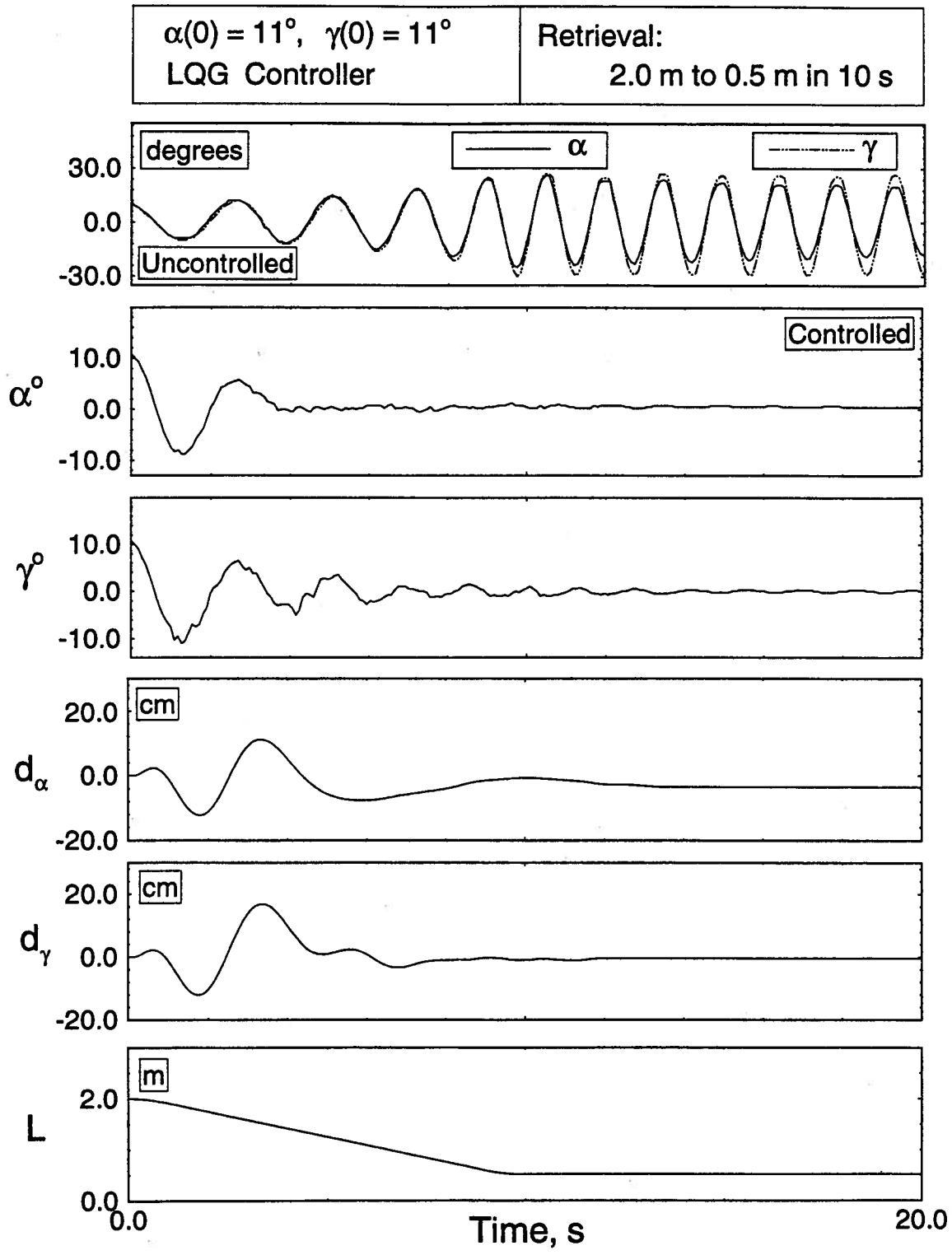

Figure 7-13 Experimentally observed system response during retrieval with the LQG controller.

adjusted at 0.75 m and 1.5 m. The LQG controller is quite successful in regulating such a large initial disturbance within 12 s. The steady state errors are less than 5 % of the initial disturbance for the angles and less than $\pm$ 1 cm for the offset position.

Finally, performance of the LQG controller in regulating the spherical pendulum type motion was evaluated (Figure 7-14). This required application of a rather severe set of initial disturbances both to the angular velocity and position. The controller continues to be remarkably effective as shown by the inward spiral motion. The corresponding carriage position also converges to the steady state value. The time to damp the disturbance was found to be around 15 s.

A video of the experimental set–up, presenting in some detail the sensor, actuator and the controller, was taken. It shows, rather dramatically, effectiveness of the offset control strategy in damping a variety of severe disturbances.

7.5 Concluding Remarks

Experiments carried out employing a unique ground based test–facility suggests that the offset control strategy, using the FLT as well as LQG algorithms, can effectively damp rather severe disturbances during both stationkeeping and retrieval phases. The controllers continue to be effective even during a faster retrieval rate of 0.33 m/s. Note, the above mentioned performance is attained within the specified limit of the offset motion. Correlation between the experimental and the numerically predicted results is also good considering the frictional effects encountered in the real-life situation. A video captures, quite effectively, the remarkable performance of the offset control procedure.

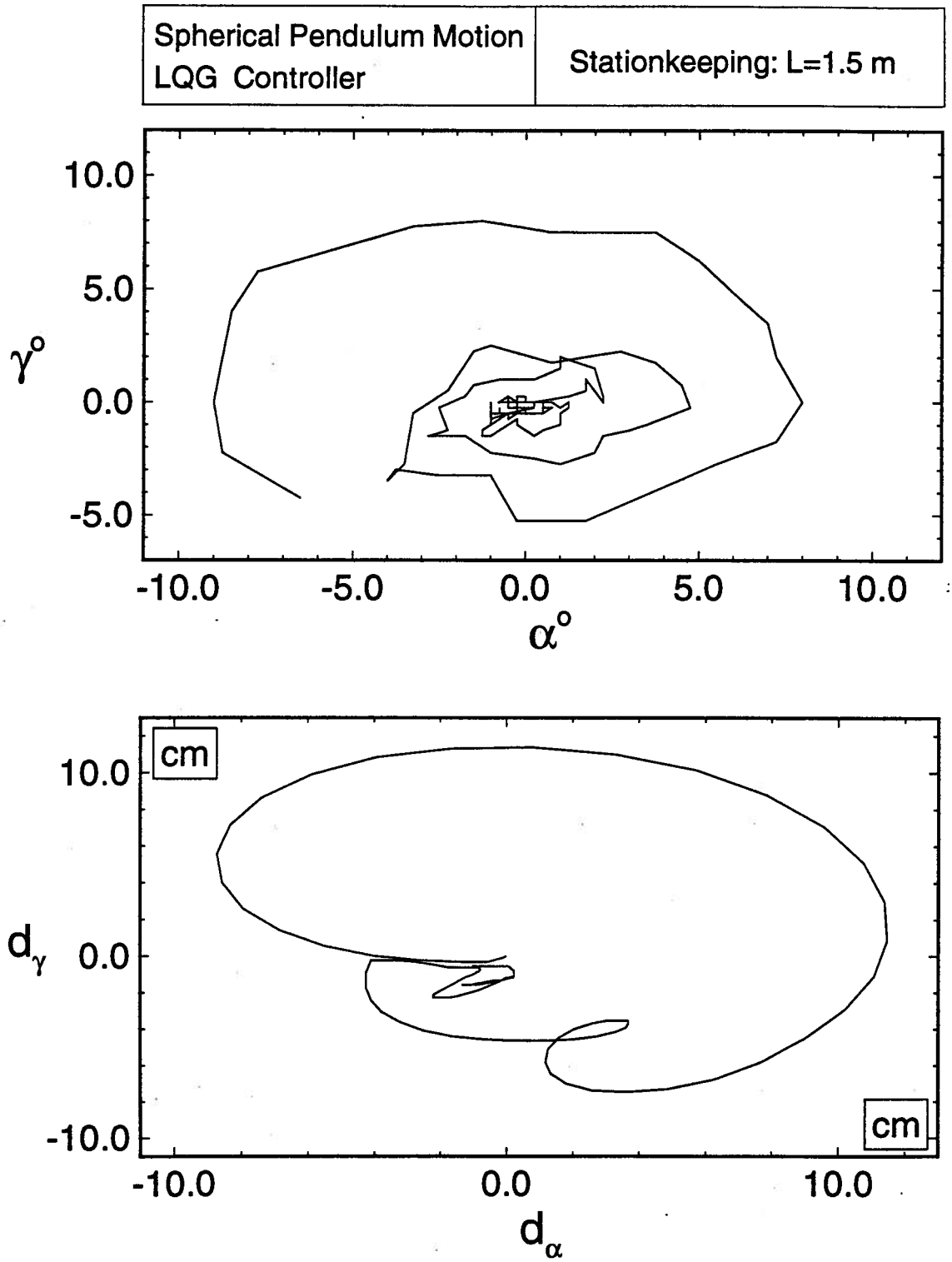

Figure 7-14 Subsatellite and carriage positions during control of the spherical pendulum using the LQG regulator.

8. CLOSING COMMENTS

8.1 Concluding Remarks

Using a relatively general model, the thesis develops a methodology and associated computational tools for studying planar dynamics and control of tethered satellite systems. Versatility of the model is illustrated through its application during all the three phases of a typical mission involving deployment, stationkeeping, and retrieval. The focus is on the system control using two distinctly different types of actuators: thrusters located at the subsatellite; and movement of tether attachment at the platform. Both linear as well as nonlinear controllers, using the actuators and their hybrid combinations, are developed applying the Linear Quadratic Gaussian (LQG) regulator and the Feedback Linearization Technique (FLT). It may be recalled that the FLT accounts for the complete nonlinear dynamics of the system.

As can be expected, the governing equations of motion are highly nonlinear, nonautonomous and coupled. They were used to assess uncontrolled dynamical performance of the system as affected by the important system parameters. However, widely spaced frequency for the rigid and flexible degrees of freedom was often taken advantage of through decoupling during the controller design. Thus controllers for the rigid and flexible parts of the system were designed separately using the coupled sets of linearized equations. Of course, effectiveness of the designed controllers was assessed through their application to the original nonlinear and coupled system.

The thesis presents innovations in several areas. More important contributions of the thesis, which have not been reported in the literature, include the following:

(i) the system model that accounts for the tether flexibility and motion of the tether attachment point at the platform end;

(ii) control of the system's attitude dynamics using the offset scheme in presence of tether flexibility;

(iii) application of the Feedback Linearization Technique, which accounts for the complete nonlinear dynamics, to tethered systems;

(iv) vibration suppression along both the longitudinal and transverse directions using the offset strategy;

(v) simultaneous attitude and vibration control of the tethered systems;

(vi) ground based experiment to substantiate effectiveness of the FLT and LQG based offset control synthesis.

It should be emphasized that the objective here was to establish a methodology to understand dynamics and control of such a complex system. It was not intended to acquire large amount of information useful in the system design. Of course, such information can be generated quite readily as the dynamics and control programs are operational. Even then the amount of information obtained is rather extensive. The thesis presents only some typical results useful in establishing trends. Based on the analysis following general conclusions can be made:

(a) Offset of the tether attachment point leads to coupling between the platform and tether dynamics. The tether pitch libration significantly affects the platform dynamics, however, the effect of platform motion on the tether dynamics is relatively unsignificant.

(b) As can be expected, static deflection of the tether as well as frequency of both transverse and longitudinal oscillations are affected by the mass density and elastic properties of the tether material. Higher modes of the longitudinal vibrations have rapidly decaying characteristics due to the structural damping, which has only the second order effect on the transverse tether vibrations.

(c) The tether dynamics is susceptible to instability when the deployment/retrieval rate exceeds the critical value.

(d) The FLT based controller using the rigid nonlinear model of the system is quite successful in regulating attitude dynamics of the system with a flexible tether. The controller structure is relatively easy to implement. A single control algorithm is applicable to all the three operational phases of deployment, stationkeeping and retrieval.

(e) The FLT based controller is found to be better than linear, time invariant regulators designed using the graph theoretic approach and implemented through gain scheduling.

(f) A hybrid strategy, relying on the thruster control at longer tether lengths and the offset control for shorter tethers, appears quite promising for regulating the tether pitch libration. Results show that a pair of passive dampers can be used to control the unstable elastic degrees of freedom.

(g) Besides controlling the tether pitch motion, the offset strategy can be used to regulate, simultaneously, both longitudinal and transverse oscillations of the tether duing the stationkeeping. Results for a 20 km tether showed the controller to be remarkably effective in damping the motions with the tether offset maintained much below the specified $\pm$ 20 m limit.

(h) Substantiation as to the effectiveness of the FLT and LQG based offset control strategies using a rather unique test facility represents a significant contribution to the field. Results show that the concept of controlling the motion of a tethered payload through specification of the acceleration at the point of attachment is not only effective but can also be implemented in practice.

8.2 Recommendations for Future Work

The present thesis represents a modest contribution to the challenging field of tether system dynamics and control. There are several avenues open for future exploration which are likely to improve our understanding of the field. A few of them, more directly related to the present study, are indicated below:

(i) Extension of the present investigation to three dimensions, i.e. generalization of the model to account for inplane as well as out-of-plane dynamics represents the logical next step.

(ii) Offset control of the tether vibrations during a retrieval maneuver needs to be explored. If successful, it will make the offset strategy more attractive and versatile.

(iii) In presence of an offset along the local horizontal, the tether dynamics significantly affects the platform motion. This presents an exciting possibility of controlling the platform libration through an offset strategy. Simultaneous control of the platform and tether dynamics through offset would represent an important contribution to the field.

(iv) It would be useful to assess effect of the free molecular environment forces on the tether dynamics and control.

(v) Multibody tethers have been proposed for several scientific experiments, including monitoring of Earth's environment as in the case of Mission to Planet Earth. The present model can be extended, through a recursive formulation, to account for such configurations.

(vi) Extension of the ground based experiment to attest effectiveness of the offset strategy in controlling transverse and longitudinal oscillations of the tether would represent an important step forward.

(vii) Validation of various offset control strategies using a longer tether is desirable particularly during retrieval. It would also help study the concept of tethered elevator system. The larger facility, already constructed, which can accommodate a 5 m tether may be used to that end.

BIBLIOGRAPHY

[1] Tsiolkovsky, K. E., "Speculation Between Earth and Sky," izd-vo AN-SSSR *Science Fiction Works*, 1859, (reprinted 1959).

[2] Starly, W. H., and Adlhock, R. W., "Study of the Retrieval of an Astronaut from an Extra-Vehicular Assignment," *TMC* Report No. S-356, November 1963.

[3] Perrine, B. S., "A Method for Soft Tether Stationkeeping," *NASA TM X-53643*, July 1967.

[4] Lang, D. L., and Nolting, R. K., "Operations with Tethered Space Vehicles," *NASA SP-138*, Gemini Summary Conference, February 1967, pp. 55-64.

[5] Sasaki, S., *et al.*, "Results from a Series of Tethered Rocket Experiments," *Journal of Spacecraft and Rocket*, Vol. 24, No. 5, 1987, pp.444-453.

[6] Gullahorn, G. E., *et al.*, "Observations of Tethered Satellite System (TSS-1) Dynamics," *AAS/AIAA Astrodynamics Specialist Conference*, Victoria, Canada, August 1993, Paper No. AAS 93-704.

[7] Tyc, G., *et al.*,"Dynamics and Stability of a Spinning Tethered Spacecraft with Flexible Appendages," *Advances in Astronautical Sciences*, Editors: A. K. Misra, *et al.*, Vol. 85, Part I, 1993, pp. 877-896.

[8] Bortolami, S. B., *et al.*, "Control Law for the Deployment of SEDS–II," *AAS/AIAA Astrodynamics Specialist Conference*, Victoria, Canada, 1993, Paper No. AAS 93-706.

[9] Colombo, G., et al., "Shuttle-Borne 'Skyhook' : A New Tool for Low-Orbital-Altitude Research," Smithsonian Astrophysical Observatory, Report in Geoastronomy, No. 1, September 1974.

[10] Bekey, I., "Tethers Open New Space Options," *Astronautics and Aeronautics*, Vol. 21, No. 4, April 1983, pp. 32-40.

[11] Gilruth, R. R., "Why Space Stations ?," *Astronautics and Aeronautics*, Vol. 6, No. 11, 1968, pp. 54-60.

[12] Pasca, M., and Lorenzini, E., "Collection of Martian Atmospheric Dust with a low Altitude Tethered Probe," *AAS/AIAA Spaceflight Mechanics Meeting*, Houston, Texas, U.S.A., February 11-13, 1991, Paper No. AAS 91-178.

[13] Sutton, G. W., and Diederich, F. W., "Synchronous Rotation of a Satellite at Less than Synchronous Altitude," *AIAA Journal*, Vol. 5, No. 4, April 1967, pp. 813-815.

[14] Yasaka, T., and Hatsuda, T., "Geostationary Tethered Satellite System and Its Application to Communication Systems," *IEEE Transactions on Aerospace and Electronics systems*, Vol. AES 24, No. 1, 1988, pp. 68-75.

[15] Yasaka, T., "The Structural Feasibility of a Gravity Stabilized Antenna," *Acta*

Astronautica, Vol. 8, No. 5-6, 1981, pp. 689-701.

[16] DeCou, A. B., "Attitude and Tether Vibration Control in Spinning Tethered Triangles for Orbiting Interferometry," *The Journal of the Astronautical Sciences*, Vol. 14, No. 3, 1993, pp. 373-398.

[17] Kumar, K., Khosla, A., and Chaudhary, K., "Tether as a Satellite Attitude Stabilizer in Elliptic Orbits : A New Concept," *Advances in Astronautical Sciences*, Editors: A. K. Misra, *et al.*, Vol. 85, Part I, 1993, pp. 859-875.

[18] Rupp, C. C., et al., "Shuttle/Tethered Satellite System Conceptual Design Study," *NASA TM X*-73365, December 1976.

[19] Misra, A. K., and Modi, V. J., "A Survey on the Dynamics and Control of Tethered Satellite Systems," *NASA/AIAA/PSN International Conference on Tethers,* Arlington, VA, U.S.A., September 1986, Paper No. AAS-86-246 ; also *Advances in the Astronautical Sciences*, Editors : P. M. Bainum et al., American Astronautical Society, Vol. 62, pp. 667-719.

[20] Misra, A.K., and Modi, V. J., "Dynamics and Control of Tether Connected Two-Body System – A Brief Review," 33^{rd} *Congress of the International Astronautical Federation*, Paris, France, September 1982, Paper No. 82-315; also *Space 2000*, Selection of papers from the 33^{rd} *IAF Congress*, Editor: L. G. Napolitano, AIAA Publishers, pp. 473-514.

[21] "Special Issue on Tethered Satellites," *The Journal of the Astronautical Sciences*, Guest Editor: Paul A. Penzo, Vol. 35, No. 1, 1987.

[22] Chobotov, V. A., "Gravity-Gradient Exitation of a Rotating Cable-Counterweight Space Station in Orbit," *Journal of Applied Mechanics,* Vol. 30, No. 4, 1963, pp. 547-554.

[23] Bainum, P. A., and Evans, K. S., "The Effect of Gravity-Gradient Torques on the Three Dimensional Motion of a Rotating Space Station Cable-Counterweight System," *AIAA* 13^{th} *Aerospace Sciences Meeting*, Pasadena, California, U.S.A., 1975, Paper No. 75-157.

[24] Tai, C. L., and Loh, M. M. H., "Planar Motion of a Rotating Cable-Connected Space Station in Orbit," *Journal of Spacecraft and Rocket*, Vol. 2, No. 6, 1965, pp. 889-894.

[25] Rupp, C. C., "A Tether Tension Control Law for Tethered Subsatellites Deployed along Local Vertical," *NASA TM X*-64963, September 1975.

[26] Baker, P. W., et al., "Tethered Subsatellite Study," *NASA TM X*-73314, March 1976.

[27] Modi, V. J., and Misra, A. K., "Deployment Dynamics of a Tethered Satellite System," *AIAA/AAS Astrodynamics Conference*, Palo Alto, California, U.S.A., August 1978, Paper No. 78-1398.

[28] Spencer, T. M., "Atmospheric Perturbation and Control of a Shuttle/Tethered

Satellite," 8^{th} *IFAC Space Symposium*, Oxford, U.K., July 1979, Paper No. 79-165.

[29] Banerjee, A. K., and Kane, T. R., "Tether Deployment Dynamics," *The Journal of the Astronautical Sciences*, Vol. 30, No. 4, 1982, pp. 347-366.

[30] Xu, D. M., Misra, A. K., and Modi, V. J., "On Vibration Control of Tethered Satellite Systems," Proceedings of the*NASA/JPL Workshop on Applications of Distributed Systems Theory to the Control of Large Space Structures*, Pasadena, California, U.S.A., July 1982, pp. 317-327.

[31] Bergamaschi, S., and Bonon, F., "Coupling of Tether Lateral Vibration and Subsatellite Attitude Motion," *Journal of Guidance, Control, and Dynamics*, Vol. 15, No. 5, 1992, pp. 1284-1286.

[32] Quadrelli, B. M., and Lorenzini, E. C., "Dynamics and Stability of a Tethered Centrifuge in Low Earth Orbit," *The Journal of the Astronautical Sciences*, Vol. 40, No. 1, 1992, pp. 3-25.

[33] Kohler, P., et al., "Dynamics of a System of Two Satellites Connected by a Deployable and Extensible Tether of Finite Mass," *ESTEC* Contract Report No. 2992/76/ NL/ Ak (sc), Vol. 1 and 2, October 1978.

[34] Keshmiri, M., and Misra, A. K., "A General Formulation for N-Body Tethered Satellite System Dynamics," *Advances in Astronautical Sciences*, Editors: A. K. Misra, *et al.*, Vol. 85, Part I, 1993, pp. 623-644.

[35] He, X., and Powell, J. D., "Tether Damping in Space," *Journal of Guidance, Control, and Dynamics*, Vol. 13, No. 1, 1990, pp. 104-112.

[36] Xu, D. M., *The Dynamics and Control of the Shuttle Supported Tethered Subsatellite System,* Ph.D. Thesis, Department of Mechanical Engineering, McGill University, Montreal, Canada, November 1984.

[37] de Matteis, G., and de Socio, L. M., "Dynamics of a Tethered Satellite Subjected to Aerodynamics Forces," *Journal of Guidance, Control, and Dynamics*, Vol. 14, No. 6, 1991, pp. 1129-1135.

[38] Warnock, T. W., and Cochran Jr., J. E., "Orbital Lifetime of Tethered Satellite," *The Journal of the Astronautical Sciences*, Vol. 41, No. 2, 1993, pp. 165-188.

[39] Misra, A. K., and Diamond, G. S., "Dynamics of a Subsatellite System Supported by two Tethers," *Journal of Guidance, Control, and Dynamics*, Vol. 9, No. 1, 1986, pp. 12-16.

[40] DeCou, A. B., "Tether Static Shape for Rotating Multimass, Multitether, Spacecraft for "Triangle" Michelson Interferometer," *Journal of Guidance, Control, and Dynamics*, Vol. 12, No. 2, 1989, pp. 273-275.

[41] Bergamaschi, S., "Tether Motion After Failure," *The Journal of the Astronautical Sciences*, Vol. 30, No. 1, 1982, pp. 49-59.

[42] Kulla, P., "Stabilization of Tethered Satellites," *ESTEC* Report *TMM*/78-07/PK-avs, December 1977.

[43] Kalagan, P. N., et al., "Study of the Dynamics of a Tethered Satellite System (Skyhook)," Final Report, Contract *NAS*8-32199, Smithsonian Astrophysical Observatory, March 1978.

[44] Bainum, P. M., and Kumar, V. K., "Optimal-Control of the Shuttle-Tethered System," *Acta Astronautica*, Vol. 7, No. 12, 1980, pp. 1333-1348.

[45] Misra, A.K, and Modi, V. J., "Deployment and Retrieval of Shuttle Supported Tethered Satellite," *Journal of Guidance, Control, and Dynamics*, Vol. 5, No. 3, 1982, pp. 278-285.

[46] Banerjee, A. K. and Kane, T. R., "Tethered Satellite Retrieval with Thruster Augmented Control," *Journal of Guidance, Control, and Dynamics*, Vol. 7, No. 1, 1984, pp. 45-50.

[47] Xu, D. M., Misra, A. K., and Modi, V. J., "Thruster Augmented Active Cintrol of a Tethered Satellite System During its Retrieval," *Journal of Guidance, Control, and Dynamics*, Vol. 9, No. 6, November-December 1986, pp. 663-672.

[48] Modi, V. J., Lakshmanan, P. K., and Misra, A. K., "Offset Control of Tethered Satellite Systems: Analysis and Experimental Verification", *Acta Astronautica*, Vol. 21, No. 5, 1990, pp. 283-294.

[49] Modi, V. J., Lakshmanan, P. K. and Misra, A. K., "On the Control of Tethered Satellite Systems," *Proceedings of the AIAA/ ASME/ ASCE/ AHS/ ASC 32nd Structures, Structural Dynamics, and Materials Conference*, Baltimore, Maryland, U.S.A., April 1991, Paper No. AIAA-91-1002.

[50] Vadali, S. R., and Kim, E., "Feedback Control of Tethered Satellite Using Lyapunov Stability Theory," *Journal of Guidance, Control, and Dynamics*, Vol. 14, No. 4, 1991, pp. 729-735.

[51] Kim, E., and Vadali, S. R., "Nonlinear Feedback Deployment and Retrieval of Tethered Satellite Systems," *Journal of Guidance, Control, and Dynamics*, Vol. 15, No. 1, 1992, pp. 28-34.

[52] Monshi, N., Misra, A. K., and Modi, V. J., "A Parametric Study on the Reel Rate Control of Retrieval Dynamics of Tethered Satellite Systems," *AAS/AIAA Spaceflight Mechanics Meeting*, Houston, Texas, U.S.A., February, 1991, Paper No. AAS-91-175.

[53] Liaw, D. C., and Abed, E. H., "Tethered Satellite System Stability," *Contemporary Mathematics*, Vol. 97, 1989, pp. 241-267.

[54] Fleurisson, E. J., *et al.*, "Trajectory Design, Feedforward, and Feedback Stabilization of Tethered Spacecraft Retrieval," *Journal of Guidance, Control, and Dynamics*, Vol. 16, No. 1, 1993, pp. 160-167.

[55] Fujii, H., *et al.*,"Mission Function Control of Tethered Subsatellite Deploy-

ment/Retrieval: In-Plane and Out-of-Plane Motion," *Journal of Guidance, Control, and Dynamics*, Vol. 14, No. 2, 1991, pp. 471-473.

[56] Onoda, J., and Watanabe, N., " Effects of Atmospheric Density Gradient on Control of Tethered Subsatellites," *Journal of Guidance, Control, and Dynamics*, Vol. 12, No. 3, 1989, pp.431-433.

[57] Fujii, H., *et al.*,"Deployment/Retrieval Control of a Tethered Subsatellite under Aerodynamic Effect of Atmosphere," *The Journal of the Astronautical Sciences*, Vol. 40, No. 2, 1992, pp. 171-188.

[58] Grassi, M., *et al.*, "Tethered System Attitude Control After Attachment Point Blocking," *Acta Astronautica*, Vol. 32, No. 5, 1994, pp. 355-362.

[59] Kline-Schoder, R. J., and Powell, J. D., "Precision Attitude Control for Tethered Satellite," *Journal of Guidance, Control, and Dynamics*, Vol. 16, No. 1, 1993, pp. 168-174.

[60] Thornburg, S. L., and Powell, J. D., "Thrusterless Vibration Control for Tethered Artificial Gravity Spacecraft," *Advances in Astronautical Sciences*, Editors: A. K. Misra, *et al.*, Vol. 85, Part I, 1993, pp. 839-857.

[61] Maron, J. P., "Effect of Planar Librations on the Orbital Motion of a Dumbbell Satellite," *ARS Journal*, Vol. 31, No. 8, August 1961, pp. 1089-1096.

[62] Yu, E.Y., "Long-term Coupling Effects Between the Librational and Orbital Motions of a Satellite," *AIAA Journal*, Vol. 2, No. 3, 1964, pp.553-555.

[63] Misra, A.K., and Modi, V. J., "The Influence of Satellite Flexibility on Orbital Motion," *Celestial Mechanics*, 17, 1978, pp.145-165.

[64] Meirovitch, L., *Computational Methods in Structural Dynamics*, Sijthoff & Noordhoff, The Netherlands, 1980, pp. 229-322.

[65] Misra, A. K., Xu, D. M., and Modi, V. J., "Nonlinear Vibrations of Orbiting Tethers," *AAS/AIAA Astrodynamics Specialist Conference,* Lake Placid, New York, U.S.A, August, 1983, Paper No. 83-300.

[66] Etkin, B., *Dynamics of Atmospheric Flight,* John Wiley and Sons, New York, U.S.A., 1972, pp. 104-120.

[67] Nayfeh, A. H., and Mook, D. T., *Nonlinear Oscillations*, John Wiley and Sons, New York, U.S.A., 1979, pp. 485-500.

[68] Crawley, E. F., Sawer, G. C., and Mohr, D. G., "Experimental Measurement of Passive Material and Structural Damping for Flexible Space Structures," 33^{rd} *Congress of the International Astronautical Federation*, Paris, France, September 1982, Paper No. 82-380.

[69] Greenwood, D. T., *Principles of Dynamics,* Prentice Hall Inc., New-Jersy, U.S.A., 1965, pp. 489-491.

[70] *IMSL Library Reference Manual,* Vol.1, IMSL Inc., Houston, Texas, U.S.A.,

1980, pp. DGEAR 1 - DGEAR 9.

[71] Gear, C. W., *Numerical Initial Value Problems in Ordinary Differential Equations,* Prentice-Hall, Englewood Cliffs, New Jersey, U.S.A., 1971, pp. 158-166.

[72] Pasca, M., Pignataro, M., and Luongo, A., "Three-Dimensional Vibrations of Tethered Satellite Systems," *Journal of Guidance, Control, and Dynamics*, Vol. 14, No. 2, 1991, pp.312-320.

[73] Thomson, W. T., *Vibration Theory and Applications*, Prentice–Hall, Inc., Englewood Cliffs, N.J., U.S.A., 1965, pp. 264-267.

[74] Astrom, K.J., and Wittenmark, B., *Adaptive Control*, Addison-Wesley, Mass., U.S.A., 1989.

[75] Al-Sunni, F. M., and Lewis, F. L.,"Gain Scheduling Simplification by Simultaneous Control Design," *Journal of Guidance, Control, and Dynamics*, Vol. 16, No. 3, May-June 1993, pp.602-603.

[76] Debowski, A., and Kurylowicz, A.,"Simultaneous Stabilization of Linear Single-Input/ Single-Output Plants," *International Journal of Control*, Vol. 44, No. 5, 1986, pp.1257-1264.

[77] Ghosh, B., and Byrnes, C.,"Simultaneous Stabilization and Pole Placement by Nonswitching Dynamic Compensation," *IEEE Transactions on Automatic Control*, Vol. AC-28, No. 6, June 1983, pp.735-741.

[78] Peterson, I.,"A Procedure for Simultaneously Stabilizing a Collection of Single Input Linear Systems Using Non-Linear State Feedback Control," *Automatica*, Vol. 23, No. 1, 1987, pp.33-40.

[79] Schmitendorf, W., and Holot, C.,"Simultaneous Stabilization via Linear State Feedback Control," *IEEE Transactions on Automatic Control*, Vol. AC-34, No. 9, 1989, pp.1001-1005.

[80] Seaks, R., and Murray, J.,"Fractional Representation Algebraic Geometry, and the Simultaneous Problem," *IEEE Transactions on Automatic Control*, Vol. AC-27, Aug. 1982, pp. 895-903.

[81] Vidyasagar, M., "Some Results on Simultaneous Stabilization with Multiple Domains of Stability," *Automatica*, 1987, pp. 535-540.

[82] Beijezy, A. K., *Robot Arm Dynamics and Control*, JPL TM 33-669, California Institute of Technology, Pasadena, California, U.S.A., 1974.

[83] Isidori, A., *Nonlinear Control Systems : An Introduction*, Lecture Notes in Control and Information Sciences, Vol. 72, Springer-Varlag, Berlin, Germany, 2nd Edition, 1989, pp. 145-281.

[84] Modi, V. J., Karray, F., and Chan, J. K., "On the Control of a Class of Flexible Manipulators Using Feedback Linearization Approach," *42nd Congress of the International Astronautical Federation*, Montreal, Canada, October 1991, Paper No. IAF-91-324; also *Acta Astronautica*, Vol. 29, No. 1, 1993, pp. 17-27.

[85] Singh, S. N., and Schy, A. A.,"Invertibility and Robust Nonlinear Control of Robotic Systems," *Proceedings of 23rd Conference on Decision Control*, Las Vegas, Nevada, U.S.A., December 1984, pp.1058-1063.

[86] Su, R.,"On the Linear Equivalents of Nonlinear Systems," *Systems and Control Letter*, Vol. 2, No. 1, 1982, pp. 48-52.

[87] Spong, M., and Vidyasagar, M., *Robot Dynamics and Control*, John Wiley and Sons, New York, 1989, pp. 274-279.

[88] Wang, D., and Vidyasagar, M.,"Control of a Class of Manipulators with a Single Flexible Link – Part I: Feedback Linearization," *Journal of Dynamic Systems, Measurement, and Control*, Transactions of the ASME, Vol. 113, 1991, pp. 655-661.

[89] Balas, G. J., Garrard, W. L., and Reiner, J.,"Robust Dynamic Inversion Control Laws for Aircraft Control," *Proceedings of the 1992 AIAA Guidance, Navigation, and Control Conference*, Hilton Head Island, SC, U.S.A., August 1992, pp.192-205.

[90] Alfriend, K. T.,"Partially Filled Viscous Ring Nutation Damper," *Journal of Spacecraft and Rocket*, Vol. 11, No. 7, 1974, pp.456-462.

[91] Hunt, L.R., and Su, R.,"Linear Equivalent of Non-Linear Time-Varying Systems," *Proceedings of the International Symposium on Mathematical Theory of Networks and Systems*, Santa Monica, California, U.S.A., Editor: N. Levan, August 1981, pp. 119-123.

[92] Rosenbrock, H. H., "The Stability of Multivariable Systems," *IEEE Transactions on Automatic Control*, Vol. AC-17, No.1, 1972, pp.105-107.

[93] Yuan, J. S. C., and Stieber, M.E., "Robust Beam-Pointing and Attitude Control of a Flexible Spacecraft," *Journal of Guidance, Control, and Dynamics*, Vol.9, No.2, 1986, pp.228-234.

[94] Maciejowski, J. M., *Multivariable Feedback Design*, Addison-Wesley Publishing Company, Wokingham, England, 1989, Chapters 3,5.

[95] "Special Issue on the LQG Problem," *IEEE Transactions on Automatic Control*, Vol. 16, No. 6, December 1971.

[96] Joshi, S. M., Armstrong, E. S., and Sunderrajan, N., "Application of LQG/LTR Technique to Robust Controller Synthesis for a Large Flexible Space Antenna," *NASA TP-2560*, 1986.

[97] Safonov, M. G., and Athans, M., "Gain and Phase Margins of Multiloop LQG Regulators," *IEEE Transactions on Automatic Control*, Vol. AC-22, No. 2, 1977, pp.173-179.

[98] Kalman, R. E., "When is a Linear System Optimal?," *Tansactions of ASME, Series D, Journal of Basic Engineering*, Vol. 86, 1964, pp.51-60.

[99] Doyle, J. C., and Stein, G., "Robustness with Observers," *IEEE Transactions*

on Automatic Control, Vol. AC-24, 1979, pp. 607-611.

[100] Doyle, J. C., and Stein, G., "Multivariable Feedback Design : Concepts for a Classical/Modern Synthesis," *IEEE Transactions on Automatic Control*, Vol. AC-26, No. 1, 1981, pp. 4-16.

[101] Kwakernaak, H., and Sivan, R., *Linear Optimal Control Systems*, Wiley-Interscience Publisher, New-York, U.S.A., 1972.

[102] Chiang, R. Y., and Safonov, M. G., *Robust Control Toolbox User's Guide*, The Math Works Inc., 1992, pp. 2.72-2.74.

[103] Jablonski, A. M., *et al.*, "The Tether Laboratory Demonstration System (TE-LAB) for Dynamics of OEDIPUS," *Advances in Astronautical Sciences*, Editors: A. K. Misra, *et al.*, Vol. 85, Part I, 1993, pp. 711-731.

[104] Tyc, G., *et al.*,"Ground Experiments of a Hanging Spinning Tethered Body," *Proceedings of the AIAA/AAS Astrodynamics Conference*, Scottsdale, AZ, U.S.A., August 1994, pp. 341-350.

[105] Gwaltney, D. A., and Greene, M. E.,"Ground-Based Implementation and Verification of Control Laws for Tethered Satellite," *Journal of Guidance, Control, and Dynamics*, Vol. 15, No. 1, 1992, pp. 271-273.

[106] Shoichi, Y. and Osamu, O.,"An Experimental Study of Tether Reel System - A Laboratory Model," *TR-1176T*, National Aerospace Laboratory, Chofu, Tokyo, Japan, August 1992.

[107] *User's Manual : PCL-812PG Enhanced Multi-Lab Card*, Advantech Co., 1990.

[108] *Model 5030, Software Guide*, Manual No. 40041–009–10A, Industrial Computer Source, San Diego, California, U.S.A., 1992

[109] deSilva, C. W., *Control Sensors and Actuators*. Prentice Hall, Englewood Cliffs, New Jersey, U.S.A., 1989, pp.5-30.

[110] Lakshmanan, P. K., *Dynamics and Control of an Orbiting Space Platform Based Tethered Satellite System*, Ph.D. Thesis, Department of Mechanical Engineering, University of British Columbia, Vancouver, Canada, 1989, pp. 216-220.

APPENDIX I: MATRICES USED IN THE FORMULATION

For concise derivation and efficient computer implementation of the governing equations of motion, a number of matrices are defined to express the system energies. The matrices, dependent on modal integrals and attitude angles, are also reported here.

Matrices used in the Kinetic Energy (Eq. 2.25)

$$\{K_1\} = L\dot{L}\{A_{k_0}\} + L^2\omega_{tx}\{B_{k_0}\} + m_s\dot{L}\{D_{k_1}\} + m_sL\omega_{tx}\{D_{k_2}\} \quad \in \mathbf{R}^3;$$

$$[K_2] = [A_{k_2}] + m_s[A_{p_1}] \quad \in \mathbf{R}^{3\times N_{tl}};$$

$$[K_3] = \dot{L}[A_{k_1}] + \omega_{tx}[B_{k_1}] + m_s\omega_{tx}[U_k][A_{p_1}] \quad \in \mathbf{R}^{3\times N_{tl}};$$

$$[K_4] = \frac{1}{2}m_s[A_{p_1}]^T[A_{p_1}] + \frac{1}{2}[C_{k_2}] \quad \in \mathbf{R}^{N_{tl}\times N_{tl}};$$

$$[K_5] = m_s\omega_{tx}[A_{p_1}]^T[U_k][A_{p_1}] + \frac{1}{2}\dot{L}[C_{k_3}] + \omega_{tx}[H_{k_4}] \quad \in \mathbf{R}^{N_{tl}\times N_{tl}};$$

$$[K_6] = \frac{1}{2}m_s\omega_{tx}^2[A_{p_1}]^T[U_k]^T[U_k][A_{p_1}] + \frac{1}{2}\dot{L}^2[C_{k_1}] + \dot{L}\omega_{tx}[H_{k_3}] \quad \in \mathbf{R}^{N_{tl}\times N_{tl}};$$

$$\{K_7\} = \frac{1}{2}\dot{L}\{C_{k_5}\}^T + \omega_{tx}\{H_{k_2}\}^T + m_s\dot{L}\{D_{k_1}\}[A_{p_1}] + m_sL\omega_{tx}\{D_{k_2}\}[A_{p_1}] \quad \in \mathbf{R}^{N_{tl}};$$

$$\{K_8\} = \frac{1}{2}\dot{L}^2\{C_{k_4}\}^T + \dot{L}\omega_{t_x}\{H_{k_1}\}^T + m_s\dot{L}\omega_{t_x}\{D_{k_1}\}^T[U_k][A_{p_1}]$$
$$+ m_sL\omega_{t_x}^2\{D_{k_2}\}^T[U_k][A_{p_1}] \quad \in \mathbf{R}^{N_{tl}}.$$

Matrices used in the Potential Energy (Eq. 2.28)

$$[P_1] = M[U] - 3M[V_{po}] \quad \in \mathbf{R}^{3\times 3};$$

$$[P_2] = m_a[U] - 3m_a[V_{po}] \quad \in \mathbf{R}^{3\times 3};$$

$$[P_3] = \begin{bmatrix} 2\rho_t\left\{\int_0^L\{F_\psi(y_t)\}dy_t\right\}\{W_{tp}\}^T - 6\rho_t\cos(\alpha_t)\left\{\int_0^L\{F_\psi(y_t)\}dy_t\right\}\{\hat{W}_{po}\}^T \\ 2\rho_t\left\{\int_0^L\{F_\phi(y_t)\}dy_t\right\}\{U_{tp}\}^T + 6\rho_t\sin(\alpha_t)\left\{\int_0^L\{F_\phi(y_t)\}dy_t\right\}\{\hat{W}_{po}\}^T \end{bmatrix}$$
$$+ 2m_s[A_{p_1}]^T[T_{tp}] - 6m_s[A_{p_1}]^T\{\hat{W}_{to}\}\{\hat{W}_{po}\}^T \quad \in \mathbf{R}^{N_{tl}\times 3};$$

$$\{P_4\} = 2m_sL\begin{Bmatrix}\{F_\psi(L)\}\\ 0\end{Bmatrix} - 6m_sL\cos(\alpha_t)[A_{p_1}]^T\{\hat{W}_{to}\} \quad \in \mathbf{R}^{N_{tl}};$$

$$[P_5] = m_s[A_{p_1}]^T[A_{p_1}] - 3m_s[A_{p_1}]^T\{\hat{W}_{to}\}\{\hat{W}_{to}\}^T[A_{p_1}] \quad \in \mathbf{R}^{N_{tl}\times N_{tl}};$$

$$\{P_6\} = (2m_s + \rho_tL)L\{W_{tp}\} - 3(2m_s + \rho_tL)L\cos(\alpha_t)\{\hat{W}_{po}\} \quad \in \mathbf{R}^3;$$

$$\hat{V}_{to} = \cos^2(\alpha_t) \quad \in \mathbf{R}.$$

Inertia Dyadics and Their Derivatives

The terms associated with the inertia matrices and their derivatives, used in derivation of the governing equations of motion, are presented here.

$$[I_p] = \begin{bmatrix} I_{px} & I_{pxy} & I_{pxz} \\ I_{pxy} & I_{py} & I_{pyz} \\ I_{pxz} & I_{pyz} & I_{pz} \end{bmatrix};$$

$$[I_t] = \begin{bmatrix} I_{t_x} & 0 & 0 \\ 0 & I_{t_y} & I_{t_{yz}} \\ 0 & I_{t_{yz}} & I_{t_z} \end{bmatrix} \triangleq \begin{bmatrix} I_b + I_c & 0 & 0 \\ 0 & I_c & I_{bc} \\ 0 & I_{bc} & I_b \end{bmatrix},$$

where:

$$\begin{aligned}
I_b &= \frac{1}{3}\rho_t L^3 + \{B\}^T[I_{b_1}]\{B\} + 2\{I_{b_2}\}\{B\}; \\
I_c &= \{C\}^T[I_{c_1}]\{C\}; \\
I_{bc} &= -\{I_{bc_1}\}\{C\} - \{B\}^T[I_{bc_2}]\{C\}; \\
[I_{b_1}] &= \rho_t \int_0^L \{F_\psi\}\{F_\psi\}^T dy_t; \\
\{I_{b_2}\} &= \rho_t \int_0^L y_t\{F_\psi\}^T dy_t; \\
[I_{c_1}] &= \rho_t \int_0^L \{F_\phi\}\{F_\phi\}^T dy_t; \\
\{I_{bc_1}\} &= \rho_t \int_0^L y_t\{F_\phi\}^T dy_t; \\
[I_{bc_2}] &= \rho_t \int_0^L \{F_\psi\}\{F_\phi\}^T dy_t.
\end{aligned}$$

The time derivative of $[I_p]$ is zero. The derivatives of the elements of $[I_t]$, used in the equations of motion, are as follows:

$$\begin{aligned}
\frac{\mathrm{d}I_{t_x}}{\mathrm{d}t} = {} & \rho_t L^2 \dot{L} + 2\{B\}^T[I_{b_1}]\{\dot{B}\} + \{B\}^T[\dot{I}_{b_1}]\{B\} \\
& + 2\{I_{b_2}\}\{\dot{B}\} + 2\{\dot{I}_{b_2}\}\{B\} + 2\{C\}^T[I_{c_1}]\{\dot{C}\} \\
& + \{C\}^T[\dot{I}_{c_1}]\{C\};
\end{aligned}$$

$$\frac{\partial}{\partial\{X\}}\Big(tr[I_t]\Big) = 2\left\{\begin{matrix}\{I_{t_{x_B}}\}\\ \{I_{t_{x_C}}\}\end{matrix}\right\};$$

$$\frac{\partial}{\partial\{X\}}\Big(\{l_t\}^T[I_t]\{l_t\}\Big) = \left\{\begin{matrix}-\sin(2\alpha_t)\{I_{t_{yz_B}}\} + \sin^2(\alpha_t)\{I_{t_{x_B}}\}\\ \cos^2(\alpha_t)\{I_{t_{x_C}}\} - \sin(2\alpha_t)\{I_{t_{yz_C}}\}\end{matrix}\right\};$$

$$\frac{\partial}{\partial\{X\}}\Big(\{\omega_t\}^T[I_t]\{\omega_t\}\Big) = \omega_{t_x}\left\{\begin{matrix}\{I_{t_{x_B}}\}\\ \{I_{t_{x_C}}\}\end{matrix}\right\},$$

where:

$$\left\{I_{t_{x_B}}\right\} = 2[I_{b_1}]\{B\} + 2\{I_{b_2}\}^T;$$

$$\left\{I_{t_{x_C}}\right\} = 2[I_{c_1}]\{C\};$$

$$\left\{I_{t_{yz_B}}\right\} = -[I_{bc_2}]\{C\};$$

$$\left\{I_{t_{yz_C}}\right\} = -\{I_{bc_1}\}^T - [I_{bc_2}]^T\{B\};$$

$$[\dot{I}_{b_1}] = \rho_t\dot{L}\left[\int_0^L\left\{\{DF_\psi\}\{F_\psi\}^T + \{F_\psi\}\{DF_\psi\}^T\right\}\mathrm{d}y_t + \{F_\psi\}\{F_\psi\}^T\right];$$

$$\{\dot{I}_{b_1}\} = \rho_t\dot{L}\left\{\int_0^L\Big\{\{F_\psi\} + y_t\{SF_\psi\}\Big\}\mathrm{d}y_t + L\{f_\psi\}\right\};$$

$$[\dot{I}_{c_1}] = \rho_t\dot{L}\left[\int_0^L\left\{\{DF_\phi\}\{F_\phi\}^T + \{F_\phi\}\{DF_\phi\}^T\right\}\mathrm{d}y_t + \{F_\phi\}\{F_\phi\}^T\right].$$

Modal Integral and other Constant Matrices

$$\{A_{k_0}\} = \left\{\begin{matrix}0\\ \rho_t\\ 0\end{matrix}\right\} \in \mathbf{R}^3;$$

$$[A_{k_1}] = \begin{bmatrix} 0 & 0 \\ \rho_t \int_0^L \{DF_\psi\} \mathrm{d}y_t & 0 \\ 0 & \rho_t \int_0^L \{DF_\phi\} \mathrm{d}y_t \end{bmatrix} \in \mathbf{R}^{3 \times N_{tl}};$$

$$[A_{k_2}] = \begin{bmatrix} 0 & 0 \\ \rho_t \int_0^L \{F_\psi(y_t)\}^T dy_t & 0 \\ 0 & \rho_t \int_0^L \{F_\phi(y_t)\}^T dy_t \end{bmatrix} \in \mathbf{R}^{3 \times N_{tl}};$$

$$[A_{p_1}] = \begin{bmatrix} 0 & 0 \\ \{F_\psi(L)\}^T & 0 \\ 0 & \{F_\phi(L)\}^T \end{bmatrix} \in \mathbf{R}^{3 \times N_{tl}};$$

$$\{B_{k_0}\} = \begin{Bmatrix} 0 \\ 0 \\ \rho_t/2 \end{Bmatrix} \in \mathbf{R}^3;$$

$$[B_{k_1}] = \begin{bmatrix} 0 & 0 \\ 0 & -\rho_t \int_0^L \{F_\phi(y_t)\}^T dy_t \\ \rho_t \int_0^L \{F_\psi(y_t)\}^T dy_t & 0 \end{bmatrix} \in \mathbf{R}^{3 \times N_{tl}};$$

$$[C_{k_1}] = \begin{bmatrix} \rho_t \int_0^L \{DF_\psi\}\{DF_\psi\}^T \mathrm{d}y_t & 0 \\ 0 & \rho_t \int_0^L \{DF_\phi\}\{DF_\phi\}^T \mathrm{d}y_t \end{bmatrix} \in \mathbf{R}^{N_{tl} \times N_{tl}};$$

$$[C_{k_2}] = \begin{bmatrix} \rho_t \int_0^L \{F_\psi(y_t)\}\{F_\psi(y_t)\}^T dy_t & 0 \\ 0 & \rho_t \int_0^L \{F_\phi(y_t)\}\{F_\phi(y_t)\}^T dy_t \end{bmatrix} \in \mathbf{R}^{N_{tl} \times N_{tl}};$$

$$[C_{k_3}] = \begin{bmatrix} 2\rho_t \int_0^L \{F_\psi(y_t)\}\{DF_\psi\}^T \mathrm{d}y_t & 0 \\ 0 & 2\rho_t \int_0^L \{F_\phi(y_t)\}\{DF_\phi\}^T \mathrm{d}y_t \end{bmatrix} \in \mathbf{R}^{N_{tl} \times N_{tl}};$$

$$\{C_{k_4}\} = \begin{Bmatrix} 2\rho_t \int_0^L \{DF_\psi\} \mathrm{d}y_t \\ 0 \end{Bmatrix} \in \mathbf{R}^{N_{tl}};$$

$$\{C_{k_5}\} = \begin{Bmatrix} 2\rho_t \int_0^L \{F_\psi(y_t)\} \\ 0 \end{Bmatrix} \in \mathbf{R}^{N_{tl}};$$

$$\{D_{k_1}\} = \begin{Bmatrix} 0 \\ 1 \\ 0 \end{Bmatrix} \in \mathbf{R}^3;$$

$$\{D_{k_2}\} = \begin{Bmatrix} 0 \\ 0 \\ 1 \end{Bmatrix} \in \mathbf{R}^3;$$

$$\{H_{k_1}\} = \begin{Bmatrix} 0 \\ \rho_t \int_0^L \Big\{ y_t \{DF_\phi\} - \{F_\phi\} \Big\} \mathrm{d}y_t \end{Bmatrix} \in \mathbf{R}^{N_{tl}};$$

$$\{H_{k_2}\} = \begin{Bmatrix} 0 \\ \rho_t \int_0^L y_t \{F_\phi\} dy_t \end{Bmatrix} \in \mathbf{R}^{N_{tl}};$$

$$[H_{k_3}] = \begin{bmatrix} 0 & \rho_t \int_0^L \{F_\psi(y_t)\}\{DF_\phi\}^T \mathrm{d}y_t \\ -\rho_t \int_0^L \{F_\phi(y_t)\}\{DF_\psi\}^T \mathrm{d}y_t & 0 \end{bmatrix} \in \mathbf{R}^{N_{tl} \times N_{tl}};$$

$$[H_{k_4}] = \begin{bmatrix} 0 & -\rho_t \int_0^L \{F_\psi(y_t)\}\{F_\phi(y_t)\}^T dy_t \\ \rho_t \int_0^L \{F_\phi(y_t)\}\{F_\psi(y_t)\}^T dy_t & 0 \end{bmatrix} \in \mathbf{R}^{N_{tl} \times N_{tl}};$$

$$[T_{tp}] = \begin{bmatrix} 1 & 0 & 0 \\ 0 & \cos(\alpha_t - \alpha_p) & \sin(\alpha_t - \alpha_p) \\ 0 & -\sin(\alpha_t - \alpha_p) & \cos(\alpha_t - \alpha_p) \end{bmatrix};$$

$$[U] = \begin{bmatrix} 1 & 0 & 0 \\ 0 & 1 & 0 \\ 0 & 0 & 1 \end{bmatrix}.$$

$$[U_k] = \begin{bmatrix} 0 & 0 & 0 \\ 0 & 0 & -1 \\ 0 & 1 & 0 \end{bmatrix} \in \mathbf{R}^{3 \times 3};$$

$$\{U_{tp}\} = \begin{Bmatrix} 0 \\ -\sin(\alpha_t - \alpha_p) \\ \cos(\alpha_t - \alpha_p) \end{Bmatrix};$$

$$[V_{po}] = \begin{bmatrix} 0 & 0 & 0 \\ 0 & \cos^2(\alpha_p) & -\sin(\alpha_p)\cos(\alpha_p) \\ 0 & -\sin(\alpha_p)\cos(\alpha_p) & \sin^2(\alpha_p) \end{bmatrix};$$

$$\{W_{tp}\} = \begin{Bmatrix} 0 \\ \cos(\alpha_t - \alpha_p) \\ \sin(\alpha_t - \alpha_p) \end{Bmatrix};$$

$$\{\hat{W}_{po}\} = \begin{Bmatrix} 0 \\ \cos(\alpha_p) \\ -\sin(\alpha_p) \end{Bmatrix};$$

$$\{\hat{W}_{to}\} = \begin{Bmatrix} 0 \\ \cos(\alpha_t) \\ -\sin(\alpha_t) \end{Bmatrix};$$

$$\{F_\phi(y_t)\} = \Big\{\Phi_n(y_t, L)\Big\}_{n=1}^{N_t} \in \mathbf{R}^{N_t};$$

$$\{F_\psi(y_t)\} = \left\{ \Psi_n(y_t, L) \right\}_{n=1}^{N_l} \quad \in \mathbf{R}^{N_l};$$

$$\{DF_\phi\} = \frac{\partial F_\phi}{\partial y_t} + \frac{\partial F_\phi}{\partial L} \quad \in \mathbf{R}^{N_t};$$

$$\{DF_\psi\} = \frac{\partial F_\psi}{\partial y_t} + \frac{\partial F_\psi}{\partial L} \quad \in \mathbf{R}^{N_l}.$$

Here:

N_l = number of modes used to represent the longitudinal tether vibration;

N_t = number of modes for transverse oscillation of the tether;

$N_{tl} = N_t + N_l$.

Time Derivative of Matrices

$$\{\dot{A}_{k_0}\} = \{0\};$$

$$[\dot{A}_{k_1}] = \rho_t \dot{L} \begin{bmatrix} 0 & 0 \\ \int_0^L \{D2F_\psi\}^T dy_t + \{DF_\psi(L)\}^T & 0 \\ 0 & \int_0^L \{D2F_\phi\}^T dy_t + \{DF_\phi(L)\}^T \end{bmatrix};$$

$$[\dot{A}_{k_2}] = \dot{L}\ [A_{k_1}];$$

$$\{\dot{B}_{k_0}\} = \{0\};$$

$$[\dot{B}_{k_1}] = \begin{bmatrix} 0 & 0 \\ 0 & -[\dot{A}_{k_2}(3, N_l+1 : N_{tl})] \\ [\dot{A}_{k_2}(2, 1 : N_l)] & 0 \end{bmatrix};$$

$$[\dot{C}_{k_1}] = \rho_t \dot{L} \begin{bmatrix} \int_0^L \Big\{ \{D2F_\psi\}\{DF_\psi\}^T + \{DF_\psi\}\{D2F_\psi\}^T \Big\} dy_t & \vdots \\ +\{DF_\psi(L)\}\{DF_\psi(L)\}^T & \vdots \\ \cdots\cdots\cdots\cdots\cdots\cdots\cdots\cdots\cdots\cdots\cdots\cdots & \\ 0 & \vdots \end{bmatrix}$$

$$\begin{bmatrix} \vdots & 0 \\ \cdots\cdots\cdots\cdots\cdots\cdots\cdots\cdots\cdots\cdots\cdots\cdots & \\ \vdots & \int_0^L \Big\{ \{D2F_\phi\}\{DF_\phi\}^T + \{DF_\phi\}\{D2F_\phi\}^T \Big\} dy_t \\ \vdots & +\{DF_\phi(L)\}\{DF_\phi(L)\}^T \end{bmatrix};$$

$$[\dot{C}_{k_2}] = \rho_t \dot{L} \begin{bmatrix} \int_0^L \Big\{ \{DF_\psi\}\{F_\psi\}^T + \{F_\psi\}\{DF_\psi\}^T \Big\} dy_t & \vdots \\ +\{F_\psi(L)\}\{F_\psi(L)\}^T & \vdots \\ \cdots\cdots\cdots\cdots\cdots\cdots\cdots\cdots\cdots\cdots & \\ 0 & \vdots \end{bmatrix}$$

$$\begin{bmatrix} \vdots & 0 \\ \cdots\cdots\cdots\cdots\cdots\cdots\cdots\cdots\cdots\cdots & \\ \vdots & \int_0^L \Big\{ \{DF_\phi\}\{F_\phi\}^T + \{F_\phi\}\{DF_\phi\}^T \Big\} dy_t \\ \vdots & +\{F_\phi(L)\}\{F_\phi(L)\}^T \end{bmatrix};$$

$$[\dot{C}_{k_3}] = 2\rho_t \dot{L} \begin{bmatrix} \int_0^L \Big\{ \{DF_\psi\}\{DF_\psi\}^T + \{F_\psi\}\{D2F_\psi\}^T \Big\} dy_t & \vdots \\ +\{F_\psi(L)\}\{DF_\psi(L)\}^T & \vdots \\ \cdots\cdots\cdots\cdots\cdots\cdots\cdots\cdots\cdots\cdots & \\ 0 & \vdots \end{bmatrix}$$

$$
\begin{array}{c}
\vdots \quad 0 \\
\cdots\cdots\cdots\cdots\cdots\cdots\cdots\cdots \\
\vdots \quad \int_0^L \Big\{\{DF_\phi\}\{DF_\phi\}^T + \{F_\phi\}\{D2F_\phi\}^T\Big\}\mathrm{d}y_t \\
\vdots \quad +\{F_\phi(L)\}\{DF_\phi(L)\}^T
\end{array}
\Bigg] ;
$$

$$
\{\dot{C}_{k_4}\} = 2\rho_t \dot{L} \left\{ \begin{array}{c} \int_0^L \{D2F_\psi\}\mathrm{d}y_t + \{DF_\psi(L)\} \\ 0 \end{array} \right\};
$$

$$
\{\dot{C}_{k_5}\} = \dot{L}\{C_{k_4}\};
$$

$$
\{\dot{H}_{k_1}\} = \rho_t \dot{L} \left\{ \begin{array}{c} 0 \\ \int_0^L y_t\{D2F_\phi\}\mathrm{d}y_t + L\{DF_\phi(L)\} - \{F_\phi(L)\} \end{array} \right\};
$$

$$
\{\dot{H}_{k_2}\} = \rho_t \dot{L} \left\{ \begin{array}{c} 0 \\ \int_0^L \Big\{\{F_\phi\} + y_t\{DF_\phi\}\Big\}\mathrm{d}y_t + L\{F_\phi(L)\} \end{array} \right\};
$$

$$
[\dot{H}_{k_3}] = \rho_t \dot{L} \left[\begin{array}{c}
0 \quad \vdots \\
\cdots\cdots\cdots\cdots\cdots\cdots\cdots\cdots \\
-\int_0^L \Big\{\{DF_\phi\}\{DF_\psi\}^T + \{F_\phi\}\{D2F_\psi\}^T\Big\}\mathrm{d}y_t \quad \vdots \\
-\{F_\phi(L)\}\{DF_\psi(L)\}^T \quad \vdots
\end{array} \right.
$$

$$
\left. \begin{array}{c}
\vdots \quad \int_0^L \Big\{\{DF_\psi\}\{DF_\phi\}^T + \{F_\psi\}\{D2F_\phi\}^T\Big\}\mathrm{d}y_t \\
\vdots \quad +\{F_\psi(L)\}\{DF_\phi(L)\}^T \\
\cdots\cdots\cdots\cdots\cdots\cdots\cdots\cdots \\
\vdots \quad 0
\end{array} \right] ;
$$

$$[\dot{H}_{k_4}] = \rho_t \dot{L} \begin{bmatrix} 0 & \vdots & \\ \cdots & & \\ \int_0^L \Big\{ \{DF_\phi\}\{F_\psi\}^T + \{F_\phi\}\{DF_\psi\}^T \Big\} dy_t & \vdots & \\ +\{F_\phi(L)\}\{F_\psi(L)\}^T & \vdots & \end{bmatrix}$$

$$\begin{bmatrix} \vdots & \int_0^L \Big\{ \{F_\psi\}\{DF_\phi\}^T + \{DF_\psi\}\{F_\phi\}^T \Big\} dy_t \\ \vdots & +\{F_\phi(L)\}\{F_\psi(L)\}^T \\ \cdots & \\ \vdots & 0 \end{bmatrix};$$

$$[\dot{T}_{tp}] = (\dot{\alpha}_t - \dot{\alpha}_p) \begin{bmatrix} 0 & 0 & 0 \\ 0 & -\sin(\alpha_t - \alpha_p) & \cos(\alpha_t - \alpha_p) \\ 0 & -\cos(\alpha_t - \alpha_p) & -\sin(\alpha_t - \alpha_p) \end{bmatrix},$$

where:

$$\{D2F_\phi\} = \frac{\partial \{DF_\phi\}}{\partial y_t} + \frac{\partial \{DF_\phi\}}{\partial L} \quad \in \mathbf{R}^{N_t};$$

$$\{D2F_\psi\} = \frac{\partial \{DF_\psi\}}{\partial y_t} + \frac{\partial \{DF_\psi\}}{\partial L} \quad \in \mathbf{R}^{N_l}.$$

Derivatives of Matrices used in the Potential Energy

$$[P_1]_{\alpha_p} = -3M[V_{po}]_{\alpha_p};$$

$$[P_2]_{\alpha_p} = -3m_a[V_{po}]_{\alpha_p};$$

$$[P_3]_{\alpha_p} = \begin{bmatrix} 2\rho_t \Big\{ \int_0^L \{F_\psi(y_t)\} dy_t \Big\} \{W_{tp}\}^T_{\alpha_p} - 6\rho_t \cos(\alpha_t) \Big\{ \int_0^L \{F_\psi(y_t)\} dy_t \Big\} \{\hat{W}_{po}\}^T_{\alpha_p} \\ 2\rho_t \Big\{ \int_0^L \{F_\phi(y_t)\} dy_t \Big\} \{U_{tp}\}^T_{\alpha_p} + 6\rho_t \sin(\alpha_t) \Big\{ \int_0^L \{F_\phi(y_t)\} dy_t \Big\} \{\hat{W}_{po}\}^T_{\alpha_p} \end{bmatrix}$$

$$+ 2m_s[A_{p_1}]^T[T_{tp}]\alpha_p - 6m_s[A_{p_1}]^T\{\hat{W}_{to}\}\{\hat{W}_{po}\}^T_{\alpha_p};$$

$$\{P_4\}_{\alpha_p} = \{O\};$$

$$[P_5]_{\alpha_p} = [O];$$

$$\{P_6\}_{\alpha_p} = (2m_s + \rho_t L)L\{W_{tp}\}_{\alpha_p} - 3(2m_s + \rho_t L)L\cos(\alpha_t)\{\hat{W}_{po}\}_{\alpha_p};$$

$$[P_1]_{\alpha_t} = [O];$$

$$[P_2]_{\alpha_t} = [O];$$

$$[P_3]_{\alpha_t} = \begin{bmatrix} 2\rho_t\Big\{\int_0^L\{F_\psi(y_t)\}dy_t\Big\}\{W_{tp}\}^T_{\alpha_t} + 6\rho_t\sin(\alpha_t)\Big\{\int_0^L\{F_\psi(y_t)\}dy_t\Big\}\{\hat{W}_{po}\}^T \\ 2\rho_t\Big\{\int_0^L\{F_\phi(y_t)\}dy_t\Big\}\{U_{tp}\}^T_{\alpha_t} + 6\rho_t\cos(\alpha_t)\Big\{\int_0^L\{F_\phi(y_t)\}dy_t\Big\}\{\hat{W}_{po}\}^T \end{bmatrix}$$

$$+ 2m_s[A_{p_1}]^T[T_{tp}]_{\alpha_t} - 6m_s[A_{p_1}]^T\{\hat{W}_{to}\}_{\alpha_t}\{\hat{W}_{po}\}^T;$$

$$\{P_4\}_{\alpha_t} = -6m_sL\cos(\alpha_t)[A_{p_1}]^T\{\hat{W}_{to}\}_{\alpha_t} + 6m_sL\sin(\alpha_t)[A_{p_1}]^T\{\hat{W}_{to}\};$$

$$[P_5]_{\alpha_t} = -3m_s[A_{p_1}]^T\Big[\{\hat{W}_{to}\}_{\alpha_t}\{\hat{W}_{to}\}^T + \{\hat{W}_{to}\}\{\hat{W}_{to}\}^T_{\alpha_t}\Big][A_{p_1}];$$

$$\{P_6\}_{\alpha_t} = (2m_s + \rho_t L)L\{W_{tp}\}_{\alpha_t} + 3(2m_s + \rho_t L)L\sin(\alpha_t)\{\hat{W}_{po}\},$$

where:

$$\big(\cdot\big)_{\alpha_i} \triangleq \frac{\partial\big(\cdot\big)}{\partial\alpha_i}, \qquad i = p,\ t;$$

$$[T_{tp}]_{\alpha_p} = \begin{bmatrix} 0 & 0 & 0 \\ 0 & \sin(\alpha_t - \alpha_p) & -\cos(\alpha_t - \alpha_p) \\ 0 & \cos(\alpha_t - \alpha_p) & \sin(\alpha_t - \alpha_p) \end{bmatrix};$$

$$[T_{tp}]_{\alpha_t} = -[T_{tp}]_{\alpha_p};$$

$$[V_{po}]_{\alpha_p} = \begin{bmatrix} 0 & 0 & 0 \\ 0 & -\sin(2\alpha_p) & -\cos(2\alpha_p) \\ 0 & -\cos(2\alpha_p) & \sin(2\alpha_p) \end{bmatrix};$$

$$\{W_{tp}\}_{\alpha_p} = \begin{Bmatrix} 0 \\ \sin(\alpha_t - \alpha_p) \\ -\cos(\alpha_t - \alpha_p) \end{Bmatrix};$$

$$\{W_{tp}\}_{\alpha_t} = -\{W_{tp}\}_{\alpha_p};$$

$$\{U_{tp}\}_{\alpha_p} = \begin{Bmatrix} 0 \\ \cos(\alpha_t - \alpha_p) \\ \sin(\alpha_t - \alpha_p) \end{Bmatrix};$$

$$\{U_{tp}\}_{\alpha_t} = -\{U_{tp}\}_{\alpha_p};$$

$$\{\hat{W}_{po}\}_{\alpha_p} = \begin{Bmatrix} 0 \\ -\sin(\alpha_p) \\ -\cos(\alpha_p) \end{Bmatrix};$$

$$\{\hat{W}_{to}\}_{\alpha_t} = \begin{Bmatrix} 0 \\ -\sin(\alpha_t) \\ -\cos(\alpha_t) \end{Bmatrix}.$$

APPENDIX II: ELEMENTS OF MATRICES 'M' AND 'F'

The matrices $M(q,t)$ and $F(q,\dot{q},t)$ appearing in Eq. (2.37) can be partitioned as follows :

$$M(q,t) = \left[\begin{array}{ccc} M_r(1,1)+M_{SM_r}(1,1) & \vdots\; M_r(1,2)+M_{SM_r}(2,1) & \vdots\; M_{rf}(1,:)+M_{SM_{rf}}(1,:) \\ M_r(2,1)+M_{SM_r}(2,1) & \vdots\; M_r(2,2)+M_{SM_r}(2,2) & \vdots\; M_{rf}(2,:)+M_{SM_{rf}}(2,:) \\ \cdots\cdots & \cdots\cdots & \cdots\cdots \\ M_{fr}(:,1)+M_{SM_{fr}}(:,1) & \vdots\; M_{fr}(:,2)+M_{SM_{fr}}(:,2) & \vdots\; M_f+M_{SM_f} \end{array}\right] \in \mathbf{R}^{(2+N_{tl})\times(2+N_{tl})};$$

$$F(q,\dot{q},t) = \left\{\begin{array}{c} F_r(1)+F_{SM_r}(1) \\ F_r(2)+F_{SM_r}(2) \\ \cdots\cdots \\ F_f+F_{SM_f} \end{array}\right\} \in \mathbf{R}^{(2+N_{tl})};$$

where :

$$\begin{aligned}
N_{tl} &= N_t + N_l; \\
M_r(1,1) &= I_{px} + m_a\{d_p\}^T[U_k]^T[U_k]\{d_p\}; \\
M_r(1,2) &= \{d_p\}^T[U_k]^T[T_{tp}]^T\Big\{L^2\{B_{k_0}\} + m_sL\{D_{k_2}\} \\
&\quad + \Big[[B_{k_1}] + m_s[U_k][A_{p_1}]\Big]\{X\}\Big\}; \\
\{M_{rf}(1,:)\} &= \{d_p\}^T[U_k]^T[T_{tp}][K_2]; \\
M_r(2,1) &= M_r(1,2);
\end{aligned}$$

$$
\begin{aligned}
M_r(2,2) = {} & I_{t_x} + m_s L^2 + m_s \{X\}^T [A_{p_1}]^T [U_k]^T [U_k][A_{p_1}]\{X\} \\
& + 2m_s L \{D_{k_2}\}^T [U_k][A_{p_1}]\{X\}; \\
\{M_{rf}(2,:)\} = {} & \{X\}^T \Big[[H_{k_4}]^T + m_s [A_{p_1}]^T [U_k]^T [A_{p_1}] \Big] \\
& + \{H_{k_2}\}^T + m_s L \{D_{k_2}\}^T [A_{p_1}]; \\
\{M_{fr}(:,1)\} = {} & \{M_{rf}(1,:)\}^T; \\
\{M_{fr}(:,2)\} = {} & \{M_{rf}(2,:)\}^T; \\
M_f = {} & 2[K_4]; \\
F_r(1) = {} & \Big(M_r(1,1) + M_r(1,2) \Big) \ddot{\theta} + m_o \{d_p\}^T [U_k]^T \{\ddot{d}_p\} \\
& + \{d_p\}^T [U_k]^T [T_{tp}]^T \Big\{ L\{A_{k_0}\} + m_s \{D_{k_1}\} + [A_{k_1}]\{X\} \Big\} \ddot{L} \\
& + m_a \{\dot{d}_p\}^T [U_k]\{\dot{d}_p\} + 2m_a \omega_{p_x} \{d_p\}^T [U_k]^T [U_k]\{\dot{d}_p\} \\
& + \{d_p\}^T [U_k]^T [T_{tp}]^T \Big\{ \dot{L}^2 \{A_{k_0}\} + 2L\dot{L}\omega_{t_x} \{B_{k_0}\} + m_s \dot{L} \omega_{t_x} \{D_{k_2}\} \\
& \qquad + \Big[[\dot{A}_{k_2}] + [K_3] \Big] \{\dot{X}\} + \Big[\dot{L}[\dot{A}_{k_1}] + \omega_{t_x} [\dot{B}_{k_1}] \Big] \{X\} \Big\} \\
& + \Big\{ \{d_p\}^T [U_k]^T [\dot{T}_{tp}]^T + \{\dot{d}_p\}^T [U_k]^T [T_{tp}]^T \Big\} \\
& \qquad \Big\{ \{K_1\} + [K_2]\{\dot{X}\} + [K_3]\{X\} \Big\} \\
& - \Big\{ \{\dot{d}_p\}^T + \omega_{p_x} \{d_p\}^T [U_k]^T \Big\} [T_{tp}]_{\alpha_p}^T \Big\{ \{K_1\} + [K_2]\{\dot{X}\} + [K_3]\{X\} \Big\} \\
& + \frac{GM_e}{2R_c^3} \Big(\{d_p\}^T [P_2]_{\alpha_p} \{d_p\} + \{X\}^T [P_3]_{\alpha_p} \{d_p\} \\
& \qquad + \{P_6\}_{\alpha_p}^T \{d_p\} + 6\{l_p\}_{\alpha_p}^T [I_p]\{l_p\} \Big); \\
F_r(2) = {} & \Big(M_r(1,1) + M_r(1,2) \Big) \ddot{\theta} \\
& + \dot{I}_{t_x} \omega_{tx} + 2m_s L \dot{L} \omega_{t_x} + \Big\{ L^2 \{B_{k_0}\} + m_s L \{D_{k_2}\} \Big\}^T [\dot{T}_{tp}]\{\dot{d}_p\} \\
& + \Big\{ L^2 \{B_{k_0}\} + m_s L \{D_{k_2}\} + \Big[[B_{k_1}] + m_s [U_k][A_{p_1}] \Big] \{X\} \Big\}^T [T_{tp}]\{\ddot{d}_p\}
\end{aligned}
$$

$$+\left(\{X\}^T[H_{k_3}]\{X\}+\left\{\{H_{k_1}\}^T+m_s\{D_{k_1}\}^T[U_k][A_{p_1}]\right\}\{X\}\right)\ddot{L}$$

$$+\left\{2L\dot{L}\{B_{k_0}\}+m_s\dot{L}\{D_{k_2}\}\right\}^T[T_{tp}]\{\dot{d}_p\}$$

$$+\{d_p\}^T[U_k]^T[T_{tp}]^T\left\{2L\dot{L}\{B_{k_0}\}+m_s\dot{L}\{D_{k_2}\}\right\}\omega_{px}$$

$$+\left\{\{\dot{d}_p\}^T[U_k]^T[T_{tp}]^T+\{d_p\}^T[U_k]^T[\dot{T}_{tp}]^T\right\}$$
$$\left\{L^2\{B_{k_0}\}+m_sL\{D_{k_2}\}\right\}\omega_{px}$$

$$+\{\dot{d}_p\}^T[\dot{T}_{tp}]^T\left[[B_{k_1}]+m_s[U_k][A_{p_1}]\right]\{X\}$$

$$+\{\dot{d}_p\}^T[T_{tp}]^T\left[[B_{k_1}]+m_s[U_k][A_{p_1}]\right]\{\dot{X}\}+\{\dot{d}_p\}^T[T_{tp}]^T[\dot{B}_{k_1}]\{X\}$$

$$+\left[\{\dot{d}_p\}^T[U_k]^T[T_{tp}]^T+\{d_p\}^T[U_k]^T[\dot{T}_{tp}]^T\right]$$
$$\left[[B_{k_1}]+m_s[U_k][A_{p_1}]\right]\{X\}\omega_{px}$$

$$+\{d_p\}^T[U_k]^T[T_{tp}]^T[\dot{B}_{k_1}]\{X\}\omega_{px}$$

$$+\{d_p\}^T[U_k]^T[T_{tp}]^T\left[[B_{k_1}]+m_s[U_k][A_{p_1}]\right]\{\dot{X}\}\omega_{px}$$

$$+\{\dot{X}\}^T\left[[H_{k_4}]^T+m_s[A_{p_1}]^T[U_k]^T[A_{p_1}]\right]\{\dot{X}\}+\{\dot{X}\}^T[\dot{H}_{k_4}]\{X\}$$

$$+\{\dot{X}\}^T\left[4m_s\omega_{t_x}[A_{p_1}]^T[U_k]^T[U_k][A_{p_1}]+\dot{L}[H_{k_3}]+\dot{L}[H_{k_3}]^T\right]\{X\}$$

$$+\left\{\{\dot{H}_{k_2}\}+m_s\dot{L}\{D_{k_2}\}^T[A_{p_1}]\right\}\{\dot{X}\}+\dot{L}\{X\}^T[\dot{H}_{k_3}]\{X\}$$

$$+\left\{\dot{L}\{H_{k_1}\}^T+m_s\dot{L}\{D_{k_1}\}^T[U_k][A_{p_1}]\right.$$
$$\left.+2m_sL\omega_{t_x}\{D_{k_2}\}^T[U_k][A_{p_1}]\right\}\{\dot{X}\}$$

$$+\left\{\dot{L}\{\dot{H}_{k_1}\}^T+2m_s\dot{L}\omega_{t_x}\{D_{k_2}\}^T[U_k][A_{p_1}]\right\}\{X\}$$

$$-\left\{\{\dot{d}_p\}^T+\omega_{px}\{d_p\}^T[U_k]^T\right\}[T_{tp}]^T_{\alpha_t}\left\{\{K_1\}+[K_2]\{\dot{X}\}+[K_3]\{X\}\right\}$$

$$+\frac{GM_e}{2R_c^3}\left(\{X\}^T[P_3]_{\alpha_t}\{d_p\}+\{X\}^T\{P_4\}_{\alpha_t}+\{X\}^T[P_5]_{\alpha_t}\{X\}\right.$$

$$+\{P_6\}\alpha_t\{d_p\} - 3m_sL^2(\hat{V}_{to})\alpha_t + 6\{l_t\}^T_{\alpha_t}[I_t]\{l_t\}\Big);$$

$$\begin{aligned}
\{F_f\} = &\Big(M_{fr}(:,1) + M_{fr}(:,2)\Big)\ddot{\theta} \\
&+ [K_2]^T[T_{tp}]\{\ddot{d}_p\} + \left\{\frac{1}{2}\{C_{k_5}\} + m_s[A_{p_1}]^T\{D_{k_1}\} + \frac{1}{2}[C_{k_3}]\{X\}\right\}\ddot{L} \\
&+ \left[[K_2]^T[\dot{T}_{tp}] + [\dot{A}_{k_2}]^T[T_{tp}]\right]\left\{\{\dot{d}_p\} + \omega_{px}[U_k]\{d_p\}\right\} \\
&+ [K_2]^T[T_{tp}][U_k]\{\dot{d}_p\}\omega_{px} + \left[[\dot{C}_{k_2}] + [K_5]\right]\{\dot{X}\} \\
&+ \left[\frac{1}{2}\dot{L}[\dot{C}_{k_3}] + \omega_{t_x}[\dot{H}_{k_4}]\right]\{X\} \\
&+ \left\{\frac{1}{2}\dot{L}\{\dot{C}_{k_5}\} + \omega_{t_x}\{\dot{H}_{k_2}\} + m_s\dot{L}\omega_{t_x}[A_{p_1}]^T\{D_{k_2}\}\right\} \\
&- [K_3]^T[T_{tp}]\left\{\{\dot{d}_p\} + \omega_{px}[U_k]\{d_p\}\right\} - [K_5]^T\{\dot{X}\} \\
&- \left[[K_6] + [K_6]^T\right]\{X\} - \{K_8\}^T - \frac{1}{2}\frac{\partial}{\partial\{X\}}\Big(\{\omega_t\}^T[I_t]\{\omega_t\}\Big) \\
&+ \frac{\partial U_s}{\partial\{X\}} + \frac{GM_e}{2R_c^3}\Big\{[P_3]\{d_p\} + \{P_4\} + \Big[[P_5] + [P_5]^T\Big]\{X\} \\
&\qquad - \frac{\partial}{\partial\{X\}}\Big(tr[I_t]\Big) + \frac{\partial}{\partial\{X\}}\Big(\{l_t\}^T[I_t]\{l_t\}\Big)\Big\} \\
&+ \left(\frac{EA\eta}{\omega_o}\right)\begin{Bmatrix} \int_0^L(\dot{\epsilon})\left\{\frac{\partial\dot{\epsilon}}{\partial\{\dot{B}\}}\right\}\mathrm{d}y_t \\ \int_0^L(\dot{\epsilon})\left\{\frac{\partial\dot{\epsilon}}{\partial\{\dot{C}\}}\right\}\mathrm{d}y_t \end{Bmatrix};
\end{aligned}$$

$$M_{SM_r}(1,1) = -M\left\{\frac{\partial\dot{R}_{SM}}{\dot{\alpha}_p}\right\}^T\{CM_{\alpha_p}\};$$

$$M_{SM_r}(1,2) = -M\left\{\frac{\partial\dot{R}_{SM}}{\dot{\alpha}_p}\right\}^T\{CM_{\alpha_t}\};$$

$$\Big\{M_{SM_{rf}}(1,:)\Big\} = -M\left\{\frac{\partial\dot{R}_{SM}}{\dot{\alpha}_p}\right\}^T[CM_X];$$

$$M_{SM_r}(2,1) = -M\left\{\frac{\partial\dot{R}_{SM}}{\dot{\alpha}_t}\right\}^T\{CM_{\alpha_p}\};$$

$$M_{SM_r}(2,2) = -M\left\{\frac{\partial\dot{R}_{SM}}{\dot{\alpha}_t}\right\}^T\{CM_{\alpha_t}\};$$

$$\left\{M_{SM_{rf}}(2,:)\right\} = -M\left\{\frac{\partial \dot{R}_{SM}}{\dot{\alpha}_t}\right\}^T [CM_X];$$

$$\left\{M_{SM_{fr}}(:,1)\right\} = \left\{M_{SM_{rf}}(1,:)\right\}^T;$$

$$\left\{M_{SM_{fr}}(:,2)\right\} = \left\{M_{SM_{rf}}(2,:)\right\}^T;$$

$$\left[M_{SM_{ff}}\right] = -M\left[\frac{\partial \dot{R}_{SM}}{\dot{X}}\right]^T [CM_X];$$

$$\begin{aligned}
F_{SM_r}(1) = & \left(M_{SM_r}(1,1) + M_{SM_r}(1,2)\right)\ddot{\theta} \\
& + \left\{\frac{\mathrm{d}}{\mathrm{d}t}\left(\frac{\partial \dot{R}_{SM}}{\dot{\alpha}_p}\right)\right\}^T \left\{-M\{\dot{R}_{SM}\} - \rho_t \dot{L}\left(L\{D_{k_1}\} + [A_{p_1}]\{X\}\right)\right\} \\
& - \rho_t \left\{\frac{\partial \dot{R}_{SM}}{\dot{\alpha}_p}\right\}^T \left\{(L\ddot{L} + \dot{L}^2)\{D_{k_1}\} + \ddot{L}[A_{p_1}]\{X\} + \dot{L}[A_{p_1}]\{\dot{X}\}\right\} \\
& - M\left\{\frac{\partial \dot{R}_{SM}}{\dot{\alpha}_p}\right\}^T \{CM_F\} \\
& - \left\{\frac{\partial \dot{R}_{SM}}{\alpha_p}\right\}^T \left\{-M\{\dot{R}_{SM}\} - \rho_t \dot{L}\left(L\{D_{k_1}\} + [A_{p_1}]\{X\}\right)\right\} \\
& + \frac{GM_e}{2R_c^3}\left(\left\{\frac{\partial R_{SM}}{\partial \alpha_p}\right\}^T \left\{2[P_1]\{R_{SM}\} + 2[P_2]\{d_p\}\right.\right. \\
& \qquad \left.\left. + [P_3]^T\{X\} + \{P_6\}\right\}\right) \\
& + \frac{GM_e}{2R_c^3}\left(\{R_{SM}\}^T \left\{[P_1]_{\alpha_p}\{R_{SM}\} + 2[P_2]_{\alpha_p}\{d_p\}\right.\right. \\
& \qquad \left.\left. + [P_3]^T_{\alpha_p}\{X\} + \{P_6\}_{\alpha_p}\right\}\right);
\end{aligned}$$

$$\begin{aligned}
F_{SM_r}(2) = & \left(M_{SM_r}(2,1) + M_{SM_r}(2,2)\right)\ddot{\theta} \\
& \left\{\frac{\mathrm{d}}{\mathrm{d}t}\left(\frac{\partial \dot{R}_{SM}}{\dot{\alpha}_t}\right)\right\}^T \left\{-M\{\dot{R}_{SM}\} - \rho_t \dot{L}\left(L\{D_{k_1}\} + [A_{p_1}]\{X\}\right)\right\} \\
& - \rho_t \left\{\frac{\partial \dot{R}_{SM}}{\dot{\alpha}_t}\right\}^T \left\{(L\ddot{L} + \dot{L}^2)\{D_{k_1}\} + \ddot{L}[A_{p_1}]\{X\} + \dot{L}[A_{p_1}]\{\dot{X}\}\right\} \\
& - M\left\{\frac{\partial \dot{R}_{SM}}{\dot{\alpha}_t}\right\}^T \{CM_F\} \\
& - \left\{\frac{\partial \dot{R}_{SM}}{\alpha_t}\right\}^T \left\{-M\{\dot{R}_{SM}\} - \rho_t \dot{L}\left(L\{D_{k_1}\} + [A_{p_1}]\{X\}\right)\right\}
\end{aligned}$$

$$+\frac{GM_e}{2R_c^3}\left(\left\{\frac{\partial R_{SM}}{\partial \alpha_t}\right\}^T\left\{2[P_1]\{R_{SM}\}+2[P_2]\{d_p\}\right.\right.$$
$$\left.\left.+[P_3]^T\{X\}+\{P_6\}\right\}\right)$$
$$+\frac{GM_e}{2R_c^3}\left(\{R_{SM}\}^T\left\{[P_3]^T_{\alpha_t}\{X\}+\{P_6\}_{\alpha_t}\right\}\right);$$

$$\{F_{SM_f}\}=\left\{M_{SM_{fr}}(:,1)+M_{SM_{fr}}(:,2)\right\}\ddot{\theta}$$
$$\left[\frac{\mathrm{d}}{\mathrm{d}t}\left(\frac{\partial \dot{R}_{SM}}{\dot{X}}\right)\right]^T\left\{-M\{\dot{R}_{SM}\}-\rho_t\dot{L}\left(L\{D_{k_1}\}+[A_{p_1}]\{X\}\right)\right\}$$
$$-\rho_t\left[\frac{\partial \dot{R}_{SM}}{\dot{X}}\right]^T\left\{(L\ddot{L}+\dot{L}^2)\{D_{k_1}\}+\ddot{L}[A_{p_1}]\{X\}+\dot{L}[A_{p_1}]\{\dot{X}\}\right\}$$
$$-M\left[\frac{\partial \dot{R}_{SM}}{\dot{X}}\right]^T\{CM_F\}+\rho_t\dot{L}[A_{p_1}]^T\{\dot{R}_{SM}\}$$
$$-\left[\frac{\partial \dot{R}_{SM}}{X}\right]^T\left\{-M\{\dot{R}_{SM}\}-\rho_t\dot{L}\left(L\{D_{k_1}\}+[A_{p_1}]\{X\}\right)\right\}$$
$$+\frac{GM_e}{2R_c^3}\left(\left[\frac{\partial R_{SM}}{\partial X}\right]^T\left\{2[P_1]\{R_{SM}\}+2[P_2]\{d_p\}\right.\right.$$
$$\left.\left.+[P_3]^T\{X\}+\{P_6\}\right\}\right)$$
$$+\frac{GM_e}{2R_c^3}\left([P_3]\{R_{SM}\}\right);$$

where:

$$\left\{\frac{\partial U_s}{\partial\{X\}}\right\}=\left\{\begin{matrix}\partial U_s/\partial\{B\}\\ \partial U_s/\partial\{C\}\end{matrix}\right\};$$
$$\left\{\frac{\partial U_s}{\partial\{B\}}\right\}=EA\left[\int_0^L\left\{\frac{\partial F_\psi}{\partial y_t}\right\}\left\{\frac{\partial F_\psi}{\partial y_t}\right\}^T\mathrm{d}y_t\right]\{B\}$$
$$+(EA/2)\int_0^L\left(\left\{\frac{\partial F_\phi}{\partial y_t}\right\}^T\{C\}\right)^2\left\{\frac{\partial F_\psi}{\partial y_t}\right\}\mathrm{d}y_t;$$

$$\left\{\frac{\partial U_s}{\partial\{C\}}\right\}=EA\int_0^L\left\{\frac{\partial F_\psi}{\partial y_t}\right\}^T\{B\}\left\{\frac{\partial F_\phi}{\partial y_t}\right\}^T\{C\}\left\{\frac{\partial F_\phi}{\partial y_t}\right\}\mathrm{d}y_t$$
$$+(EA/2)\int_0^L\left(\left\{\frac{\partial F_\phi}{\partial y_t}\right\}^T\{C\}\right)^3\left\{\frac{\partial F_\phi}{\partial y_t}\right\}\mathrm{d}y_t;$$

$$\dot{\epsilon} = \left\{\frac{\partial F_\psi}{\partial y_t}\right\}^T \{\dot{B}\} + \left\{\frac{\mathrm{d}}{\mathrm{d}t}\left\{\frac{\partial F_\psi}{\partial y_t}\right\}\right\}^T \{B\}$$
$$\left(\left\{\frac{\partial F_\phi}{\partial y_t}\right\}^T \{C\}\right)\left(\left\{\frac{\partial F_\phi}{\partial y_t}\right\}^T \{\dot{C}\} + \left\{\frac{\mathrm{d}}{\mathrm{d}t}\left\{\frac{\partial F_\phi}{\partial y_t}\right\}\right\}^T \{C\}\right);$$

$$\left\{\frac{\partial \dot{\epsilon}}{\partial \{\dot{B}\}}\right\} = \left\{\frac{\partial F_\psi}{\partial y_t}\right\};$$

$$\left\{\frac{\partial \dot{\epsilon}}{\partial \{\dot{B}\}}\right\} = \left(\left\{\frac{\partial F_\phi}{\partial y_t}\right\}^T \{C\}\right)\left\{\frac{\partial F_\phi}{\partial y_t}\right\};$$

$$\{R_{SM}\} = -\frac{1}{M}\Big\{m_a\{d_p\} + (m_s L + \rho_t L^2/2)[T_{tp}]^T\{D_{k_1}\}$$
$$+ [T_{tp}]^T\Big[m_s[A_{p_1}] + [A_{k_2}]\Big]\{X\}\Big\};$$

$$\{\dot{R}_{SM}\} = -\frac{1}{M}\Big\{m_a[\dot{T}_{tp}]\{d_p\} + m_a[T_{tp}]\{\dot{d}_p\} + (m_s + \rho_t L)\dot{L}\{D_{k_1}\}$$
$$+ [\dot{A}_{k_2}]\{X\} + \Big[m_s[A_{p_1}] + [A_{k_2}]\Big]\{\dot{X}\}\Big\}$$
$$+ \{\omega_t\} \times \Big\{[T_{tp}]\{R_{SM}\}\Big\};$$

$$\{CM_{\alpha_p}\} = \frac{m_a}{M}[T_1]\{d_p\};$$

$$\{CM_{\alpha_t}\} = -\frac{m_a}{M}[T_1]\{d_p\} + [U_k][T_{tp}]\{R_{SM}\};$$

$$[CM_X] = -\frac{1}{M}\Big[m_s[A_{p_1}] + [A_{k_2}]\Big];$$

$$\{CM_F\} = -\frac{1}{M}\Big\{m_a(\dot{\alpha}_t - \dot{\alpha}_p)^2[T_2]\{d_p\} + 2m_a[\dot{T}_{tp}]\{\dot{d}_p\}$$

$$+ m_a[T_{tp}]\{\ddot{d}_p\} + \Big((m_s + \rho_t L)\ddot{L} + \rho_t \dot{L}^2\Big)\{D_{k_1}\}$$
$$+ \Big[\ddot{L}[A_{k_1}] + \dot{L}[\dot{A}_{k_1}]\Big]\{X\} + 2[\dot{A}_{k_2}]\{\dot{X}\}\Big\}$$
$$+ \ddot{\theta}[U_k][T_{tp}]\{R_{SM}\} + \omega_{t_x}[U_k][\dot{T}_{tp}]\{R_{SM}\}$$
$$+ \omega_{t_x}[U_k][T_{tp}]\{\dot{R}_{SM}\};$$

$$\left\{\frac{\partial \dot{R}_{SM}}{\partial \dot{\alpha}_p}\right\} = \frac{m_a}{M}[T_1]\{d_p\};$$

$$\frac{\mathrm{d}}{\mathrm{d}t}\left\{\frac{\partial \dot{R}_{SM}}{\partial \dot{\alpha}_p}\right\} = \frac{m_a}{M}[T_1]\{\dot{d}_p\} + \frac{m_a}{M}[\dot{T}_1]\{d_p\};$$

$$\left\{\frac{\partial \dot{R}_{SM}}{\partial \alpha_p}\right\} = -\frac{m_a}{M}(\dot{\alpha}_t - \dot{\alpha}_p)[T_1]_{\alpha_p}\{d_p\} - \frac{m_a}{M}[T_{tp}]_{\alpha_p}\{\dot{d}_p\}$$
$$+ \omega_{tx}[U_k][T_{tp}]_{\alpha_p}\{R_{SM}\} + \omega_{tx}[U_k][T_{tp}]\{R_{SM}\}_{\alpha_p};$$

$$\left\{\frac{\partial \dot{R}_{SM}}{\partial \dot{\alpha}_t}\right\} = -\frac{m_a}{M}[T_1]\{d_p\} + [U_k][T_{tp}]\{R_{SM}\};$$

$$\frac{\mathrm{d}}{\mathrm{d}t}\left\{\frac{\partial \dot{R}_{SM}}{\partial \dot{\alpha}_t}\right\} = -\frac{m_a}{M}[T_1]\{\dot{d}_p\} - \frac{m_a}{M}[\dot{T}_1]\{d_p\} + [U_k]\{\dot{R}_{SM}\};$$

$$\left\{\frac{\partial \dot{R}_{SM}}{\partial \alpha_t}\right\} = -\frac{m_a}{M}(\dot{\alpha}_t - \dot{\alpha}_p)[T_1]_{\alpha_t}\{d_p\} - \frac{m_a}{M}[T_{tp}]_{\alpha_t}\{\dot{d}_p\}$$
$$+ \omega_{tx}[U_k][T_{tp}]_{\alpha_t}\{R_{SM}\} + \omega_{tx}[U_k][T_{tp}]\{R_{SM}\}_{\alpha_t};$$

$$\left[\frac{\partial \dot{R}_{SM}}{\partial \dot{X}}\right] = -\frac{1}{M}\Big[m_s[A_{p_1}] + [A_{k_2}]\Big];$$

$$\frac{\mathrm{d}}{\mathrm{d}t}\left[\frac{\partial \dot{R}_{SM}}{\partial \dot{X}}\right] = -\frac{1}{M}[\dot{A}_{k_2}];$$

$$\left[\frac{\partial \dot{R}_{SM}}{\partial X}\right] = \omega_{t_x}[U_k][T_{tp}]\left[\frac{\partial R_{SM}}{\partial X}\right] - \frac{1}{M}[\dot{A}_{k_2}];$$

$$\left\{\frac{\partial R_{SM}}{\partial \alpha_p}\right\} = -\frac{1}{M}\left\{(m_s L + \rho_t L^2/2)[T_{tp}]^T_{\alpha_p}\{D_{k_1}\} + [T_{tp}]^T_{\alpha_p}\left[m_s[A_{p_1}] + [A_{k_2}]\right]\{X\}\right\};$$

$$\left\{\frac{\partial R_{SM}}{\partial \alpha_t}\right\} = -\frac{1}{M}\left\{(m_s L + \rho_t L^2/2)[T_{tp}]^T_{\alpha_t}\{D_{k_1}\} + [T_{tp}]^T_{\alpha_t}\left[m_s[A_{p_1}] + [A_{k_2}]\right]\{X\}\right\};$$

$$\left[\frac{\partial R_{SM}}{\partial X}\right] = -\frac{1}{M}[T_{tp}]^T\left[m_s[A_{p_1}] + [A_{k_2}]\right];$$

$$[T_1] = \begin{bmatrix} 0 & 0 & 0 \\ 0 & -\sin(\alpha_t - \alpha_p) & \cos(\alpha_t - \alpha_p) \\ 0 & -\cos(\alpha_t - \alpha_p) & -\sin(\alpha_t - \alpha_p) \end{bmatrix};$$

$$[T_2] = \begin{bmatrix} 0 & 0 & 0 \\ 0 & -\cos(\alpha_t - \alpha_p) & -\sin(\alpha_t - \alpha_p) \\ 0 & \sin(\alpha_t - \alpha_p) & -\cos(\alpha_t - \alpha_p) \end{bmatrix};$$

$$[\dot{T}_1] = (\dot{\alpha}_t - \dot{\alpha}_p)\,[T_2];$$

$$[T_1]_{\alpha_p} = -\,[T_2];$$

$$[T_1]_{\alpha_t} = [T_2].$$

The matrices used in the above equations were defined in Appendix I.

APPENDIX III: NONLINEAR AND LINEARIZED EQUATIONS OF MOTION FOR THE RIGID SUBSYSTEM

Nonlinear Equation

The nonlinear equations of motion for the rigid degrees of freedom can be expressed as

$$\begin{bmatrix} M_{11} & M_{12} \\ M_{21} & M_{22} \end{bmatrix} \begin{Bmatrix} \ddot{\alpha}_p \\ \ddot{\alpha}_t \end{Bmatrix} + \begin{Bmatrix} F_1 \\ F_2 \end{Bmatrix} = \begin{Bmatrix} M_x \\ LT_{\alpha_t} \end{Bmatrix}, \qquad (III.1)$$

where:

$$M_{11} = m_a m_c (d_{py}^2 + d_{pz}^2) + I_{px};$$

$$M_{12} = m_1 m_c \Big(d_{py} \cos(\alpha) + d_{pz} \sin(\alpha) \Big);$$

$$M_{21} = M_{12};$$

$$M_{22} = \rho_t L^3/3 + m_s L^2 - m_1^2/M;$$

$$\begin{aligned} F_1 =& (M_{11} + M_{12})\ddot{\theta} + m_a m_c d_{py} \ddot{d}_{pz} + 2 m_a m_c d_{pz} \dot{d}_{pz} \omega_{p_x} \\ &+ \Big\{ (m_s m_c + \rho_t L)\ddot{L} + \rho_t \dot{L}^2 - m_1 \omega_{t_x}^2 m_c \Big\} \Big(d_{py} \sin(\alpha) - d_{pz} \cos(\alpha) \Big) \\ &+ \Big\{ (m_s m_c + \rho_t L + m_2 m_c) \dot{L} \omega_{t_x} \Big\} \Big(d_{py} \cos(\alpha) + d_{pz} \sin(\alpha) \Big) \\ &+ \Big(-m_s \dot{L} \cos(\alpha) + m_1 \omega_{t_x} \sin(\alpha) \Big) m_a \dot{d}_{pz}/M \\ &+ 3\mu m_a (D_{t_y}^2 - D_{t_z}^2) \sin(2\alpha_p) + 6\mu m_a D_{t_y} D_{t_z} \cos(2\alpha_p) \\ &+ 2\mu m_1 \Big(D_{t_y} \sin(\alpha) - D_{t_z} \cos(\alpha) \Big) \\ &+ 6\mu m_1 \cos(\alpha_t) \Big(D_{t_y} \sin(\alpha_p) + D_{t_z} \cos(\alpha_p) \Big) \\ &+ 3\mu (I_{pz} - I_{py}) \sin(2\alpha_p) - 6\mu I_{pyz} \cos(2\alpha_p) \end{aligned}$$

$$
\begin{aligned}
&+ 3\mu m_p(R_{SM_y}^2 - R_{SM_z}^2)\sin(2\alpha_p) \\
&+ 6\mu m_p R_{SM_y} R_{SM_z}\cos(2\alpha_p) + \mu p_1 + \mu p_2; \\
F_2 =&(M_{21} + M_{22})\ddot{\theta} + m_1 m_c \cos(\alpha)\ddot{d}_{pz} \\
&+ \Big(\rho_t L^2 \dot{L} + 2m_s \dot{L}\dot{L} - 2m_1 m_2 \dot{L}/M\Big)\omega_{t_x} \\
&+ m_1 m_c \omega_{px}^2 \Big(d_{py}\sin(\alpha) - d_{pz}\cos(\alpha)\Big) \\
&+ m_1(1 + m_c)\dot{d}_{pz}\omega_{p_x}\sin(\alpha) - m_a \rho_t L \dot{L}\omega_{p_x}\Big(d_{py}\cos(\alpha) + d_{pz}\sin(\alpha)\Big)/M \\
&- m_a \rho_t L \dot{L}\dot{d}_{pz}\cos(\alpha)/M - 2\mu m_1\Big(D_{t_y}\sin(\alpha) - D_{t_z}\cos(\alpha)\Big) \\
&+ 6\mu m_1 \sin(\alpha_t)\Big(D_{t_y}\cos(\alpha_p) - D_{t_z}\sin(\alpha_p)\Big) \\
&+ 3\mu(m_s L^2 + \rho_t L^3/3)\sin(2\alpha_t) - \mu p_1 - \mu p_2; \\
p_1 =&\Big(\frac{m_1}{M}\Big)\Big\{-2m_a D_{t_y}\sin(\alpha)\Big(1 - 3\cos^2(\alpha_p)\Big) + 2m_a D_{t_z}\cos(\alpha)\Big(1 - 3\sin^2(\alpha_p)\Big) \\
&+ 3m_a \sin(2\alpha_p)\Big(D_{t_y}\cos(\alpha) - D_{t_z}\sin(\alpha)\Big) + 3m_1\sin(2\alpha_t)\Big\}; \\
p_2 =&\Big(\frac{m_p m_1}{M}\Big)\Big\{-2\Big(R_{SM_y}\sin(\alpha) - R_{SM_z}\cos(\alpha)\Big) + 6R_{SM_y}\sin(\alpha)\cos^2(\alpha_p) \\
&- 6R_{SM_z}\cos(\alpha)\sin^2(\alpha_p) + 3\sin(2\alpha_p)\Big(R_{SM_y}\cos(\alpha) - R_{SM_z}\sin(\alpha)\Big)\Big\};
\end{aligned}
$$

$$
\begin{aligned}
R_{SM_y} =&\Big(-m_a d_{py} - m_1\cos(\alpha)\Big)/M; \\
R_{SM_z} =&\Big(-m_a d_{pz} - m_1\sin(\alpha)\Big)/M; \\
D_{t_y} =&R_{SM_y} + d_{py}; \\
D_{t_z} =&R_{SM_z} + d_{pz}; \\
m_a =&\rho_t L + m_o + m_s; \\
m_1 =&m_s L + \rho_t L^2/2; \\
m_2 =&m_s + \rho_t L; \\
m_c =&1 - m_a/M; \\
M =&m_p + m_o + \rho_t L + m_s;
\end{aligned}
$$

$$\mu = \frac{GM_e}{2R_c^3}.$$

Linear Equation

The nonlinear equations of motion for the attitude dynamics of the tethered system are linearized about some arbitrary trajectory for the platform and tether pitch, and offset motion along the local horizontal. The offset along the local vertical is kept fixed at D_{py}. The governing equations of motion can be represented as

$$\begin{aligned}
&\begin{bmatrix} ML_{11} & ML_{12} \\ ML_{21} & ML_{22} \end{bmatrix} \begin{Bmatrix} \ddot{\alpha}_p \\ \ddot{\alpha}_t \end{Bmatrix} + \begin{bmatrix} GL_{11} & GL_{12} \\ GL_{21} & GL_{22} \end{bmatrix} \begin{Bmatrix} \dot{\alpha}_p \\ \dot{\alpha}_t \end{Bmatrix} \\
&\quad + \begin{bmatrix} KL_{11} & KL_{12} \\ KL_{21} & KL_{22} \end{bmatrix} \begin{Bmatrix} \alpha_p \\ \alpha_t \end{Bmatrix} + \begin{Bmatrix} MD_1 \\ MD_2 \end{Bmatrix} \ddot{D}_z \\
&\quad + \begin{Bmatrix} GD_1 \\ GD_2 \end{Bmatrix} \dot{D}_z + \begin{Bmatrix} KD_1 \\ KD_2 \end{Bmatrix} D_z + \begin{Bmatrix} PL_1 \\ PL_2 \end{Bmatrix} = \begin{Bmatrix} M_x \\ LT_{\alpha_t} \end{Bmatrix}, \quad (III.2)
\end{aligned}$$

where:

$$\begin{aligned}
ML_{11} &= m_a(D_{py}^2 + D_{pz}^2) + I_{px}; \\
ML_{12} &= m_1\Big(D_{py}\cos(\bar{\alpha}) + D_{pz}\sin(\bar{\alpha})\Big); \\
ML_{21} &= ML_{12}; \\
ML_{22} &= m_s L^2 + \rho_t L^3/3; \\
GL_{11} &= 2m_a D_{pz}\dot{D}_{pz}; \\
GL_{12} &= -2m_1\dot{\theta}\Big(D_{py}\sin(\bar{\alpha}) - D_{pz}\cos(\bar{\alpha})\Big) + 2m_2\dot{L}\Big(D_{py}\cos(\bar{\alpha}) + D_{pz}\sin(\bar{\alpha})\Big); \\
GL_{21} &= 2m_1\dot{\theta}\Big(D_{py}\sin(\bar{\alpha}) - D_{pz}\cos(\bar{\alpha})\Big) + 2m_1\dot{D}_{pz}\sin(\bar{\alpha}); \\
GL_{22} &= 2m_s L\dot{L} + \rho_t L^2\dot{L}; \\
KL_{11} &= m_1\ddot{\theta}\Big(D_{py}\sin(\bar{\alpha}) - D_{pz}\cos(\bar{\alpha})\Big) - m_2\ddot{L}\Big(D_{py}\cos(\bar{\alpha}) + D_{pz}\sin(\bar{\alpha})\Big)
\end{aligned}$$

$$
\begin{aligned}
&- \rho_t \dot{L}^2 \Big(D_{py}\cos(\bar{\alpha}) + D_{pz}\sin(\bar{\alpha}) \Big) + m_1 \dot{\theta}^2 \Big(D_{py}\cos(\bar{\alpha}) + D_{pz}\sin(\bar{\alpha}) \Big) \\
&+ 2m_2 \dot{L}\dot{\theta} \Big(D_{py}\sin(\bar{\alpha}) - D_{pz}\cos(\bar{\alpha}) \Big) + 6m_a\mu(D_{py}^2 - D_{pz}^2)\cos(2\bar{\alpha}_p) \\
&- 12m_a\mu D_{py} D_{pz}\sin(2\bar{\alpha}_p) - 2m_1\mu \Big(D_{py}\cos(\bar{\alpha}) + D_{pz}\sin(\bar{\alpha}) \Big) \\
&+ 6m_1\mu\cos(\bar{\alpha}_t) \Big(D_{py}\cos(\bar{\alpha}_p) - D_{pz}\sin(\bar{\alpha}_p) \Big) - 6\mu(I_{py} - I_{pz})\cos(2\bar{\alpha}_p) \\
&+ 12\mu I_{pyz}\sin(2\bar{\alpha}_p);
\end{aligned}
$$

$$
\begin{aligned}
KL_{12} = &- m_1 \ddot{\theta} \Big(D_{py}\sin(\bar{\alpha}) - D_{pz}\cos(\bar{\alpha}) \Big) + m_2 \ddot{L} \Big(D_{py}\cos(\bar{\alpha}) + D_{pz}\sin(\bar{\alpha}) \Big) \\
&+ \rho_t \dot{L}^2 \Big(D_{py}\cos(\bar{\alpha}) + D_{pz}\sin(\bar{\alpha}) \Big) - m_1 \dot{\theta}^2 \Big(D_{py}\cos(\bar{\alpha}) + D_{pz}\sin(\bar{\alpha}) \Big) \\
&- 2m_2 \dot{L}\dot{\theta} \Big(D_{py}\sin(\bar{\alpha}) - D_{pz}\cos(\bar{\alpha}) \Big) + 2m_1\mu \Big(D_{py}\cos(\bar{\alpha}) + D_{pz}\sin(\bar{\alpha}) \Big) \\
&- 6m_1\mu\sin(\bar{\alpha}_t) \Big(D_{py}\sin(\bar{\alpha}_p) + D_{pz}\cos(\bar{\alpha}_p) \Big);
\end{aligned}
$$

$$
\begin{aligned}
KL_{21} = \; & m_1 \ddot{\theta} \Big(D_{py}\sin(\bar{\alpha}) - D_{pz}\cos(\bar{\alpha}) \Big) + m_1 \ddot{D}_{pz}\sin(\bar{\alpha}) \\
&- m_1 \dot{\theta}^2 \Big(D_{py}\cos(\bar{\alpha}) + D_{pz}\sin(\bar{\alpha}) \Big) - 2m_1 \dot{\theta}\dot{D}_{pz}\cos(\bar{\alpha}); \\
&+ 2m_1\mu \Big(D_{py}\cos(\bar{\alpha}) + D_{pz}\sin(\bar{\alpha}) \Big) \\
&- 6m_1\mu\sin(\bar{\alpha}_t) \Big(D_{py}\sin(\bar{\alpha}_p) + D_{pz}\cos(\bar{\alpha}_p) \Big);
\end{aligned}
$$

$$
\begin{aligned}
KL_{22} = &- m_1 \ddot{\theta} \Big(D_{py}\sin(\bar{\alpha}) - D_{pz}\cos(\bar{\alpha}) \Big) - m_1 \ddot{D}_{pz}\sin(\bar{\alpha}) \\
&+ m_1 \dot{\theta}^2 \Big(D_{py}\cos(\bar{\alpha}) + D_{pz}\sin(\bar{\alpha}) \Big) + 2m_1 \dot{\theta}\dot{D}_{pz}\cos(\bar{\alpha}) \\
&- 2m_1\mu \Big(D_{py}\cos(\bar{\alpha}) + D_{pz}\sin(\bar{\alpha}) \Big) \\
&+ 6m_1\mu\cos(\bar{\alpha}_t) \Big(D_{py}\cos(\bar{\alpha}_p) - D_{pz}\sin(\bar{\alpha}_p) \Big) \\
&+ 6\mu(m_s L^2 + \rho_t L^3/3)\cos(2\bar{\alpha}_t);
\end{aligned}
$$

$$
MD_1 = m_a D_{py};
$$

$$
MD_2 = m_1\cos(\bar{\alpha});
$$

$$GD_1 = 2m_a\dot{\theta}D_{pz};$$

$$GD_2 = 2m_1\dot{\theta}\sin(\bar{\alpha});$$

$$\begin{aligned}KD_1 = {} & 2m_a\ddot{\theta}D_{pz} + m_1\ddot{\theta}\sin(\bar{\alpha}) - m_2\ddot{L}\cos(\bar{\alpha}) + 2m_a\dot{\theta}\dot{D}_{pz} \\ & - \rho_t\dot{L}^2\cos(\bar{\alpha}) + m_1\dot{\theta}^2\cos(\bar{\alpha}) + 2m_2\dot{L}\dot{\theta}\sin(\bar{\alpha}) - 6m_a\mu D_{pz}\sin(2\bar{\alpha}_p) \\ & + 6m_a\mu D_{py}\cos(2\bar{\alpha}_p) - 2m_1\mu\cos(\bar{\alpha}) + 6m_1\mu\cos(\bar{\alpha}_t)\cos(\bar{\alpha}_p);\end{aligned}$$

$$KD_2 = m_1\ddot{\theta}\sin(\bar{\alpha}) + m_1(2\mu - \dot{\theta}^2)\cos(\bar{\alpha}) - 6m_1\mu\sin(\bar{\alpha}_t)\sin(\bar{\alpha}_p);$$

$$\begin{aligned}PL_1 = {} & (M_{11} + M_{12})\ddot{\theta} \\ & + m_a(D_{py}^2 + D_{pz}^2)\ddot{\theta} + I_{px}\ddot{\theta} + m_1\ddot{\theta}\Big(D_{py}\cos(\bar{\alpha}) + D_{pz}\sin(\bar{\alpha})\Big) \\ & + m_aD_{py}\ddot{D}_{pz} + m_2\ddot{L}\Big(D_{py}\sin(\bar{\alpha}) - D_{pz}\cos(\bar{\alpha})\Big) \\ & + 2m_a\dot{\theta}D_{pz}\dot{D}_{pz} + (\rho_t\dot{L}^2 - m_1\dot{\theta}^2)\Big(D_{py}\sin(\bar{\alpha}) - D_{pz}\cos(\bar{\alpha})\Big) \\ & + 2m_2\dot{L}\dot{\theta}\Big(D_{py}\cos(\bar{\alpha}) + D_{pz}\sin(\bar{\alpha})\Big) + 3m_a\mu(D_{py}^2 - D_{pz}^2)\sin(2\bar{\alpha}_p) \\ & + 6m_a\mu D_{py}D_{pz}\cos(2\bar{\alpha}_p) + 2m_1\mu\Big(D_{py}\sin(\bar{\alpha}) - D_{pz}\cos(\bar{\alpha})\Big) \\ & + 6m_1\mu\cos(\bar{\alpha}_t)\Big(D_{py}\sin(\bar{\alpha}_p) + D_{pz}\cos(\bar{\alpha}_p)\Big) - 3\mu(I_{py} - I_{pz})\sin(2\bar{\alpha}_p) \\ & - 6\mu I_{pyz}\cos(2\bar{\alpha}_p);\end{aligned}$$

$$\begin{aligned}PL_2 = {} & (M_{11} + M_{12})\ddot{\theta} \\ & + m_1\ddot{\theta}\Big(D_{py}\cos(\bar{\alpha}) + D_{pz}\sin(\bar{\alpha})\Big) + (m_sL^2 + \rho_tL^3/3)\ddot{\theta} \\ & + m_1\ddot{D}_{pz}\cos(\bar{\alpha}) + (2m_sL\dot{L} + \rho_tL^2\dot{L})\dot{\theta} \\ & + m_1\dot{\theta}^2\Big(D_{py}\sin(\bar{\alpha}) - D_{pz}\cos(\bar{\alpha})\Big) + 2m_1\dot{\theta}\dot{D}_{pz}\sin(\bar{\alpha}) \\ & - 2m_1\mu\Big(D_{py}\sin(\bar{\alpha}) - D_{pz}\cos(\bar{\alpha})\Big) \\ & + 6m_1\mu\sin(\bar{\alpha}_t)\Big(D_{py}\cos(\bar{\alpha}_p) - D_{pz}\sin(\bar{\alpha}_p)\Big) \\ & + 3\mu(m_sL^2 + \rho_tL^3/3)\sin(2\bar{\alpha}_t);\end{aligned}$$

$$\bar{\alpha} = \bar{\alpha}_t - \bar{\alpha}_p.$$

Here, $\bar{\alpha}_p$, $\bar{\alpha}_t$ define the reference trajectories for platform and tether pitch angles, respectively; α_p and α_t are the differences between the actual and reference values for the platform and tether pitch angles, respectively; D_{py} and D_{pz} are the reference values for the offsets along the local vertical and local horizontal, respectively; and D_z is the offset required by the controller along the local horizontal direction.

Equations for the Offset Control

The dynamic model for the offset control of the tether attitude is based on the linear equation which is decoupled from the platform motion. However, since the platform dynamics is strongly coupled with the tether attitude in the presence of nonzero offset, the platform pitch controller is based on the complete nonlinear equation. These can be presented as

$$m_{\alpha p}(\alpha_p, x, t)\ddot{\alpha}_p + f_{\alpha p}(\alpha_p, \dot{\alpha}_p, x, \dot{x}, t) = M_x; \qquad (III.3)$$

$$\ddot{\alpha}_t = a_1\alpha_t + a_2 D_z + a_3\dot{\alpha}_t + a_4\dot{D}_z + b + c\ddot{D}_z, \qquad (III.4)$$

where:

$$m_{\alpha p}(\alpha_p, x, t) = M_{11} - M_{12}M_{21}/M_{22};$$

$$f_{\alpha p}(\alpha_p, \dot{\alpha}_p, x, \dot{x}, t) = F_1 - M_{12}F_2/M_{22};$$

$$\begin{aligned} a_1 = -\frac{1}{m_{\alpha_t}}\Big\{ & m_1\ddot{\theta}\Big(-D_{py}\sin(\bar{\alpha}) + D_{pz}\cos(\bar{\alpha})\Big) \\ & + m_1(\dot{\theta}^2 - 2\mu)\Big(D_{py}\cos(\bar{\alpha}) + D_{pz}\sin(\bar{\alpha})\Big) \\ & + 6\mu m_1\cos(\bar{\alpha}_t)\Big(D_{py}\cos(\bar{\alpha}_p) - D_{pz}\sin(\bar{\alpha}_p)\Big) \\ & + 6\mu m_{\alpha_t}\cos(2\bar{\alpha}_t)\Big\}; \end{aligned}$$

$$
\begin{aligned}
a_2 = &- \frac{1}{m_{\alpha_t}}\Big\{m_1\ddot{\theta}\sin(\bar{\alpha}) + m_1(2\mu - \dot{\theta}^2)\cos(\bar{\alpha}) \\
&\quad - 6\mu m_1 \sin(\bar{\alpha}_t)\sin(\bar{\alpha}_p)\Big\}; \\
a_3 = &- \frac{\dot{m}_{\alpha_t}}{m_{\alpha_t}}; \\
a_4 = &- \frac{1}{m_{\alpha_t}}\Big\{2m_1\dot{\theta}\sin(\bar{\alpha})\Big\}; \\
b = &- \frac{1}{m_{\alpha_t}}\Big\{m_1\ddot{\theta}\Big(D_{py}\cos(\bar{\alpha}) + D_{pz}\sin(\bar{\alpha})\Big) + m_{\alpha_t}\ddot{\theta} + \dot{m}_{\alpha_t}\dot{\theta} \\
&\quad + m_1(\dot{\theta}^2 - 2\mu)\Big(D_{py}\sin(\bar{\alpha}) - D_{pz}\cos(\bar{\alpha})\Big) \\
&\quad + 6\mu m_1 \sin(\bar{\alpha}_t)\Big(D_{py}\cos(\bar{\alpha}_p) - D_{pz}\sin(\bar{\alpha}_p)\Big) \\
&\quad + 3\mu m_{\alpha_t}\sin(2\bar{\alpha}_t)\Big\}; \\
c = &- \frac{m_1\cos(\bar{\alpha})}{m_{\alpha_t}}; \\
m_{\alpha_t} = &\rho_t L^3/3 + m_s L^2; \\
\dot{m}_{\alpha_t} = &\rho_t L^2 \dot{L} + 2m_s L\dot{L}.
\end{aligned}
$$

The terms used to define the platform pitch equation, Eq.(III.3), were given in the sub–section titled "Nonlinear Equation", Eq.(III.1).

APPENDIX IV: CONTROLLER DESIGN USING GRAPH THEORETIC APPROACH

Some details of the mathematical background and the controller design procedure which assigns specified eigenvalues to the linear time invariant tethered system are described here.

Mathematical Background

Definitions *

A **directed graph** (also called **digraph**) $D = (V, E)$ consists of two finite sets :

- V, the **vertex set**, a nonempty set of elements called the **vertices** of D; and
- E, the **directed edge set**, a (possibly empty) set of elements called the **directed edges** of D;

such that each e in E is assigned an ordered pair of vertices (u, v). If e is a directed edge (also called **edge**) in the digraph D, with associated ordered pair of vertices (u, v), then e is said to join u to v. u is called the origin or the initial vertex of e, and v is referred to as the terminus or the terminal vertex of e. If a number (or an edge weight) is assigned to each edge of a digraph, then the graph is called the **weighted digraph**. In $G = (V, E)$, if the element e of E is assigned an unordered pair (u, v), then G is called a **graph**.

---

* Clark, J., and Holton, D. A., *A First Look at Graph Theory*, World Scientific Publishers, Singapore, 1991, Chapters 1, 7.

A **directed walk** in the digraph D is a finite sequence

$$W = v_0 e_1 v_1 \quad \cdots \quad e_k v_k,$$

whose terms are alternately vertices and edges such that for $i = 1, 2, \cdots, k$, the edge e_i has the origin v_{i-1} and terminus v_i. If u and v are the starting and ending vertices, respectively, of the walk W then the $u - v$ walk (i.e. W) is called closed or open depending on whether $u = v$ or $u \neq v$, respectively. If W does not contain an edge then it is called a trivial walk, else it is nontrivial.

A nontrivial closed walk in a digraph D is called a **cycle** if its origin and internal vertices are distinct. In detail, the closed walk $C = v_0 e_1 v_1 \cdots v_{k-1} e_k v_k (v_k = v_0)$ is a cycle if:

(i) C has at least one edge; and

(ii) $v_0,\ v_1,\ v_2,\ \cdots\ ,\ v_{k-1}$ are k distinct vertices.

Since C contains distinct vertices, it also has distinct edges. The integer k, the number of edges in the cycle, is called the **length** of C. A cycle C, of length k, is denoted by C_k. A set of vertex disjoint cycles is referred to as a **cycle family**. The **width** of the cycle family is the total number of vertices in it.

A graph G is called connected if every two of its vertices are connected. A **tree** is a connected graph whose number of edges is one less than the number of vertices. A **spanning tree** (or complete tree) of a connected graph G is a subgraph which is a tree that involves all the vertices of G. A digraph is said to have a **root** r if r is a vertex and, for every other vertex v, there is a path which starts in r and ends in v. A digraph D is called a **rooted tree** if D has a root from which there is a unique path to every other vertex.

Mapping of linear state-space model into diagraphs *

Consider the Linear Time Invariant (LTI) equation

$$\dot{x} = Ax + Bu, \qquad (IV.1)$$

where $x \in \mathbf{R}^n$ is the state vector; $u \in \mathbf{R}^m$ is the control input vector; $A \in \mathbf{R}^{n \times n}$; and $B \in \mathbf{R}^{n \times m}$. For the state feedback situation the control law can be expressed as

$$u = Fx, \qquad (IV.2)$$

where $F \in \mathbf{R}^{m \times n}$ is the controller matrix. The closed-loop system of Eqs. (IV.1) and (IV.2) can be mapped into the digraph (G^s) defined by a vertex set and an edge set as follows:

- the vertex set consists of m input vertices denoted by $u_1, u_2, \cdots, u_m$, and n state vertices denoted by $1, 2, \cdots, n$;
- the edge set results from the following rules:
  - if the state variable x_j occurs in the x_i-equation, i.e. $a_{ij} \neq 0$, then there exists an edge from the vertex j to the vertex i with a_{ij} as its weight;
  - if the input variable u_k occurs in the x_i-equation, i.e. $b_{ik} \neq 0$, then there exists an edge from the input vertex u_k to the vertex i with the weight b_{ik};
  - finally, if the state variable x_i occurs in the u_k-equation, i.e. $f_{ki} \neq 0$, then there exists an edge from the vertex i to the vertex u_k with the weight f_{ki}.

---

* Reinschke, K. J., *Multivariable Control: A Graph Theoretic Approach*, Lecture Notes in Control and Information Sciences, Edited by: M. Thoma and A. Wyner, Berlin, Springer-Verlag, 1988, Chapters 1,2.

Here, a_{ij} is the i^{th} row and j^{th} column entry of the matrix A; and b_{ik} and f_{ki} are the entries of B and F, respectively.

For illustration, consider a system defined by the matrices

$$A = \begin{bmatrix} 0 & 0 & 1 & 0 \\ 0 & 0 & 0 & 1 \\ a_{31} & a_{32} & a_{33} & a_{34} \\ a_{41} & a_{42} & a_{43} & a_{44} \end{bmatrix}; \quad B = \begin{bmatrix} 0 \\ 0 \\ b_3 \\ b_4 \end{bmatrix}; \quad F = [f_1 \quad f_2 \quad f_3 \quad f_4].$$

The digraph G^s for this dynamic system can be represented as in Figure IV-1.

Obviously, the diagraph G^s contains less information than Eqs. (IV.1) and (IV.2). Actually, G^s reflects the structure of a closed-loop system with state feedback. As far as the small scale systems are concerned, it seems unnecessary to investigate their structures separately. In case of the large scale systems, however, one should start with a structural investigation. Thus, particularly for higher order systems, the diagraph approach is extremely useful.

A typical feature of large scale systems is their sparsity. This structural property becomes evident in the digraph G^s. The digraph reflects only the non-vanishing couplings of the system. So, instead of n^2 state edges and nm control edges one has really to take into account only a small percentage of this number in most sparse systems. Moreover, the diagraph G^s gives an immediate impression of the information flow within the closed loop system. So for higher order systems, the digraph approach to controller design is advantageous from computational point of view.

For lower order systems, which is the case in the present study, this design method gives a simple closed-form expression for the controller that can be readily included in the dynamic simulation program or implemented in real system. This feature allows for efficient simulation with a gain scheduling control for the highly

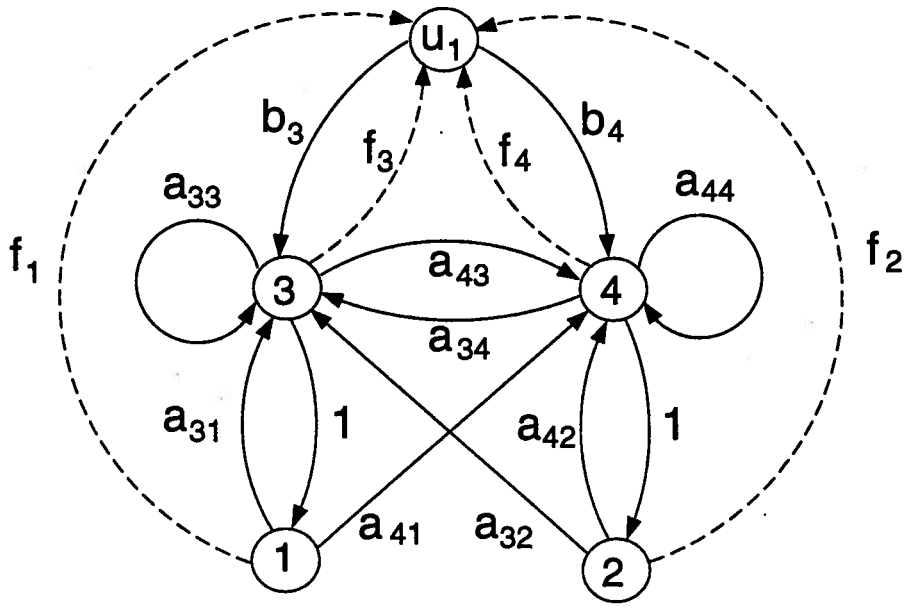

Figure IV-1 Digraph representation of a linear, time-invariant system.

time varying dynamics of the tethered systems.

Controllability

A class of systems characterized by the structure matrix pair $[A, B]$ is said to be **structurally controllable** (or s-controllable) if there exists at least one admissible realization $(A, B) \in [A, B]$ that is controllable in the usual numerical sense.

The $n \times (n + m)$ structure matrix pair $[A, B]$ is s-controllable if and only if its associated digraph $G([Q])$ contains a set of $\bar{m}$ $(\leq m)$ disjoint cacti, each of them rooted in another input vertex and, together, touching all the state vertices. Here

$$[Q] = \begin{pmatrix} [A] & [B] \\ [F] & [O] \end{pmatrix}, \qquad (IV.3)$$

and the **'cactus'** associated with $G([Q])$ is the spanning input-connected graph consisting of a simple path with an input vertex as the initial vertex, p (≥ 0) vertex disjoint cycles and p distinguished edges each of which connects exactly one cycle with the path or with another cycle.

Note, the digraph $G([Q])$ associated with the structure matrix $[Q]$ is the same as the diagraph G^s corresponding to Eqs.(IV.1) and (IV.2) defined earlier.

Characteristic polynomial of a square matrix

Let the characteristic polynomial of the closed-loop system be represented by

$$p(s) = s^n + p_1 s^{n-1} + \quad \cdots \quad + p_{n-1} s + p_n. \qquad (IV.4)$$

The coefficients p_i, $1 \leq i \leq n$, can be determined by the cycle families of width i within the graph $G([Q])$. Each cycle family of width i corresponds to one term in p_i. The numerical value of the term results from the weight of the corresponding cycle family. The value must be multiplied by a sign factor $(-1)^d$ if the cycle family under consideration consists of d vertex disjoint cycles. In particular, p_1 results from all cycles of length 1, with the common sign factor as -1; and p_2 arises from all cycles of length 2, each with a sign factor -1, as well as all disjoint pairs of cycles of length 1, each pair with a sign factor $+1$, etc.

Controller Design Algorithm

Based on the preliminaries discussed above, the state feedback controller

which assigns the closed-loop poles at the desired locations in the complex plane can be obtained by the following procedure.

Step 1: Consider the digraph $G([Q])$, Eq.(IV.3), and choose a subgraph consisting of $\bar{m} \leq m$ disjoint cacti as indicated before. Enumerate these cacti arbitrarily from 1 to $\bar{m}$. There are $\bar{m}!$ possible different enumerations.

Step 2: Choose an $m \times n$ feedback structure matrix $[\bar{F}]$ whose $\bar{m}-1$ nonvanishing elements correspond to feedback edges leading from the final vertex of the path of cactus j to the root of cactus $j+1$ $(j = 1, \cdots, \bar{m}-1)$.

Choose a unit structure vector $[g]$ such that the input vertex associated with the column structure vector $[Bg]$, is the root of cactus 1.

The matrix $[\bar{F}]$ and the vector $[g]$ assure the s-controllability of the single input pair $[A + B\bar{F}, Bg]$. Moreover, for almost all admissible $(A, B) \in [A, B]$, $\bar{F} \in [\bar{F}]$, $g \in [g]$, the pair $(A + B\bar{F}, Bg)$ is controllable in the numerical sense.

Step 3: Choose admissible $(A, B, \bar{F}, g) \in [A, B, \bar{F}, g]$ such that the pair $(A + B\bar{F}, Bg)$ becomes controllable. Set up the system of equations

$$p - p^0 = [P^1]^T f \qquad (IV.5)$$

where: $p = \{p_1,\ p_2,\ \cdots\ ,\ p_n\}^T$ is the vector of characteristic polynomial coefficients defined by the desired pole locations of the closed loop system; p^0 contains the characteristic polynomial coefficients determined by the cycle families in $G(A + B\bar{F})$; and

$$[P^1] = [p^1_{(w,j)}],\quad w = 1, 2, \cdots, n;\ \ j = 1, 2, \cdots, n.$$

The element of $[P^1]$, i.e. $p^1_{(w,j)}$, is the (sign weighted) sum of weights

of all those cycle families of width w within the diagraph of Eq.(IV.3) that contain one feedback edge (with weight 1), from state vertex j to the input of cactus 1.

$[P^1]$ has rank n, if and only if $(A + B\bar{F}, Bg)$ is controllable. Hence, Eq.(IV.5) can be solved for f for almost all $(A, B) \in [A, B]$.

Step 4: The overall feedback matrix

$$F = \bar{F} + gf^T \qquad (IV.6)$$

provides the desired eigenvalue placement.

For single input systems, the controller can directly be designed from Eq.(IV.5) with $\bar{F} = [0]$ and $g = \{0\}$.

Design of the Controller

The state feedback controller is designed to regulate the rigid degrees of freedom, i.e. α_p and α_t. The governing linearized equations of motion for the rigid system are used to that end (Appendix III, Eq.(III.2)). The platform and tether pitch controllers are designed based on the decoupled equations of motion. For the offset control, to regulate the offset motion, the tether pitch equation is augmented by the identity

$$\ddot{D}_z = u_t.$$

The equations governing the tether dynamics can be written in the state space form as

$$\dot{x} = Ax + bu, \qquad (IV.7)$$

where:

$$x = \{\alpha_t,\ d_{pz},\ \dot{\alpha}_t,\ \dot{d}_{pz}\}^T;$$

$$A = \begin{bmatrix} 0 & 0 & 1 & 0 \\ 0 & 0 & 0 & 1 \\ a_{31} & a_{32} & a_{33} & a_{34} \\ a_{41} & a_{42} & a_{43} & a_{44} \end{bmatrix}; \quad b = \begin{bmatrix} 0 \\ 0 \\ b_3 \\ b_4 \end{bmatrix}.$$

The entries in A and b matrices are obtained from Eq.(III.2), Appendix III. The digraph of this system with the state feedback controller is shown in Fig. IV-1. The controller, $u = fx$, can now be designed using Eq.(IV.5) with p^o and $[P^1]$ as given below:

$$p^o = \begin{Bmatrix} -a_{33} - a_{44} \\ a_{33}a_{44} - a_{31} - a_{42} - a_{34}a_{43} \\ -a_{32}a_{43} + a_{42}a_{33} + a_{31}a_{44} - a_{34}a_{41} \\ a_{31}a_{42} - a_{32}a_{41} \end{Bmatrix};$$

$$[P^1] = \begin{bmatrix} 0 & -b_3 & b_3a_{44} - b_4a_{34} & b_3a_{42} - b_4a_{32} \\ 0 & -b_4 & -b_3a_{43} + b_4a_{33} & -b_3a_{41} + b_4a_{31} \\ -b_3 & b_3a_{44} - b_4a_{34} & b_3a_{42} - b_4a_{32} & 0 \\ -b_4 & -b_3a_{43} + b_4a_{33} & -b_3a_{41} + b_4a_{31} & 0 \end{bmatrix}.$$

Similarly, the state model of the platform dynamics can be represented by the matrices

$$A = \begin{bmatrix} 0 & 1 \\ a_{21} & a_{22} \end{bmatrix} \text{ and } \quad b = \begin{Bmatrix} 0 \\ b_2 \end{Bmatrix}.$$

The corresponding matrices for the controller design are

$$p^o = \begin{Bmatrix} -a_{22} \\ -a_{21} \end{Bmatrix} \text{ and } \quad [P^1] = \begin{bmatrix} 0 & -b_2 \\ -b_2 & 0 \end{bmatrix}.$$

APPENDIX V: LINEARIZED EQUATIONS OF MOTION AND CONTROLLER FOR THE FLEXIBLE SUBSYSTEM

Linearized Equations of Motion

The governing equations of motion (Appendix II) are decoupled separating the rigid and flexible subsystems. Neglecting the nonlinear terms from the decoupled equations, the linear model for the flexible system can be represented by the vector equation

$$M_z\ddot{Z} + G_z\dot{Z} + K_z Z + M_{dy}\ddot{d}_{py} + G_{dy}\dot{d}_{py} + K_{dy}d_{py} + M_{dz}\ddot{d}_{pz} + G_{dz}\dot{d}_{pz} + K_{dz}d_{pz} + P_z = Q_z T_L, \quad \text{(IV.1)}$$

where:

$$Z = \left\{\{B - B_{eq}\}^T,\ C^T\right\}^T;$$

$\{B_{eq}\} =$ equillibrium value of $\{B\}$;

$$M_z = 2[K_4];$$

$$G_z = [\dot{C}_{k_2}] + [K_5] - [K_5]^T + \left(\frac{\eta}{\omega_o}\right)\begin{bmatrix}[AB] & [O]\\ [O] & [AC_{sd}]\end{bmatrix} + \begin{bmatrix}\{F_\psi(Y_{dl})\} & \{O\}\\ \{O\} & \{F_\phi(Y_{dt})\}\end{bmatrix}\begin{bmatrix}C_{dl}\{F_\psi(Y_{dl})\}^T & \{O\}\\ \{O\} & C_{dl}\{F_\phi(Y_{dt})\}^T\end{bmatrix};$$

$$K_z = m_s\ddot{\theta}[A_{p_1}]^T[U_k][A_{p_1}] + \ddot{\theta}[H_{k_4}] + \frac{1}{2}\ddot{L}[C_{k_3}] + \frac{1}{2}\dot{L}[\dot{C}_{k_3}] + \dot{\theta}[\dot{H}_{k_4}] - [K_6] - [K_6]^T + \mu[P_5] + \mu[P_5]^T$$

$$+\begin{bmatrix}(-\dot{\theta}^2-4\mu)[I_{b_1}]+[AB] & [O]\\ [O] & (-\dot{\theta}^2+2\mu)[I_{c_1}]+[AC]\end{bmatrix}$$
$$+\begin{bmatrix}\{F_\psi(Y_{dl})\} & \{O\}\\ \{O\} & \{F_\phi(Y_{dt})\}\end{bmatrix}\begin{bmatrix}C_{dl}\dot{L}\{DF_\psi(Y_{dl})\}^T & C_{dl}\{F_\phi(Y_{dl})\}^T\\ C_{dt}\{F_\psi(Y_{dt})\}^T & C_{dt}\dot{L}\{DF_\phi(Y_{dt})\}^T\end{bmatrix};$$

$$M_d = [K_2]^T[T_{tp}];$$

$$G_d = [\dot{A}_{k_2}]^T[T_{tp}]+\dot{\theta}[K_2]^T[T_{tp}][U_k]-[K_3]^T[T_{tp}]$$
$$+\begin{bmatrix}\{O\} & \{O\}\\ F_\psi(Y_{dl})\} & \{O\}\\ \{O\} & \{F_\phi(Y_{dt})\}\end{bmatrix}\begin{bmatrix}0 & C_{dl} & 0\\ 0 & 0 & C_{dt}\end{bmatrix};$$

$$K_d = \ddot{\theta}[K_2]^T[T_{tp}][U_k]+\dot{\theta}[\dot{A}_{k_2}]^T[T_{tp}][U_k]-\dot{\theta}[K_3]^T[T_{tp}][U_k]+\mu[P_3]$$
$$+\dot{\theta}\begin{bmatrix}\{O\} & \{O\}\\ F_\psi(Y_{dl})\} & \{O\}\\ \{O\} & \{F_\phi(Y_{dt})\}\end{bmatrix}\begin{bmatrix}0 & -C_{dl} & 0\\ 0 & 0 & C_{dt}\end{bmatrix};$$

$$P_z = \left\{\{H_{k_2}\}+m_sL[A_{p_1}]^T\{D_{k_2}\}\right\}\ddot{\theta}+\left\{\frac{1}{2}\{C_{k_5}\}+m_s[A_{p_1}]^T\{D_{k_1}\}\right\}\ddot{L}$$
$$-\{K_8\}^T+\frac{\dot{L}}{2}\{\dot{C}_{k5}\}+\dot{\theta}\{\dot{H}_{k_2}\}+m_s\dot{L}\dot{\theta}[A_{p_1}]^T\{D_{k_2}\}+\mu\{P_4\}$$
$$-\begin{Bmatrix}(\dot{\theta}^2+4\mu)\{I_{b_2}\}\\ \{O\}\end{Bmatrix}+\begin{bmatrix}\{O\} & \{O\}\\ F_\psi(Y_{dl})\} & \{O\}\\ \{O\} & \{F_\phi(Y_{dt})\}\end{bmatrix}\begin{Bmatrix}\dot{L}C_{dl}\\ \dot{\theta}Y_{dt}C_{dt}\end{Bmatrix};$$

$$[AB] = EA\left[\int_0^L\left\{\frac{\partial F_\psi}{\partial y_t}\right\}\left\{\frac{\partial F_\psi}{\partial y_t}\right\}^T\mathrm{d}y_t\right];$$

$$[AC] = EA\left[\int_0^L\left(\left\{\frac{\partial F_\psi}{\partial y_t}\right\}^T\{B_e\}\right)\left\{\frac{\partial F_\phi}{\partial y_t}\right\}\left\{\frac{\partial F_\phi}{\partial y_t}\right\}^T\mathrm{d}y_t\right];$$

$$[AC_{sd}] = EA\left[\int_0^L\left(\left\{\frac{\mathrm{d}}{\mathrm{d}t}\left\{\frac{\partial F_\psi}{\partial y_t}\right\}\right\}^T\{B_e\}\right)\left\{\frac{\partial F_\phi}{\partial y_t}\right\}\left\{\frac{\partial F_\phi}{\partial y_t}\right\}^T\mathrm{d}y_t\right].$$

Here: C_{dl} and C_{dt} are the damping coefficients of the longitudinal and transverse

dampers located at distances Y_{dl} and Y_{dt}, respectively; η and ω_o are as defined in Eqs.(2.32) and (2.33); $\{B\}$ and $\{C\}$ are the vector containing longitudinal and transverse modes of the tether; and the coefficient matrices are defined in Appendix I.

Numerical Values of the Coefficient Matrices

The numerical values for the coefficient matrices in Eq.$(IV.1)$ are given below. They correspond to the stationkeeping case with a tether length of 20 km, and mass and elastic properties as given in Chap.4.

$$M_z = \begin{bmatrix} \begin{bmatrix} 532.7 & 519.6 \\ 519.6 & 514.0 \end{bmatrix} & [O] \\ [O] & [Diag.(98.0)] \end{bmatrix} \in \mathbf{R^{12\times 12}};$$

$$G_z = \begin{bmatrix} \begin{bmatrix} 0.405 & 0.405 \\ 0.405 & 0.729 \end{bmatrix} & [G_t]^T \\ [G_t] & [O] \end{bmatrix} \in \mathbf{R^{12\times 12}};$$

$$G_t = 0.1 \times \begin{bmatrix} -1.023 & -0.401 \\ 0.512 & 0.434 \\ -0.341 & -0.318 \\ 0.256 & 0.246 \\ -0.205 & -0.199 \\ 0.171 & 0.168 \\ -0.146 & -0.144 \\ 0.128 & 0.127 \\ -0.114 & -0.113 \\ 0.102 & 0.102 \end{bmatrix};$$

$$K_z = \begin{bmatrix} \begin{bmatrix} 3.08 & 3.08 \\ 3.08 & 5.54 \end{bmatrix} & [O] \\ [O] & [Diag.\{K_t\}] \end{bmatrix} \in \mathbf{R^{12\times 12}};$$

$$P_z = \left\{ \begin{array}{c} -42.982 \\ -41.928 \\ 0.0 \\ 0.0 \\ 0.0 \\ 0.0 \\ 0.0 \\ 0.0 \\ 0.0 \\ 0.0 \end{array} \right\}; \qquad K_t = \left\{ \begin{array}{c} 0.0211 \\ 0.0845 \\ 0.1902 \\ 0.3382 \\ 0.5284 \\ 0.7609 \\ 1.0357 \\ 1.3527 \\ 1.7120 \\ 2.1136 \end{array} \right\};$$

$$M_{dy} = \left\{ \begin{array}{c} -549.0 \\ -524.5 \\ 0.0 \\ 0.0 \\ 0.0 \\ 0.0 \\ 0.0 \\ 0.0 \\ 0.0 \\ 0.0 \end{array} \right\}; \qquad M_{dz} = \left\{ \begin{array}{c} 0.0 \\ 0.0 \\ -88.231 \\ 0.0 \\ -29.410 \\ 0.0 \\ -17.646 \\ 0.0 \\ -12.604 \\ 0.0 \\ -9.803 \\ l0.0 \end{array} \right\};$$

$$G_{dy} = \left\{ \begin{array}{c} 0.0 \\ 0.0 \\ 0.2046 \\ 0.0 \\ 0.0682 \\ 0.0 \\ 0.0409 \\ 0.0 \\ 0.0292 \\ 0.0 \\ 0.0227 \\ 0.0 \end{array} \right\}; \qquad G_{dz} = \left\{ \begin{array}{c} -1.2733 \\ -1.2165 \\ 0.0 \\ 0.0 \\ 0.0 \\ 0.0 \\ 0.0 \\ 0.0 \\ 0.0 \\ 0.0 \end{array} \right\};$$

$$K_{dy} = \left\{ \begin{array}{c} -0.2215e-2 \\ -0.2116e-2 \\ 0.0 \\ 0.0 \\ 0.0 \\ 0.0 \\ 0.0 \\ 0.0 \\ 0.0 \\ 0.0 \end{array} \right\}; \qquad K_{dz} = \{O\}; \qquad Q_z = \left\{ \begin{array}{c} 1.0 \\ 1.0 \\ 0.0 \\ 0.0 \\ 0.0 \\ 0.0 \\ 0.0 \\ 0.0 \\ 0.0 \\ 0.0 \end{array} \right\};$$

$$C_o = \begin{bmatrix} 1.0 & 0.0 \\ 1.0 & 0.0 \\ 0.0 & 0.2221e-3 \\ 0.0 & 0.4443e-3 \\ 0.0 & 0.6664e-3 \\ 0.0 & 0.8886e-3 \\ 0.0 & 0.1111e-2 \\ 0.0 & 0.1333e-2 \\ 0.0 & 0.1555e-2 \\ 0.0 & 0.1777e-2 \\ 0.0 & 0.1999e-2 \\ 0.0 & 0.2221e-2 \end{bmatrix}^T ;$$

where:

$$C_o = \begin{bmatrix} \psi_1(L) & \cdots & \psi_{N_2}(L) & 0 & \cdots & 0 \\ 0 & \cdots & 0 & \left(\partial\Phi_1/\partial y_t\right)_{y_t=0} & \cdots & \left(\partial\Phi_{N_1}/\partial y_t\right)_{y_t=0} \end{bmatrix};$$

$[Diag.(\alpha)] = [D_{ij}];$

with $D_{ij} = 0, \quad \forall\, i \neq j;$

$D_{ii} = \alpha,$ if α is a scalar;

$= \alpha(i),$ if α is a vector.

Design Parameters and Controller Matrices

The numerical values for the weighting matrices used for the controller design and final controller matrices are given below.

B_1- Controller (LQG/LTR)

$$q = 1.0e5;$$

$$Q_o = [C_b]^T[C_b];$$

$$R = 1.0e5;$$

$$\Xi = \begin{bmatrix} 3.0e-2 & 0.0 & 0.0 & 0.0 \\ 0.0 & 3.0e-4 & 0.0 & 0.0 \\ 0.0 & 0.0 & 1.0e-2 & 0.0 \\ 0.0 & 0.0 & 0.0 & 1.0e-4 \end{bmatrix};$$

$$\Theta = 1.5e2;$$

$$A_{fb} = \begin{bmatrix} -1.811e-2 & 1.0 & -1.811e-2 & 0.0 \\ 7.277e-1 & 9.480 & 1.029 & 1.053e+1 \\ -4.460e-2 & 0.0 & -4.460e-2 & 1.0 \\ -7.135e-1 & -9.199 & -1.001 & -1.022e+1 \end{bmatrix};$$

$$B_{fb} = \begin{Bmatrix} -1.8110e-2 \\ -1.0165e-3 \\ -4.4601e-2 \\ -8.1649e-4 \end{Bmatrix};$$

$$C_{fb} = \{0.7126 \quad 9.1993 \quad 1.0002 \quad 10.2202\};$$

C_1- Controller (LQG)

$$Q = \begin{bmatrix} 1.0e-1 & 0.0 & 0.0 & 0.0 \\ 0.0 & 1.0e-2 & 0.0 & 0.0 \\ 0.0 & 0.0 & 1.0e-1 & 0.0 \\ 0.0 & 0.0 & 0.0 & 1.0e-3 \end{bmatrix};$$

$$R = 1.0e+8;$$

$$\Xi = \begin{bmatrix} 1.0e+9 & 0.0 & 0.0 & 0.0 \\ 0.0 & 1.0e+7 & 0.0 & 0.0 \\ 0.0 & 0.0 & 1.0e+1 & 0.0 \\ 0.0 & 0.0 & 0.0 & 1.0e-1 \end{bmatrix};$$

$$\Theta = \begin{bmatrix} 1.0e+9 & 0.0 \\ 0.0 & 1.0e+9 \end{bmatrix};$$

$$A_{fc} = \begin{bmatrix} -1.2363e-3 & 1.0 & 0.0 & 0.0 \\ -2.3062e-4 & -1.6433e-3 & 2.8471e-5 & 7.3920e-3 \\ 0.0 & 0.0 & -4.4732e-3 & 1.0 \\ 1.5779e-5 & 1.4645e-3 & -4.1623e-5 & -8.2105e-3 \end{bmatrix};$$

$$B_{fc} = \begin{bmatrix} 5.5654 & 0.0 \\ 3.3292e-3 & 0.0 \\ 0.0 & 4.4732e-3 \\ 0.0 & 1.0e-5 \end{bmatrix};$$

$$C_{fc} = \{1.5779e-5 \quad 1.4646e-3 \quad -3.1623e-5 \quad -8.2105e-3\};$$

APPENDIX VI: LABORATORY TEST SETUP

The experimental setup used three step-motors with corresponding translator modules and two optical potentiometers. The motors consist of permanent magnet rotors while the stators contain a stack of teeth with several pairs of field windings. The windings can be switched on and off in sequence to produce electromagnetic pole pairs that cause the rotors to move in increaments. The sequential switching of the windings is accomplished by a translator module. The translator module has logic circuitry to interpret a pulse train and "translate" it into the corresponding switching sequence for stator field windings (on/off/reverse state for each phase of the stator). The details of the motors and translators are well documented in reference [110]. Relevant mass, geometry, and other system parameters used in the analysis are listed below:

Mass of Carriage	$= 70.43\ kg$
Mass of inplane traverse	$= 2.23\ kg$
Mass of the pendulum	$= 0.1108\ kg$
Deployment/Retrieval reel diameter	$= 2 \times 10^{-2}\ m$
Pulley diameter	$= 4.4 \times 10^{-2}\ m$
Maximum tether length	$= 2.25\ m$
Maximum offset motion in $X - Y$ plane	$= (\pm\ 0.7\ m) \times (\pm\ 0.7\ m)$
Number of pulses required to move the motors	$= 200\ pulses/rev$

A pair of Softpot optical shaft encoders (S1 series, U.S. Digital Corp.) is used to measure the angular deviation of the tether from the vertical position. The

Softpot is available with ball bearings for motion control applications or torque-loaded to feel like a potentiometer for front panel manual interface. Characteristic features of the Softpot are given below:

- 2-channel quadrature, TTL (Transistor – Transistor Logic) squarewave output;
- 3^{rd} channel index option;
- tracking capability – 0 to 10,000 RPM;
- ball bearing option tracks to 10,000 RPM;
- $-$ 40 to $+$ 100°C operating temperature;
- single $+$ $5v$ supply;
- 100 to 1024 $cycles/rev$;
- small size;
- low cost.